



HAL
open science

Coupling mechanical frictional contact with interfacial fluid flow at small and large scales

Andrei Shvarts

► **To cite this version:**

Andrei Shvarts. Coupling mechanical frictional contact with interfacial fluid flow at small and large scales. Computational Physics [physics.comp-ph]. Université Paris sciences et lettres, 2019. English. NNT : 2019PSLEM009 . tel-02396951

HAL Id: tel-02396951

<https://pastel.hal.science/tel-02396951>

Submitted on 6 Dec 2019

HAL is a multi-disciplinary open access archive for the deposit and dissemination of scientific research documents, whether they are published or not. The documents may come from teaching and research institutions in France or abroad, or from public or private research centers.

L'archive ouverte pluridisciplinaire **HAL**, est destinée au dépôt et à la diffusion de documents scientifiques de niveau recherche, publiés ou non, émanant des établissements d'enseignement et de recherche français ou étrangers, des laboratoires publics ou privés.



THÈSE DE DOCTORAT

DE L'UNIVERSITÉ PSL

Préparée à MINES ParisTech

**Couplage mécano-fluidique pour le contact et le frottement
à petites et à grandes échelles**

Coupling mechanical frictional contact with interfacial fluid flow
at small and large scales

Soutenue par

Andrei SHVARTS

Le 20 mars 2019

École doctorale n°621

**Ingénierie des Systèmes,
Matériaux, Mécanique,
Énergétique**

Spécialité

Mécanique

Composition du jury :

Didier LASSEUX

Directeur de recherche, I2M Université de Bordeaux *Président*

Marco PAGGI

Professeur, IMT School for Advanced Studies Lucca *Rapporteur*

Stanisław STUPKIEWICZ

Professeur, IPPT, Polish Academy of Sciences *Rapporteur*

James GREENWOOD

Reader, University of Cambridge *Examineur*

Valentine REY

Maître de conférence, Université de Nantes *Examineur*

Julien VIGNOLLET

Ingénieur de recherche, Safran Tech, Safran Group *Maître de thèse*

Vladislav YASTREBOV

Chargé de recherche, MINES ParisTech *Maître de thèse*

Georges CAILLETAUD

Professeur, MINES ParisTech *Directeur de thèse*

Nicolas MOULIN

Maître de conférence,
École des Mines de Saint-Étienne *Invité*

Abstract

This thesis deals with the problem of a thin fluid flow in narrow interfaces between contacting solids subject to a normal loading, which is relevant for a range of tribological and engineering applications, as well as for geophysical sciences. The treatment of this problem requires coupling between fluid and solid mechanics, further complicated by contact constraints and potentially complex geometrical features of contacting surfaces. In this thesis a monolithic finite-element framework for handling frictional contact, thin incompressible viscous flow and transfer of fluid-induced tractions to the solid is developed. Additionally, we considered fluid entrapment in “pools” delimited by contact patches and formulated a novel trapped-fluid element using a non-linear compressible constitutive law. This computational framework makes use of image analysis algorithms to distinguish between contact, fluid flow and trapped fluid zones. The constructed framework is suitable for both one- and two-way coupling approaches. First, the developed framework was applied to a study of a fluid trapped between a deformable solid with a wavy surface and a rigid flat. We showed how the contact area and the global coefficient of friction evolve under increasing external load, depending on fluid and solid properties and on the slope of the surface profile. Next, we studied a thin fluid flow between a rigid flat and a deformable solid with a model geometry or random surface roughness. An approximate analytical solution for the fluid flow across a wavy contact interface was derived and compared with numerical results. We showed that for a range of physically relevant parameters, one-way coupling underestimates the interface permeability and the critical external load needed to seal the interface, compared to the two-way approach. A refined non-local phenomenological law for macroscopic permeability of rough contact interfaces was proposed. Finally, the developed framework was used to calculate the evolution of the fluid leakage through a metal-to-sapphire contact interface using an elasto-plastic material behaviour and real measurements of surface roughness.

Résumé en français

Cette thèse traite du problème de l'écoulement d'un fluide dans des interfaces étroites entre des solides en contact sous un chargement normal, ce qui est important pour de nombreuses applications en tribologie, ingénierie et géophysique. Le traitement de ce problème nécessite de prévoir un couplage entre la mécanique des fluides et celle des solides. Les contraintes liées à la présence du contact, ainsi que les caractéristiques spécifiques de la géométrie de surface rajoutent un niveau de complexité significatif. Dans cette thèse, un solveur monolithique par éléments finis permettant la gestion du contact frottant, des écoulements visqueux incompressibles et du transfert des efforts induits par le fluide sur le solide est développé. De plus, la possibilité que le fluide se retrouve piégé dans des cavités délimitées par des zones de contact est prise en compte par l'élaboration d'un nouvel élément dit “de fluide piégé”, qui utilise une loi de comportement compressible non linéaire. Le code résultant de cette méthode comprend des algorithmes d'analyse

d'image permettant de distinguer les zones de contact, d'écoulement de fluide et de fluide piégé. En outre, le code convient aux approches de couplage uni- et bidirectionnel. Le cadre développé a été appliqué dans un premier temps à l'étude d'un fluide piégé entre un solide déformable présentant une surface de contact ondulée et un plan rigide. Pour un système soumis à une charge externe croissante, nous avons examiné l'évolution de la surface de contact et du coefficient de frottement global en fonction des propriétés du fluide et du solide, ainsi que de la pente du profil de surface. Nous avons ensuite étudié l'écoulement d'un fluide entre un plan rigide et un solide déformable avec une géométrie modèle ou une surface rugueuse. Nous avons obtenu une solution analytique approchée qui gouverne le flux de fluide à travers une interface de contact ondulée, et cette dernière a été comparée à nos résultats numériques. Enfin, nous avons montré pour un intervalle de paramètres physiquement pertinents, que le couplage unidirectionnel sous-estime, par rapport à une approche bidirectionnelle, la perméabilité de l'interface ainsi que la charge externe critique nécessaire à la fermeture de l'interface. Une loi phénoménologique raffinée de perméabilité macroscopique des interfaces de contact rugueuses a été proposée. Enfin, le cadre développé a été utilisé pour calculer l'évolution de la fuite de fluide à travers une interface de contact métal sur saphir en utilisant un comportement matériau élasto-plastique et des mesures réelles de la rugosité de surface.

Acknowledgements

Looking back at three (and a half) years that I worked on the PhD thesis, I see this period as a turning point in my life, not only because of academic achievements which I was pursuing, but, more importantly, because of the people whom I met and who helped me to expand boundaries of my mind in various directions.

First of all, I wish to thank Vladislav A. Yastrebov, who devised the ideas on which my PhD is based, and, moreover, constantly helped me during all this time. Every day in his presence I saw an outstanding example of the balance between brave ambition and thoughtful reflection, intensive work and joyful life, between being a demanding supervisor and a caring friend. I am also grateful to Julien Vignollet for his interest in my work (which resulted in investing a great amount of time into helping me see clearer most challenging aspects of this thesis) and for his friendly advices. Likewise, I am obliged to Georges Cailletaud for his wisdom, deep knowledge, guidance and support, which he provided for me in moments when I needed them the most.

I greatly appreciate that James Greenwood, Didier Lasseux, Valentine Rey and Nicolas Moulin found time to evaluate my dissertation. I am very grateful to Stanisław Stupkiewicz and Marco Paggi for reviewing this thesis and for providing constructive and detailed comments. It was an honour for me to present my work in front of such committee.

I would like to thank William Hilth, Alexiane Arnaud, Fang Lu, Faisal Islam, Liliana Moniz da Silva Sancho, Paul Chauchat, Manuel Petersmann, Clement Olivier, Harris Farooq, Juan-Manuel Garcia, Anass Assadiki, Raphaël Cusset, Laurent Lacourt, Aurelien Fouque, Paolo Cinat and many others for an open-minded, friendly and inspiring atmosphere at Mines ParisTech, and, in particular, at *Centre des Matériaux*. A special word is reserved for Basava Raju Akula, with whom I went side-by-side through this PhD journey, to Moubine Al Kotob for a kind welcome in France when it was most needed (and his *amour vache*), and to Anna Ask for a warm and cheerful mood she always creates. I was happy to meet in Paris Denis Kurlov, my friend from Russia, whom I also thank for friendly support and for calculating an important integral in a decisive moment. I am also grateful to Vladimir Esin, Arina Marchenko and Dmitry Tkalich for bringing the “Russian spirit” to the lab. A special thanks goes to my elder colleagues such as Samuel Forest, Jacques Besson, Matthieu Maziere and Jean-Didier Garaud, interaction with whom allowed me to learn much more in Computational Mechanics. I would like to thank also Andreas Almqvist and Francesc Pérez Ràfols for hosting me in snowy Luleå, introducing me to Tribology and for providing essential comments about my work.

The software development performed in this dissertation would not be possible without constant help from Djamel Missoum-Benziane, Nikolay Osipov and Stéphane Quilici. A special thanks goes to Basile Marchand and Grégory Sainte-Luce for helping me in running massive simulations on the lab cluster. I thank all my French colleagues for their patience during the time when I refused to speak French, and for an even bigger patience they needed during the moments when I tried to speak it. Regarding these

attempts, I wish to thank my French teacher Françoise Herbet-Pain, who was also very patient and yet motivated me to learn this language.

I am thankful to Mines ParisTech and Safran Tech (particularly, to Arjen Roos) for the possibility to work on this “*Thèse-Open*” and for the freedom to choose research directions I experienced. I am also thankful to Transvalor for permitting me to prolong the work by three additional (and important) months.

I wish to thank Sergei V. Lupuleac, Senior Lecturer at Peter the Great St. Petersburg Polytechnic University, for his motivating courses on the Mathematical Theory of the Finite-Element Method, which turned out to be essential for my work. I am also grateful for the chance to learn Nonlinear Mechanics from late Professor Alexander M. Samsonov, who guided my first steps as a researcher and introduced me to the culture of scientific writing.

Finally, I owe an everlasting thanks to my parents, whose love and encouragement I have been experiencing all my life. Last, but definitively not the least, I wish to mention my beloved wife Olga, whom I met during my PhD study. Without her inspiration, patience and constant support my thesis could not be finished. With her by my side, I hope this work could become a step towards broader research goals.

June 19th, 2019

Glasgow, UK

“Mathematicians are like a sort of Frenchmen; if you talk to them, they translate it into their own language, and then it is immediately something quite different.”

Johann Wolfgang von Goethe

“It’s a trap!”

Star Wars Episode VI: Return of the Jedi

Contents

Part I	Problem Statement	9
1	Introduction	11
1.1	Contact between rough surfaces	12
1.2	Trapped fluid in contact interface	13
1.3	Fluid-structure interaction approaches	15
1.3.1	One-way and two-way coupling approaches	15
1.3.2	Partitioned and monolithic implementation approaches	16
1.4	Objectives	16
2	Governing equations	19
2.1	Continuum solid mechanics	19
2.1.1	Strain and stress tensors	20
2.1.2	Boundary value problem	22
2.2	Contact mechanics	23
2.2.1	Hertz-Signorini-Moreau conditions	23
2.2.2	Frictional constraints	24
2.3	Continuum fluid mechanics	26
2.3.1	Derivation of Navier-Stokes equations	26
2.3.2	Continuity equation	28
2.3.3	Reynolds equation	29
2.3.4	Boundary conditions for the Reynolds equation	33
2.4	Hydrostatic fluid models	34
2.5	Coupled problem statement	35
2.5.1	Solid mechanics problem with unilateral contact	36
2.5.2	Thin fluid flow	37
2.5.3	Fluid-structure interface	37
2.5.4	Trapped fluid zones	38
2.5.5	Remarks on the coupled problem	39
Part II	Computational framework	41
3	Variational formulation of the coupled problem	43
3.1	Weak formulation of the solid mechanics problem with contact constraints	43
3.1.1	Homogeneous Dirichlet boundary condition	44
3.1.2	Weak form of the contact problem	44
3.1.3	Variational formulation for the frictionless case	45
3.1.4	Variational formulation for the frictional case	46
3.2	Weak formulation of the coupled problem	48
3.2.1	Weak form of the fluid-structure interface balance	49
3.2.2	Virtual work of trapped fluid zones	49
3.2.3	Weak formulation of the fluid flow problem	50

3.2.4	Variational formulation of the coupled problem	51
4	Mechanical contact problem	53
4.1	Contact resolution methods	54
4.1.1	Method of Lagrange multipliers	54
4.1.2	Penalty method	56
4.1.3	Augmented Lagrangian method	60
4.2	Node-to-rigid-surface discretization approach	63
4.2.1	Method of Lagrange multipliers	64
4.2.2	Penalty method	66
4.2.3	Augmented Lagrangian method	69
4.3	Face-to-rigid-surface discretization approach	74
4.3.1	Augmented Lagrangian method	75
4.3.2	Post-processing computation of the real contact area	78
5	Resolution of the trapped fluid problem	81
5.1	Trapped fluid constraints	82
5.1.1	Incompressible fluid model	82
5.1.2	Compressible fluid models	83
5.2	“Super-element” formulation	84
5.2.1	Incompressible fluid	85
5.2.2	Compressible fluid	86
5.2.3	Extension of the trapped fluid zone on the active contact zone	87
5.3	Standard finite-element formulation	88
6	Monolithic resolution of the coupled problem	91
6.1	Thin fluid flow sub-problem	92
6.2	Balance of tractions on the fluid-structure interface	94
6.3	The global residual vector and tangent matrix for the coupled problem	96
6.4	Resolution algorithm	97
Part III	Results and discussions	101
7	Trapped fluid in contact interface	103
7.1	Problem statement	104
7.2	Analytical solutions	104
7.2.1	Westergaard’s solution	104
7.2.2	Kuznetsov’s solution	105
7.3	Numerical problem set-up	106
7.4	Incompressible fluid	109
7.4.1	Evolution of the real contact area	109
7.4.2	Distortion of the periodic wavy surface under a uniform hydrostatic pressure	110
7.4.3	Evolution of maximal frictional traction and global coefficient of friction	112
7.5	Compressible fluid with constant bulk modulus	115
7.6	Compressible fluid with pressure-dependent bulk modulus	117
7.7	Elastic-perfectly plastic solid	119
7.8	Friction in the contact interface	122
7.8.1	Validation of the numerical framework	122
7.8.2	Effect of the trapped fluid on frictional tractions	123

7.9	Conclusions	126
8	Fluid flow in contact interface with model geometry	129
8.1	Fluid flow across a wavy channel brought in contact	129
8.1.1	Problem set-up	130
8.1.2	Wavy profile with pressurized fluid in the interface	131
8.1.3	Approximate analytical solution	133
8.1.4	Numerical results and discussions	135
8.2	Fluid flow across a wavy channel with an “atoll” island and trapped “lagoon”	142
8.2.1	Comparison of the interface transmissivity between one-way and two-way coupling approaches	144
8.2.2	Convergence of the Newton-Raphson method	146
8.3	Conclusions	148
9	Fluid flow through rough contact interface	149
9.1	Fluid flow through rough contact interface with multiple trapped fluid pools	149
9.2	Comparison of the interface transmissivity in one- and two-way coupling approaches	153
9.3	Effective interface transmissivity as a function of the mean fluid pressure and its gradient	155
9.4	Comparison of two methods of the real contact area computation	158
9.5	Effect of elasto-plastic material behaviour on sealing properties	159
9.5.1	Problem set-up	159
9.5.2	Material properties	160
9.5.3	Surface topography	161
9.5.4	Computational framework	162
9.5.5	Results	163
9.6	Conclusions	165
10	Conclusions and perspectives	169
10.1	Original contributions	170
10.1.1	Computational framework	170
10.1.2	Trapped fluid in contact interface	170
10.1.3	Fluid flow in contact interface with model geometries	171
10.1.4	Fluid flow through representative rough contact interface	171
10.2	Perspectives	172
10.2.1	Computational framework	172
10.2.2	Studies	173
	Bibliography	174

Part I

Problem Statement

Chapter 1

Introduction

Résumé de Chapitre 1 “Introduction”

Dans le premier chapitre, nous présentons le sujet principal de cette thèse : l'écoulement d'une couche mince de fluide dans les interfaces de contact, problème important pour de nombreuses applications d'ingénierie et de géophysiques. Ce problème, qui est important pour de nombreuses applications en ingénierie et géophysique, nécessite la résolution d'un problème couplé entre la mécanique des fluides et des solides. Les contraintes de contact, ainsi que les caractéristiques déterministes ou rugueuses de la géométrie de surface, rajoutent un niveau de complexité significatif. Dans un premier temps, nous proposons une revue bibliographique de la description des surfaces rugueuses et des modèles analytiques et numériques de contact. En raison de la rugosité de la surface, le fluide peut se retrouver piégé dans des cavités formées par des zones de contact, offrant ainsi une capacité de charge supplémentaire et réduisant le frottement entre les surfaces en contact. Nous proposons une discussion sur les traitements expérimentaux et analytiques existants du problème de fluide piégé. Nous décrivons ensuite différentes approches d'interaction fluide-structure (unidirectionnelles et bidirectionnelles, partitionnées et monolithiques) et mettons en évidence les modèles les plus pertinents pour le problème étudié. Enfin, nous élaborons le premier objectif de cette thèse qui est le développement d'un schéma de couplage monolithique bidirectionnel pour le problème à l'étude. Le deuxième objectif est l'application de ce schéma pour la comparaison des approches de couplage uni- et bidirectionnelles ainsi qu'à l'étude de l'influence du fluide piégé.

The problem of thin fluid flow in narrow interfaces between contacting or slightly separated deformable solids appears in numerous contexts from tribological, engineering and biological applications to geophysical sciences. Rigorous handling of such problems requires the resolution of a strongly non-linear contact problem, which is further complicated by a multi-field coupling of essentially interrelated fluid and solid mechanics. Moreover, the free volume¹ between contacting surfaces depends on their initial geometry, which can be rather complex, may have deterministic features or, at a certain magnification, may be considered as randomly rough (self-affine) down to atomistic scale.

Numerous applications of the problem of thin fluid flow in contact interfaces include sealing engineering [Müller and Nau, 1998], lubrication in elasto-hydrodynamic and mixed regimes [Sahlin et al., 2010, Stupkiewicz and Marciniszyn, 2009], functioning of human joints [Caligaris and Ateshian, 2008]. Such an interaction between fluids and solids in contact is also relevant for hydraulic fracturing [Bažant et al., 2014], extraction

¹By free volume, here, we mean the space between solids available for fluid to occupy.

of shale gas and oil from rocks and at larger scales in landslides [Viesca and Rice, 2012], slip in pressurized faults [Garagash and Germanovich, 2012] and basal sliding of glaciers [Fischer and Clarke, 1997].

1.1 Contact between rough surfaces

The roughness of contacting surfaces has strong implications in mechanics and physics of contact [Whitehouse, 2010, Thomas, 1999]. Since the contact between solids occurs on separate patches corresponding to asperities of surfaces, [Archard, 1953, Archard, 1957, Greenwood and Williamson, 1966, Bowden and Tabor, 2001], the real contact area is a fraction of the apparent one. The evolution of their ratio under increasing external load determines essential contact properties such as friction, wear, adhesion, is responsible for heat transport through contact interfaces, and, moreover, determines the electric contact resistance. At the same time, the distribution of the free volume between contacting surfaces governs the fluid transport along the interface and thus is responsible for leakage/percolation phenomena, see for example [Dapp et al., 2012, Paggi and He, 2015].

The roughness or more generally the surface morphology may contain deterministic features (turned surfaces [Pérez-Ràfols et al., 2016], patterned surfaces [Prodanov et al., 2013, Sahlin et al., 2010]) or be purely random, self-affine [Nayak, 1971] down to atomistic scale [Krim and Palasantzas, 1995, Ponson et al., 2006]. Surface morphology may be affected by surface processing, underlying microstructure and its deformation [Šiška et al., 2006, Bao-Tong and Laird, 1989], corrosion and oxidation. The resulting surface geometry can be characterized by numerous parameters and characteristics: standard deviation of heights and the height gradient, height distribution (in particular, its kurtosis and skewness), power spectral density, spectral moments, fractal dimension and others.

The roughness of many natural and engineering surfaces may be described as a self-affine two-dimensional manifold with a power spectral density (PSD) which decays as a power law of the wavenumber [Power and Tullis, 1991]. At the macroscopic scale the PSD might have a plateau [Majumdar and Bhushan, 1991], while longer wavelengths determine the shape of contacting surfaces. For mechanical contact problems, since in most applications only the highest asperities come in contact, an approximation of the roughness by a number of isolated spherical or elliptic asperities results in an accurate and helpful model [Archard, 1957, Greenwood and Williamson, 1966, Bush et al., 1975, Greenwood, 2006], especially in case of a small real contact area.

Analytical models for mechanical contact based on either the notion of asperities [Greenwood and Williamson, 1966], combined with the random process model [Nayak, 1971, Greenwood, 2006, Carbone and Bottiglione, 2008], or on the Persson's model [Persson, 2001, Manners and Greenwood, 2006, Dapp et al., 2014] provide an approximate solution for the evolution of the contact area with the applied pressure. More rigorous results can be obtained if local asperity deformation model is complemented by long-range elastic interactions between asperities as it was done in [Ciavarella et al., 2008, Yastrebov et al., 2011, Yastrebov, 2018]. Accurate numerical simulations, free of assumptions of analytical models, predict an intermediate result for contact area evolution between the asymptotic linear evolution for asperity based models and Persson's error-function solution [Hyun et al., 2004, Putignano et al., 2012, Prodanov et al., 2014, Yastrebov et al., 2012, Yastrebov et al., 2015, Yastrebov et al., 2017b].

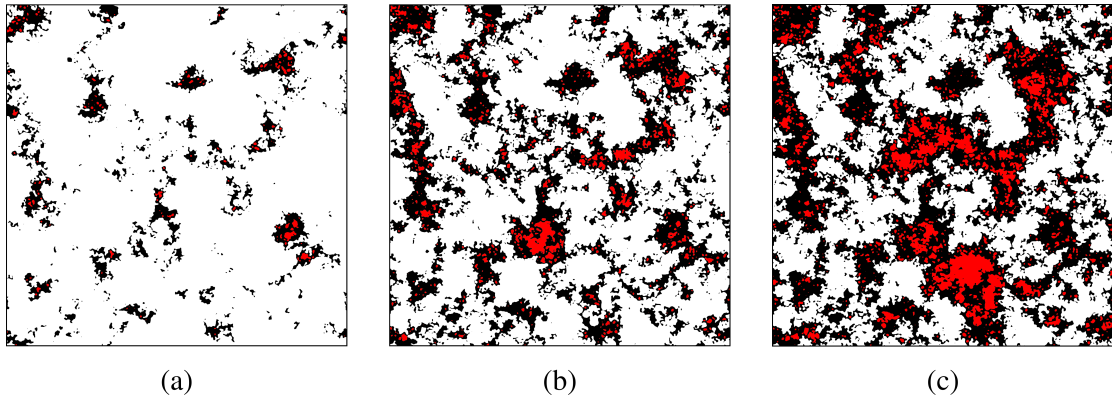


Figure 1.1: Morphology of the contact interface between an elastic half-space with a rough surface and a rigid flat under increasing external load, numerical simulation results [Yastrebov et al., 2015]: black is the real contact area, white is the “free” out-of-contact area and red is the “trapped” out-of-contact area, bounded inside non-simply connected contact patches.

1.2 Trapped fluid in contact interface

Lubrication, i.e. separation of contacting surfaces by a fluid lubricant, is an efficient mechanism for friction and wear reduction. However, if the applied external load, pushing the contacting bodies together, is high enough or if the sliding velocities are small, the hydrodynamic pressure developing in the fluid is not sufficient to separate the solids, and asperities of both surfaces can get in direct contact despite the presence of the lubricant, inevitably increasing friction. This scenario corresponds to the so-called mixed regime, at which the load-bearing capacity is split between the fluid and the contact areas. For even higher pressures and lower velocities, the whole load is carried by the mechanical contacts, this regime is termed as the boundary lubrication, see [Hamrock et al., 2004, Azushima, 2016] for details. On the other hand, under increasing external load the lubricating fluid may be trapped in valleys (pools) delimited completely by the contact zone. Fig. 1.1 shows an example of the morphology of the contact interface between two elastic half-spaces with rough surfaces under external load [Pei et al., 2005, Carbone and Bottiglione, 2008, Putignano et al., 2012, Yastrebov et al., 2017b]. Note that the fraction of the trapped out-of-contact area (highlighted by red colour), surrounded by contact patches, is significant.

The entrapment of the fluid in the interface can have a strong effect on the contact properties, especially if the fluid is highly incompressible [Persson et al., 2012, Matsuda et al., 2016]. First, the trapped fluid resists the compression, and thus opposes the growth of the real contact area. Second, the applied external load is shared between contacting asperities of the bodies and the pressurized fluid, so that the trapped fluid provides an additional load-carrying capacity (even in absence of relative tangential motion), reducing the normal pressure in the contact spots between the solid bodies. If the Coulomb’s law of friction is assumed valid at contact spots, i.e. the maximal frictional traction is proportional to the normal pressure, then the maximal macroscopic frictional force (of the whole contact interface) is proportional to the integral value of the normal pressure over the real contact area. Consequently, by taking into account the presence of the pressurized trapped fluid, a reduction of the global (apparent) coefficient of friction should take place.

The effect of lubricant entrapment on reduction of friction was first recognized in the study of cold metal forming processes [Kudo, 1965, Nellesmann et al., 1977], in [Azushima

and Kudo, 1995] authors performed experiments on the sheet metal drawing test and identified three states, corresponding to different levels of the external pressure. Low values of external load are supported completely by the mechanical contact between asperities, and both global and local coefficients of friction are equal. At medium range of pressures, the global coefficient of friction decreases with increasing load due to closing of lubricant pools and generation of hydrostatic pressure in the fluid, which supports a part of the external load. At even higher load, fluid escapes from the pools and permeates into the contact zones, so that both the real contact area and the coefficient of friction decrease with increasing load. This effect is however biased by the fact that the real contact area does not evolve linearly under high pressures [Archard, 1957], but rather as a concave function of pressure [Persson, 2001, Yastrebov et al., 2017b], thus also resulting in formal decrease of the friction coefficient in contact spots. The experimental results together with finite-element simulations of the problem of entrapment and permeation of the fluid into the contact interface during upsetting of a cylinder were presented and aforementioned states were also identified in [Azushima, 2000, Azushima et al., 2011]. An extensive experimental study of lubricant entrapping and escape in plane strip drawing processes was presented in [Bech et al., 1999].

The behaviour of trapped fluid accounts for a significant reduction of friction in tire-road contact [Scaraggi and Persson, 2012]. In biological sciences the effect of trapped lubricant in human joints was investigated in the view of reduction of friction between rough cartilage surfaces [Soltz et al., 2003, Chan et al., 2011]. The concept of trapped fluid rises in the study of fatigue cracks in the rolling contact, which considers the process of crack growth due to pressurized fluid lubricant, forced inside of the crack by the external load and trapped there [Bower, 1988]. The trapped fluid problem is also relevant to the geophysical studies: a landslide or an earthquake can be caused by an elevation of the pressure of the fluid in the pores inside the rock, see for example [Viesca and Rice, 2012, Garagash and Germanovich, 2012]. The effect of the trapped fluid is also of interest for the study of basal sliding of glaciers, [Cuffey and Paterson, 2010]: the melt water, which is responsible for the lubrication, flows in a linked system of cavities in the interface between the glacier and the bedrock, and may be trapped there. Finally, the trapped fluid problem is also of importance, in general, for poromechanics [Yu and Cheng, 2002, Dormieux et al., 2002, Budiansky and O’connell, 1976, Coussy, 2004].

An important theoretical result highlighting the effect of the trapped fluid on the contact problem was obtained in [Kuznetsov, 1985]. In this paper, the Westergaard’s celebrated analytical solution for the problem of contact between a regular wavy surface and a rigid half-plane [Westergaard, 1939] was extended by taking into account the presence of a compressible fluid, trapped in the valleys between contacting asperities. Kuznetsov’s solution demonstrates how the external pressure is divided between the fluid and the solid contact, which results in the decrease of the global coefficient of friction under increasing external load. However, due to the assumptions (i) that the wavy surface behaves as a flat one and that Flamant’s solution [Johnson, 1987] holds for every surface point, and (ii) that the horizontal component of the fluid pressure is negligible, Kuznetsov’s solution cannot describe the escape of the lubricant and depletion of the real contact area. Limitations of Kuznetsov’s solution will be analysed in detail in this dissertation. Recently an analytical solution was proposed for the problem of sliding of a rigid periodical punch along a viscoelastic Winkler’s foundation with the incompressible fluid present in the gap [Goryacheva and Shpenev, 2012].

Despite a significant attention to the problem of the trapped fluid in the contact interface, a few questions remain open, such as: the mechanism of the trap opening, the evolution of the real contact area and of the global coefficient of friction during this process, and also the distribution of the frictional shear tractions in the contact interface

under external normal loading in the presence of the pressurized fluid in the interface. Note that these questions cannot be addressed in the framework of the boundary element method (BEM) based on the Flamant's solution, since it assumes infinitesimal slopes of the surface roughness, which is, as we will show, a too restrictive assumption for the considered problem. We will address these questions in the current study in the framework of the finite-element method (FEM).

1.3 Fluid-structure interaction approaches

The problem of the thin fluid flow in contact interfaces belongs to a vast domain of fluid-structure interaction (FSI) problems, which involve deformation and/or motion of the solids interacting with the internal and/or external fluid. These problems are of very wide range, spanning from deformation of airplane wings and rotor blades subjected to the sub- or supersonic air flow [Farhat et al., 2003, Bazilevs et al., 2011] to modelling of the blood flow [Bazilevs et al., 2006, Gerbeau and Vidrascu, 2003] and heart valves [van Loon et al., 2006, De Hart et al., 2003], scaling up to suspended bridge instabilities under wind load [Païdoussis et al., 2010], ship stability [Wackers et al., 2011] or large iceberg's capsize in water [Sergeant et al., 2018]. All these problems correspond to different space and time scales, operating conditions and other requirements, therefore a unified FSI approach fit for all cases does not exist, and rather different techniques have been developed for particular problems.

Many problems of fluid-structure interaction, such as aeroelasticity and haemodynamics, correspond to the case of the high-Reynolds-number flow. Therefore, different mesh density, and often different time stepping, are required for the solid and fluid domains. Furthermore, the fluid domain evolves due to motion and deformation of solids. A number of methods have been used to overcome the associated computational complexity, such as arbitrary Lagrangian-Eulerian method [Donea et al., 1982, Takashi and Hughes, 1992], fictitious domain method [Baaijens, 2001, De Hart et al., 2003], immersed boundary method [Peskin, 2002, Mittal and Iaccarino, 2005] and extended finite element method [Mayer et al., 2010, Gerstenberger and Wall, 2008]. On the contrary, fluid flow in contacting or slightly separated interfaces is usually of low Reynolds number and, moreover, the thickness of the fluid film is usually much smaller than other length scales. In this case general Navier-Stokes equations could be readily simplified down to the Reynolds equation for the viscous flow [Hamrock et al., 2004]. This simplification permits to use compatible meshes for the fluid and the solid domains and, under assumption of constant pressure through the film thickness, to define the Reynolds equation on the so-called lubrication surface, so that specific methods discussed above are not required, see [Stupkiewicz and Marcinişzyn, 2009, Stupkiewicz et al., 2016]. This approach is also used in the current study.

1.3.1 One-way and two-way coupling approaches

From the point of view of the underlying physical processes, FSI strategies can be divided into one-way and two-way coupling approaches. In the context of thin fluid flow through contact interfaces, the former implies that the solution of the solid mechanics problem defines the distribution of the free volume in the interface, which can be occupied by the fluid flow, however the fluid pressure does not affect the deformation of the solids, i.e. the fluid problem is solved assuming rigid walls of the solids. In the two-way coupling this approximation is dropped down, and the fluid-induced traction acting on the surface of the deformable solid is taken into account.

In elastohydrodynamic lubrication regime, as well as for non-contact seals, two-

way coupling is often used, see [Stupkiewicz and Marciniszyn, 2009, Stupkiewicz et al., 2016, Yang and Laursen, 2009]. However, for the important case of contact seals, or more generally if contact is present in the interface, one-way coupling was rather utilized in previous studies, see [Dapp et al., 2012, Dapp and Müser, 2016, Pérez-Ràfols et al., 2016]. It is widely assumed that the deformation of the solids results mainly from the contact interaction and the fluid pressure effect on the solid is negligible, since the contact pressure at asperities is considerably higher than the physically relevant fluid pressure. However, to the best of the author’s knowledge, the range of validity of one-way coupling for problems involving thin fluid flow in contact interfaces, depending on the surface geometry, material properties and the fluid pressure, has not been studied yet.

1.3.2 Partitioned and monolithic implementation approaches

From the implementation point of view two distinct approaches for any FSI problem exist: partitioned and monolithic. The former is based on two different solvers for the fluid and solid sub-problems, and in order to take into account the coupling, one- or two-way data exchange between them must be established. Furthermore, a certain iterative process is required to obtain the convergence. The utilization of the partitioned approach benefits from modularity, since different solvers tailored for the sub-problems could be used [Küttler and Wall, 2008, Matthies and Steindorf, 2003], however, convergence and stability of such a scheme could raise issues, and special techniques may become necessary, see, for example [Heil, 1998]. On the contrary, under the *monolithic* approach all equations which govern sub-problems and the interaction between them are rendered into a single system, and upon its solution, degrees of freedom (DOF) values corresponding to both sub-problems are obtained simultaneously [Hübner et al., 2004, Michler et al., 2004, Heil, 2004]. The data exchange in this case is not needed, the stability and convergence are easier to obtain, however, solution of the vast system of algebraic equations is necessary. Nevertheless, for the problem under discussion this last issue is not relevant, since the number of unknowns in the interface is considerably smaller than in the bulk of the solid, if, for example, finite-element discretization is used.

Elastohydrodynamic lubrication problems are often solved under the monolithic approach [Stupkiewicz et al., 2016, Stupkiewicz and Marciniszyn, 2009, Yang and Laursen, 2009], whilst for the contact sealing problems the partitioned approach is generally preferred [Pérez-Ràfols et al., 2016]. Moreover, as was already mentioned, the problem is often solved under the one-way coupling approach and using the assumption of the infinitesimal slopes of the surface profile and the small deformation formulation. Boundary element method [Pérez-Ràfols et al., 2016] and Green’s function molecular dynamics [Dapp et al., 2012] are frequently used for the mechanical contact problem and the Reynolds equation is often solved by the finite-differences method.

1.4 Objectives

In accordance with the discussed above, the first objective of this dissertation is to develop a robust computational framework aimed at solving coupled problems involving fluid flow in contact interfaces. A detailed description of this framework is presented in Part II of the thesis, while Part III is devoted to the application of the constructed framework to relevant problems. In particular, we will compare one-way and two-way coupling approaches for the problem of thin fluid flow in contact interfaces, which represents the second objective of the dissertation. To make this comparison quantitative, we will use an integral parameter of the interface, e.g. the effective transmissivity, and

study its dependence on the material properties and fluid pressure. In addition, we will discuss the effect of the trapped fluid on the contact problem: investigate the possibility for fluid to escape the trap. The study of the evolution of the contact area and of the global coefficient of friction under increasing external loading, depending on the material properties of the solid and of the fluid, and also on the slope of the surface profile, is also of interest.

We note that the two-way coupling of the mechanical contact and fluid flow sub-problems could require rather frequent and considerable data exchange in case of partitioned approach. Moreover, if a significant number of trapped fluid pools appear in the interface (which is possible, for example, in case of contact between rough surfaces or deterministic surfaces with dimples), then a resolution under the partitioned approach becomes even more complicated, since the history tracking of trapped zones is needed. The *monolithic* approach appears beneficial for our purposes and, therefore, will be applied throughout this study. Furthermore, we will use the finite-element method in order to make possible application of the proposed framework for different surface geometries (e.g. with finite slopes of the profile), under larger deformation formulation and with different material models of the solid (e.g. elastoplastic, viscoelastic, etc).

Chapter 2

Governing equations

Résumé de Chapitre 2 “Les équations gouvernant”

Dans le deuxième chapitre, nous examinons l'énoncé de la forme forte du problème couplé du flux de fluide dans les interfaces de contact, sous l'hypothèse de couches minces. Premièrement, le problème de mécanique du solide est formulé en considérant séparément les contraintes de contact unilatérales et le frottement. Ensuite, le problème de mécanique des fluides est exposé : la dérivation des équations de Navier-Stokes est analysée et nous dérivons aussi leur forme simplifiée par rapport à l'équation de Reynolds pour l'écoulement de couches minces de fluide. De plus, nous présentons les équations régissant le comportement d'un fluide soumis à une pression hydrostatique, équations pertinentes pour le piégeage du fluide dans l'interface de contact. Enfin, nous regroupons toutes ces équations et discutons la partition de l'interface en zones de contact, d'écoulement de fluide et de fluide piégé, ainsi que les détails de l'énoncé du problème couplé.

In this chapter we discuss the general statement of the coupled problem of the thin fluid flow in contact interfaces. First, we provide the formulation of the continuum solid mechanics problem, considering separately contact constraints, and then proceed to the statement of the continuum fluid mechanics problem with the emphasis on the thin film flow case. Additionally, we present equations governing the hydrostatically pressurized fluid, relevant if the fluid entrapment in the contact interface is taken into account. Finally, we group together all aforementioned equations and discuss details of the coupled problem statement.

2.1 Continuum solid mechanics

We introduce here briefly basic concepts of solid mechanics, which are necessary for subsequent discussions. More details of theoretical formulations may be found in various textbooks, for example, in [Muskhelishvili, 2013, Lurie and Belyaev, 2005, Lurie, 2012, Besson et al., 2009, Ibrahimbegovic, 2009].

Let us choose an orthogonal coordinate system with unit vectors $\mathbf{e}_x, \mathbf{e}_y, \mathbf{e}_z$. Each point of the solid in the *reference* configuration Ω_0 , which usually corresponds to the initial (undeformed) state, is defined by a vector $\mathbf{X} = [X, Y, Z]^\top$, hereinafter we denote by $(\cdot)^\top$ the transpose operator. Components of \mathbf{X} are also often termed as the *material* coordinates. The position of the same point in the *current* (deformed) configuration Ω is given by a vector $\mathbf{x} = [x, y, z]^\top$. The displacement vector $\mathbf{u} = [u, v, w]^\top$ of each point is calculated as:

$$\mathbf{u} = \mathbf{x} - \mathbf{X}, \quad (2.1)$$

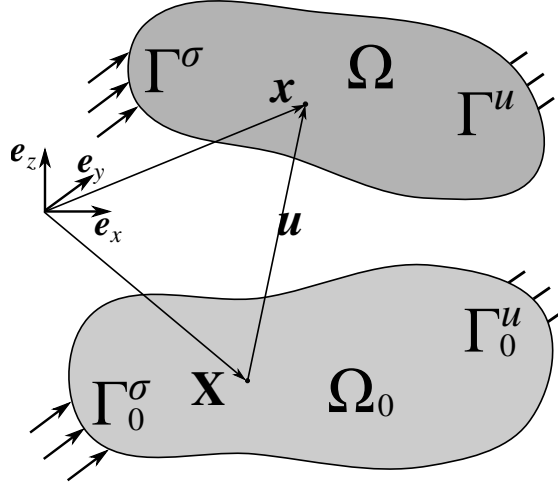


Figure 2.1: Reference (initial) configuration $\mathbf{X} \in \Omega_0$ and current (deformed) configuration $\mathbf{x} \in \Omega$ of the deformable solid; $\mathbf{u} = \mathbf{x} - \mathbf{X}$ is the displacement vector field.

i.e., in other words, \mathbf{u} is a vector field which describes the transformation of the solid from configuration Ω_0 to Ω , see Fig. 2.1.

2.1.1 Strain and stress tensors

In order to describe the deformation process locally, we introduce the deformation gradient tensor \mathbf{F} as

$$\mathbf{F} = \frac{\partial \mathbf{x}}{\partial \mathbf{X}}, \quad (2.2)$$

determinant $J = \det \mathbf{F} > 0$ of which is called the Jacobian and must be positive to avoid self-penetration of points of the solid. Substituting (2.1) into (2.2) we may write:

$$\mathbf{F} = \mathbf{I} + \tilde{\nabla} \mathbf{u}, \quad (2.3)$$

where \mathbf{I} is the unit tensor and $\tilde{\nabla}(\cdot)$ is the gradient of the vector field with respect to the reference coordinates \mathbf{X} .

In order to evaluate how a displacement of a point differs from a rigid body motion, strain tensors are introduced. For example, the Cauchy-Green strain tensor \mathbf{C} is defined in the reference configuration as:

$$\mathbf{C} = \mathbf{F}^\top \cdot \mathbf{F}. \quad (2.4)$$

However, since in the initial state $\tilde{\nabla} \mathbf{u} = 0$, and, accordingly, $\mathbf{C} = \mathbf{I}$, it is often more convenient to use the Green-Lagrange strain tensor \mathbf{E} , which vanishes in the undeformed configuration:

$$\mathbf{E} = \frac{1}{2} (\mathbf{C} - \mathbf{I}) = \frac{1}{2} \left[\tilde{\nabla} \mathbf{u} + (\tilde{\nabla} \mathbf{u})^\top + (\tilde{\nabla} \mathbf{u})^\top \cdot \tilde{\nabla} \mathbf{u} \right]. \quad (2.5)$$

In the index notation tensor \mathbf{E} may be written as:

$$E_{ij} = \frac{1}{2} \left(\frac{\partial u_i}{\partial X_j} + \frac{\partial u_j}{\partial X_i} + \frac{\partial u_k}{\partial X_i} \frac{\partial u_k}{\partial X_j} \right), \quad (2.6)$$

where u_i and X_i ($i = 1, 2, 3$) are corresponding components of the vectors \mathbf{u} and \mathbf{X} , respectively, and summation over repeating indices is assumed.

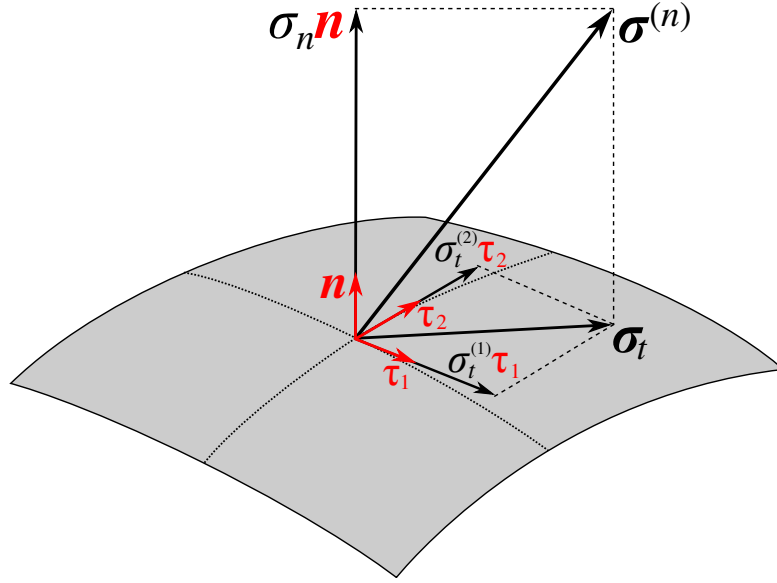


Figure 2.2: Normal $\sigma_n \mathbf{n}$ and tangential σ_t components of the traction vector $\sigma^{(n)}$, corresponding to a normal \mathbf{n} .

Furthermore, in the current (deformed) configuration the Almansi strain tensor \mathbf{e} is defined as:

$$\mathbf{e} = \frac{1}{2} [\mathbf{I} - \mathbf{F}^{-T} \cdot \mathbf{F}^{-1}] = \frac{1}{2} [\nabla \mathbf{u} + (\nabla \mathbf{u})^\top - (\nabla \mathbf{u})^\top \cdot \nabla \mathbf{u}], \quad (2.7)$$

where $\nabla(\cdot)$ is the gradient of the vector field with respect to the actual coordinates \mathbf{x} , or, in the index notation,

$$e_{ij} = \frac{1}{2} \left(\frac{\partial u_i}{\partial x_j} + \frac{\partial u_j}{\partial x_i} - \frac{\partial u_k}{\partial x_i} \frac{\partial u_k}{\partial x_j} \right). \quad (2.8)$$

Note that tensor \mathbf{e} is connected to the Green-Lagrange tensor \mathbf{E} via transformation

$$\mathbf{E} = \mathbf{F}^\top \cdot \mathbf{e} \cdot \mathbf{F}. \quad (2.9)$$

It is also important to note that in the infinitesimal strain theory (which will be used in certain parts of this dissertation), the displacement gradient is assumed small compared to unity, i.e. $\|\nabla \mathbf{u}\| \ll 1$. Therefore, nonlinear (second-order) terms of strain tensors may be neglected, and both Green-Lagrange tensor \mathbf{E} and Almansi tensor \mathbf{e} can be linearised down to the so-called small (infinitesimal) strain tensor $\boldsymbol{\varepsilon}$:

$$E_{ij} \approx e_{ij} \approx \varepsilon_{ij} = \frac{1}{2} \left(\frac{\partial u_i}{\partial x_j} + \frac{\partial u_j}{\partial x_i} \right). \quad (2.10)$$

The infinitesimal strain theory therefore does not differentiate between reference and current configurations.

The stress state in the solid can also be described in both considered configurations: in the current by the Cauchy stress tensor $\boldsymbol{\sigma}$ and in the reference configuration by the first Piola-Kirchhoff stress tensor \mathbf{P} , which are connected via a transformation:

$$\mathbf{P} = J \boldsymbol{\sigma} \cdot \mathbf{F}^{-\top}. \quad (2.11)$$

According to Cauchy's fundamental theorem, the traction (stress) vector $\sigma^{(n)}$ in any point of the body is computed with respect to a normal \mathbf{n} to an arbitrary plane passing through that point as:

$$\sigma^{(n)} = \mathbf{n} \cdot \boldsymbol{\sigma}. \quad (2.12)$$

For a point located on the surface of the solid, if \mathbf{n} is the outward normal at this point, Eq. (2.12) yields the surface traction vector.

Furthermore, it is often convenient to consider separately normal and tangential (shear) components of the traction vector, see Fig. 2.2. The normal traction σ_n is defined as the following dot product:

$$\sigma_n = \boldsymbol{\sigma}^{(n)} \cdot \mathbf{n} = \mathbf{n} \cdot \boldsymbol{\sigma} \cdot \mathbf{n}, \quad (2.13)$$

while the tangential component $\boldsymbol{\sigma}_t$ is described by a vector lying in a plane orthogonal to the normal \mathbf{n} :

$$\boldsymbol{\sigma}_t = (\mathbf{I} - \mathbf{n} \otimes \mathbf{n}) \cdot \boldsymbol{\sigma}^{(n)} = \boldsymbol{\sigma}^{(n)} - \sigma_n \mathbf{n}, \quad (2.14)$$

where \otimes is the tensor product. Equivalently, the tangential traction vector can be described by a pair of coordinates $\{\sigma_t^{(1)}, \sigma_t^{(2)}\}$ in the local coordinate system $\{\boldsymbol{\tau}_1, \boldsymbol{\tau}_2\}$, associated with the plane orthogonal to the normal vector \mathbf{n} :

$$\boldsymbol{\sigma}_t = \sigma_t^{(1)} \boldsymbol{\tau}_1 + \sigma_t^{(2)} \boldsymbol{\tau}_2. \quad (2.15)$$

It is important to note, that the resolution of the contact problem, which is in the center of discussion of this thesis, includes finding the actual contact zone on the surface of the solid and the distribution of contact tractions in this zone. Therefore, the description of the contact problem in the deformed state appears preferable, and, where appropriate, we will consider stress and strain tensors associated with the current configuration.

2.1.2 Boundary value problem

The general statement of the boundary value problem, studied in solid mechanics, reads:

$$\begin{cases} \nabla \cdot \boldsymbol{\sigma} + \mathbf{f}_v = 0 & \text{in } \Omega & (2.16a) \\ \boldsymbol{\sigma}^{(n)} = \boldsymbol{\sigma}_0 & \text{on } \Gamma^\sigma & (2.16b) \\ \mathbf{u} = \mathbf{u}_0 & \text{on } \Gamma^u, & (2.16c) \end{cases}$$

where (2.16a) is the static local balance of momentum equation, \mathbf{f}_v is the vector density of volume forces, (2.16b) are the Neumann boundary conditions with a prescribed surface traction $\boldsymbol{\sigma}_0$, defined at the part of the solid's surface $\Gamma^\sigma \subset \partial\Omega$, and (2.16c) are the Dirichlet boundary conditions with a prescribed displacement \mathbf{u}_0 , defined on $\Gamma_u \subset \partial\Omega$, see also Fig. 2.1. Note that the balance of angular momentum is assumed in this problem, which dictates the symmetry of the Cauchy stress tensor, i.e. $\boldsymbol{\sigma}^\top = \boldsymbol{\sigma}$.

Note also that the problem statement (2.16) must be complemented by a relevant constitutive law, which defines the relation between stress and strain tensors. For example, in case of linear isotropic elastic solid, this relation is provided by the Hooke's law:

$$\boldsymbol{\sigma} = \lambda \text{trace}(\boldsymbol{\varepsilon}) \mathbf{I} + 2\mu \boldsymbol{\varepsilon}, \quad (2.17)$$

where λ and μ are the Lamé constants (elastic moduli). However, a physically realistic material behaviour can be much more complex, described by nonlinear hyper-elastic, plastic, viscous constitutive laws, or by a certain combination of those. At the same time, the coupled framework, formulated in this thesis, concerns processes occurring in contact interfaces and permits arbitrary constitutive laws for the underlying solids. Therefore, details of more complex material behaviour laws are not essential for the developed framework and are not discussed here, while the interested reader is referred to [Besson et al., 2009, Wriggers, 2008, Ibrahimbegovic, 2009].

2.2 Contact mechanics

Throughout this dissertation we consider the problem of the unilateral contact between a deformable solid and a rigid flat. This set-up is chosen to simplify the formulation of the contact problem and to concentrate the discussion on the handling of the fluid/solid coupling. Moreover, under linear isotropic elasticity and infinitesimal strain assumptions this set-up is equivalent to the case of contact between two deformable bodies (if the “single” solid has an effective surface geometry and elastic modulus, which take into account geometric features and elastic properties of the two solids, respectively), see, for example, [Barber, 2003]. However, this equivalence does not hold in the general case of inelastic material response, frictional contact and/or large deformations formulation. Nevertheless, the numerical framework, developed here for the case of unilateral contact, can be extended to handle the problem of contact between two deformable solids with arbitrary surface geometries. At the same time, the problem statement with one of the contacting solids being rigid is also relevant, when the elasticity modulus of this solid is sufficiently higher than that of the other body. This is the case, for example, in tire-road contact, see [Scaraggi and Persson, 2012], and in rubber sealing applications, see [Persson and Yang, 2008].

2.2.1 Hertz-Signorini-Moreau conditions

Let us consider first frictionless non-adhesive contact between a deformable solid Ω and a rigid flat; the latter can be defined by a normal $\boldsymbol{\nu}$ and any point \boldsymbol{c} belonging to the plane, see Fig 2.3. In this case the contact is unilateral, i.e. the motion of the solid is restricted to the half-space on one side from the plane. To formalize this constraint, we introduce a scalar function g_n , termed as the normal gap:

$$g_n(\boldsymbol{x}) = (\boldsymbol{x} - \boldsymbol{c}) \cdot \boldsymbol{\nu}, \quad (2.18)$$

which represents a signed distance from a point \boldsymbol{x} on the surface of the deformable body to the rigid plane:

- $g_n > 0$, when the point is separated from the plane (i.e. is not in contact)
- $g_n < 0$, when the point penetrates the plane (which is not admissible),
- $g_n = 0$, when the point is on the plane (i.e. is in contact).

Since the position of the rigid flat is fixed in this problem set-up, the normal gap depends only on the current coordinate \boldsymbol{x} and can be evaluated using any point \boldsymbol{c} belonging to the plane.

Let us denote by $\Gamma \subset \partial\Omega$ a part of the surface of the solid which may come in contact with the rigid flat for a given external loading process, i.e. the *potential* contact zone. While by definition of the gap function $g_n \geq 0$ on Γ , we introduce also $\Gamma^c \subset \Gamma$, termed as the *active* contact zone and defined as the part of the surface, which is currently in contact with the rigid flat, i.e. $g_n = 0$ on Γ^c . Consequently, we may write that $g_n > 0$ on $\Gamma \setminus \Gamma^c$.

The constraint on the normal gap $g_n \geq 0$ on Γ can be stated in another way, which will be important for subsequent derivations. Remembering that $\boldsymbol{x} = \boldsymbol{X} + \boldsymbol{u}$, we may write:

$$g_n = (\boldsymbol{x} - \boldsymbol{c}) \cdot \boldsymbol{\nu} = (\boldsymbol{X} - \boldsymbol{c}) \cdot \boldsymbol{\nu} + \boldsymbol{u} \cdot \boldsymbol{\nu} = g_{n0} + \boldsymbol{u} \cdot \boldsymbol{\nu} \geq 0 \iff \boldsymbol{u} \cdot \boldsymbol{\nu} \geq -g_{n0}, \quad (2.19)$$

where $g_{n0} = (\boldsymbol{X} - \boldsymbol{c}) \cdot \boldsymbol{\nu}$ is the initial normal gap, observed in the reference configuration. Note also that on the active contact zone Γ^c the normal to the surface of the deformable body is $\boldsymbol{n} = -\boldsymbol{\nu}$, and, therefore, $\boldsymbol{u} \cdot \boldsymbol{n} = -\boldsymbol{u} \cdot \boldsymbol{\nu} = g_{n0}$ holds on Γ^c .

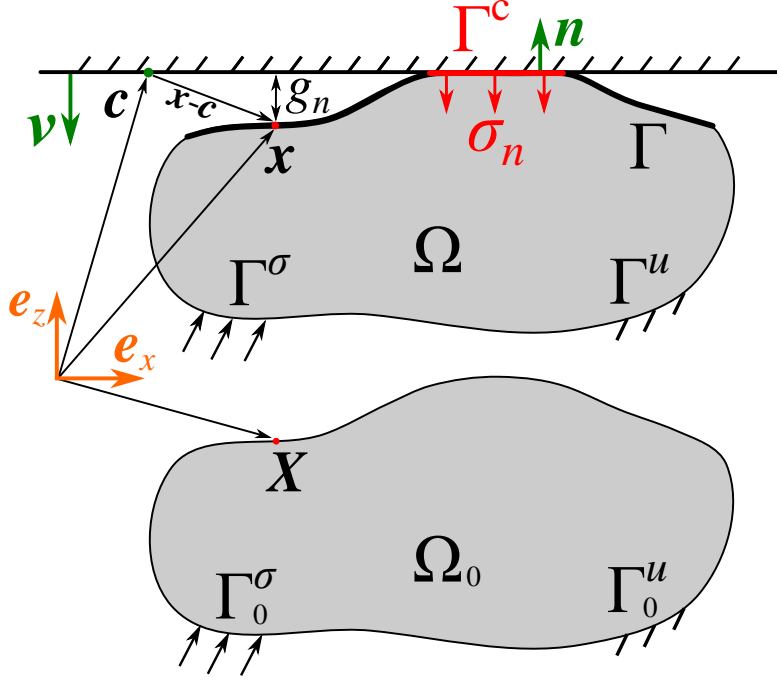


Figure 2.3: Unilateral contact between a deformable solid and a rigid flat: Γ is the *potential* contact zone, and $\Gamma^c \subset \Gamma$ is the *active* contact zone.

At the same time, we may consider how the contact interaction affects the traction vector $\boldsymbol{\sigma}^{(n)}$ on the surface of the solid. First, friction is neglected, and therefore the tangential component of the traction vector is zero on the potential contact zone, i.e. $\boldsymbol{\sigma}_t = 0$ on Γ . Secondly, since only non-adhesive contact is considered, the normal traction component is non-positive, i.e. $\sigma_n \leq 0$ on Γ . Furthermore, due to the nature of the contact interaction, the active contact zone is compressed: $\sigma_n < 0$ on Γ^c , while the non-contact part of the surface is free of traction: $\sigma_n = 0$ on $\Gamma \setminus \Gamma^c$. Note that often the absolute value of the normal traction component is termed as the *contact pressure*: $p^c = |\sigma_n|$. For brevity, and to follow terminology of other studies, we will also use this term for σ_n , bearing in mind the difference in sign.

Constraints on the normal gap and on the normal traction, resulting from the contact interaction, may be combined together to form the following set of conditions:

$$g_n \geq 0, \quad \sigma_n \leq 0, \quad \sigma_n g_n = 0 \quad \text{on } \Gamma, \quad (2.20)$$

or, using the introduced notations of potential Γ and active Γ^c contact zones:

$$\begin{cases} g_n = 0, & \sigma_n < 0 & \text{on } \Gamma^c \\ g_n > 0, & \sigma_n = 0 & \text{on } \Gamma \setminus \Gamma^c, \end{cases} \quad (2.21)$$

with a special case of $g_n = 0$ and $\sigma_n = 0$ corresponding to $\partial\Gamma^c$, i.e. to the boundary of the active contact zone. Constraints (2.21) are known as Hertz-Signorini-Moreau conditions, or, from the point of view of the optimization theory, may be termed as Karush-Kuhn-Tucker conditions, see also [Kikuchi and Oden, 1988, Wriggers, 2006, Yastrebov, 2013]. Therefore, the conditions (2.20) together with the non-friction condition ($\boldsymbol{\sigma}_t = 0$ on Γ), complement the general problem statement (2.16).

2.2.2 Frictional constraints

Now let us consider the same unilateral contact problem, as in Section 2.2.1, but with the interfacial friction taken into account. In this case, when the solid comes into contact

with the rigid immobile flat, the traction vector arising in the active contact zone has not only the normal component σ_n , but also the tangential one $\sigma_t \neq 0$, which is caused by the frictional interaction, see Fig. 2.4.

In general, the frictional traction may be a function of multiple parameters:

$$\sigma_t = \sigma_t(\sigma_n, \dot{\sigma}_n, \dot{\mathbf{g}}_t, t, \dots), \quad (2.22)$$

where $\dot{\sigma}_n$ is the rate of the contact pressure, $\dot{\mathbf{g}}_t$ is the tangential sliding velocity of a point on the solid's surface with respect to the rigid flat, t is time. However, in this dissertation we will limit the consideration to the classical non-associated Coulomb's friction law. For a discussion of non-classical frictional models and their implementation in the finite-element framework the reader is referred to [Johnson, 1987, Wriggers, 2006] and also to [Mróz and Stupkiewicz, 1994, Stupkiewicz and Mróz, 1999, Stupkiewicz, 2001].

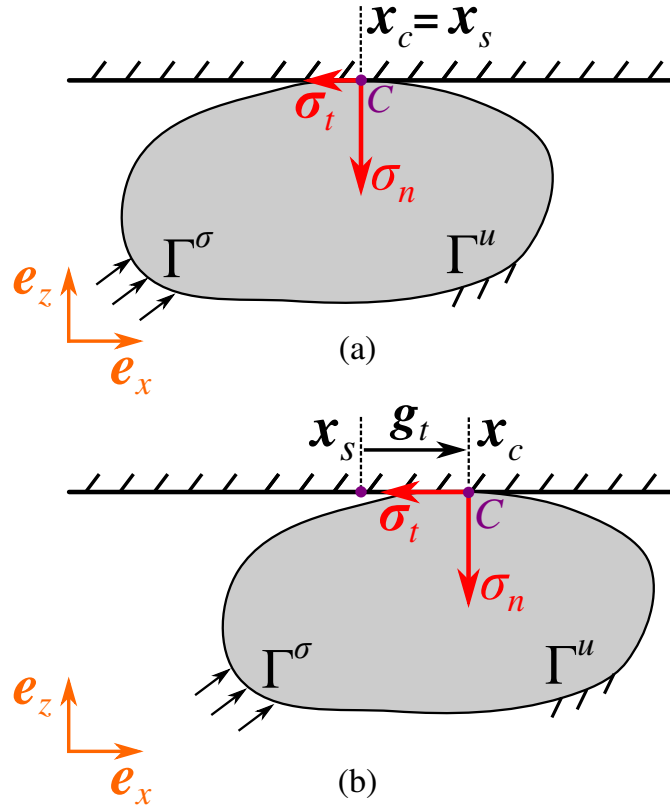


Figure 2.4: Unilateral frictional contact: (a) material point C is in the *stick* state, and \mathbf{x}_s is the position it adheres to; (b) point C is in the *slip* state, and \mathbf{g}_t is the tangential slip with respect to the stick position \mathbf{x}_s .

According to the classical Coulomb's law of friction, the shear resistance of the contact interface depends on the contact pressure, and the direction of frictional traction is opposite to the sliding direction:

$$\sigma_t = \sigma_t(\sigma_n, \mathbf{s}), \quad (2.23)$$

where \mathbf{s} is a unit vector, which describes the direction of sliding:

$$\mathbf{s} = \begin{cases} \frac{\dot{\mathbf{g}}_t}{\|\dot{\mathbf{g}}_t\|}, & \|\dot{\mathbf{g}}_t\| > 0 \\ \mathbf{0}, & \|\dot{\mathbf{g}}_t\| = 0. \end{cases} \quad (2.24)$$

Let us consider an arbitrary point C on the surface of the solid, defined by material coordinates \mathbf{X}_c in the reference configuration. Let us assume that this point belongs to the active contact zone, then it can be present in one of the two states: *stick* or *slip*.

In the stick state, see Fig. 2.4(a), the point C adheres to the so-called stick position, i.e. its current coordinates \mathbf{x}_c remain equal to \mathbf{x}_s , which are the coordinates that this point occupied once it came into the stick state. The point stays in stick while the norm of the frictional traction vector is less than (or equal to) a certain critical value, proportional to the contact pressure at the same point:

$$\|\dot{\mathbf{g}}_t\| = 0, \quad \|\boldsymbol{\sigma}_t\| \leq \mu |\sigma_n|, \quad (2.25)$$

where μ is the coefficient of proportionality, termed as the coefficient of friction (CoF).

Once the frictional traction reaches the critical value, the point starts sliding, which corresponds to the *slip* state, Fig. 2.4(b). In this state, the direction of the frictional traction is opposite to the one of the relative sliding velocity of the point C with respect to the rigid flat, and the norm of $\boldsymbol{\sigma}_t$ equals exactly to the aforementioned critical value:

$$\boldsymbol{\sigma}_t = -\mu |\sigma_n| \mathbf{s}. \quad (2.26)$$

Therefore, in addition to the Hertz-Signorini-Moreau conditions (2.20), taking the classical Coulomb's friction into account results in the following frictional constraints, which correspond to the two possible active contact states:

- Stick: $\|\dot{\mathbf{g}}_t\| = 0, \quad \|\boldsymbol{\sigma}_t\| \leq \mu |\sigma_n|,$
- Slip: $\|\dot{\mathbf{g}}_t\| > 0, \quad \boldsymbol{\sigma}_t = -\mu |\sigma_n| \mathbf{s}.$

Frictional constraints can be also viewed as a combination of a slip rule, a frictional criterion and a complementarity condition, respectively:

$$\dot{\mathbf{g}}_t = \|\dot{\mathbf{g}}_t\| \frac{\boldsymbol{\sigma}_t}{\|\boldsymbol{\sigma}_t\|}, \quad \|\boldsymbol{\sigma}_t\| \leq \mu |\sigma_n|, \quad \|\dot{\mathbf{g}}_t\| (\|\boldsymbol{\sigma}_t\| - \mu |\sigma_n|) = 0, \quad (2.27)$$

see [Alart and Curnier, 1991].

2.3 Continuum fluid mechanics

Here we will outline briefly the derivation of Navier-Stokes equations, which define the mechanics of a viscous fluid in the general case, and then discuss their simplification down to the Reynolds equation for the thin film flow. For more details an interested reader is referred, for example, to the textbook [Hamrock et al., 2004], notations of which will be used here.

2.3.1 Derivation of Navier-Stokes equations

Let us consider the fluid flow between two solid surfaces, which may have macroscopic velocities \mathbf{U}_1 and \mathbf{U}_2 , respectively, and study the stress state of a fluid element (particle), see Fig. 2.5. Note that the zero slip conditions at the fluid-solid interface are assumed. Due to the effect of the viscosity, stresses in fluid increase with the deformation rate. In case of the Newtonian fluid this relationship is linear:

$$\tau_{ij} = \eta \left(\frac{\partial U_i}{\partial x_j} + \frac{\partial U_j}{\partial x_i} \right), \quad (2.28)$$

where τ_{ij} are shear stresses (components of the stress tensor $\boldsymbol{\sigma}$, s.t. $i \neq j$), η [N · s/m²] is the coefficient of proportionality, which is termed as the absolute viscosity, and U_i

($i = 1, 2, 3$) is a component of the velocity vector $\mathbf{U} = [U, V, W]^T$. Since $\mathbf{U} = \dot{\mathbf{u}}$, where \mathbf{u} is the displacement vector, introduced in (2.1), terms in parenthesis in (2.28) describe the shear strain rate and can be seen as a measure of the distortion of the fluid element. Note that, similarly to the solid mechanics case, the balance of angular momentum requires the symmetry of the stress tensor, i.e. $\tau_{ij} = \tau_{ji}$.

Furthermore, we introduce the hydrostatic pressure p in the fluid as the average of the normal stresses:

$$p = -\frac{1}{3}(\sigma_x + \sigma_y + \sigma_z), \quad (2.29)$$

where we used a simplified notation: $\sigma_x = \sigma_{11}$, $\sigma_y = \sigma_{22}$ and $\sigma_z = \sigma_{33}$, i.e. the term in brackets is equal to the trace of the stress tensor $\boldsymbol{\sigma}$. Note that the minus sign was used since hydrostatic pressure is always compressive, while positive normal stresses correspond to a tensile loading.

Due to the similarity in description of solid and fluid mechanics, we may write normal stresses, according to the constitutive relationship (2.17), as:

$$\sigma_i = \lambda(\nabla \cdot \mathbf{U}) + 2\eta \frac{\partial U_i}{\partial x_i}, \quad (2.30)$$

where λ and η play the roles of the two Lamé parameters, λ being the second viscosity coefficient, and $\nabla \cdot \mathbf{U}$ is the divergence of the velocity vector, sometimes termed as the dilatation. By summing up expressions for the three normal stresses σ_i and using the introduced above hydrostatic pressure p , we arrive at the following equality:

$$p = -\left(\lambda + \frac{2}{3}\eta\right) \nabla \cdot \mathbf{U}, \quad (2.31)$$

which permits us to exclude the second viscosity coefficient λ and write the normal stresses finally as:

$$\sigma_i = -p - \frac{2}{3}\eta \nabla \cdot \mathbf{U} + 2\eta \frac{\partial U_i}{\partial x_i}. \quad (2.32)$$

For the subsequent derivation it is important to introduce the total derivative of the fluid velocity vector $\mathbf{U} = [U, V, W]^T$, which is considered as a function of the spatial coordinates and time:

$$\mathbf{U} = \mathbf{U}(x, y, z, t). \quad (2.33)$$

Therefore, the total time derivative of the first component of the velocity vector reads:

$$\frac{DU}{Dt} = \frac{\partial U}{\partial t} + \frac{\partial U}{\partial x} \frac{\partial x}{\partial t} + \frac{\partial U}{\partial y} \frac{\partial y}{\partial t} + \frac{\partial U}{\partial z} \frac{\partial z}{\partial t}, \quad (2.34)$$

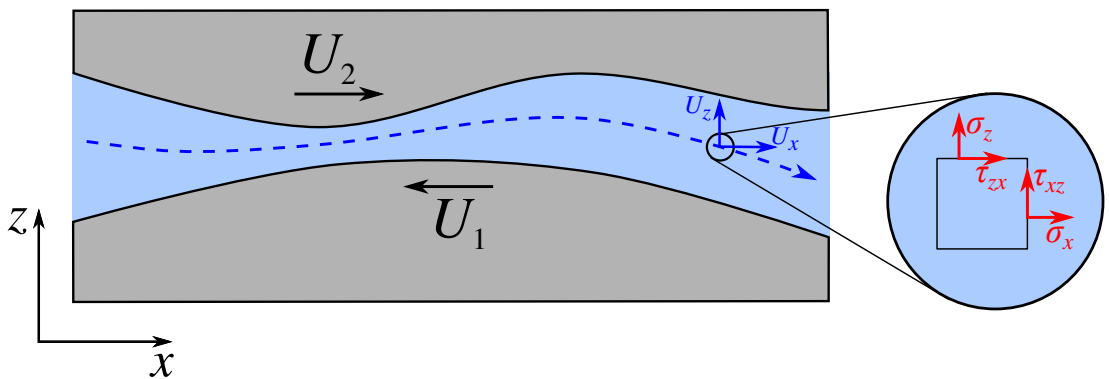


Figure 2.5: Laminar fluid flow between two surface with macroscopic velocities \mathbf{U}_1 and \mathbf{U}_2 . Note that the fluid velocity and stress components corresponding to the y -direction are not shown to avoid overcrowding.

while derivatives of two remaining components are obtained by replacing U with V and W , respectively. Since $\mathbf{x} = \mathbf{X} + \mathbf{u}$, where \mathbf{X} is the position in the fixed reference configuration, we may write that $\dot{x} = \dot{u} = U, \dot{y} = \dot{v} = V, \dot{z} = \dot{w} = W$ and arrive at the following expressions:

$$\left\{ \begin{array}{l} \frac{DU}{Dt} = \frac{\partial U}{\partial t} + U \frac{\partial U}{\partial x} + V \frac{\partial U}{\partial y} + W \frac{\partial U}{\partial z}, \\ \frac{DV}{Dt} = \frac{\partial V}{\partial t} + U \frac{\partial V}{\partial x} + V \frac{\partial V}{\partial y} + W \frac{\partial V}{\partial z}, \\ \frac{DW}{Dt} = \frac{\partial W}{\partial t} + U \frac{\partial W}{\partial x} + V \frac{\partial W}{\partial y} + W \frac{\partial W}{\partial z}. \end{array} \right. \quad (2.35a)$$

$$\left. \begin{array}{l} \frac{DV}{Dt} = \frac{\partial V}{\partial t} + U \frac{\partial V}{\partial x} + V \frac{\partial V}{\partial y} + W \frac{\partial V}{\partial z}, \\ \frac{DW}{Dt} = \frac{\partial W}{\partial t} + U \frac{\partial W}{\partial x} + V \frac{\partial W}{\partial y} + W \frac{\partial W}{\partial z}. \end{array} \right\} \quad (2.35b)$$

$$\left. \begin{array}{l} \frac{DW}{Dt} = \frac{\partial W}{\partial t} + U \frac{\partial W}{\partial x} + V \frac{\partial W}{\partial y} + W \frac{\partial W}{\partial z}. \end{array} \right\} \quad (2.35c)$$

Therefore, the *total* derivative describes the change of velocity of a fluid element as it moves in space, while the first term in the right hand side of each equation in (2.35) is termed as the *local* derivative and shows the variation of the velocity at a fixed point during time.

Finally, we write down the equations of the dynamic equilibrium, cf. (2.16):

$$\rho \frac{DU}{Dt} = \nabla \cdot \boldsymbol{\sigma} + \mathbf{f}_v, \quad (2.36)$$

where ρ is the fluid density, \mathbf{f}_v is the vector density of the volume forces, while $\rho (DU/Dt)$ is the vector density of the inertia forces. Substituting the introduced above expressions for the stress components (2.28) and (2.32), we arrive at Navier-Stokes equations:

$$\rho \frac{DU}{Dt} = -\nabla p + \frac{1}{3} \nabla (\eta \nabla \cdot \mathbf{U}) + \nabla \cdot (\eta \nabla \mathbf{U}) + \mathbf{f}_v, \quad (2.37)$$

where $\nabla \mathbf{U}$ is the gradient of the vector field \mathbf{U} . Note that the terms proportional to the fluid viscosity η are called the viscous forces. Note also that the system (2.37) consists of three equations for four unknowns: three components of the velocity vector U, V, W and the hydrostatic pressure p . The required fourth equation is provided by the principle of mass conservation, and is termed as the continuity equation, see Section 2.3.2.

2.3.2 Continuity equation

First, we introduce the mass flux vector \mathbf{q}_m as the mass of fluid flowing per unit time through a unit area:

$$\mathbf{q}_m = \rho \mathbf{U}, \quad (2.38)$$

where ρ is the fluid density and \mathbf{U} is the velocity vector.

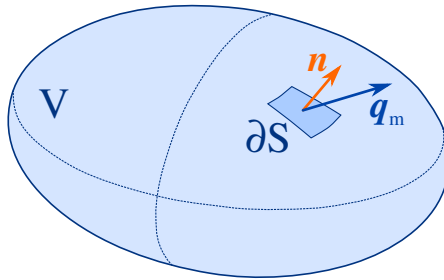


Figure 2.6: Outflow of fluid from a volume V , bounded by a surface S : \mathbf{n} is the outer normal to a surface element ∂S and \mathbf{q}_m is the mass flux vector.

The principle of mass conservation states, that the outflow of mass from a volume equals to the decrease of mass in this volume. It results in the integral form of continuity equation:

$$\frac{dm}{dt} + \iint_S (\mathbf{q}_m \cdot \mathbf{n}) dS = 0, \quad (2.39)$$

where m is the mass of fluid inside the volume V , surface S is the boundary of the volume V , and \mathbf{n} is the outer normal to this surface, see Fig. 2.6. Applying the divergence theorem:

$$\iint_S (\mathbf{q}_m \cdot \mathbf{n}) dS = \iiint_V (\nabla \cdot \mathbf{q}_m) dV, \quad (2.40)$$

and considering mass as the volume integral of the fluid density:

$$m = \iiint_V \rho dV, \quad (2.41)$$

we arrive at the differential (local) form of the continuity equation:

$$\frac{\partial \rho}{\partial t} + \nabla \cdot (\rho \mathbf{U}) = 0. \quad (2.42)$$

If the fluid is considered incompressible, i.e. the density ρ is constant, the continuity equation reduced to a simpler form:

$$\nabla \cdot \mathbf{U} = 0, \quad (2.43)$$

which states that the divergence of the velocity field is zero in every point of the flow.

2.3.3 Reynolds equation

The Reynolds equation is a simplified case of the general Navier-Stokes equations (2.37), valid for thin fluid films, which are studied in the theory of lubrication [Hamrock et al., 2004]. This simplification is obtained under following assumptions:

- (i) the flow is laminar;
- (ii) viscous shear forces dominate over inertia forces;
- (iii) fluid volume forces are negligible;
- (iv) fluid film thickness is small, relative to other lateral dimensions.

Although not explicitly used in the subsequent derivation, an additional assumption of sufficiently small slopes of solid's surfaces, bounding the fluid film, is required in certain applications. Omitting this assumptions results in inconsistencies between predictions of the Reynolds equation and solutions of full Navier-Stokes equations, for example, in the problem of the fluid flow through fractures, see [Brown et al., 1995].

We will start the derivation of the Reynolds equation, introducing the following dimensionless variables and parameters, see also Fig. 2.7:

$$\begin{aligned} \bar{x} &= \frac{x}{l_0}, & \bar{y} &= \frac{y}{b_0}, & \bar{z} &= \frac{z}{h_0}, & \bar{t} &= \frac{t}{t_0}, \\ \bar{U} &= \frac{U}{U_0}, & \bar{V} &= \frac{V}{V_0}, & \bar{W} &= \frac{W}{W_0}, \\ \bar{\rho} &= \frac{\rho}{\rho_0}, & \bar{\eta} &= \frac{\eta}{\eta_0}, & P &= \frac{h_0^2}{\eta_0 U_0 l_0} p, \end{aligned} \quad (2.44)$$

where l_0 , b_0 and h_0 are the characteristic lengths of the fluid channel in x , y and z directions, respectively, $l_0/b_0 \sim 1$, t_0 is time scale, U_0 , V_0 and W_0 are the characteristic velocity components in the three directions, ρ_0 and η_0 are the relevant scales for the density and the viscosity, respectively. The assumption (iv) of the thin flow requires, therefore, that $h_0/l_0 \ll 1$ and $h_0/b_0 \ll 1$.

Using the introduced scales, we may consider the Reynolds number \mathcal{R} , which is a quantity describing the ratio between the inertia and the viscous forces:

$$\mathcal{R} = \frac{\rho_0 U_0 l_0}{\eta_0}. \quad (2.45)$$

However, in the fluid film lubrication theory, due to the difference between the scale for the channel thickness h_0 and scales for other lateral dimensions (l_0 and b_0), the modified Reynolds number is defined for each of three spatial directions, see also [Hamrock et al., 2004]:

$$\mathcal{R}_x = \frac{\rho_0 U_0 h_0^2}{\eta_0 l_0}, \quad \mathcal{R}_y = \frac{\rho_0 V_0 h_0^2}{\eta_0 b_0}, \quad \mathcal{R}_z = \frac{\rho_0 W_0 h_0}{\eta_0}. \quad (2.46)$$

Note that the first two modified Reynolds numbers \mathcal{R}_x and \mathcal{R}_y are of order h_0/l_0 , and so is the third one (\mathcal{R}_z), since, in accordance with the assumption (iv), we may consider the ratio W_0/U_0 to be of the same order as h_0/l_0 . Therefore, the assumption of the thin flow (iv) also implies that the viscous forces dominate over the inertia, i.e. the assumption (ii).

Substituting expressions (2.44) into the Navier-Stokes equations (2.37) and neglecting terms of order h_0/l_0 , h_0/b_0 and smaller, we obtain the following equations for the dimensional variables:

$$\begin{cases} \frac{\partial p}{\partial x} = \frac{\partial}{\partial z} \left(\eta \frac{\partial U}{\partial z} \right) & (2.47a) \\ \frac{\partial p}{\partial y} = \frac{\partial}{\partial z} \left(\eta \frac{\partial V}{\partial z} \right) & (2.47b) \\ \frac{\partial p}{\partial z} = 0, & (2.47c) \end{cases}$$

where inertia and volume forces are not present. Moreover, the last equation (2.47c) immediately states that the fluid pressure is constant across the thickness of the film and is a function of the x and y coordinates only: $p = p(x, y)$.

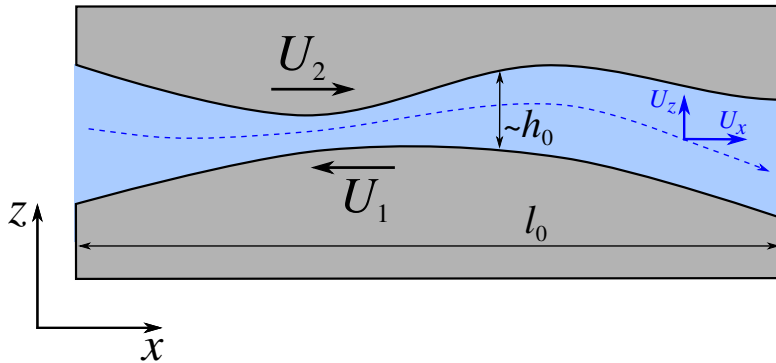


Figure 2.7: Fluid flow in a thin channel between two solids: h_0 is the characteristic thickness of the fluid film, and l_0 is the scale of the lateral extent of the channel in the x -direction. Note that the scales corresponding to the y -direction are not shown to avoid overcrowding.

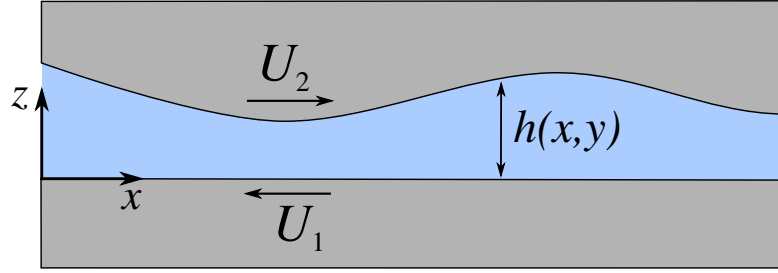


Figure 2.8: Fluid flow in a thin channel between two solids: one of the two surfaces is flat and aligned with the plane $z = 0$, while the other surface is given by an equation $z = h(x, y)$, where h determines the film thickness.

Without adding any assumptions to what was outlined above, we may consider for simplicity that the surface of the one of the solids forming the channel is flat and aligned with the plane $z = 0$, while another surface is given by an equation $z = h(x, y)$, where h represents the film thickness, see Fig. 2.8. If, under the assumption (iv), we consider the constant viscosity in the z -direction, then equations (2.47a) and (2.47b) can be integrated twice along the film thickness, providing velocity components as:

$$U = \frac{\partial p}{\partial x} \frac{z^2 - zh}{2\eta} + U_1 \left(1 - \frac{z}{h}\right) + U_2 \frac{z}{h}, \quad (2.48a)$$

$$V = \underbrace{\frac{\partial p}{\partial y} \frac{z^2 - zh}{2\eta}}_{\text{Poiseuille term}} + \underbrace{V_1 \left(1 - \frac{z}{h}\right) + V_2 \frac{z}{h}}_{\text{Couette term}} \quad (2.48b)$$

where the following boundary values for velocity components were used:

$$z = 0 : U = U_1, V = V_1; \quad (2.49a)$$

$$z = h : U = U_2, V = V_2. \quad (2.49b)$$

Therefore, the fluid velocity profile along the film thickness is parabolic. Note that in the expressions of velocity components U and V the Poiseuille and the Couette terms were outlined: the former corresponds to the pressure-driven flow between immobile walls, while the latter describes the shear-driven flow, which is solely due to the relative motion of solid walls, see Fig. 2.9.

It is important to note here, that using the obtained expressions for the fluid velocity (2.48), we may write down the viscous shear stresses acting on the solid surfaces, for example, at $z = 0$:

$$\tau_{zx}|_{z=0} = \left(\eta \frac{\partial U}{\partial z} \right) \Big|_{z=0} = -\frac{h}{2} \frac{\partial p}{\partial x} - \frac{\eta(U_1 - U_2)}{h}, \quad (2.50a)$$

$$\tau_{zy}|_{z=0} = \left(\eta \frac{\partial V}{\partial z} \right) \Big|_{z=0} = -\frac{h}{2} \frac{\partial p}{\partial y} - \frac{\eta(V_1 - V_2)}{h}, \quad (2.50b)$$

which will be used below.

Since the fluid pressure does not depend on the z -coordinate, both equations (2.47a) and (2.47b) can be considered on the so-called *lubrication surface*, which we will denote by Γ^f . This can be one of the surfaces of the two solids, or an intermediate surface between them, see [Stupkiewicz et al., 2016] for more details. For the present case it is natural to consider the plane $z = 0$ as the lubrication surface. Thus, for each point (x, y) on the plane $z = 0$ we compute the volumetric fluid flux, integrated over the film

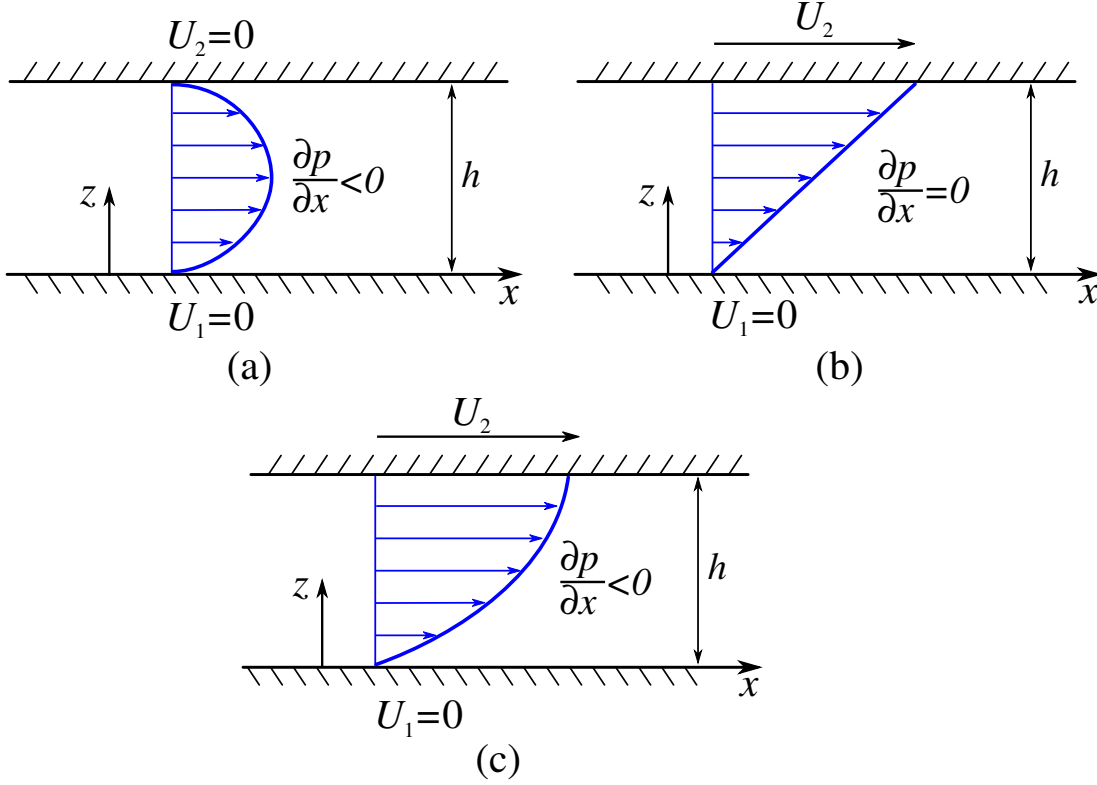


Figure 2.9: Velocity profiles for: (a) Poiseuille pressure-driven flow between immobile walls; (b) Couette shear-driven flow due to the relative motion of the walls; (c) Combination of the Poiseuille and the Couette flow.

thickness, in the x and y directions as:

$$q_x = \int_0^h U dz = -\frac{h^3}{12\eta} \frac{\partial p}{\partial x} + \frac{U_1 + U_2}{2} h, \quad (2.51a)$$

$$q_y = \int_0^h V dz = -\frac{h^3}{12\eta} \frac{\partial p}{\partial y} + \frac{V_1 + V_2}{2} h. \quad (2.51b)$$

In the following, for brevity, we will term the in-plane vector \mathbf{q} with components q_x and q_y simply as the fluid flux vector.

Now, we integrate also the local form of the continuity equation (2.42) across the film thickness:

$$\int_0^h \left[\frac{\partial \rho}{\partial t} + \frac{\partial}{\partial x} (\rho U) + \frac{\partial}{\partial y} (\rho V) + \frac{\partial}{\partial z} (\rho W) \right] dz = 0. \quad (2.52)$$

Considering also the constant density ρ across the fluid film, and using the Leibniz rule for differentiation under the integral sign, we find that:

$$\int_0^h \frac{\partial}{\partial x} (\rho U) dz = \frac{\partial}{\partial x} \left(\int_0^h \rho U dz \right) - (\rho U)|_{z=h} \frac{\partial h}{\partial x} = \frac{\partial}{\partial x} (\rho q_x) - \rho U_2 \frac{\partial h}{\partial x}, \quad (2.53)$$

where the definition of the fluid flux component q_x (2.51a) was used. Similarly for the y -component:

$$\int_0^h \frac{\partial}{\partial y} (\rho V) dz = \frac{\partial}{\partial y} (\rho q_y) - \rho V_2 \frac{\partial h}{\partial y}, \quad (2.54)$$

while the z -component may be integrated directly to give:

$$\int_0^h \frac{\partial}{\partial z} (\rho W) dz = \rho (W_2 - W_1), \quad (2.55)$$

where W_1 and W_2 are z -components of the velocity vector at $z = 0$ and $z = h$, respectively. Finally, substituting expressions (2.53)-(2.55) into integrated continuity equation (2.52), and using formulas (2.51a) and (2.51b), we arrive at the general form of the Reynolds equation:

$$\begin{aligned} h \frac{\partial \rho}{\partial t} - \frac{\partial}{\partial x} \left(\frac{\rho h^3}{12\eta} \frac{\partial p}{\partial x} \right) - \frac{\partial}{\partial y} \left(\frac{\rho h^3}{12\eta} \frac{\partial p}{\partial y} \right) + \frac{(U_1 + U_2)}{2} \frac{\partial(\rho h)}{\partial x} + \frac{(V_1 + V_2)}{2} \frac{\partial(\rho h)}{\partial y} \\ - \rho U_2 \frac{\partial h}{\partial x} - \rho V_2 \frac{\partial h}{\partial y} + \rho (W_2 - W_1) = 0. \end{aligned} \quad (2.56)$$

The Reynolds equation permits a number of reduced forms. If we limit the study to only tangential relative motion of solid surfaces, then $W_1 = 0$, while the velocity z -component at $z = h$ can be expressed as $W_2 = U_2 \partial h / \partial x + V_2 \partial h / \partial y$, and, therefore, three last terms in (2.56) vanish. If fluid is assumed incompressible, i.e. the fluid density ρ is constant, then the Reynolds equation takes the form:

$$\frac{\partial}{\partial x} \left(\frac{h^3}{\eta} \frac{\partial p}{\partial x} \right) + \frac{\partial}{\partial y} \left(\frac{h^3}{\eta} \frac{\partial p}{\partial y} \right) = 12\tilde{U} \frac{\partial h}{\partial x} + 12\tilde{V} \frac{\partial h}{\partial y}, \quad (2.57)$$

where $\tilde{U} = (U_1 + U_2) / 2$ and $\tilde{V} = (V_1 + V_2) / 2$. If, additionally, the fluid is isoviscous, i.e. the viscosity η is constant, the Reynolds equation is:

$$\frac{\partial}{\partial x} \left(h^3 \frac{\partial p}{\partial x} \right) + \frac{\partial}{\partial y} \left(h^3 \frac{\partial p}{\partial y} \right) = 12\eta \tilde{U} \frac{\partial h}{\partial x} + 12\eta \tilde{V} \frac{\partial h}{\partial y}, \quad (2.58)$$

Finally, if, in addition to aforementioned assumptions, solids are motionless, the Reynolds equation is reduced to the following form:

$$\nabla \cdot (h^3 \nabla p) = 0, \quad (2.59)$$

which will be used throughout this dissertation. Accordingly, in this latter case the fluid flux vector, defined in (2.51), reads:

$$\mathbf{q} = -\frac{h^3}{12\eta} \nabla p, \quad (2.60)$$

where $\nabla(\cdot) := \partial(\cdot) / \partial x \mathbf{e}_x + \partial(\cdot) / \partial y \mathbf{e}_y$.

2.3.4 Boundary conditions for the Reynolds equation

The Reynolds equation in the general form (2.56), as well as in any of the reduced forms (2.57)-(2.59), is defined on the lubrication surface Γ^f . In order to complete the statement of a boundary value problem for the thin fluid flow, this equation has to be considered together with a relevant set of boundary conditions, such as:

$$\begin{cases} p = p_0 & \text{on } \gamma^p \\ \mathbf{q} \cdot \mathbf{m} = q_0 & \text{on } \gamma^q, \end{cases} \quad (2.61a)$$

$$\begin{cases} p = p_0 & \text{on } \gamma^p \\ \mathbf{q} \cdot \mathbf{m} = q_0 & \text{on } \gamma^q, \end{cases} \quad (2.61b)$$

where (2.61a) are Dirichlet boundary conditions with a prescribed fluid pressure p_0 and (2.61b) are Neumann boundary conditions with a prescribed fluid flux q_0 , defined on curves $\gamma^p \subset \partial\Gamma^f$ and $\gamma^q \subset \partial\Gamma^f$, respectively, and \mathbf{m} is an outward normal to Γ^f , see Fig. 2.10. Note that $\gamma^p \cup \gamma^q = \partial\Gamma^f$ and $\gamma^p \cap \gamma^q = \emptyset$.

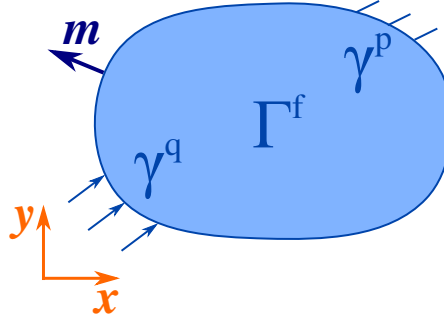


Figure 2.10: Sketch for the boundary value problem statement for the thin fluid flow.

2.4 Hydrostatic fluid models

As was mentioned in the first chapter, one of the objectives of this study is to take into account the possibility of fluid entrapment in the contact interface. Therefore, we will consider here the behaviour of a hydrostatically pressurized fluid trapped in a domain completely bounded by the solid's surface. Since the fluid pressure is assumed uniform in the whole volume of a trapped pool, the Reynolds equations for the fluid flow, derived in the previous section, is not relevant here. We will describe the behaviour of the trapped fluid using an additional equation, which takes the form of a constraint on the trapped volume in case of incompressible fluid model, or the form of a constitutive relation between the fluid pressure and the relative change of volume, if the fluid compressibility is taken into account.

If the trapped fluid is assumed incompressible, the required constraint is straightforward: the fluid volume V must be constant. However, the pressure developed in such fluid pocket can rise significantly, so that the assumption of the incompressible fluid becomes invalid, and, therefore, the fluid compressibility must be taken into account in this case. The relation between the fluid pressure and its volume change can be formalized by considering the bulk modulus K , which is defined as the ratio of infinitesimal pressure increase to the relative decrease of the volume:

$$K = -V \frac{dp}{dV}. \quad (2.62)$$

In the *constant* compressibility model, K is simply a coefficient of proportionality between the relative change of the fluid volume and the pressure change:

$$p = p_0 + K \left(1 - \frac{V}{V_0} \right), \quad (2.63)$$

where p_0 is the fluid pressure at some reference volume V_0 (for example, at the moment of formation of the trapped fluid pocket) and p is the fluid pressure corresponding to a smaller volume V . Note, that using the linear compressible model, an ideal gas equation could also be considered in the trapped zone, which is relevant for a gaseous fluid: $pV = nRT$; assuming an isothermal process, we obtain:

$$p = p_0 \left(1 + \frac{V_0 - V}{V} \right). \quad (2.64)$$

However, the constant compressibility model (2.63) does not provide satisfactory results for most of the fluids used in real-life lubrication problems, since a significant dependence of the compressibility modulus K on the pressure p takes place [Kuznetsov, 1985]. The simplest model, and yet quite precise for most of lubricating fluids, which

takes into account this dependence, is the *linear* compressibility model, see [Kuznetsov, 1985, Nellesmann et al., 1977]. According to this model, K is linearly evolving with pressure:

$$K = K_0 + K_1 p, \quad (2.65)$$

where K_0 [Pa], K_1 [dimensionless] are model parameters: K_0 is the value of the bulk modulus in unpressurized state, and K_1 is the tangent of the linear dependence. The affine expression (2.65), substituted into (2.62), upon integration results in the following *non-linear* relation between the fluid pressure and its volume change, cf. (2.63):

$$p = \left(\frac{K_0}{K_1} + p_0 \right) \left(\frac{V}{V_0} \right)^{-K_1} - \frac{K_0}{K_1}, \quad (2.66)$$

where, again, p_0 is the pressure at volume V_0 and the pressure p corresponds to a smaller volume V .

2.5 Coupled problem statement

In the end of this chapter we use the discussed above description of the solid and fluid continuum to provide the general formulation of the coupled problem statement, which will be studied in this dissertation.

We consider a problem of a thin fluid flow in contact interface between a solid with an arbitrary surface geometry and a rigid flat. Let us denote by Ω the deformable solid and by $\Gamma \subset \partial\Omega$ the part of its surface, which represents the *potential* contact zone, i.e. defines the extent of the contact interface. At the same time, Γ determines the maximal possible extent of the domain, where the solid interacts with the fluid. For concreteness, we shall assume that the surface of the solid is given by a function $z(x, y)$, while the rigid plane is $z = 0$.

The resolution of the coupled problem under discussion requires subdivision of the surface Γ into following parts, according to the local status² of the interface, see Fig. 2.11:

$$\Gamma = \Gamma^c \cup \Gamma^{\text{fsi}} \bigcup_{i=1}^{n_{\text{tf}}} \Gamma_i^{\text{tf}}, \quad (2.67)$$

where Γ^c is the *active* contact zone, where normal contact tractions are non-zero, Γ^{fsi} is part of the solid's surface, which interacts with the flowing fluid and where the surface tractions are equal to the corresponding tractions in the fluid (so-called fluid-structure interface), Γ_i^{tf} , $i = \overline{1, n_{\text{tf}}}$, are trapped fluid zones, i.e. parts of the surface Γ which are out of contact, but completely delimited by non-simply connected contact patches.

The partition of the interface, introduced in (2.67), requires several explanatory remarks. First, by definition of the active contact zone, $\Gamma^c \cap \Gamma^{\text{fsi}} = \emptyset$ and $\Gamma^c \cap \Gamma_i^{\text{tf}} = \emptyset \forall i = \overline{1, n_{\text{tf}}}$. Note also, that $\Gamma^{\text{fsi}} \cap \Gamma_i^{\text{tf}} = \emptyset \forall i = \overline{1, n_{\text{tf}}}$, i.e. even though all trapped pockets contain the same fluid, as the one present in the fluid-flow domain, the behaviour of the trapped fluid is not governed by the Reynolds equation. Furthermore, each trapped zone is considered separately from others, i.e. $\Gamma_i^{\text{tf}} \cap \Gamma_j^{\text{tf}} = \emptyset \forall i = \overline{1, n_{\text{tf}}}, j = \overline{1, n_{\text{tf}}}, i \neq j$, since the behaviour of the fluid in each pocket depends on the volume of this pocket at the moment of its formation, and also on corresponding fluid pressure, see Sec. 2.4. Finally, we term by Γ^f the projection of Γ^{fsi} on the rigid plane $z = 0$, which shall serve as the lubrication surface, where the Reynolds equation for the fluid flow is defined.

²By local status in this context we mean the location of each point of the interface in the active contact zone, fluid flow, or one of the trapped fluid zones.

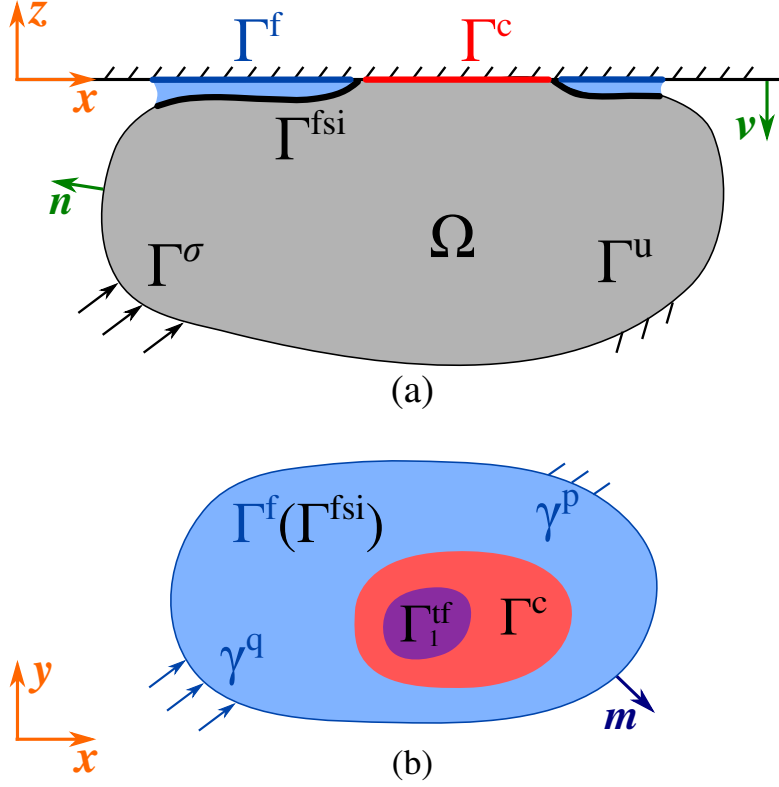


Figure 2.11: Sketch of the problem under study: (a) contact between a solid and a rigid plane with fluid present in the interface; (b) view of the contact interface. Notations: Γ^c is the active contact zone, Γ^f is the lubrication surface (where the Reynolds equation is solved), Γ^{fsi} is the fluid-structure interface, Γ_1^{tf} is a trapped fluid zone, see (2.67). Note that Γ^f is the projection of Γ^{fsi} on the rigid flat.

2.5.1 Solid mechanics problem with unilateral contact

The deformation of the solid (in absence of the fluid) is governed by the balance of momentum equation complemented by the contact and boundary conditions:

$$\begin{cases} \nabla \cdot \boldsymbol{\sigma}(\mathbf{u}) + \mathbf{f}_v = 0 & \text{in } \Omega & (2.68a) \\ g_n(\mathbf{u}) \geq 0, \sigma_n(\mathbf{u}) \leq 0, g_n(\mathbf{u}) \sigma_n(\mathbf{u}) = 0 & \text{on } \Gamma & (2.68b) \\ \mathbf{u} = \mathbf{u}_0 & \text{on } \Gamma^u & (2.68c) \\ \mathbf{n} \cdot \boldsymbol{\sigma} = \boldsymbol{\sigma}_0 & \text{on } \Gamma^\sigma & (2.68d) \end{cases}$$

where (2.68a) is the static local balance of momentum equation (see Section 2.1), (2.68a) are the Hertz-Signorini-Moreau conditions of the non-adhesive frictionless unilateral contact (see Sec. 2.2), (2.68c) are the Dirichlet boundary conditions with a prescribed displacement \mathbf{u}_0 and (2.68d) are the Neumann boundary conditions with a prescribed surface traction $\boldsymbol{\sigma}_0$.

If the interfacial friction is taken into account, then the following frictional constraints complement the problem statement (2.68):

$$\begin{cases} \|\boldsymbol{\sigma}_t\| < \mu |\sigma_n|, \|\dot{\mathbf{g}}_t\| = 0 & \text{on } \Gamma^{\text{stick}} & (2.69a) \\ \boldsymbol{\sigma}_t = -\mu |\sigma_n| \frac{\dot{\mathbf{g}}_t}{\|\dot{\mathbf{g}}_t\|}, \|\dot{\mathbf{g}}_t\| > 0, & \text{on } \Gamma^{\text{slip}}, & (2.69b) \end{cases}$$

where μ is the coefficient of friction (CoF) in the classic Coulomb's model, Γ^{stick} and Γ^{slip} are the stick and slip contact zones, respectively: $\Gamma^{\text{stick}} \cap \Gamma^{\text{slip}} = \emptyset$, $\Gamma^{\text{stick}} \cup \Gamma^{\text{slip}} = \Gamma^c$. It

is important to note, that the constraints (2.68b) do not take into account the coupling of the contact problem with the fluid flow and/or trapped fluid problems. When this coupling is considered (especially in case of the two-way approach), the problem becomes much more complicated, since additional constraints governing the non-contact part of the interface $\Gamma \setminus \Gamma^c$ appear. In other words, Hertz-Signorini-Moreau conditions need to be amended since the pressure in non-contact zones is non-zero (and is unknown). Note that in the subsequent simulations the active contact zone Γ^c emerges in the convergence loop of the Newton-Raphson method, which will be utilized for the resolution of this strongly non-linear problem.

2.5.2 Thin fluid flow

The thin fluid flow is governed by:

$$\begin{cases} \nabla \cdot [g_n(\mathbf{u})^3 \nabla p] = 0 & \text{in } \Gamma^f & (2.70a) \\ p = p_0 & \text{on } \gamma^p & (2.70b) \\ \mathbf{q} \cdot \mathbf{m} = q_0 & \text{on } \gamma^q & (2.70c) \end{cases}$$

where (2.70a) is the Reynolds equation for isoviscous incompressible Newtonian fluid (see Section 2.3, note that the tangential relative motion of the solid walls is not considered here, whereas the normal motion is assumed to be quasi-static), $p(x, y)$ is the fluid pressure field defined on the lubrication surface Γ^f , which is a projection of the fluid-structure interface Γ^{fsi} on the rigid flat ($z = 0$), (2.70b) are the Dirichlet boundary conditions with a prescribed fluid pressure p_0 and (2.70c) are the Neumann boundary conditions with a prescribed fluid flux q_0 , defined at $\gamma^p \subset \partial\Gamma^f$ and $\gamma^q \subset \partial\Gamma^f$, respectively, \mathbf{m} is the outward normal to Γ^f , and the fluid flux \mathbf{q} was defined in (2.60). Note that for each point $(x, y) \in \Gamma^f$ the thickness of the film is computed as the normal gap $g_n(\mathbf{u})$ of the corresponding point $(x, y, z) \in \Gamma^{\text{fsi}}$.

2.5.3 Fluid-structure interface

The equilibrium of the solid and fluid tractions on the fluid-structure interface Γ^{fsi} needs to fulfill the following equation:

$$\boldsymbol{\sigma} \cdot \mathbf{n} = -p \mathbf{n} - \frac{g_n(\mathbf{u})}{2} \nabla p \quad \text{on } \Gamma^{\text{fsi}}, \quad (2.71)$$

where the term on the left-hand side is nothing but the surface traction vector of the solid: $\boldsymbol{\sigma}^{(n)} = \boldsymbol{\sigma} \cdot \mathbf{n}$. The first right-hand side term is the normal traction due to the hydrostatic pressure, while the second one is the tangential traction due to viscous shear stresses in the fluid that act on the solid's surface (here, it results from the Poiseuille flow, see Eqs. (2.50a)-(2.50b) in Sec. 2.3). However, note that the gradient operator in (2.71) is defined on the lubrication surface Γ^f as $\nabla(\cdot) := \partial(\cdot)/\partial x \mathbf{e}_x + \partial(\cdot)/\partial y \mathbf{e}_y$. Therefore, the second term in (2.71) is not exactly perpendicular to the outward normal \mathbf{n} to the surface Γ^{fsi} . Nevertheless, this slight inconsistency is justified (at least partially) by the requirement of small slopes of the surface geometry for validity of the Reynolds equation in certain applications (see discussion in Sec. 2.3) and is often accepted in elasto-hydrodynamic lubrication problems, see, for example, [Stupkiewicz, 2009, Stupkiewicz et al., 2016].

We recall also, that in the derivation of the Reynolds equation (see Sec. 2.3.3), the scale h_0 for thickness of the fluid film, represented here by the normal gap g_n , was assumed to be much smaller than the lateral extent of the channel l_0 (and also relevant wavelengths of the surface spectrum). Using definitions of scales, introduced

in (2.44), we observe that the absolute value of the normal component of the traction vector $|\sigma_n| = p \sim P$, where P is the scale for the fluid pressure. At the same time, the magnitude of the tangential component of the traction vector in the fluid $\|\sigma_t\| \sim h_0 P/l_0$, i.e. smaller than the normal one by an order of h_0/l_0 . Due to this difference in scales, the effect of fluid shear stresses on the deformation of the solid is often neglected in lubrication problems, see [Stupkiewicz, 2018].

However, in sealing applications, studies of the elasto-hydrodynamic lubrication regime show a noticeable effect of the shear tractions on the seal's leakage, see [Stupkiewicz and Marcinişzyn, 2009]. Besides, it is important to note, that the difference in scales between normal and shear traction components is valid only if the pressure drop occurs over a length $\sim l_0$, i.e. the change of pressure is sufficiently gradual. This may not be the case, for example, in contact seals, when the external load is close to the critical value, under which the interface is completely sealed (the fluid leakage ceases). Just before that happens, a fluid path which connects chambers under different pressure exists, and almost the whole pressure drop occurs over a narrow and short constriction located on this path, see [Persson and Yang, 2008, Persson, 2010]. At this constriction, due to a locally high pressure gradient, the tangential traction becomes of the same order of magnitude as the normal term. Therefore, for the sake of completeness, we will consider both normal and shear components of the fluid-induced traction in the numerical framework presented in following chapters.

It is important to note also, that we do not need to consider the so-called no-slip condition (i.e. zero flow velocity at the fluid-structure boundary), as, for example, in [Farhat et al., 1998], since it is already taken into account in the derivation of the Reynolds equation (2.59).

2.5.4 Trapped fluid zones

The hydrostatic pressure p_i^{tf} , developed in the i -th trapped fluid zone, is applied to the surface of the solid body as the normal traction:

$$\sigma_n = -p_i^{\text{tf}} \quad \text{on } \Gamma_i^{\text{tf}}, \quad i = 1 \dots n_{\text{tf}}, \quad (2.72)$$

which has a form similar to the Neumann boundary condition for the solid mechanics problem, cf. (2.68d). However, the pressure p_i^{tf} is *a priori* unknown, and to take into account the behaviour of the trapped fluid, we will use hydrostatic fluid models discussed in Sec. 2.4. Thus, if the fluid in trapped zones is assumed incompressible, then the following constraint on the fluid volume V_i^{tf} in the i -th trapped zone is considered:

$$V_i^{\text{tf}} = V_{i0}^{\text{tf}}, \quad (2.73)$$

where V_{i0}^{tf} is the volume of the fluid in the i -th trapped pool at the moment when it was formed. Due to the increasing external load, which brings the solid in contact with the rigid flat, the fluid pressure inside of trapped zones also increases and may become significantly higher than the pressure in the fluid-flow domain. Therefore, while still assuming incompressible fluid in the Reynolds equation (2.70a), for the trapped fluid zones we may consider compressibility models discussed in. Sec. 2.4.

If the trapped fluid compressibility is taken into account, then instead of (2.73) a constitutive relation between the fluid pressure and its volume change is to be provided. In the case of constant fluid bulk modulus K this equation is given by:

$$p_i^{\text{tf}} = p_{i0}^{\text{tf}} + K \left(1 - \frac{V_i^{\text{tf}}}{V_{i0}^{\text{tf}}} \right), \quad (2.74)$$

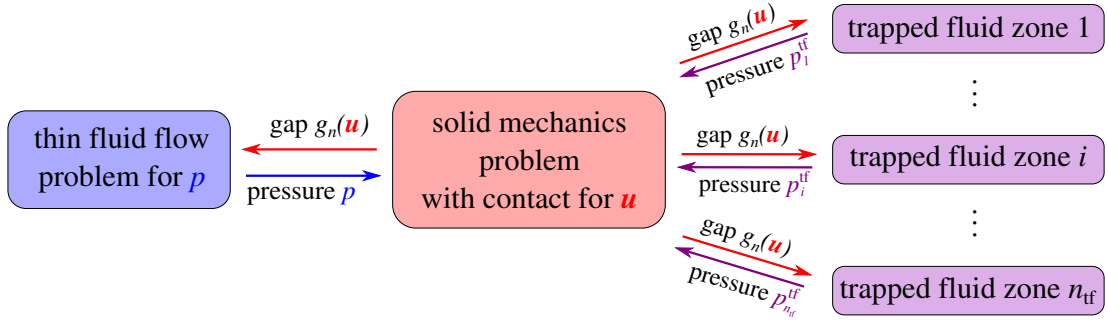


Figure 2.12: Schematic diagram showing dependencies between coupled sub-problems.

where p_{i0}^{tf} is the initial pressure of the trapped fluid, corresponding to the volume V_{i0}^{tf} . In the case of pressure-dependent fluid bulk modulus $K = K_0 + K_1 p_i^{\text{tf}}$, the relation becomes nonlinear and takes the following form:

$$p_i^{\text{tf}} = \left(p_{i0}^{\text{tf}} + \frac{K_0}{K_1} \right) \left(\frac{V_i^{\text{tf}}}{V_{i0}^{\text{tf}}} \right)^{-K_1} - \frac{K_0}{K_1}. \quad (2.75)$$

In the discussed above statement of the coupled problem involving contact, fluid flow and trapped fluid pools, we assume that the fluid occupies the whole free volume between the contacting surfaces. Accordingly, the volume of the fluid in the i -th pool V_i^{tf} is equal to the volume of the gap $V_i(\mathbf{u})$ between the surface Γ_i^{tf} and the rigid flat:

$$V_i^{\text{tf}} = V_i(\mathbf{u}) = \int_{\Gamma_i^{\text{tf}}} g_n(\mathbf{X} + \mathbf{u})(-\mathbf{n} \cdot \boldsymbol{\nu}) d\Gamma, \quad (2.76)$$

where \mathbf{n} is the outward normal to the surface Γ_i^{tf} , and $\boldsymbol{\nu}$ is the normal to the rigid flat, see Fig. 2.11. However, in the Chapter 7 of this dissertation we will study the problem of the trapped fluid in the contact interface, excluding the fluid flow. In that context only we will consider a more general statement of the trapped fluid sub-problem, allowing a partial filling of the trapped pool by fluid, i.e. $V_i^{\text{tf}} < V_i(\mathbf{u})$.

2.5.5 Remarks on the coupled problem

Equations, discussed in Sections 2.5.1-2.5.4, demonstrate essential dependencies between coupled sub-problems, see also a schematic diagram in Fig. 2.12. On the one hand, the fluid film thickness, necessary for solving the Reynolds equation, is defined by the current normal gap $g_n(\mathbf{u})$, i.e. by the displacement field \mathbf{u} . On the other hand, the fluid pressure field p determines fluid-induced tractions on Γ^{fsi} , see (3.41d). However, not only the thickness of the fluid film is defined by \mathbf{u} , but the fluid-flow domain Γ^{f} itself depends on the solution of the contact problem. Likewise, the morphology of the contact area determines the existence and the extent of trapped fluid zones Γ_i^{tf} . Trapped fluid, in its turn, creates additional pressure applied to the surface of the solid, see (2.72).

Apart from an intrinsic nonlinearity of this multi-field problem, the dependence of fluid-flow domain Γ^{f} and trapped fluid zones Γ_i^{tf} on the resolution of contact constraints creates an additional complexity. Moreover, it can be enhanced by a possibly sophisticated morphology of the contact area resulting from deterministic or random features of the surface geometry. Another significant difficulty is encountered in handling edge effects, e.g. enforcing continuity of surface tractions across boundaries between contact and fluid-flow zones $\partial\Gamma^{\text{c}} \cap \partial\Gamma^{\text{fsi}}$, and also between contact and trapped fluid zones $\partial\Gamma^{\text{c}} \cap \partial\Gamma_i^{\text{tf}}$ $i = \overline{1, n_{\text{tf}}}$. Below we will discuss in detail our recipes of partitioning the interface and handling the multi-field problem.

Finally, we note that the presented problem set-up corresponds to the two-way coupling approach, which considers reciprocal dependencies between sub-problems. The one-way coupling for this problem, which neglects the action of the fluid pressure on surface of the solid, can also be studied, if corresponding equations are omitted, e.g. Eqs. (2.71) and (2.72).

Part II

Computational framework

Chapter 3

Variational formulation of the coupled problem

Résumé de Chapitre 3 “Formulation variationnelle du problème couplé”

Le chapitre 3 est consacré à la forme faible du problème couplé, dont la forme forte a été présentée dans le chapitre précédent. Premièrement, nous énonçons la formulation variationnelle du problème de mécanique du solide avec le contact (avec et sans frottement). En particulier, nous discutons de la manière dont le contact conduit au problème de minimisation sous contraintes (ou, de manière équivalente, à l'inéquation variationnelle) et décrivons la méthode pour sa résolution. Ensuite, nous incorporons le problème d'écoulement de fluide dans la forme faible et gérons l'équilibre des tractions fluide et solide à l'interface fluide-structure. De plus, nous considérons le travail virtuel dans zones de fluide piégé, qui s'ajoute à la forme faible. Enfin, nous présentons la formulation variationnelle du problème couplé, en considérant les approches de couplage unidirectionnel et bidirectionnel.

In this chapter we will discuss the weak statement of the coupled problem, formulated in the previous chapter. In particular, we will provide the variational formulation for the solid mechanics problem with contact constraints and for the fluid mechanics problem in case of thin fluid flow. We will incorporate the equilibrium of fluid and solid tractions on the fluid-structure interface into the weak form, and also take into account the influence of trapped fluid zones. We will finalize our discussion by outlining the variational formulation of the coupled problem as a whole, considering both one-way and two-way coupling approaches.

3.1 Weak formulation of the solid mechanics problem with contact constraints

In this section we will address the weak formulation of the solid mechanics problem with contact constraints, presented in the strong form in Section 2.5, Eqs. (2.68)-(2.69). We will search for a weak solution of this problem represented by a vector-valued function $\mathbf{u} \in \mathbf{H}^1(\Omega)$, by which we mean that each component of the vector \mathbf{u} belongs to the Sobolev space $H^1(\Omega)$:

$$\mathbf{u} \in \mathbf{H}^1(\Omega) = \left\{ (u_1, u_2, \dots, u_{\dim}) \mid u_i \in H^1(\Omega), 1 \leq i \leq \dim \right\}, \quad (3.1)$$

where “dim” stands for the dimension of the physical space, i.e. number of components in vector \mathbf{u} ; see [Adams and Fournier, 2003, Kikuchi and Oden, 1988] for more details and definitions.

3.1.1 Homogeneous Dirichlet boundary condition

First, we note that the problem under discussion involves an inhomogeneous Dirichlet boundary condition (2.68c). In order to apply available theoretical results, this problem statement needs to be transformed to a one with homogeneous (zero) Dirichlet boundary conditions, which can be achieved without losing generality, see, for example [Evans, 2010]. To show that, we consider a simpler boundary value problem, which includes the local balance of momentum equation (2.68a) only with the Dirichlet boundary condition (2.68c):

$$\begin{cases} \nabla \cdot \boldsymbol{\sigma}(\mathbf{u}) + \mathbf{f}_v = 0 & \text{in } \Omega \\ \mathbf{u} = \mathbf{u}_0 & \text{on } \Gamma^u. \end{cases} \quad (3.2a)$$

It is important to note, that we may consider the known function $\mathbf{u}_0 \in \mathbf{H}^{1/2}(\Gamma^u)$, defined only on the boundary $\Gamma^u \subset \partial\Omega$, as a trace of some other function $\mathbf{w} \in \mathbf{H}^1(\Omega)$, i.e. $\mathbf{w} = \mathbf{u}_0$ on Γ^u . Then the function $\tilde{\mathbf{u}} = \mathbf{u} - \mathbf{w}$ belongs to a linear subspace \mathbf{V} of the Sobolev space $\mathbf{H}^1(\Omega)$, defined as:

$$\mathbf{V} = \left\{ \mathbf{u} \in \mathbf{H}^1(\Omega) \mid \mathbf{u} = 0 \text{ on } \Gamma^u \right\}. \quad (3.3)$$

Next, assuming linearity of $\boldsymbol{\sigma}(\mathbf{u})$, we note that function $\tilde{\mathbf{u}} \in \mathbf{V}$ is a weak solution of the following problem:

$$\begin{cases} \nabla \cdot \boldsymbol{\sigma}(\tilde{\mathbf{u}}) + \tilde{\mathbf{f}}_v = 0 & \text{in } \Omega \\ \tilde{\mathbf{u}} = 0 & \text{on } \Gamma^u, \end{cases} \quad (3.4a)$$

where $\tilde{\mathbf{f}}_v = \mathbf{f}_v + \nabla \cdot \boldsymbol{\sigma}(\mathbf{w})$. Therefore, without losing generality, in the remaining of this chapter we will consider the problem (2.68)-(2.69) with a homogeneous Dirichlet boundary condition

$$\mathbf{u} = 0 \text{ on } \Gamma^u, \quad (3.5)$$

instead of (2.68c). Nevertheless, in the numerical resolution of the solid mechanics problem, e.g. using the finite-element method, inhomogeneous Dirichlet boundary conditions can be readily considered. They can be enforced either by direct altering the global tangent matrix and the residual vector, or, alternatively, using the method of Lagrange multipliers or the penalty method, see, for example [Utku and Carey, 1982].

3.1.2 Weak form of the contact problem

Now, since homogeneous Dirichlet boundary conditions are considered, the solution \mathbf{u} will also belong to the space \mathbf{V} , defined in (3.3). Moreover, we shall introduce contact constraints into the variational formulation by considering functions from a subset \mathbf{K} of \mathbf{V} , defined as follows:

$$\mathbf{K} = \left\{ \mathbf{u} \in \mathbf{V} \mid \mathbf{u} \cdot \boldsymbol{\nu} \geq -g_{n0} \text{ on } \Gamma \right\}, \quad (3.6)$$

where $\boldsymbol{\nu}$ is the normal to the rigid flat, and g_{n0} is the initial gap, see (2.19). Let us assume that \mathbf{u} is the “classic” (strong) solution of the contact problem, then, naturally, $\mathbf{u} \in \mathbf{K}$. We will consider also an arbitrary function $\mathbf{v} \in \mathbf{K}$, note that the function $\delta\mathbf{u} = \mathbf{v} - \mathbf{u}$, which we will term as the test function (or the virtual displacement),

also satisfies the homogeneous Dirichlet boundary conditions (3.5), i.e. $(\mathbf{v} - \mathbf{u}) \in \mathbf{V}$. Multiplying the local balance of momentum equation (2.68a) by this test function and integrating over the volume of the solid Ω , we obtain:

$$\int_{\Omega} (\nabla \cdot \boldsymbol{\sigma}(\mathbf{u}) + \mathbf{f}_v) \cdot (\mathbf{v} - \mathbf{u}) \, d\Omega = 0, \quad \forall \mathbf{v} \in \mathbf{K}. \quad (3.7)$$

Next, integrating by parts and applying the divergence theorem, we arrive at:

$$\int_{\Omega} \boldsymbol{\sigma}(\mathbf{u}) : (\nabla \mathbf{v} - \nabla \mathbf{u}) \, d\Omega - \int_{\Omega} \mathbf{f}_v (\mathbf{v} - \mathbf{u}) \, d\Omega - \int_{\partial\Omega} \mathbf{n} \cdot \boldsymbol{\sigma}(\mathbf{u}) \cdot (\mathbf{v} - \mathbf{u}) \, d\Gamma = 0, \quad (3.8)$$

where $\{:\}$ is the double inner product (contraction) of second-order tensors, and we used $d\Gamma$ for the elementary surface area, i.e. $d\Gamma \equiv d(\partial\Omega)$. Observing that $\mathbf{n} \cdot \boldsymbol{\sigma}$ is nothing but the traction vector $\boldsymbol{\sigma}^{(n)}$, we may divide the integral over the surface $\partial\Omega$ into the two parts where $\boldsymbol{\sigma}^{(n)} \neq 0$: Γ^σ with non-trivial Neumann boundary conditions (prescribed traction $\boldsymbol{\sigma}_0$) and the active contact zone Γ^c to obtain:

$$\begin{aligned} \int_{\Omega} \boldsymbol{\sigma}(\mathbf{u}) : (\nabla \mathbf{v} - \nabla \mathbf{u}) \, d\Omega - \int_{\Omega} \mathbf{f}_v (\mathbf{v} - \mathbf{u}) \, d\Omega - \\ \int_{\Gamma^\sigma} \boldsymbol{\sigma}_0 \cdot (\mathbf{v} - \mathbf{u}) \, d\Gamma - \int_{\Gamma^c} \boldsymbol{\sigma}^{(n)} \cdot (\mathbf{v} - \mathbf{u}) \, d\Gamma = 0, \quad \forall \mathbf{v} \in \mathbf{K} \end{aligned} \quad (3.9)$$

which we will term as the weak form for the contact problem. We will consider first the frictionless case, and after that discuss the contact problem with friction.

3.1.3 Variational formulation for the frictionless case

We recall that the traction vector can be divided into normal and tangential components. In the frictionless case $\boldsymbol{\sigma}_t = 0$ on Γ^c and thus $\boldsymbol{\sigma}^{(n)} = \sigma_n \mathbf{n}$. Considering the integrand of the contact term, we observe that:

$$\boldsymbol{\sigma}^{(n)} \cdot (\mathbf{v} - \mathbf{u}) = \sigma_n (\mathbf{n} \cdot \mathbf{v} - \mathbf{n} \cdot \mathbf{u}) = \sigma_n (\mathbf{n} \cdot \mathbf{v} - g_{n0}) \geq 0, \quad (3.10)$$

where we used that $\mathbf{n} \cdot \mathbf{u} = -\boldsymbol{\nu} \cdot \mathbf{u} = g_{n0}$ on Γ^c , since \mathbf{u} is the solution of the contact problem and satisfies (2.68b), and $\mathbf{n} \cdot \mathbf{v} = -\boldsymbol{\nu} \cdot \mathbf{v} \leq g_{n0}$ on Γ^c , since $\mathbf{v} \in \mathbf{K}$. Thus, $\mathbf{n} \cdot \mathbf{v} - g_{n0} \leq 0$, while $\sigma_n \leq 0$ on Γ^c also due to (2.68b). Therefore, the last integral in (3.9) is non-negative and we arrive at the following inequality:

$$\int_{\Omega} \boldsymbol{\sigma}(\mathbf{u}) : (\nabla \mathbf{v} - \nabla \mathbf{u}) \, d\Omega - \int_{\Omega} \mathbf{f}_v (\mathbf{v} - \mathbf{u}) \, d\Omega - \int_{\Gamma^\sigma} \boldsymbol{\sigma}_0 \cdot (\mathbf{v} - \mathbf{u}) \, d\Gamma \geq 0, \quad \forall \mathbf{v} \in \mathbf{K}, \quad (3.11)$$

which is termed as the variational inequality characterizing the solution $\mathbf{u} \in \mathbf{K}$ of the frictionless unilateral contact problem (2.68). It may be written in a more abstract form:

$$\text{Find } \mathbf{u} \in \mathbf{K} \text{ such that: } a(\mathbf{u}, \mathbf{v} - \mathbf{u}) - f(\mathbf{v} - \mathbf{u}) \geq 0, \quad \forall \mathbf{v} \in \mathbf{K}, \quad (3.12)$$

where $a(\cdot, \cdot)$ is a bilinear form defined on $\mathbf{V} \times \mathbf{V}$:

$$a(\mathbf{u}, \mathbf{v}) = \int_{\Omega} \boldsymbol{\sigma}(\mathbf{u}) : \nabla \mathbf{v} \, d\Omega, \quad (3.13)$$

and $f(\cdot)$ is a linear functional on \mathbf{V} :

$$f(\mathbf{v}) = \int_{\Omega} \mathbf{f}_v \cdot \mathbf{v} \, d\Omega + \int_{\Gamma^\sigma} \boldsymbol{\sigma}_0 \cdot \mathbf{v} \, d\Gamma. \quad (3.14)$$

The variational inequality (3.12) is equivalent to the following constrained minimization problem:

$$\text{Find } \mathbf{u} \in \mathbf{K} \text{ such that: } J_0(\mathbf{u}) = \inf_{\mathbf{v} \in \mathbf{K}} J_0(\mathbf{v}), \quad (3.15)$$

where the functional $J_0(\mathbf{v})$ is defined as:

$$J_0(\mathbf{v}) = \frac{1}{2} a(\mathbf{v}, \mathbf{v}) - f(\mathbf{v}). \quad (3.16)$$

It is important to note that we obtained the variational inequality (3.12), instead of a standard variational principle (i.e. equality) used in solid mechanics, because of the presence of contact constraints, introduced through the restriction of the space of admissible functions to $\mathbf{K} \subset \mathbf{V}$. For more details interested reader is referred to [Kikuchi and Oden, 1988].

We may rewrite (3.9) using the notation $\delta \mathbf{u} = \mathbf{v} - \mathbf{u}$ for the virtual displacement:

$$\int_{\Omega} \boldsymbol{\sigma}(\mathbf{u}) : \nabla \delta \mathbf{u} \, d\Omega - \int_{\Omega} \mathbf{f}_v \cdot \delta \mathbf{u} \, d\Omega - \int_{\Gamma^\sigma} \boldsymbol{\sigma}_0 \cdot \delta \mathbf{u} \, d\Gamma - \int_{\Gamma^c} \sigma_n \mathbf{n} \cdot \delta \mathbf{u} \, d\Gamma = 0, \quad (3.17)$$

and obtain the weak form known as the balance of the virtual work. Next, we compute the variation of the normal gap function, corresponding to the virtual displacement $\delta \mathbf{u}$:

$$\delta g_n(\mathbf{u}) = \frac{\partial g_n}{\partial \mathbf{u}} \cdot \delta \mathbf{u} = \boldsymbol{\nu} \cdot \delta \mathbf{u}. \quad (3.18)$$

Remembering that $\boldsymbol{\nu} \cdot \delta \mathbf{u} = -\mathbf{n} \cdot \delta \mathbf{u}$, we may rewrite now the balance of virtual work as:

$$\int_{\Omega} \boldsymbol{\sigma}(\mathbf{u}) : \nabla \delta \mathbf{u} \, d\Omega - \int_{\Omega} \mathbf{f}_v \cdot \delta \mathbf{u} \, d\Omega - \int_{\Gamma^\sigma} \boldsymbol{\sigma}_0 \cdot \delta \mathbf{u} \, d\Gamma + \int_{\Gamma^c} \sigma_n \delta g_n \, d\Gamma = 0, \quad \forall \delta \mathbf{u} \in \mathbf{V}. \quad (3.19)$$

It is important to note that in practical studies, e.g. in the finite-element framework, direct resolution of the variational inequality (3.12) or, equivalently, the constrained minimization problem (3.15)-(3.16) is usually avoided. The most popular approach is to handle the contact constraints using methods of the optimization theory (such as the method of Lagrange multipliers or the penalty method), which permits to find the current active contact zone Γ^c and the corresponding contact tractions σ_n . Then we may compute *a priori* unknown contact term in the balance of virtual works (3.19), and, therefore, transform the problem with contact constraints into an unconstrained minimization problem, for which classic resolution methods can be applied. The next chapter of this dissertation is devoted to a discussion of this approach.

3.1.4 Variational formulation for the frictional case

Let us consider now the frictional case, i.e. the weak solution of the problem (2.68)-(2.69), and examine separately the contact integral in the weak form (3.9):

$$\int_{\Gamma^c} \boldsymbol{\sigma}^{(n)} \cdot (\mathbf{v} - \mathbf{u}) \, d\Gamma = \int_{\Gamma^c} \sigma_n \mathbf{n} \cdot (\mathbf{v} - \mathbf{u}) \, d\Gamma + \int_{\Gamma^c} \boldsymbol{\sigma}_t \cdot (\mathbf{v} - \mathbf{u}) \, d\Gamma, \quad (3.20)$$

where the first term on the right-hand side corresponds to the normal contact traction and was already showed to be non-negative. On the contrary, the second term is due to the frictional contact resistance and is non-positive, since the direction of the frictional traction is opposite to the (virtual) sliding direction. Next, we note that the frictional traction $\boldsymbol{\sigma}_t$ is non-zero at a certain point of the solid's surface only while this point is in contact with the rigid plane, i.e. belongs to Γ^c . Therefore we may rewrite the frictional term in the following way:

$$\int_{\Gamma^c} \boldsymbol{\sigma}_t \cdot (\mathbf{v} - \mathbf{u}) d\Gamma = \int_{\Gamma^c} \boldsymbol{\sigma}_t \cdot (\mathbf{v}_t - \mathbf{u}_t) d\Gamma, \quad (3.21)$$

where \mathbf{u}_t is the tangential slip, see Sec. 2.2 and discussions in [Demkowicz and Oden, 1982, Yastrebov, 2013], while \mathbf{v}_t is the tangential component of the vector \mathbf{v} .

Next, we note that the frictional term cannot be represented by a differentiable functional due to the non-smooth Coulomb's law (2.69). Therefore, the contact problem with friction cannot be written in the form of inequality (3.12), nor as the constrained minimization of the functional (3.16). In order to proceed, we consider a more general variational inequality:

$$\text{Find } \mathbf{u} \in \mathbf{K} \text{ such that: } a(\mathbf{u}, \mathbf{v} - \mathbf{u}) - f(\mathbf{v} - \mathbf{u}) + j(\mathbf{v}) - j(\mathbf{u}) \geq 0, \quad \forall \mathbf{v} \in \mathbf{K}, \quad (3.22)$$

where the functional $j(\cdot)$, defined on \mathbf{V} , is non-differentiable. We will show now that solution of the frictional contact problem $\mathbf{u} \in \mathbf{K}$ satisfies the variational inequality (3.22) if the functional $j(\cdot)$ is defined as:

$$j(\mathbf{v}) = \int_{\Gamma^c} \mu |\sigma_n| \|\mathbf{v}_t\| d\Gamma, \quad (3.23)$$

where μ is the coefficient of friction. Using Eq. (3.9) together with the notations (3.13) and (3.14) for the forms $a(\cdot, \cdot)$ and $f(\cdot)$, respectively, we may write the following:

$$\begin{aligned} a(\mathbf{u}, \mathbf{v} - \mathbf{u}) - f(\mathbf{v} - \mathbf{u}) + j(\mathbf{v}) - j(\mathbf{u}) = \\ \int_{\Gamma^c} \sigma_n \mathbf{n} \cdot (\mathbf{v} - \mathbf{u}) d\Gamma + \int_{\Gamma^c} \boldsymbol{\sigma}_t \cdot (\mathbf{v}_t - \mathbf{u}_t) d\Gamma + \int_{\Gamma^c} \mu |\sigma_n| (\|\mathbf{v}_t\| - \|\mathbf{u}_t\|) d\Gamma. \end{aligned} \quad (3.24)$$

Consequently, it needs to be proved that the left-hand side of (3.24) is non-negative for any $\mathbf{v} \in \mathbf{K}$, if \mathbf{u} is the solution of the frictional contact problem. Note that the first integral on the right-hand side of (3.24) is non-negative, and thus it remains to show that:

$$\boldsymbol{\sigma}_t \cdot (\mathbf{v}_t - \mathbf{u}_t) + \mu |\sigma_n| (\|\mathbf{v}_t\| - \|\mathbf{u}_t\|) \geq 0, \quad \forall \mathbf{v} \in \mathbf{K}. \quad (3.25)$$

Following the logic of the Coulomb's laws of friction, we will consider separately stick and slip contact states. Note that hereinafter we shall relate the frictional traction to the tangential displacement u_t rather than to its rate, which is consistent with incremental quasi-static analysis employed in Chapter 4, see, for example, [Alart and Curnier, 1991]. Therefore, in the stick state $\|\boldsymbol{\sigma}_t\| \leq \mu |\sigma_n|$ and $\mathbf{u}_t = 0$, consequently:

$$\begin{aligned} \boldsymbol{\sigma}_t \cdot (\mathbf{v}_t - \mathbf{u}_t) + \mu |\sigma_n| (\|\mathbf{v}_t\| - \|\mathbf{u}_t\|) &= \boldsymbol{\sigma}_t \cdot \mathbf{v}_t + \mu |\sigma_n| \|\mathbf{v}_t\| \\ &\geq -\|\boldsymbol{\sigma}_t\| \|\mathbf{v}_t\| + \mu |\sigma_n| \|\mathbf{v}_t\| > 0. \end{aligned} \quad (3.26)$$

In case of slip, $\boldsymbol{\sigma}_t = -\mu |\sigma_n| \mathbf{s}$, where \mathbf{s} is the sliding direction, see (2.69b). Then we

may write:

$$\begin{aligned}
\boldsymbol{\sigma}_t \cdot (\mathbf{v}_t - \mathbf{u}_t) + \mu |\sigma_n| (\|\mathbf{v}_t\| - \|\mathbf{u}_t\|) &= \boldsymbol{\sigma}_t \cdot \mathbf{v}_t + \mu |\sigma_n| \|\mathbf{u}_t\| + \mu |\sigma_n| \|\mathbf{v}_t\| - \mu |\sigma_n| \|\mathbf{u}_t\| \\
&= \boldsymbol{\sigma}_t \cdot \mathbf{v}_t + \mu |\sigma_n| \|\mathbf{v}_t\| \\
&\geq -\|\boldsymbol{\sigma}_t\| \|\mathbf{v}_t\| + \mu |\sigma_n| \|\mathbf{v}_t\| = 0.
\end{aligned} \tag{3.27}$$

Therefore, we have proved that (3.25) holds and, consequently, $\mathbf{u} \in \mathbf{K}$ satisfies the variational inequality (3.22). For the proof that a sufficiently smooth (regular) solution \mathbf{u} of the variational inequality is also the solution of the initial problem, the interested reader is referred to [Kikuchi and Oden, 1988].

Similarly to the frictionless case, the variational inequality (3.22) is equivalent to a constrained minimization problem, which takes now the following form:

$$\text{Find } \mathbf{u} \in \mathbf{K} \text{ such that: } J(\mathbf{u}) = \inf_{\mathbf{v} \in \mathbf{K}} J(\mathbf{v}). \tag{3.28}$$

The functional $J(\mathbf{v})$ is defined as:

$$J(\mathbf{v}) = J_0(\mathbf{v}) + j(\mathbf{v}) = \frac{1}{2} a(\mathbf{v}, \mathbf{v}) - f(\mathbf{v}) + j(\mathbf{v}), \tag{3.29}$$

where the non-differentiable functional $j(\cdot)$ was given in (3.23).

Therefore, despite the complexity due to additional constraints, the contact problem with friction can still be represented by a variational inequality. The practical resolution for this problem follows the approach discussed above for the frictionless case, i.e. using the constrained optimization theory, handle the contact conditions and obtain an unconstrained minimization problem, or, in other words, transform the variational inequality to the standard (equality) formulation.

We will finish this section by presenting the weak form as the balance of virtual work for the frictional case:

$$\begin{aligned}
\int_{\Omega} \boldsymbol{\sigma}(\mathbf{u}) : \nabla \delta \mathbf{u} \, d\Omega - \int_{\Omega} \mathbf{f}_v \cdot \delta \mathbf{u} \, d\Omega - \int_{\Gamma^\sigma} \boldsymbol{\sigma}_0 \cdot \delta \mathbf{u} \, d\Gamma \\
+ \int_{\Gamma^c} \sigma_n \delta g_n \, d\Gamma + \int_{\Gamma^c} \boldsymbol{\sigma}_t \cdot \delta \mathbf{g}_t \, d\Gamma = 0, \quad \forall \delta \mathbf{u} \in \mathbf{V},
\end{aligned} \tag{3.30}$$

where $\delta \mathbf{g}_t = \mathbf{v}_t - \mathbf{u}_t = \delta \mathbf{u}_t$ is the tangential component of the virtual displacement, sometimes termed as the variation of the tangential gap:

$$\delta \mathbf{g}_t = (\mathbf{I} - \boldsymbol{\nu} \otimes \boldsymbol{\nu}) \cdot \delta \mathbf{u}. \tag{3.31}$$

3.2 Weak formulation of the coupled problem

In the previous section we discussed the weak formulation of the solid mechanics problem with contact constraints, see Eq. (3.30). In order to describe the coupling between the solid and the fluid sub-problems, this result needs to be elaborated by taking into account other equations of the coupled framework. To simplify the explanation, first, we will complement the weak form of the contact problem by the virtual work of fluid-induced tractions on the surface of the solid. Next, will take into account contribution of trapped fluid pools, and finally, discuss the weak formulation of the fluid-flow sub-problem. Upon that, the weak statement of the coupling between solid and fluid equations will be complete.

3.2.1 Weak form of the fluid-structure interface balance

First, we note that the equilibrium of fluid and solid tractions on the surface Γ^{fsi} (2.71) is represented by an equation similar to a Neumann boundary condition, cf. (2.68d). However, it is important to bear in mind that the traction vector representing the right-hand side of (2.71) is not *a priori* prescribed: it depends on the fluid pressure p , its gradient ∇p and the normal gap g_n , which is defined, in its turn, by the displacement field \mathbf{u} . Nevertheless, we may compute the work of the fluid-induced tractions on the surface Γ^{fsi} on a virtual displacement $\delta \mathbf{u}$ as:

$$\delta W^{\text{fsi}} = \int_{\Gamma^{\text{fsi}}} \left(-p \mathbf{n} - \frac{g_n}{2} \nabla p \right) \cdot \delta \mathbf{u} \, d\Gamma. \quad (3.32)$$

Thereupon, we include it into the balance of virtual work (3.30) with the minus sign, since the virtual work of surface tractions has a sign opposite to the one of the work of internal forces, see, for example, (3.8). Note also, that the gradient operator in (3.32) is defined on the lubrication surface Γ^{f} as $\nabla(\cdot) := \partial(\cdot)/\partial x \mathbf{e}_x + \partial(\cdot)/\partial y \mathbf{e}_y$, see discussion in Sec. 2.5 for more details.

3.2.2 Virtual work of trapped fluid zones

Let us examine now the contribution of trapped fluid pools to the coupled problem. On the one hand, the hydrostatic fluid pressure developed in each zone, similarly to the discussed above fluid-flow traction, is applied to the surface of the solid as the normal traction, see Eq. (2.72). On the other hand, we assume that there is not gradient of the fluid pressure inside of a trapped pool. Therefore, the behaviour of the trapped fluid is not described by a partial differential equation, unlike the solid mechanics (2.68) and the thin fluid flow (2.70) problems, but rather by constitutive models, providing the relation between the fluid pressure and its volume, see (2.73)-(2.75).

Thus, to capture the effect of the trapped fluid pressure on the solid, and also to take into account the trapped fluid's constitutive equation, we recall the classic thermodynamic definition of the elementary work done on a system, corresponding to an infinitesimal change of its volume. Following that, we compute the virtual work of an i -th trapped pool on the surface of the solid as:

$$\delta W_i^{\text{tf}} = -p_i^{\text{tf}} \delta V_i, \quad (3.33)$$

where the minus sign is used since an increase of the volume of a trapped pool leads to a decrease of its pressure, and consequently, to a release of the energy of the trapped fluid. Since the volume of the fluid inside a trap V_i is a functional of the displacement field \mathbf{u} as defined by the integral (2.76), δV_i can be treated as its first variation and computed using the *directional derivative*:

$$\delta V_i = D V_i(\mathbf{u}) \cdot \delta \mathbf{u} = \left. \frac{dV_i(\mathbf{u} + \epsilon \delta \mathbf{u})}{d\epsilon} \right|_{\epsilon=0}, \quad (3.34)$$

see [Wriggers, 2006, Wriggers, 2008] for more details. Therefore, the virtual work of the trapped fluid corresponding to a virtual displacement $\delta \mathbf{u}$ can be expressed as:

$$\delta W_i^{\text{tf}} = -p_i^{\text{tf}} D V_i(\mathbf{u}) \cdot \delta \mathbf{u}, \quad (3.35)$$

which can now be included into the weak form (3.30), taking into account that (3.35) is valid for each trapped fluid zone.

Furthermore, if the fluid is considered compressible, the fluid pressure p_i^{tf} becomes

a function of the trapped fluid volume, and, consequently, p_i^{tf} also depends on the displacement \mathbf{u} , see (2.74) and (2.75). If the fluid is assumed incompressible, it can still be included into the framework as compressible with a bulk modulus K sufficiently higher than that of the solid. Alternatively, the approach of Lagrange multipliers from the optimization theory can be used to enforce the constraint on the fluid volume (2.73). In Chapter 5 we will show that this approach also results in a formulation of the virtual work, equivalent to (3.35).

3.2.3 Weak formulation of the fluid flow problem

The thin flow of an isoviscous incompressible Newtonian fluid is governed by the Reynolds equation (2.70a) for the fluid pressure p , defined on the so-called lubrication surface Γ^{f} . As was discussed in Sec. 2.3, it is natural to consider the projection on the rigid flat $z = 0$ of the fluid-structure interface Γ^{fsi} (attached to the surface of the solid) as the lubrication surface. Consequently, we will solve the Reynolds equation on a two-dimensional domain Γ^{f} . Accordingly, the operator $\nabla(\cdot)$ in (2.70a) is a two-dimensional operator defined as $\nabla(\cdot) := [\partial(\cdot)/\partial x; \partial(\cdot)/\partial y]^T$.

We notice that the Dirichlet boundary conditions (2.70b) for the fluid flow problem are inhomogeneous. As we showed for the solid mechanics problem in Sec. (3.1.1), to simplify the derivation and study of the weak form, the initial problem can be transformed to the one with the homogeneous (zero) Dirichlet boundary conditions, without losing generality. Therefore, in this section we will also consider the problem (2.70) with the following boundary condition:

$$p = 0 \text{ on } \gamma^p \quad (3.36)$$

instead of (2.70b), bearing in mind that the practical resolution of the problem using the finite-element method easily permits to study inhomogeneous boundary conditions.

Next, we introduce the following set of admissible scalar functions, cf. (3.3):

$$\mathcal{P} = \left\{ p \in H^1(\Gamma^{\text{f}}) \mid p = 0 \text{ on } \gamma^p \right\}. \quad (3.37)$$

Let p be the strong solution of the problem (2.70) with the homogeneous boundary condition (3.36). Then, following the standard approach to elliptic (e.g. steady-state heat) equations, see, for example, [Zienkiewicz and Taylor, 1977], we obtain the weak form of (2.70a) by multiplying it with the test function $\delta p \in \mathcal{P}$ and integrating:

$$\int_{\Gamma^{\text{f}}} \nabla \cdot (g_n^3 \nabla p) \delta p \, d\Gamma = 0, \quad \forall \delta p \in \mathcal{P}. \quad (3.38)$$

Integrating by parts and applying the divergence theorem we may write:

$$\int_{\Gamma^{\text{f}}} g_n^3 \nabla p \cdot \nabla \delta p \, d\Gamma - \int_{\gamma^q} g_n^3 \nabla p \cdot \mathbf{m} \delta p \, d\gamma = 0, \quad \forall \delta p \in \mathcal{P}. \quad (3.39)$$

Using the definition of the fluid flux vector \mathbf{q} , see Eq. (2.60), we arrive at the weak form of the problem (2.70):

$$\int_{\Gamma^{\text{f}}} \frac{g_n^3}{12\eta} \nabla p \cdot \nabla \delta p \, d\Gamma + \int_{\gamma^q} q_0 \delta p \, d\gamma = 0, \quad \forall \delta p \in \mathcal{P}, \quad (3.40)$$

where $q_0 = \mathbf{q} \cdot \mathbf{m}$ is the prescribed flux on γ^q , see (2.70c).

3.2.4 Variational formulation of the coupled problem

We provide a variational statement of the coupled problem in the spirit of the monolithic approach, following [Yang and Laursen, 2009, Stupkiewicz, 2018]. For clarity, we will write separately equations for the solid phase (with the effect of trapped fluid zones included) and for the fluid-flow phase. The former reads:

$$G^s(\mathbf{u}, p, \delta \mathbf{u}) = 0 \quad \forall \delta \mathbf{u} \in \mathbf{V}; \quad (3.41a)$$

$$G^s(\mathbf{u}, p, \delta \mathbf{u}) = \int_{\Omega} \boldsymbol{\sigma}(\mathbf{u}) : \nabla \delta \mathbf{u} \, d\Omega - \int_{\Omega} \mathbf{f}_v \cdot \delta \mathbf{u} \, d\Omega - \int_{\Gamma^\sigma} \boldsymbol{\sigma}_0 \cdot \delta \mathbf{u} \, d\Gamma \quad (3.41b)$$

$$+ \int_{\Gamma^c} \sigma_n \delta g_n \, d\Gamma + \int_{\Gamma^c} \boldsymbol{\sigma}_t \cdot \delta \mathbf{g}_t \, d\Gamma \quad (3.41c)$$

$$+ \int_{\Gamma^{\text{fsi}}} \left(p \mathbf{n} + \frac{g_n(\mathbf{u})}{2} \nabla p \right) \cdot \delta \mathbf{u} \, d\Gamma \quad (3.41d)$$

$$- \sum_{i=1}^{n_{\text{tf}}} p_i^{\text{tf}} DV_i(\mathbf{u}) \cdot \delta \mathbf{u}, \quad (3.41e)$$

where $\delta g_n = \boldsymbol{\nu} \cdot \delta \mathbf{u}$ is the variation of the normal gap, and $\delta \mathbf{g}_t = (\mathbf{I} - \boldsymbol{\nu} \otimes \boldsymbol{\nu}) \cdot \delta \mathbf{u}$ is the variation of the tangential gap, see (3.18) and (3.31), respectively. Note that terms in (3.41b) correspond to the weak form of the solid mechanics problem without contact constraints, (3.41c) is the virtual work of the normal and frictional contact tractions, while (3.41d) is the virtual work of the tractions induced by the fluid flow on the surface of the solid, and, finally, (3.41e) is the virtual work of n_{tf} trapped fluid zones. Next, we provide the weak form for the fluid-flow phase:

$$G^f(p, \mathbf{u}, \delta p) = 0 \quad \forall \delta p \in \mathcal{P}; \quad (3.42a)$$

$$G^f(p, \mathbf{u}, \delta p) = \int_{\Gamma^f} \frac{g_n^3(\mathbf{u})}{12\eta} \nabla p \cdot \nabla \delta p \, d\Gamma + \int_{\gamma^q} q_0 \delta p \, d\gamma, \quad (3.42b)$$

Therefore, combining the two sub-problems together, the variational formulation of the coupled problem reads:

Find vector-valued function $\mathbf{u}(x, y, z) \in \mathbf{K}$ and scalar function $p(x, y) \in \mathcal{P}$ such that:

$$G^s(\mathbf{u}, p, \delta \mathbf{u}) = 0, \quad \forall \delta \mathbf{u} \in \mathbf{V}, \quad (3.43a)$$

and

$$G^f(p, \mathbf{u}, \delta p) = 0, \quad \forall \delta p \in \mathcal{P}. \quad (3.43b)$$

Note that the discussion above is valid for the two-way coupling approach, when both sub-problems have impact on each other. The one-way coupling for the problem under study can also be considered in the presented framework, upon three modifications:

- (i) omitting the fluid-induced tractions on the surface of the solid, i.e. the term (3.41d);
- (ii) neglecting the effect of trapped fluid zones, i.e. the sum (3.41e);
- (iii) assuming rigid solid walls while solving fluid-flow equation (3.43b).

Therefore, in case of one-way coupling, instead of (3.43), we have the following equations:

$$G^s(\mathbf{u}, \delta\mathbf{u}) = 0, \quad \forall \delta\mathbf{u} \in \mathbf{V}, \quad (3.44a)$$

$$G_u^f(p, \delta p) = 0, \quad \forall \delta p \in \mathcal{P}. \quad (3.44b)$$

Note that the weak form for the solid sub-problem does not depend on the fluid pressure p . Similarly, the weak form for the fluid sub-problem does not include displacement \mathbf{u} as an unknown. However, \mathbf{u} is still required as an input to compute the normal gap, which is considered fixed according to modification (iii), hence the subscript “ \mathbf{u} ” of G^f . In other words, in the one-way coupling approach, the solution of the solid sub-problem is not influenced by the fluid pressure, and for any given displacement field \mathbf{u} the fluid sub-problem is linear, which has an impact on the structure of the global matrix (considered upon the finite-element discretization). This will be discussed in detail in following chapters.

Chapter 4

Mechanical contact problem

Résumé de Chapitre 4 “Problème de contact mécanique”

Dans ce chapitre, plusieurs méthodes de résolution des contraintes de contact dans le cadre des éléments finis sont détaillées. Premièrement, nous montrons comment les méthodes issues de la théorie de l’optimisation (méthode des multiplicateurs de Lagrange, méthode de la pénalité, méthode du Lagrangien augmenté) peuvent être utilisées pour résoudre les problèmes de contact. Ensuite, nous considérons deux approches de la construction des éléments de contact : la première basée sur chaque nœud de la surface du corps déformable, la seconde basée sur chaque face de cette surface. Ensuite, nous présentons une formulation dans le cadre des éléments finis pour ces deux approches en utilisant les méthodes de la théorie d’optimisation. Nous décrivons la construction des vecteurs résiduels et des matrices tangentes, nécessaires à la résolution du problème non linéaire à l’aide de la méthode de Newton-Raphson.

In this chapter we present a numerical framework for resolution of contact constraints. We assume that the standard finite-element discretization of the deformable solid provides a corresponding discretised version of the contact interface (potential contact zone Γ). Note that for brevity and simplicity we preserve the same notations for discretised entities as were introduced in the continuous problem statement.

The resolution of the contact problem requires construction of interface elements, which are responsible for enforcement of contact constraints and are termed as contact elements. Different approaches can be utilized for construction of these elements, this process is recognized as the contact discretization. For the general case of contact between two deformable solids the most popular approaches are *node-to-node* (NTN), *node-to-segment* (NTS), and *segment-to-segment* (STS), for detailed information the reader is referred to [Wriggers, 2006].

In this dissertation we are studying the interaction between a deformable solid and a rigid flat, therefore we will discuss the *node-to-rigid-surface* and the *face-to-rigid-surface* approaches, which can be seen as particular cases of NTS and STS approaches, respectively. The considered cases represent a significant simplification of the general approaches, since the contact discretization becomes relevant only for the surface of the deformable body, while the analytical description of the second surface permits to express the normal gap in the closed form. Note that all presented formulations can be readily generalized for any analytic geometry of the rigid surface, such as a rigid cylinder, a sphere or an ellipsoid, see [Konyukhov and Schweizerhof, 2012] for details.

The difference between the two studied here approaches is in the definition of a contact element. In the node-to-rigid-surface approach each contact element is associated to one node of the surface Γ , whilst in the face-to-rigid-surface approach each element

is based on an edge (2D case) or a face (3D case) of the potential contact zone Γ , i.e. it includes all nodes adjacent to this edge or face.

4.1 Contact resolution methods

First, we will briefly discuss how methods of the optimization theory are used in resolution of contact problems. As was mentioned in Section 3.1, due to contact constraints the weak formulation of the problem takes the form of the variational inequality, instead of the equality variational principle, standard for solid mechanics. Methods of the optimization theory permit us to compute the virtual work of the contact tractions and, therefore, transform the variational inequality into a standard variational formulation. We will discuss here three different methods:

- the method of Lagrange multipliers,
- the penalty method,
- the augmented Lagrangian method,

however, other approaches for resolving contact constraints exist, and the interested reader is referred to [Wriggers, 2006].

4.1.1 Method of Lagrange multipliers

Let us denote by functional $\Pi^s(\mathbf{u})$ the potential energy of the system, in notations of Sec. 3.1 it reads:

$$\Pi^s(\mathbf{u}) = \frac{1}{2} a(\mathbf{u}, \mathbf{u}) - f(\mathbf{u}), \quad (4.1)$$

where bilinear form $a(\cdot, \cdot)$ and linear functional $f(\cdot)$ were defined in (3.13) and (3.14), respectively. As was discussed in Section 3.1, even in the frictionless case, the contact conditions lead to a constrained minimization problem:

$$\text{Find } \mathbf{u} \in \mathbf{K} \text{ such that: } \Pi^s(\mathbf{u}) = \inf_{\mathbf{v} \in \mathbf{K}} \Pi^s(\mathbf{v}), \quad (4.2)$$

where the function space was defined in (3.3) and (3.6). This problem is often easier to resolve, if it is transformed into a so-called *saddle point* problem. First, we introduce the *Lagrangian* \mathcal{L} of this problem:

$$\mathcal{L}(\mathbf{v}, \lambda_n) = \Pi^s(\mathbf{v}) + \int_{\Gamma^c} \lambda_n g_n(\mathbf{v}) d\Gamma, \quad (4.3)$$

where function $\lambda_n \in \mathcal{M}$, which is the space for so-called Lagrange multipliers, defined only on $\Gamma^c \subset \partial\Omega$, part of the boundary of Ω .

The question which naturally arises is “what is the nature of the space \mathcal{M} in theory and how is it used in practical computations?” Once the solution is obtained, the field of Lagrange multipliers λ_n represents normal traction σ_n on the contact zone. Therefore, according to the classification used in the functional analysis, the space \mathcal{M} is the dual of the space \mathbf{W} , which is, in its turn, the image under the trace operator of the space \mathbf{V} . In the context of the problem under study, recalling definition of the space \mathbf{V} , see (3.3), $\mathbf{W} = \mathbf{H}^{1/2}(\Gamma)$, and therefore

$$\mathcal{M} = \left(\mathbf{H}^{1/2}(\Gamma) \right)^*, \quad (4.4)$$

i.e. \mathcal{M} is the space of continuous linear functionals defined on $\mathbf{H}^{1/2}(\Gamma)$, which is often denoted as $\mathbf{H}^{-1/2}(\Gamma)$. Strictly speaking, in general case, the integral in (4.3) does not

have a meaning other than in the sense of the so-called *duality pairing* defined on $\mathcal{M} \times \mathbf{V}$, the interested reader is referred to [Kikuchi and Oden, 1988] for more details. However, in the practical resolution using the finite-element method, upon discretization, the Lagrange multipliers are searched in at least the Lebesgue space $L^2(\Gamma)$, i.e. in the form of square-integrable functions. Therefore, for practical purposes, the duality pairing can be represented by the corresponding integral in (4.3), see [Wohlmuth, 2000, Hieber, 2008, Popp, 2012, Gitterle, 2012] for more information.

Furthermore, to be able to reformulate the initial problem in terms of the Lagrangian (4.3), we need to consider the restriction of the space of Lagrange multipliers to the following admissible set:

$$\mathcal{N} = \{ \lambda_n \in \mathcal{M} \mid \lambda_n \leq 0 \}, \quad (4.5)$$

where the ordering relation “ \leq ” on the space \mathcal{M} in general case is defined in the sense presented in [Kikuchi and Oden, 1988]. In practice, as was stated above, Lagrange multipliers are searched in the space $L^2(\Gamma)$, and then definition of the admissible set \mathcal{N} becomes straightforward.

Then, under the discussed above conditions, the constrained minimization problem (4.2) is equivalent to the saddle point problem, formulated in the following way: Find $\mathbf{u} \in \mathbf{V}$ and $\lambda_n \in \mathcal{N}$ such that:

$$\mathcal{L}(\mathbf{u}, p) \leq \mathcal{L}(\mathbf{u}, \lambda_n) \leq \mathcal{L}(\mathbf{v}, \lambda_n), \quad \forall \mathbf{v} \in \mathbf{V}, \forall p \in \mathcal{N}, \quad (4.6)$$

or, equivalently,

$$\mathcal{L}(\mathbf{u}, \lambda_n) = \max_{p \in \mathcal{N}} \min_{\mathbf{v} \in \mathbf{V}} \mathcal{L}(\mathbf{v}, p) = \min_{\mathbf{v} \in \mathbf{V}} \max_{p \in \mathcal{N}} \mathcal{L}(\mathbf{v}, p). \quad (4.7)$$

Note that the search for a function \mathbf{u} minimizing the Lagrangian (4.3) is performed in the whole space \mathbf{V} , i.e. the constraint on the displacement field was waived, cf. (4.2). However, in a certain sense, it was transformed into restrictions of the space of the Lagrange multipliers to the admissible set (4.5), i.e. the condition $\lambda_n \leq 0$. Nevertheless, the discretised version of the problem, stated in the saddle point form, admits resolution even with the condition $\lambda_n \leq 0$, if a so-called *active set* strategy is used to determine the active contact zone Γ^c , details will be discussed in the next Section.

Let us assume that we found the saddle point (\mathbf{u}, λ_n) , i.e. the solution of the min-max problem (4.7) for the Lagrangian $\mathcal{L}(\mathbf{v}, p)$, defined in (4.3). Let us first assume that $g_n(\mathbf{u}) > 0$. Since λ_n is the maximizer of $\mathcal{L}(\mathbf{u}, p)$ with respect to $p \leq 0$, the only possible solution is $\lambda_n = 0$. Now let us investigate the case $\lambda_n < 0$. Since \mathbf{u} is the minimizer of $\mathcal{L}(\mathbf{v}, \lambda_n)$ among all $\mathbf{v} \in \mathbf{V}$, then $g_n(\mathbf{u}) \geq 0$, however, we have just shown that $g_n(\mathbf{u}) > 0$ leads to $\lambda_n = 0$. Therefore, we conclude that if $\lambda_n < 0$, then $g_n(\mathbf{u}) = 0$. Let us summarize the two cases discussed above:

$$\begin{cases} g_n(\mathbf{u}) = 0, & \lambda_n < 0 & \text{on } \Gamma^c \\ g_n(\mathbf{u}) > 0, & \lambda_n = 0 & \text{on } \Gamma \setminus \Gamma^c, \end{cases} \quad (4.8)$$

or, in a different way:

$$g_n \geq 0, \quad \lambda_n \leq 0, \quad \lambda_n g_n = 0 \quad \text{on } \Gamma, \quad (4.9)$$

which has exactly the same form as the Hertz-Signorini-Moreau conditions (2.20).

Therefore, the resolution of the frictionless contact problem is equivalent to finding the stationary (saddle) point of the Lagrangian (4.3), at which its variation vanishes,

under the condition $\lambda_n \leq 0$:

$$\begin{aligned} \delta\mathcal{L}(\mathbf{u}, \lambda_n) &= \delta\Pi^s(\mathbf{u}) + \int_{\Gamma^c} (\lambda_n \delta g_n(\mathbf{u}) + g_n(\mathbf{u}) \delta\lambda_n) d\Gamma \\ &= D\Pi^s(\mathbf{u}) \cdot \delta\mathbf{u} + \int_{\Gamma^c} \left(\lambda_n \frac{\partial g_n(\mathbf{u})}{\partial \mathbf{u}} \cdot \delta\mathbf{u} + g_n(\mathbf{u}) \delta\lambda_n \right) d\Gamma = 0, \\ &\quad \forall \delta\mathbf{u} \in \mathbf{V}, \quad \forall \delta\lambda_n \in \mathcal{M}, \end{aligned} \quad (4.10)$$

where we expressed the first variation of the functional $\Pi^s(\mathbf{u})$ using the directional derivative:

$$\delta\Pi^s(\mathbf{u}) = D\Pi^s(\mathbf{u}) \cdot \delta\mathbf{u} = \left. \frac{d\Pi^s(\mathbf{u} + \epsilon\delta\mathbf{u})}{d\epsilon} \right|_{\epsilon=0}, \quad (4.11)$$

see [Wriggers, 2006, Wriggers, 2008] for more details.

Note that applying the Lagrange multipliers method we introduced an extra equation to the weak problem statement. Now, in addition to function $\mathbf{u} \in \mathbf{V}$ we search for a function of Lagrange multipliers $\lambda_n \leq 0$ such that:

$$D\Pi^s(\mathbf{u}) \cdot \delta\mathbf{u} + \int_{\Gamma^c} \lambda_n \frac{\partial g_n(\mathbf{u})}{\partial \mathbf{u}} \cdot \delta\mathbf{u} d\Gamma = 0, \quad \forall \delta\mathbf{u} \in \mathbf{V}, \quad (4.12a)$$

$$\int_{\Gamma^c} g_n(\mathbf{u}) \delta\lambda_n d\Gamma = 0, \quad \forall \delta\lambda_n \in \mathcal{M}. \quad (4.12b)$$

Note also that Eq. (4.10) is equivalent to the system of two equations (4.12a) and (4.12b), since $\delta\mathbf{u}$ and $\delta\lambda_n$ are independent variations. Moreover, we obtained an additional term in the balance of virtual work for the solid mechanics problem, see Eq. (4.12a), which has exactly the same form as the virtual work of the contact tractions (in the frictionless case):

$$\int_{\Gamma^c} \lambda_n \delta g_n d\Gamma \sim \int_{\Gamma^c} \sigma_n \delta g_n d\Gamma, \quad (4.13)$$

cf (3.19). This similarity explains now why Lagrange multipliers λ_n represent the normal traction in the contact zone. Often Lagrange multipliers are termed as *dual* variables (degrees of freedom, upon discretization), as opposed to the *primal* ones, corresponding to the displacement vector components. At the same time, since $\delta\lambda_n \in \mathcal{M}$ is arbitrary, the equation (4.12b) ensures that $g_n = 0$ on the active contact zone Γ^c .

Note that the frictional constraints can also be treated using the Lagrange multipliers method, see for example, [Tur et al., 2009]. However, in this case the active set strategy becomes sophisticated to be able to correctly determine the stick and slip zones. Therefore, we will use the Lagrange multiplier method only in the frictionless case, while the treatment of the frictional constraints will be presented below under both penalty and augmented Lagrangian methods.

4.1.2 Penalty method

The penalty method is based on the approximate fulfilment of the contact constraints. We may consider instead of the functional $\Pi^s(\mathbf{v})$ a new functional $\Pi_\epsilon^s(\mathbf{v})$, defined as:

$$\Pi_\epsilon^s(\mathbf{v}) = \Pi^s(\mathbf{v}) + \epsilon P(\mathbf{v}), \quad (4.14)$$

where the penalty parameter ϵ is a strictly positive real number, and $P(\mathbf{v})$ is the penalty functional, which satisfies:

$$P(\mathbf{v}) \geq 0 \forall \mathbf{v} \in V, \quad P(\mathbf{v}) = 0 \text{ if and only if } \mathbf{v} \in \mathbf{K}. \quad (4.15)$$

Therefore, we may substitute the initial constrained minimization problem:

$$\text{Find } \mathbf{u} \in \mathbf{K} \text{ such that: } \Pi^s(\mathbf{u}) = \inf_{\mathbf{v} \in \mathbf{K}} \Pi^s(\mathbf{v}) \quad (4.16)$$

by the following approximate, however, unconstrained one:

$$\text{Find } \mathbf{u} \in \mathbf{V} \text{ such that: } \Pi_\epsilon^s(\mathbf{u}) = \inf_{\mathbf{v} \in \mathbf{V}} \Pi_\epsilon^s(\mathbf{v}). \quad (4.17)$$

Note that the parameter ϵ controls the accuracy of this approximation, and the exact solution is obtained if $\epsilon \rightarrow \infty$.

For simplicity, will consider first the frictionless case, and then take the Coulomb's friction law into account.

Frictionless case

Using the penalty method, we assume that contact pressure σ_n is non-zero only if the penetration ($g_n < 0$) takes place, i.e. consider the contact pressure as a function of the normal gap:

$$\sigma_n(g_n) = -\epsilon_n \langle -g_n \rangle = \begin{cases} 0, & g_n > 0 \\ \epsilon_n g_n, & g_n \leq 0, \end{cases} \quad (4.18)$$

where ϵ_n is the penalty parameter for the normal contact constraints, which controls the magnitude of the penetration. Note that the above formulation represents the *linear* penalty method, for discussions and examples, corresponding to a possible *non-linear* formulation, the reader is referred to [Yastrebov, 2013]. Note also that to simplify the notations we used the Macaulay brackets operator:

$$\langle x \rangle = \begin{cases} 0, & x < 0 \\ x, & x \geq 0. \end{cases} \quad (4.19)$$

Therefore, instead of (2.21) we have:

$$\begin{cases} g_n \leq 0, & \sigma_n \leq 0 & \text{on } \Gamma^c \\ g_n > 0, & \sigma_n = 0 & \text{on } \Gamma \setminus \Gamma^c. \end{cases} \quad (4.20)$$

Consequently, the virtual work of the frictionless contact may be written as:

$$\delta W^c = \int_{\Gamma^c} \sigma_n \delta g_n d\Gamma = \int_{\Gamma} -\epsilon_n \langle -g_n \rangle \delta g_n d\Gamma = \int_{\Gamma^c} \epsilon_n g_n \delta g_n d\Gamma. \quad (4.21)$$

Therefore, the ‘‘potential energy’’ of the contact interaction, defined as

$$W^c(\mathbf{u}) = \frac{\epsilon_n}{2} \int_{\Gamma^c} g_n(\mathbf{u})^2 d\Gamma, \quad (4.22)$$

plays the role of the functional $\epsilon P(\mathbf{u})$, see (4.14).

Frictional case

The approach to handling the frictional constraints is similar: we assume that the tangential traction $\boldsymbol{\sigma}_t$ is non-zero only if sliding occurs at the interface. It is important to note, that in numerical computations frictional contact problems are usually studied using the incremental quasi-static analysis. According to that, the tangential sliding velocity, corresponding to the k -th increment, is expressed as:

$$\dot{\boldsymbol{g}}_t^k \sim \Delta \boldsymbol{g}_t^k / (t^k - t^{k-1}), \quad (4.23)$$

where $\Delta \boldsymbol{g}_t^k = \boldsymbol{g}_t^k - \boldsymbol{g}_t^{k-1}$ is the increment of the tangential slip, and $(t^k - t^{k-1})$ is the increment in time. The latter can be omitted without loss of generality, and, for brevity and simplicity, we will write \boldsymbol{g}_t^k instead of $\Delta \boldsymbol{g}_t^k$. Moreover, the index k will be omitted, where possible, meaning that the corresponding discussions are valid for all increments.

Before writing down the expression for $\boldsymbol{\sigma}_t$, we will examine separately stick and slip cases. In the **stick** case, we do not require that a contact point does strictly adhere to the stick point \boldsymbol{x}_s , but rather allow it to slide by a small distance $\tilde{\boldsymbol{g}}_t$. This so-called “slip-in-stick”, see [Yastrebov, 2013], can be defined with respect to the previous stick position \boldsymbol{x}_s as:

$$\tilde{\boldsymbol{g}}_t = (\boldsymbol{I} - \boldsymbol{\nu} \otimes \boldsymbol{\nu}) \cdot (\boldsymbol{x} - \boldsymbol{x}_s), \quad (4.24)$$

where the multiplication with the tensor (first term in brackets) provides projection of the corresponding vector on the rigid plane. Therefore, the violation of frictional constraints results in a tangential traction, magnitude of which is proportional to this slip, while its direction is the opposite:

$$\boldsymbol{\sigma}_t = -\epsilon_t \tilde{\boldsymbol{g}}_t, \quad (4.25)$$

where the coefficient of proportionality is the penalty parameter ϵ_t for the frictional constraint (again, the *linear* penalty method is considered). According to Coulomb’s law of friction, the point will stay in the stick state, while $\|\boldsymbol{\sigma}_t\| < \mu |\sigma_n|$, or, using (4.25), while:

$$\|\tilde{\boldsymbol{g}}_t\| < \frac{\mu |\sigma_n|}{\epsilon_t}, \quad (4.26)$$

which shows how the penalty parameter ϵ_t controls the possible violation of the stick constraint.

If the magnitude of “slip-in-stick” $\tilde{\boldsymbol{g}}_t$ exceeds the limit (4.26), the point starts the “real” sliding. Therefore, this point switches to the **slip** state, during which the frictional traction equals to:

$$\boldsymbol{\sigma}_t = -\mu |\sigma_n| \boldsymbol{s} = \mu \epsilon_n g_n \boldsymbol{s}, \quad (4.27)$$

where \boldsymbol{s} is the direction of the “real” slip:

$$\boldsymbol{s} = \frac{\boldsymbol{g}_t}{\|\boldsymbol{g}_t\|}, \quad (4.28)$$

and we used the expression for the normal contact traction (4.18) (note that in the active contact zone $g_n \leq 0$). Finally, we may write the expressions for the frictional traction for both states:

$$\boldsymbol{\sigma}_t(\boldsymbol{g}_t) = \begin{cases} -\epsilon_t \tilde{\boldsymbol{g}}_t, & \epsilon_t \|\tilde{\boldsymbol{g}}_t\| < \mu |\sigma_n| \quad (\text{stick}) \\ \mu \epsilon_n g_n \boldsymbol{s}, & \epsilon_t \|\tilde{\boldsymbol{g}}_t\| \geq \mu |\sigma_n| \quad (\text{slip}), \end{cases} \quad (4.29)$$

Splitting the integrals over the active contact zone Γ^c into integrals over the stick and

slip zones and combining together terms for normal and tangential contact tractions, we may summarize the contribution of the frictional contact to the balance of virtual work:

$$\begin{aligned} \delta W^c &= \int_{\Gamma^c} \sigma_n \delta g_n d\Gamma + \int_{\Gamma^c} \boldsymbol{\sigma}_t \cdot \delta \mathbf{g}_t d\Gamma = \\ & \int_{\Gamma^{\text{stick}}} (\epsilon_n g_n \delta g_n - \epsilon_t \tilde{\mathbf{g}}_t \cdot \delta \tilde{\mathbf{g}}_t) d\Gamma + \int_{\Gamma^{\text{slip}}} (\epsilon_n g_n \delta g_n + \mu \epsilon_n g_n \mathbf{s} \cdot \delta \mathbf{g}_t) d\Gamma. \end{aligned} \quad (4.30)$$

For a discussion about the analogy between the frictional behaviour and the elasto-plastic deformation of the solid, the reader is referred to [Yastrebov, 2013, Wriggers, 2006]. Note also that for practical application of the penalty method (e.g. in finite-element framework) an additional procedure is required to distinguish between stick and slip zones, such as the *return mapping algorithm*. We will outline this algorithm briefly below, while for more details and the graphic representation the reader is referred to [Yastrebov, 2013, Wriggers, 2006].

Return mapping algorithm

In order to find whether the considered node is in stick or slip state and formulate the corresponding contribution to the virtual work, we note first that numerical resolution of contact problem, due to its strong nonlinearity, is incremental, i.e. the external load, bringing the bodies in contact is applied in a number of load steps, or increments. Therefore we may suppose that we have a solution obtained at k -th increment, i.e. the displacement vector \mathbf{u}^k . Additionally, we assume that we know \mathbf{x}_s^k , which denotes the stick point (sometimes termed as *center of stick*), computed at the k -th increment. Moreover, since a Newton-Raphson method is required to resolve the nonlinear contact problem, we assume that an approximation of the displacement vector corresponding to the new increment \mathbf{u}^{k+1} is available.

Then, according to the return mapping algorithm, we initially suppose that the whole active contact zone is in the stick state. The normal traction, according to (4.18), reads:

$$\sigma_n^{k+1} = -\epsilon_n \langle -g_n(\mathbf{u}^{k+1}) \rangle \quad (4.31)$$

while the “trial” tangential traction can be written, using (4.25), as:

$$\boldsymbol{\sigma}_{t\text{trial}}^{k+1} = -\epsilon_t \tilde{\mathbf{g}}_{t\text{trial}}^{k+1}. \quad (4.32)$$

where $\tilde{\mathbf{g}}_{t\text{trial}}^{k+1}$ is the trial “slip-in-stick” with respect to the previous stick point \mathbf{x}_s^k :

$$\tilde{\mathbf{g}}_{t\text{trial}}^{k+1} = (\mathbf{I} - \boldsymbol{\nu} \otimes \boldsymbol{\nu}) \cdot (\mathbf{x}^{k+1} - \mathbf{x}_s^k), \quad (4.33)$$

where $\mathbf{x}^{k+1} = \mathbf{X} + \mathbf{u}^{k+1}$. The term “trial” is used, because the condition (4.26), associated with the Coulomb’s law of friction, must be validated. If the following inequality holds:

$$\left\| \boldsymbol{\sigma}_{t\text{trial}}^{k+1} \right\| \leq \mu \left| \sigma_n^{k+1} \right|, \quad (4.34)$$

then the trial tangential traction is valid, the considered point is indeed in the stick state, and we store $\boldsymbol{\sigma}_t^{k+1} = \boldsymbol{\sigma}_{t\text{trial}}^{k+1}$ and $\mathbf{x}_s^{k+1} = \mathbf{x}_s^k$.

On the contrary, if the condition (4.34) does not hold, the considered point switches to the slip state, and according to (4.27) the tangential traction is computed as:

$$\boldsymbol{\sigma}_t^{k+1} = -\mu \left| \sigma_n^{k+1} \right| \mathbf{s}, \quad (4.35)$$

where \mathbf{s} is the direction of sliding, which we assume to coincide with the direction of $\tilde{\mathbf{g}}_{t_{\text{trial}}}^{k+1}$:

$$\mathbf{s} = \frac{\tilde{\mathbf{g}}_{t_{\text{trial}}}^{k+1}}{\|\tilde{\mathbf{g}}_{t_{\text{trial}}}^{k+1}\|}. \quad (4.36)$$

Furthermore, we obtain the actual “slip-in-stick” as the maximal value permitted by the Coulomb’s law, see (4.26):

$$\tilde{\mathbf{g}}_t^{k+1} = \frac{1}{\epsilon_t} \mu \left| \sigma_n^{k+1} \right| \mathbf{s}. \quad (4.37)$$

Then the real slip \mathbf{g}_t^{k+1} is computed as the difference between those two collinear vectors:

$$\mathbf{g}_t^{k+1} = \tilde{\mathbf{g}}_{t_{\text{trial}}}^{k+1} - \tilde{\mathbf{g}}_t^{k+1} = \frac{1}{\epsilon_t} \left(\left\| \boldsymbol{\sigma}_{t_{\text{trial}}}^{k+1} \right\| - \mu \left| \sigma_n^{k+1} \right| \right) \mathbf{s}, \quad (4.38)$$

where Eqs. (4.32) and (4.37) were used. Finally, the position of the stick point needs to be adjusted to take into account the real slip \mathbf{g}_t^{k+1} :

$$\mathbf{x}_s^{k+1} = \mathbf{x}_s^k + \mathbf{g}_t^{k+1} = \mathbf{x}_s^k + \frac{1}{\epsilon_t} \left(\left\| \boldsymbol{\sigma}_{t_{\text{trial}}}^{k+1} \right\| - \mu \left| \sigma_n^{k+1} \right| \right) \mathbf{s}. \quad (4.39)$$

The discussed procedure is outlined in Algorithm 1.

4.1.3 Augmented Lagrangian method

Another approach to the constrained minimization problem consists in a special combination of the Lagrange multipliers and penalty methods, which results in an unconstrained minimization problem, and, furthermore, provides an exact solution of the initial problem for a finite penalty parameter. It is known as the “augmented Lagrangian method” proposed in 1969 in [Hestenes, 1969] and in [Powell, 1969] and generalized for the case of inequality constraints in [Rockafellar, 1973]. Note that two variants of this method exist; the first one is iterative, based on independent update of primal (displacement) and dual (Lagrange multipliers) unknowns, also known as the Uzawa’s algorithm, see e.g. [Simo and Laursen, 1992] for its application for frictional contact problems. The second approach provides resolution of the problem for both types of unknowns simultaneously, therefore it is also referred to as the *monolithic* approach. Since in this dissertation we are developing a monolithic framework for coupling solid and fluid sub-problems, we will use this latter variant of the augmented Lagrangian method, employing the results obtained by [Alart and Curnier, 1991, Heegaard and Curnier, 1993, Pietrzak and Curnier, 1999].

The so-called *augmented Lagrangian* for the frictional contact problem is constructed in the following way, compare with the frictionless case (4.3):

$$\mathcal{L}^a(\mathbf{u}, \lambda_n, \boldsymbol{\lambda}_t; \hat{\sigma}_n) = \Pi^s(\mathbf{u}) + \int_{\Gamma} l_n(g_n, \lambda_n) d\Gamma + \int_{\Gamma} l_t(\mathbf{g}_t, \boldsymbol{\lambda}_t; \hat{\sigma}_n) d\Gamma, \quad (4.40)$$

where in addition to Lagrange multipliers λ_n , representing contact pressure, we considered also vector-valued multipliers $\boldsymbol{\lambda}_t$, which can be interpreted as the tangential frictional traction $\boldsymbol{\sigma}_t$. Similarly to the classical method, see discussions in Sec. 4.1.1, Lagrange multipliers λ_n and $\boldsymbol{\lambda}_t$ can be viewed here as functions defined on Γ . It is important to note, that the augmented Lagrangian depends also on $\hat{\sigma}_n = \sigma_n + \epsilon_n g_n$, by which we denote the augmented (regularized) contact pressure at the solution, ϵ_n is the augmentation (regularization) parameter. This dependency reflects the non-associated character of the Coulomb’s frictional law (see Section 2.2.2); accordingly, the term l_t

Algorithm 1 Return mapping algorithm

Require: $\mathbf{x}_s^k, \mathbf{u}^{k+1}$ // \mathbf{u}^{k+1} is known as an approximation in a Newton-Raphson loop

1: $g_n \leftarrow (\mathbf{X} - \mathbf{c}) \cdot \boldsymbol{\nu} + \mathbf{u}^{k+1} \cdot \boldsymbol{\nu}$

2: **if** $g_n > 0$ **then**

3: state \leftarrow **not active**

4: **else**

5: $\sigma_n^{k+1} \leftarrow -\epsilon_n \langle -g_n \rangle$

6: $\tilde{\mathbf{g}}_{t_{\text{trial}}}^{k+1} \leftarrow (\mathbf{I} - \boldsymbol{\nu} \otimes \boldsymbol{\nu}) \cdot (\mathbf{x}^{k+1} - \mathbf{x}_s^k)$

7: $\boldsymbol{\sigma}_{t_{\text{trial}}}^{k+1} \leftarrow -\epsilon_t \tilde{\mathbf{g}}_{t_{\text{trial}}}^{k+1}$

8: **if** $\|\boldsymbol{\sigma}_{t_{\text{trial}}}^{k+1}\| \leq \mu |\sigma_n^{k+1}|$ **then**

9: state \leftarrow **stick**

10: $\boldsymbol{\sigma}_t^{k+1} \leftarrow \boldsymbol{\sigma}_{t_{\text{trial}}}^{k+1}$

11: $\mathbf{x}_s^{k+1} \leftarrow \mathbf{x}_s^k$

12: **else**

13: state \leftarrow **slip**

14: $\mathbf{s} \leftarrow \frac{\tilde{\mathbf{g}}_{t_{\text{trial}}}^{k+1}}{\|\tilde{\mathbf{g}}_{t_{\text{trial}}}^{k+1}\|}$

15: $\boldsymbol{\sigma}_t^{k+1} \leftarrow -\mu |\sigma_n^{k+1}| \mathbf{s}$

16: $\tilde{\mathbf{g}}_t^{k+1} \leftarrow \frac{1}{\epsilon_t} \mu |\sigma_n^{k+1}| \mathbf{s}$

17: $\mathbf{g}_t^{k+1} \leftarrow \tilde{\mathbf{g}}_{t_{\text{trial}}}^{k+1} - \tilde{\mathbf{g}}_t^{k+1}$

18: $\mathbf{x}_s^{k+1} \leftarrow \mathbf{x}_s^k + \mathbf{g}_t^{k+1}$

19: **end if**

20: **end if**

is, strictly speaking, a regularization of a non-differentiable “quasi”-potential, see [Alart and Curnier, 1991, Pietrzak and Curnier, 1999] for more details.

We introduced integrands l_n and l_t as functions of g_n and \mathbf{g}_t , respectively, to simplify the subsequent formulations, however, both normal and tangential gaps are used in the same sense as before, i.e. expressed in terms of the displacement vector field \mathbf{u} . Below we will provide closed forms of integrands l_n and l_t , which depend on the contact status of the considered point on Γ : active or non-active, and, in case of l_t , on the frictional state: stick or slip. The term l_n in the first integral in (4.40) has the following form:

$$l_n(g_n, \lambda_n) = \begin{cases} \lambda_n g_n + \frac{\epsilon_n}{2} g_n^2, & \hat{\lambda}_n \leq 0 \quad (\text{contact}) \\ -\frac{1}{2\epsilon_n} \lambda_n^2, & \hat{\lambda}_n > 0 \quad (\text{non-contact}) \end{cases} \quad (4.41)$$

where $\hat{\lambda}_n$ denotes the augmented Lagrange multiplier:

$$\hat{\lambda}_n = \lambda_n + \epsilon_n g_n, \quad (4.42)$$

the sign of which defines whether the considered point is in contact or not. The integrand l_t is defined as:

$$l_t(\mathbf{g}_t, \boldsymbol{\lambda}_t; \hat{\sigma}_n) = \begin{cases} \boldsymbol{\lambda}_t \cdot \mathbf{g}_t + \frac{\epsilon_t}{2} \mathbf{g}_t \cdot \mathbf{g}_t, & \|\hat{\boldsymbol{\lambda}}_t\| \leq -\hat{\sigma}_n, \hat{\lambda}_n \leq 0 \quad (\text{stick}) \\ -\frac{1}{2\epsilon_t} \left(\boldsymbol{\lambda}_t \cdot \boldsymbol{\lambda}_t + 2\mu\hat{\sigma}_n \|\hat{\boldsymbol{\lambda}}_t\| + \mu^2 \hat{\sigma}_n^2 \right), & \|\hat{\boldsymbol{\lambda}}_t\| > -\hat{\sigma}_n, \hat{\lambda}_n \leq 0 \quad (\text{slip}) \\ -\frac{1}{2\epsilon_t} \boldsymbol{\lambda}_t \cdot \boldsymbol{\lambda}_t, & \hat{\lambda}_n > 0 \quad (\text{non-contact}) \end{cases} \quad (4.43)$$

Similarly to the augmented Lagrange multiplier $\hat{\lambda}_n$, we introduced the vector-valued multiplier $\hat{\boldsymbol{\lambda}}_t$ as:

$$\hat{\boldsymbol{\lambda}}_t = \boldsymbol{\lambda}_t + \epsilon_t \mathbf{g}_t, \quad (4.44)$$

where ϵ_t is the augmentation parameter for the frictional constraints. Similarly to the classic Lagrange multiplier method, we search for the saddle point $(\mathbf{u}, \lambda_n, \boldsymbol{\lambda}_t)$ of the augmented Lagrangian (4.40):

$$\mathcal{L}^a(\mathbf{u}, \lambda_n, \boldsymbol{\lambda}_t; \hat{\sigma}_n) = \max_{\substack{p \in \mathcal{M} \\ t \in \mathcal{M}}} \min_{\mathbf{v} \in \mathbf{V}} \mathcal{L}^a(\mathbf{v}, p, \mathbf{t}; \hat{\sigma}_n) = \min_{\mathbf{v} \in \mathbf{V}} \max_{\substack{p \in \mathcal{M} \\ t \in \mathcal{M}}} \mathcal{L}^a(\mathbf{v}, p, \mathbf{t}; \hat{\sigma}_n), \quad (4.45)$$

where by writing $\mathbf{t} \in \mathcal{M}$ we denote that every component of the vector \mathbf{t} belongs to the space \mathcal{M} , see (4.4) and discussions in Sec. 4.1.1. It is important to note, that unlike the classic Lagrange multiplier method, cf. (4.7), we do not enforce here any constraints on Lagrange multipliers λ_n and $\boldsymbol{\lambda}_t$, i.e. we obtained an unconstrained saddle point problem, owing to the special structure of the augmented Lagrangian (4.40). We compute therefore the variation of the augmented Lagrangian, which must vanish at the solution:

$$\begin{aligned} \delta \mathcal{L}^a(\mathbf{u}, \lambda_n, \boldsymbol{\lambda}_t; \hat{\sigma}_n) &= \delta \Pi^s(\mathbf{u}) + \int_{\Gamma} (\delta l_n(g_n, \lambda_n) + \delta l_t(\mathbf{g}_t, \boldsymbol{\lambda}_t; \hat{\sigma}_n)) d\Gamma = \\ &= \delta \Pi^s(\mathbf{u}) + \int_{\Gamma} \left(\frac{\partial l_n}{\partial g_n} \delta g_n + \frac{\partial l_n}{\partial \lambda_n} \delta \lambda_n + \frac{\partial l_t}{\partial \mathbf{g}_t} \cdot \delta \mathbf{g}_t + \frac{\partial l_t}{\partial \boldsymbol{\lambda}_t} \cdot \delta \boldsymbol{\lambda}_t \right) d\Gamma = 0, \\ &\quad \forall \delta \mathbf{u} \in \mathbf{V}, \forall \delta \lambda_n \in \mathcal{M}, \forall \delta \boldsymbol{\lambda}_t \in \mathbf{M}, \end{aligned} \quad (4.46)$$

where, as before,

$$\delta g_n = \frac{\partial g_n}{\partial \mathbf{u}} \cdot \delta \mathbf{u}, \quad \delta \mathbf{g}_t = \frac{\partial \mathbf{g}_t}{\partial \mathbf{u}} \cdot \delta \mathbf{u}. \quad (4.47)$$

Note that the variation of the Lagrangian with respect to the augmented contact pressure $\hat{\sigma}_n$ is not considered, see [Pietrzak and Curnier, 1999] for details. Finally, it remains to provide closed forms for the respective derivatives of the terms l_n and l_t :

$$\frac{\partial l_n(g_n, \lambda_n)}{\partial g_n} = \begin{cases} \hat{\lambda}_n, & \hat{\lambda}_n \leq 0 \quad (\text{contact}) \\ 0, & \hat{\lambda}_n > 0 \quad (\text{non-contact}) \end{cases} \quad (4.48a)$$

$$\frac{\partial l_n(g_n, \lambda_n)}{\partial \lambda_n} = \begin{cases} g_n, & \hat{\lambda}_n \leq 0 \quad (\text{contact}) \\ -\frac{1}{\epsilon_n} \lambda_n, & \hat{\lambda}_n > 0 \quad (\text{non-contact}) \end{cases} \quad (4.48b)$$

$$\frac{\partial l_t(\mathbf{g}_t, \boldsymbol{\lambda}_t; \hat{\sigma}_n)}{\partial \mathbf{g}_t} = \begin{cases} \hat{\boldsymbol{\lambda}}_t, & \|\hat{\boldsymbol{\lambda}}_t\| \leq -\hat{\sigma}_n, \hat{\lambda}_n \leq 0 \quad (\text{stick}) \\ -\mu \hat{\sigma}_n \frac{\hat{\boldsymbol{\lambda}}_t}{\|\hat{\boldsymbol{\lambda}}_t\|}, & \|\hat{\boldsymbol{\lambda}}_t\| > -\hat{\sigma}_n, \hat{\lambda}_n \leq 0 \quad (\text{slip}) \\ 0, & \hat{\lambda}_n > 0 \quad (\text{non-contact}) \end{cases} \quad (4.48c)$$

$$\frac{\partial l_t(\mathbf{g}_t, \boldsymbol{\lambda}_t; \hat{\sigma}_n)}{\partial \boldsymbol{\lambda}_t} = \begin{cases} \mathbf{g}_t, & \|\hat{\boldsymbol{\lambda}}_t\| \leq -\hat{\sigma}_n, \hat{\lambda}_n \leq 0 \quad (\text{stick}) \\ -\frac{1}{\epsilon_t} \left(\boldsymbol{\lambda}_t + \mu \hat{\sigma}_n \frac{\hat{\boldsymbol{\lambda}}_t}{\|\hat{\boldsymbol{\lambda}}_t\|} \right), & \|\hat{\boldsymbol{\lambda}}_t\| > -\hat{\sigma}_n, \hat{\lambda}_n \leq 0 \quad (\text{slip}) \\ -\frac{1}{\epsilon_t} \boldsymbol{\lambda}_t, & \hat{\lambda}_n > 0 \quad (\text{non-contact}) \end{cases} \quad (4.48d)$$

Therefore, inserting the outlined above terms into Eq. (4.46), we obtain the contribution of the normal and tangential tractions to the balance of virtual work, compare with the frictionless case (4.10).

4.2 Node-to-rigid-surface discretization approach

In the node-to-rigid-surface approach each contact element is associated to one node of the surface of the solid, and *vice versa*: each node belongs to only one element, see Fig. 4.1. Therefore, the discretised version of the potential contact zone takes the form $\Gamma = \{\mathbf{x}_i\}, 1 \leq i \leq m$, where \mathbf{x}_i are the coordinates of the i -th surface node and m is the number of nodes in the potential contact zone (note that for brevity we preserve the same notations for discretised entities as were introduced in the continuous problem statement). Accordingly, the active contact zone also becomes:

$$\Gamma^c = \{\mathbf{x}_i\}, i \in \mathcal{J}, \text{mes } \mathcal{J} = \bar{m}, \quad (4.49)$$

where \bar{m} is the number of nodes in the active contact state, \mathcal{J} is the set of their indices (i.e. the “*active set*”), and $\text{mes } \mathcal{J}$ is the measure of this set. Consequently, the contact constraints (2.20) are considered node-wise:

$$g_{ni} \geq 0, \sigma_{ni} \leq 0, \sigma_{ni} g_{ni} = 0 \quad \text{at } \Gamma \quad \Leftrightarrow \quad \begin{cases} g_{ni} = 0, & \sigma_{ni} < 0 \quad \text{on } \Gamma^c \\ g_{ni} > 0, & \sigma_{ni} = 0 \quad \text{on } \Gamma \setminus \Gamma^c, \end{cases} \quad (4.50)$$

where

$$g_{ni} = (\mathbf{x}_i - \mathbf{c}) \cdot \boldsymbol{\nu} \quad (4.51)$$

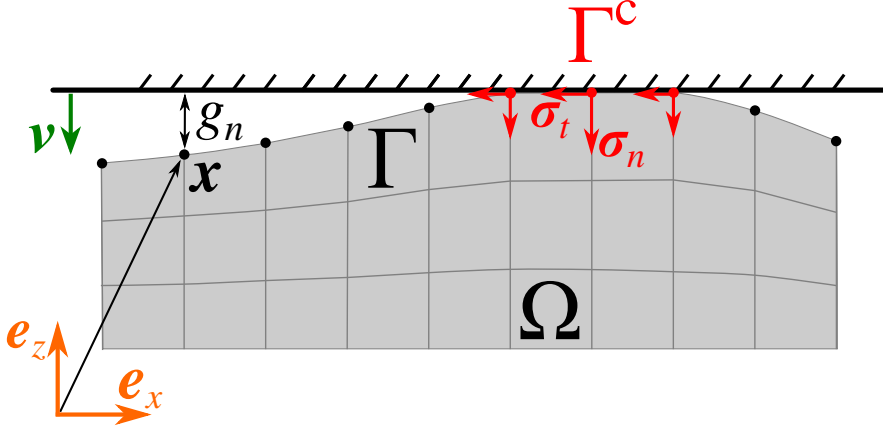


Figure 4.1: Node-to-rigid-surface contact discretization: Γ is the potential contact zone, Γ^c is the active contact zone.

is the normal gap of the i -th node, cf. (2.18), and σ_{ni} is the nodal value of the contact pressure³. Note that the treatment of this value is method-dependent and will be elaborated in subsequent sections. Therefore, if the node belongs to Γ^c , we will say that the corresponding contact element is active. Furthermore, the frictional constraints, i.e. the Coulomb's law of friction (2.69), are also considered node-wise, the detailed formulations will be given in the sections corresponding to the penalty and augmented Lagrangian methods.

4.2.1 Method of Lagrange multipliers

We recall the expression for the virtual work of the normal contact traction obtained using the Lagrange multipliers method, see (4.10):

$$\delta W^c(\mathbf{u}, \lambda_n, \delta \mathbf{u}, \delta \lambda_n) = \int_{\Gamma^c} \left(\lambda_n \frac{\partial g_n(\mathbf{u})}{\partial \mathbf{u}} \cdot \delta \mathbf{u} + g_n(\mathbf{u}) \delta \lambda_n \right) d\Gamma. \quad (4.52)$$

Using the node-to-surface approach (upon the standard finite-element discretization) we compute the virtual work δW^c as the sum of contributions from each active element:

$$\delta W^c(\mathbf{U}, \mathbf{L}_n, \delta \mathbf{U}, \delta \mathbf{L}_n) = \sum_{i \in \mathcal{J}} \delta W_i^c(\mathbf{u}_i, \lambda_{ni}, \delta \mathbf{u}_i, \delta \lambda_{ni}), \quad (4.53)$$

We denote by

$$\mathbf{U} = [\mathbf{u}_{i_1}, \dots, \mathbf{u}_{i_k}, \dots, \mathbf{u}_{i_{\bar{m}}}]^\top, \quad i_k \in \mathcal{J} \quad (4.54)$$

a vector of displacements of all nodes in the active contact zone Γ^c , see (4.49). Furthermore, we append a Lagrange multiplier to each node of the active contact surface, therefore

$$\mathbf{L}_n = [\lambda_{ni_1}, \dots, \lambda_{ni_k}, \dots, \lambda_{ni_{\bar{m}}}]^\top, \quad i_k \in \mathcal{J}. \quad (4.55)$$

Accordingly, we use the same notations for nodal virtual displacements and dual test functions:

$$\delta \mathbf{U} = [\delta \mathbf{u}_{i_1}, \dots, \delta \mathbf{u}_{i_k}, \dots, \delta \mathbf{u}_{i_{\bar{m}}}]^\top, \quad \delta \mathbf{L}_n = [\delta \lambda_{ni_1}, \dots, \delta \lambda_{ni_k}, \dots, \delta \lambda_{ni_{\bar{m}}}]^\top, \quad i_k \in \mathcal{J}. \quad (4.56)$$

³Alternatively, σ_{ni} in (4.50) can be seen as the nodal value of the contact reaction force, if linear elements are used, since nodal pressure and reaction have the same sign in this case. However, it does not generally hold for 3D quadratic elements

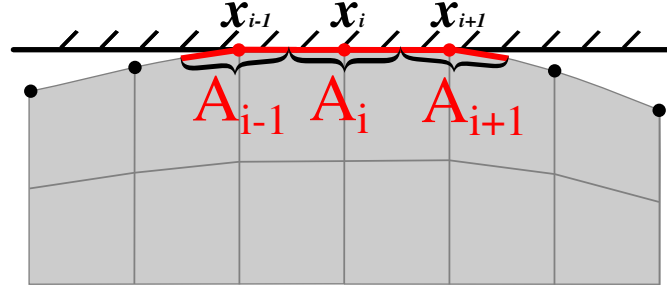


Figure 4.2: Definition of the area A_i corresponding to i -th contact element in the node-to-rigid-surface discretization approach.

Next, we write the contribution of the i -th contact element to the balance of virtual works:

$$\delta W_i^c = \left(\lambda_{ni} \frac{\partial g_{ni}}{\partial \mathbf{u}_i} \cdot \delta \mathbf{u}_i + g_{ni} \delta \lambda_{ni} \right) A_i, \quad (4.57)$$

where the computation of an integral, cf. (4.52), was replaced by a multiplier A_i representing the area associated with the i -th contact element. On the one hand, the node-to-rigid-surface approach permits to avoid the computation of the area A_i , since it can be implicitly included into the value of the Lagrange multipliers, e.g.:

$$\bar{\lambda}_{ni} = A_i \lambda_{ni}, \quad \delta \bar{\lambda}_{ni} = A_i \delta \lambda_{ni}. \quad (4.58)$$

However, in this case Lagrange multipliers $\bar{\lambda}_{ni}$ represent contact reaction, rather than traction. On the other hand, the computation of the contact area is important, being a key quantity determining the interfacial behaviour in many physical problems, see, for example [Vakis et al., 2018]. Furthermore, the calculation of contact tractions is necessary for verification of the numerical results against known analytical solution, and is also required for studies such as comparison of local and global coefficients of friction, see Part III of this dissertation for examples. The contact area corresponding to a node can be easily computed in 2D (plane strain) problem set-up, see Fig. 4.2 and also [Wriggers, 2006]. However, in the 3D case the computation of the area corresponding to a node is not straightforward, which is one of the reason for utilization of the face-to-rigid-surface approach for 3D problems in this dissertation, see next section for more details. For the sake of generality, we will include A_i in our formulations here explicitly, using the value corresponding to the current configuration, and by virtue of that Lagrange multipliers λ_{ni} will correctly represent the contact pressure.

The contact problem, due to unknown active zone and contact tractions is inevitably nonlinear, and the numerical approach based on the Newton-Raphson method requires linearisation of the equation (4.10), i.e. of the balance of virtual work, see [Yastrebov, 2013] for more details on this classic approach. To compute the contribution of each contact element to the global tangent matrix, we perform (second) variation of the virtual work (4.57):

$$\Delta \delta W_i^c = \left(\lambda_{ni} \Delta \mathbf{u}_i \cdot \frac{\partial^2 g_{ni}}{\partial \mathbf{u}_i^2} \cdot \delta \mathbf{u}_i + \Delta \lambda_{ni} \frac{\partial g_{ni}}{\partial \mathbf{u}_i} \cdot \delta \mathbf{u}_i + \Delta \mathbf{u}_i \cdot \frac{\partial g_{ni}}{\partial \mathbf{u}_i} \delta \lambda_{ni} \right) A_i, \quad (4.59)$$

where the variation of A_i is omitted, which does not have any significant effect on the convergence of the Newton-Raphson method. Moreover, if the small deformations assumption is used, the variation of the element's area is omitted systematically.

The virtual work and its variation can be expressed in a compact form, introducing the residual vector \mathbf{R}^c and the tangent matrix \mathbf{K}^c of the (frictionless) contact element

under the Lagrange multipliers method:

$$\delta W_i^c = \underbrace{\begin{bmatrix} \mathbf{R}_u^c \\ \mathbf{R}_\lambda^c \end{bmatrix}}_{\mathbf{R}^c} \cdot \begin{bmatrix} \delta \mathbf{u}_i \\ \delta \lambda_{ni} \end{bmatrix}, \quad \Delta \delta W_i^c = \begin{bmatrix} \Delta \mathbf{u}_i \\ \Delta \lambda_{ni} \end{bmatrix} \cdot \underbrace{\begin{bmatrix} \mathbf{0} & \mathbf{K}_{u\lambda}^c \\ \mathbf{K}_{\lambda u}^c & \mathbf{0} \end{bmatrix}}_{\mathbf{K}^c} \cdot \begin{bmatrix} \delta \mathbf{u}_i \\ \delta \lambda_{ni} \end{bmatrix} \quad (4.60)$$

Non-zero components of \mathbf{R}^c and \mathbf{K}^c can be expressed as:

$$\mathbf{R}_u^c = \lambda_{ni} A_i \boldsymbol{\nu}, \quad \mathbf{R}_\lambda^c = g_{ni} A_i, \quad \mathbf{K}_{u\lambda}^c = \mathbf{K}_{\lambda u}^c{}^\top = A_i \boldsymbol{\nu}, \quad (4.61)$$

where we used (4.51), according to which $\partial g_{ni}/\partial \mathbf{u}_i = \boldsymbol{\nu}$, while $\partial^2 g_{ni}/\partial \mathbf{u}_i^2 = 0$.

As was mentioned in the previous section, the Lagrange multipliers method converts the initial constrained minimization problem into the saddle point problem with a constraint on Lagrange multipliers: $\lambda_n \leq 0$, see (4.7). Therefore, a so-called *active set* strategy [Wriggers, 2006, Yastrebov, 2013] is required here for two purposes: first, enforce the constraint on the Lagrange multipliers, and, second, find the active contact zone. This strategy is essentially a test performed on every iteration of the Newton-Raphson method to determine whether each contact element is currently active or not. The test is based on the currently computed values of the normal gap g_{ni} and the Lagrange multiplier λ_{ni} and can be summarized as follows:

$$\begin{cases} \text{if } g_{ni} > 0 \text{ or } \lambda_{ni} > 0 & \Rightarrow i\text{-th element is inactive,} \\ \text{if } g_{ni} \leq 0 \text{ and } \lambda_{ni} \leq 0 & \Rightarrow i\text{-th element is active.} \end{cases} \quad (4.62)$$

Therefore, if the contact element is active, then its residual vector \mathbf{R}^c and tangent matrix \mathbf{K}^c are added to the corresponding entries of the global residual vector and tangent matrix. If, on the contrary, the element is inactive, then all terms corresponding to it should be excluded from global structures. Furthermore, the Lagrange multiplier associated to this element should be eliminated from the global vector of degrees of freedom. However, the consequent change of the global number of unknowns (possibly at every iteration) is often undesirable, especially in case of an implicit finite-element code. Alternatively, the residual vector and tangent matrix can be altered to avoid this change, e.g. by putting:

$$\mathbf{R}^c = 0, \quad \mathbf{K}_{uu}^c = 0, \quad \mathbf{K}_{u\lambda}^c = \mathbf{K}_{\lambda u}^c{}^\top = 0, \quad \mathbf{K}_{\lambda\lambda}^c = 1, \quad (4.63)$$

in case of inactive element, as suggested in [Yastrebov, 2013].

Finally, as was mentioned in Section 4.1.1, the method of Lagrange multipliers can be also used to handle frictional constraints [Tur et al., 2009]. However, the active set strategy becomes sophisticated to be able to correctly determine the stick and slip zones. Thus, we do not discuss this approach here and use the penalty or augmented Lagrangian methods in the frictional case.

4.2.2 Penalty method

Frictionless case

Let us recall the virtual work of the normal contact tractions obtained using the penalty method, see (4.21):

$$\delta W^c(\mathbf{u}, \delta \mathbf{u}) = \int_{\Gamma} -\epsilon_n \langle -g_n \rangle \delta g_n d\Gamma = \int_{\Gamma} -\epsilon_n \langle -g_n \rangle \frac{\partial g_n}{\partial \mathbf{u}} \cdot \delta \mathbf{u} d\Gamma. \quad (4.64)$$

Using the node-to-rigid-surface approach, we associate a contact element with each node of the surface Γ , and therefore, we may compute the virtual work of the contact as a sum of contributions from each element:

$$\delta W^c(\mathbf{U}, \delta \mathbf{U}) = \sum_{i=1}^m \delta W_i^c(\mathbf{u}_i, \delta \mathbf{u}_i) = \sum_{i=1}^m -\epsilon_n \langle -g_{ni} \rangle A_i \frac{\partial g_{ni}}{\partial \mathbf{u}_i} \cdot \delta \mathbf{u}_i, \quad (4.65)$$

where A_i is the contact area associated to the i -th contact element, see Fig. 4.2 and discussions in Sec. 4.2.1. Note that here $\mathbf{U} = [\mathbf{u}_1, \dots, \mathbf{u}_i, \dots, \mathbf{u}_m]^\top$, $1 \leq i \leq m$, is the vector of nodal displacements of all m nodes on Γ ; accordingly, $\delta \mathbf{U} = [\delta \mathbf{u}_1, \dots, \delta \mathbf{u}_i, \dots, \delta \mathbf{u}_m]^\top$, $1 \leq i \leq m$.

The status of the i -th contact element is readily determined by computing g_{ni} . Thus, depending on the status, the virtual work can be expressed as:

$$\delta W_i^c = \begin{cases} \epsilon_n A_i g_{ni} \frac{\partial g_{ni}}{\partial \mathbf{u}_i} \cdot \delta \mathbf{u}_i, & g_{ni} \leq 0, \quad (\text{contact}) \\ 0, & g_{ni} > 0, \quad (\text{non-contact}). \end{cases} \quad (4.66)$$

Accordingly, the second variation reads:

$$\Delta \delta W_i^c = \begin{cases} \epsilon_n A_i \Delta \mathbf{u}_i \cdot \left[\frac{\partial g_{ni}}{\partial \mathbf{u}_i} \otimes \frac{\partial g_{ni}}{\partial \mathbf{u}_i} \right] \cdot \delta \mathbf{u}_i, & g_{ni} \leq 0, \quad (\text{contact}) \\ 0, & g_{ni} > 0, \quad (\text{non-contact}), \end{cases} \quad (4.67)$$

where \otimes is the tensor product, and, similarly to the Lagrange multipliers method discussed in Sec. 4.2.1, the area A_i is not subject to variation.

Next, we introduce the residual vector \mathbf{R}^c and the tangent matrix \mathbf{K}^c of the (frictionless) contact element in the penalty formulation:

$$\delta W_i^c = \mathbf{R}_u^c \cdot \delta \mathbf{u}_i, \quad \Delta \delta W_i^c = \Delta \mathbf{u}_i \cdot \mathbf{K}_{uu}^c \cdot \delta \mathbf{u}_i. \quad (4.68)$$

Using the definition of the normal gap (2.18), we may write expressions for the residual vector and tangent matrix as:

$$\mathbf{R}_u^c = \begin{cases} \epsilon_n g_{ni} A_i \boldsymbol{\nu}, & g_{ni} \leq 0 \\ \mathbf{0}, & g_{ni} > 0, \end{cases} \quad \mathbf{K}_{uu}^c = \begin{cases} \epsilon_n A_i \boldsymbol{\nu} \otimes \boldsymbol{\nu}, & g_{ni} \leq 0 \\ \mathbf{0}, & g_{ni} > 0. \end{cases} \quad (4.69)$$

Frictional case

In the frictional case, the virtual work of the contact traction reads:

$$\delta W^c = \int_{\Gamma^{\text{stick}}} (\epsilon_n g_n \delta g_n - \epsilon_t \tilde{\mathbf{g}}_t \cdot \delta \mathbf{g}_t) d\Gamma + \int_{\Gamma^{\text{slip}}} (\epsilon_n g_n \delta g_n + \mu \epsilon_n g_n \mathbf{s} \cdot \delta \tilde{\mathbf{g}}_t) d\Gamma. \quad (4.70)$$

According to the node-to-rigid-surface approach, we replace it by a sum of contributions from each contact element, associated with a node of the surface Γ :

$$\delta W^c(\mathbf{U}, \delta \mathbf{U}) = \sum_{i=1}^m \delta W_i^c(\mathbf{u}_i, \delta \mathbf{u}_i), \quad (4.71)$$

where \mathbf{u}_i is the displacement vector of the i -th node, \mathbf{U} is a vector of displacements of all nodes on Γ , and $\delta \mathbf{U}$ is a vector of corresponding virtual displacements. We recall that the status of the contact element (active or not active) can be determined by the value of the normal gap of its node, similarly to the frictionless case (4.66). Furthermore, the

frictional state (stick or slip) of the active contact element is defined using the return mapping algorithm, outlined in Algorithm 1. Then the contribution of one contact element, depending on its status and frictional state reads:

$$\delta W_i^c = A_i \begin{cases} \epsilon_n g_{ni} \frac{\partial g_{ni}}{\partial \mathbf{u}_i} \cdot \delta \mathbf{u}_i - \epsilon_t \tilde{\mathbf{g}}_{ti} \cdot \frac{\partial \tilde{\mathbf{g}}_{ti}}{\partial \mathbf{u}_i} \cdot \delta \mathbf{u}_i, & (\text{stick}) \\ \epsilon_n g_{ni} \frac{\partial g_{ni}}{\partial \mathbf{u}_i} \cdot \delta \mathbf{u}_i + \epsilon_n \mu g_{ni} \mathbf{s}_i \cdot \frac{\partial \mathbf{g}_{ti}}{\partial \mathbf{u}_i} \cdot \delta \mathbf{u}_i, & (\text{slip}) \\ 0, & (\text{non-contact}). \end{cases} \quad (4.72)$$

We recall also that in the quasi-static analysis the slip vector \mathbf{g}_{ti} represents the incremental value of slip with respect to the previous loading step, see (4.23).

Let us examine separately the stick and slip states. In the former case, the “slip-in-stick” vector $\tilde{\mathbf{g}}_{ti}$ and its derivative with respect to the displacement degrees of freedom read, see also (4.33):

$$\tilde{\mathbf{g}}_{ti} = (\mathbf{I} - \boldsymbol{\nu} \otimes \boldsymbol{\nu}) \cdot (\mathbf{x}_i - \mathbf{x}_{si}), \quad \frac{\partial \tilde{\mathbf{g}}_{ti}}{\partial \mathbf{u}_i} = \mathbf{I} - \boldsymbol{\nu} \otimes \boldsymbol{\nu}, \quad (4.73)$$

where \mathbf{x}_{si} is the correspond stick position. Then the second variation of the virtual work in the stick state is computed as follows:

$$\Delta \delta W_{i \text{ stick}}^c = A_i \left(\epsilon_n \Delta \mathbf{u}_i \cdot \left[\frac{\partial g_{ni}}{\partial \mathbf{u}_i} \otimes \frac{\partial g_{ni}}{\partial \mathbf{u}_i} \right] \cdot \delta \mathbf{u}_i - \epsilon_t \Delta \mathbf{u}_i \cdot \left[\frac{\partial \tilde{\mathbf{g}}_{ti}}{\partial \mathbf{u}_i} \cdot \frac{\partial \tilde{\mathbf{g}}_{ti}}{\partial \mathbf{u}_i} \right] \cdot \delta \mathbf{u}_i \right). \quad (4.74)$$

In case of slip, the direction of the slip vector and its derivative read:

$$\mathbf{s}_i = \frac{(\mathbf{I} - \boldsymbol{\nu} \otimes \boldsymbol{\nu}) \cdot (\mathbf{x}_i - \mathbf{x}_{si})}{\|(\mathbf{I} - \boldsymbol{\nu} \otimes \boldsymbol{\nu}) \cdot (\mathbf{x}_i - \mathbf{x}_{si})\|}, \quad \frac{\partial \mathbf{s}_i}{\partial \mathbf{u}_i} = \frac{\mathbf{I} - \boldsymbol{\nu} \otimes \boldsymbol{\nu} - \mathbf{s}_i \otimes \mathbf{s}_i}{\|(\mathbf{I} - \boldsymbol{\nu} \otimes \boldsymbol{\nu}) \cdot (\mathbf{x}_i - \mathbf{x}_{si})\|}, \quad (4.75)$$

providing the following expression for the second variation of the virtual work:

$$\begin{aligned} \Delta \delta W_{i \text{ slip}}^c = & A_i \left(\epsilon_n \Delta \mathbf{u}_i \cdot \left[\frac{\partial g_{ni}}{\partial \mathbf{u}_i} \otimes \frac{\partial g_{ni}}{\partial \mathbf{u}_i} \right] \cdot \delta \mathbf{u}_i + \epsilon_n \mu \Delta \mathbf{u}_i \cdot \left[\frac{\partial g_{ni}}{\partial \mathbf{u}_i} \otimes \left(\mathbf{s}_i \cdot \frac{\partial \mathbf{g}_{ti}}{\partial \mathbf{u}_i} \right) \right] \cdot \delta \mathbf{u}_i \right. \\ & \left. + \epsilon_n \mu g_{ni} \Delta \mathbf{u}_i \cdot \left[\frac{\partial \mathbf{s}_i}{\partial \mathbf{u}_i} \cdot \frac{\partial \mathbf{g}_{ti}}{\partial \mathbf{u}_i} \right] \cdot \delta \mathbf{u}_i \right). \end{aligned} \quad (4.76)$$

In the non-contact state, obviously, the second variation simply vanishes:

$$\Delta \delta W_{i \text{ non-contact}}^c = 0. \quad (4.77)$$

Finally, we introduce the residual vector \mathbf{R}^c and the tangent matrix \mathbf{K}^c of the frictional contact element in the penalty formulation:

$$\delta W_i^c = \mathbf{R}_u^c \cdot \delta \mathbf{u}_i, \quad \Delta \delta W_i^c = \Delta \mathbf{u}_i \cdot \mathbf{K}_{uu}^c \cdot \delta \mathbf{u}_i, \quad (4.78)$$

which are expressed as follows:

$$\mathbf{R}_u^c = A_i \begin{cases} \epsilon_n g_{ni} \boldsymbol{\nu} - \epsilon_t (\mathbf{I} - \boldsymbol{\nu} \otimes \boldsymbol{\nu}) (\mathbf{x}_i - \mathbf{x}_{si}), & (\text{stick}) \\ \epsilon_n g_{ni} \boldsymbol{\nu} + \epsilon_n \mu g_{ni} \frac{(\mathbf{I} - \boldsymbol{\nu} \otimes \boldsymbol{\nu}) \cdot (\mathbf{x}_i - \mathbf{x}_{si})}{\|(\mathbf{I} - \boldsymbol{\nu} \otimes \boldsymbol{\nu}) \cdot (\mathbf{x}_i - \mathbf{x}_{si})\|}, & (\text{slip}) \\ 0, & (\text{non-contact}), \end{cases} \quad (4.79)$$

$$\mathbf{K}_{uu}^c = A_i \begin{cases} \epsilon_n (\boldsymbol{\nu} \otimes \boldsymbol{\nu}) - \epsilon_t (\mathbf{I} - \boldsymbol{\nu} \otimes \boldsymbol{\nu}) \cdot (\mathbf{x}_i - \mathbf{x}_{si}), & (\text{stick}) \\ \epsilon_n (\boldsymbol{\nu} \otimes \boldsymbol{\nu}) + \epsilon_n \mu (\boldsymbol{\nu} \otimes \mathbf{s}_i) + \epsilon_n \mu g_{ni} \frac{\mathbf{I} - \boldsymbol{\nu} \otimes \boldsymbol{\nu} - \mathbf{s}_i \otimes \mathbf{s}_i}{\|(\mathbf{I} - \boldsymbol{\nu} \otimes \boldsymbol{\nu}) \cdot (\mathbf{x}_i - \mathbf{x}_{si})\|}, & (\text{slip}) \\ 0, & (\text{non-contact}), \end{cases} \quad (4.80)$$

where we used that the derivative of the slip vector reads:

$$\frac{\partial \mathbf{g}_{ti}}{\partial \mathbf{u}_i} = \mathbf{I} - \boldsymbol{\nu} \otimes \boldsymbol{\nu}, \quad (4.81)$$

and, therefore, the following identities hold:

$$\mathbf{s}_i \cdot \frac{\partial \mathbf{g}_{ti}}{\partial \mathbf{u}_i} = \mathbf{s}_i, \quad \frac{\partial \mathbf{s}_i}{\partial \mathbf{u}_i} \cdot \frac{\partial \mathbf{g}_{ti}}{\partial \mathbf{u}_i} = \frac{\partial \mathbf{s}_i}{\partial \mathbf{u}_i}. \quad (4.82)$$

4.2.3 Augmented Lagrangian method

The virtual work of contact tractions, obtained using the augmented Lagrangian method, reads:

$$\delta W^c(\mathbf{u}, \lambda_n, \boldsymbol{\lambda}_t, \delta \mathbf{u}, \delta \lambda_n, \delta \boldsymbol{\lambda}_t; \hat{\sigma}_n) = \int_{\Gamma} \left(\frac{\partial l_n}{\partial g_n} \delta g_n + \frac{\partial l_n}{\partial \lambda_n} \delta \lambda_n + \frac{\partial l_t}{\partial \mathbf{g}_t} \cdot \delta \mathbf{g}_t + \frac{\partial l_t}{\partial \boldsymbol{\lambda}_t} \cdot \delta \boldsymbol{\lambda}_t \right) d\Gamma, \quad (4.83)$$

where, as before,

$$\delta g_n = \frac{\partial g_n}{\partial \mathbf{u}} \cdot \delta \mathbf{u} = \boldsymbol{\nu} \cdot \delta \mathbf{u}, \quad \delta \mathbf{g}_t = \frac{\partial \mathbf{g}_t}{\partial \mathbf{u}} \cdot \delta \mathbf{u} = (\mathbf{I} - \boldsymbol{\nu} \otimes \boldsymbol{\nu}) \cdot \delta \mathbf{u}. \quad (4.84)$$

We recall also, that the term l_t depends on the so-called augmented contact pressure $\hat{\sigma}_n = \sigma_n + \epsilon_n g_n$, however, the corresponding derivative is not included in the contact virtual work, see Sec. 4.1.3 and also [Alart and Curnier, 1991, Pietrzak and Curnier, 1999].

Following the node-to-rigid-surface discretization approach, we approximate the contact virtual work integral by a sum of contributions from each contact element:

$$\delta W^c(\mathbf{U}, \mathbf{L}_n, \mathbf{L}_t, \delta \mathbf{U}, \delta \mathbf{L}_n, \delta \mathbf{L}_t; \hat{\mathbf{S}}_n) = \sum_{i=1}^m \delta W_i^c(\mathbf{u}_i, \lambda_{ni}, \boldsymbol{\lambda}_{ti}, \delta \mathbf{u}_i, \delta \lambda_{ni}, \delta \boldsymbol{\lambda}_{ti}; \hat{\sigma}_{ni}), \quad (4.85)$$

where we introduced the nodal values of the displacement vector \mathbf{u}_i , normal and tangential gaps g_{ni} and \mathbf{g}_{ti} , nodal Lagrange multipliers λ_{ni} and $\boldsymbol{\lambda}_{ti}$. Additionally, the augmented versions of Lagrange multipliers are considered:

$$\hat{\lambda}_{ni} = \lambda_{ni} + \epsilon_n g_{ni}, \quad \hat{\boldsymbol{\lambda}}_{ti} = \boldsymbol{\lambda}_{ti} + \epsilon_n \mathbf{g}_{ti}, \quad (4.86)$$

as well as the nodal value of the augmented contact pressure $\hat{\sigma}_{ni}$. Furthermore, we denote by \mathbf{U} , \mathbf{L}_n and \mathbf{L}_t vectors of displacements and Lagrange multipliers of all nodes on the surface Γ , while $\delta \mathbf{U}$, $\delta \mathbf{L}_n$ and $\delta \mathbf{L}_t$ are vectors of corresponding test functions, and, finally, $\hat{\mathbf{S}}_n$ is a vector of nodal values of augmented contact pressure.

Note that for brevity and simplicity in this section we will omit the index i for all aforementioned entities, assuming that the presented formulation is valid for each contact element.

First, we recall that the status (active or non-active) and frictional state (stick or

slip) are determined using the values of the augmented Lagrange multipliers $\hat{\lambda}_n$ and $\hat{\lambda}_t$ as follows:

$$\begin{cases} \hat{\lambda}_n \leq 0, & \|\hat{\lambda}_t\| \leq -\mu\hat{\lambda}_n, & (\text{stick}) \\ \hat{\lambda}_n \leq 0, & \|\hat{\lambda}_t\| > -\mu\hat{\lambda}_n, & (\text{slip}) \\ \hat{\lambda}_n > 0, & & (\text{non-contact}) \end{cases} \quad (4.87)$$

Then, depending on the contact status and the frictional state, the virtual work of a contact element reads:

$$\delta W_i^c = A_i \begin{cases} \hat{\lambda}_n \delta g_n + g_n \delta \lambda_n + \hat{\lambda}_t \cdot \delta \mathbf{g}_t + \mathbf{g}_t \cdot \delta \lambda_t, & (\text{stick}) \\ \hat{\lambda}_n \delta g_n + g_n \delta \lambda_n - \mu \hat{\sigma}_n \frac{\hat{\lambda}_t}{\|\hat{\lambda}_t\|} \cdot \delta \mathbf{g}_t - \frac{1}{\epsilon_t} \left(\lambda_t + \mu \hat{\sigma}_n \frac{\hat{\lambda}_t}{\|\hat{\lambda}_t\|} \right) \cdot \delta \lambda_t, & (\text{slip}) \\ -\frac{1}{\epsilon_n} \lambda_n \delta \lambda_n - \frac{1}{\epsilon_t} \lambda_t \cdot \delta \lambda_t, & (\text{non-contact}) \end{cases} \quad (4.88)$$

where A_i is the contact area corresponding to the considered element. For the subsequent resolution in the finite-element framework, we formulate the residual vector of the contact element:

$$\delta W_i^c = \begin{bmatrix} \mathbf{R}_u^c \\ \mathbf{R}_{\lambda_n}^c \\ \mathbf{R}_{\lambda_t}^c \end{bmatrix}^\top \cdot \begin{bmatrix} \delta \mathbf{u} \\ \delta \lambda_n \\ \delta \lambda_t \end{bmatrix} \quad (4.89)$$

with the following components:

$$\mathbf{R}_u^c = A_i \begin{cases} \hat{\lambda}_n \boldsymbol{\nu} + \hat{\lambda}_t \cdot (\mathbf{I} - \boldsymbol{\nu} \otimes \boldsymbol{\nu}), & (\text{stick}) \\ \hat{\lambda}_n \boldsymbol{\nu} + \mu \hat{\sigma}_n \mathbf{s} \cdot (\mathbf{I} - \boldsymbol{\nu} \otimes \boldsymbol{\nu}), & (\text{slip}) \\ \mathbf{0}, & (\text{non-contact}) \end{cases} \quad (4.90a)$$

$$\mathbf{R}_{\lambda_n}^c = A_i \begin{cases} g_n, & (\text{stick}) \\ g_n, & (\text{slip}) \\ -\frac{1}{\epsilon_n} \lambda_n, & (\text{non-contact}) \end{cases} \quad (4.90b)$$

$$\mathbf{R}_{\lambda_t}^c = A_i \begin{cases} \mathbf{g}_t, & (\text{stick}) \\ -\frac{1}{\epsilon_t} (\lambda_t - \mu \hat{\sigma}_n \mathbf{s}), & (\text{slip}) \\ -\frac{1}{\epsilon_t} \lambda_t, & (\text{non-contact}) \end{cases} \quad (4.90c)$$

where the vector \mathbf{s} denotes the direction *opposite* to the one of the frictional traction:

$$\mathbf{s} = -\frac{\hat{\lambda}_t}{\|\hat{\lambda}_t\|}. \quad (4.91)$$

Moreover, in the above formulas a new notation is used, such as $\underline{\lambda}_t$, $\underline{\mathbf{s}}$, $\underline{\mathbf{g}}_t$ and $\underline{\lambda}_t$. We note first that the term λ_t is equivalent to the frictional traction in the contact interface, and therefore is represented by a vector which belongs to the plane corresponding to

the rigid flat. We recall also that the plane is defined by a normal $\boldsymbol{\nu}$ and a point \mathbf{c} , which belongs to the plane. Furthermore, we may introduce a local coordinate system associated with this plane and represented by two orthonormal vectors $\boldsymbol{\tau}_1$ and $\boldsymbol{\tau}_2$, see Fig. 4.3. Consequently, rather than searching for 3 unknown components of the vector

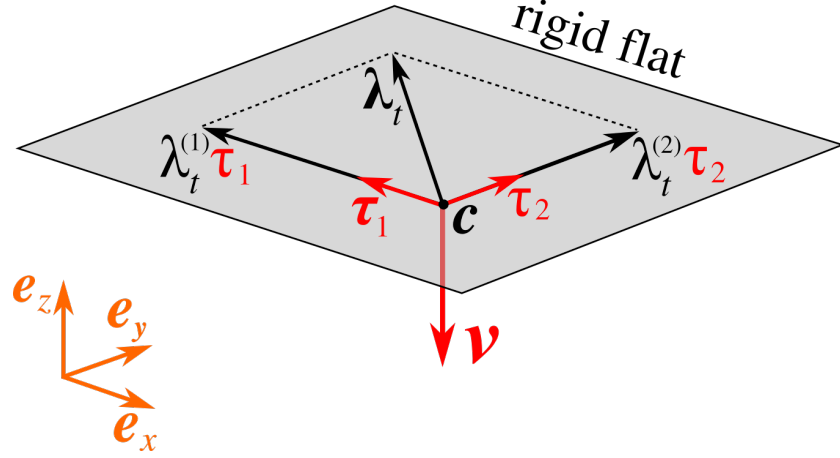


Figure 4.3

$\boldsymbol{\lambda}_t$ in the basis $\{\mathbf{e}_x, \mathbf{e}_y, \mathbf{e}_z\}$, we may consider the representation of this vector in the basis $\{\boldsymbol{\tau}_1, \boldsymbol{\tau}_2\}$:

$$\boldsymbol{\lambda}_t = \lambda_t^{(1)} \boldsymbol{\tau}_1 + \lambda_t^{(2)} \boldsymbol{\tau}_2 \quad (4.92)$$

In order to simplify the formulation of the residual vector and the tangent matrix, we introduce the following notation:

$$\boldsymbol{\lambda}_t = \underline{\underline{\boldsymbol{\lambda}}}_t \cdot \underline{\underline{\mathbf{T}}}, \quad (4.93)$$

where $\underline{\underline{\boldsymbol{\lambda}}}_t$ is a (2D) set of coordinates of the vector $\boldsymbol{\lambda}_t$ in the basis $\{\boldsymbol{\tau}_1, \boldsymbol{\tau}_2\}$:

$$\underline{\underline{\boldsymbol{\lambda}}}_t = \begin{bmatrix} \lambda_t^{(1)} \\ \lambda_t^{(2)} \end{bmatrix}, \quad (4.94)$$

termed as a “v-scalar” in the “s-structures” formalism introduced in [Yastrebov, 2013]. The second entity, $\underline{\underline{\mathbf{T}}}$, is a (2D) set of two 3D vectors $\boldsymbol{\tau}_1$ and $\boldsymbol{\tau}_2$:

$$\underline{\underline{\mathbf{T}}} = \begin{bmatrix} \boldsymbol{\tau}_1 \\ \boldsymbol{\tau}_2 \end{bmatrix}, \quad (4.95)$$

i.e. a “v-vector” in the terminology of [Yastrebov, 2013]. Note that the set of coordinates $\underline{\underline{\boldsymbol{\lambda}}}_t$ is obtained by the following operation:

$$\underline{\underline{\boldsymbol{\lambda}}}_t = \underline{\underline{\mathbf{T}}} \boldsymbol{\lambda}_t = \begin{bmatrix} \boldsymbol{\tau}_1 \cdot \boldsymbol{\lambda}_t \\ \boldsymbol{\tau}_2 \cdot \boldsymbol{\lambda}_t \end{bmatrix} = \begin{bmatrix} \lambda_t^{(1)} \\ \lambda_t^{(2)} \end{bmatrix}. \quad (4.96)$$

Furthermore, we may write in the same form the variation of the vector $\boldsymbol{\lambda}_t$:

$$\delta \boldsymbol{\lambda}_t = \delta \lambda_t^{(1)} \boldsymbol{\tau}_1 + \delta \lambda_t^{(2)} \boldsymbol{\tau}_2 = \begin{bmatrix} \delta \lambda_t^{(1)} \\ \delta \lambda_t^{(2)} \end{bmatrix}^\top \cdot \underline{\underline{\mathbf{T}}} = \delta \underline{\underline{\boldsymbol{\lambda}}}_t \cdot \underline{\underline{\mathbf{T}}}, \quad \delta \underline{\underline{\boldsymbol{\lambda}}}_t = \underline{\underline{\mathbf{T}}} \boldsymbol{\lambda}_t. \quad (4.97)$$

Moreover, we note that the representation (4.91) is possible for any vector, which belongs

to the plane corresponding to the rigid flat, such as vector \mathbf{s} :

$$\mathbf{s} = s^{(1)} \boldsymbol{\tau}_1 + s^{(2)} \boldsymbol{\tau}_2 = \begin{bmatrix} s^{(1)} \\ s^{(2)} \end{bmatrix}^\top \cdot \underline{\underline{\mathbf{T}}} = \underline{\underline{\mathbf{s}}} \cdot \underline{\underline{\mathbf{T}}}, \quad \underline{\underline{\mathbf{s}}} = \underline{\underline{\mathbf{T}}} \mathbf{s}, \quad (4.98)$$

and vector \mathbf{g}_t :

$$\mathbf{g}_t = g_t^{(1)} \boldsymbol{\tau}_1 + g_t^{(2)} \boldsymbol{\tau}_2 = \begin{bmatrix} g_t^{(1)} \\ g_t^{(2)} \end{bmatrix}^\top \cdot \underline{\underline{\mathbf{T}}} = \underline{\underline{\mathbf{g}}}_t \cdot \underline{\underline{\mathbf{T}}}, \quad \underline{\underline{\mathbf{g}}}_t = \underline{\underline{\mathbf{T}}} \mathbf{g}_t. \quad (4.99)$$

The next step is the computation of the second variation of the contact virtual work to the balance of virtual work. It is important to note that at this stage the augmented contact pressure $\hat{\sigma}_n$ becomes an unknown and is replaced by the augmented Lagrangian multiplier $\hat{\lambda}_n$, see [Pietrzak and Curnier, 1999]. Consequently, the variation is also performed with respect to this term. Therefore, separately considering the stick, slip and non-contact states, we obtain:

$$\begin{aligned} \Delta \delta W_i^c{}_{stick} = & A_i \left(\epsilon_n \Delta g_n \delta g_n + \Delta \lambda_n \delta g_n + \Delta g_n \delta \lambda_n \right. \\ & \left. + \epsilon_t \Delta \mathbf{g}_t \cdot \delta \mathbf{g}_t + \Delta \boldsymbol{\lambda}_t \cdot \delta \mathbf{g}_t + \Delta \mathbf{g}_t \cdot \delta \boldsymbol{\lambda}_t \right) \end{aligned} \quad (4.100a)$$

$$\begin{aligned} \Delta \delta W_i^c{}_{slip} = & A_i \left(\epsilon_n \Delta g_n \delta g_n + \Delta \lambda_n \delta g_n + \Delta g_n \delta \lambda_n - \frac{1}{\epsilon_t} \Delta \boldsymbol{\lambda}_t \cdot \delta \boldsymbol{\lambda}_t \right. \\ & - \mu \epsilon_n \Delta g_n \frac{\hat{\boldsymbol{\lambda}}_t}{\|\hat{\boldsymbol{\lambda}}_t\|} \cdot \delta \mathbf{g}_t - \mu \Delta \lambda_n \frac{\hat{\boldsymbol{\lambda}}_t}{\|\hat{\boldsymbol{\lambda}}_t\|} \cdot \delta \mathbf{g}_t \\ & - \frac{\mu \epsilon_t \hat{\lambda}_n}{\|\hat{\boldsymbol{\lambda}}_t\|} \Delta \mathbf{g}_t \cdot \delta \mathbf{g}_t - \frac{\mu \hat{\lambda}_n}{\|\hat{\boldsymbol{\lambda}}_t\|} \Delta \boldsymbol{\lambda}_t \cdot \delta \mathbf{g}_t \\ & - \frac{\mu \epsilon_n}{\epsilon_t} \Delta g_n \frac{\hat{\boldsymbol{\lambda}}_t}{\|\hat{\boldsymbol{\lambda}}_t\|} \cdot \delta \boldsymbol{\lambda}_t - \frac{\mu}{\epsilon_t} \Delta \lambda_n \frac{\hat{\boldsymbol{\lambda}}_t}{\|\hat{\boldsymbol{\lambda}}_t\|} \cdot \delta \boldsymbol{\lambda}_t \\ & - \frac{\mu \hat{\lambda}_n}{\|\hat{\boldsymbol{\lambda}}_t\|} \Delta \mathbf{g}_t \cdot \delta \boldsymbol{\lambda}_t - \frac{\mu \hat{\lambda}_n}{\epsilon_t \|\hat{\boldsymbol{\lambda}}_t\|} \Delta \boldsymbol{\lambda}_t \cdot \delta \boldsymbol{\lambda}_t \\ & + \frac{\mu \epsilon_t \hat{\lambda}_n}{\|\hat{\boldsymbol{\lambda}}_t\|^3} \Delta \mathbf{g}_t \cdot (\hat{\boldsymbol{\lambda}}_t \otimes \hat{\boldsymbol{\lambda}}_t) \cdot \delta \mathbf{g}_t + \frac{\mu \hat{\lambda}_n}{\|\hat{\boldsymbol{\lambda}}_t\|^3} \Delta \boldsymbol{\lambda}_t \cdot (\hat{\boldsymbol{\lambda}}_t \otimes \hat{\boldsymbol{\lambda}}_t) \cdot \delta \mathbf{g}_t \\ & \left. + \frac{\mu \hat{\lambda}_n}{\|\hat{\boldsymbol{\lambda}}_t\|^3} \Delta \mathbf{g}_t \cdot (\hat{\boldsymbol{\lambda}}_t \otimes \hat{\boldsymbol{\lambda}}_t) \cdot \delta \boldsymbol{\lambda}_t + \frac{\mu \hat{\lambda}_n}{\epsilon_t \|\hat{\boldsymbol{\lambda}}_t\|^3} \Delta \boldsymbol{\lambda}_t \cdot (\hat{\boldsymbol{\lambda}}_t \otimes \hat{\boldsymbol{\lambda}}_t) \cdot \delta \boldsymbol{\lambda}_t \right) \end{aligned} \quad (4.100b)$$

$$\Delta \delta W_i^c{}_{non-contact} = -A_i \left(\frac{1}{\epsilon_n} \Delta \lambda_n \delta \lambda_n + \frac{1}{\epsilon_t} \Delta \boldsymbol{\lambda}_t \cdot \delta \boldsymbol{\lambda}_t \right) \quad (4.100c)$$

Equivalently, the second variation of the virtual work may be represented using the tangent matrix of the element:

$$\Delta \delta W_i^c = \begin{bmatrix} \Delta \mathbf{u} \\ \Delta \lambda_n \\ \Delta \underline{\underline{\boldsymbol{\lambda}}}_t \end{bmatrix}^\top \cdot \begin{bmatrix} \mathbf{K}_{uu}^c & \mathbf{K}_{u\lambda_n}^c & \mathbf{K}_{u\boldsymbol{\lambda}_t}^c \\ \mathbf{K}_{\lambda_n u}^c & \mathbf{K}_{\lambda_n \lambda_n}^c & \mathbf{K}_{\lambda_n \boldsymbol{\lambda}_t}^c \\ \mathbf{K}_{\boldsymbol{\lambda}_t u}^c & \mathbf{K}_{\boldsymbol{\lambda}_t \lambda_n}^c & \mathbf{K}_{\boldsymbol{\lambda}_t \boldsymbol{\lambda}_t}^c \end{bmatrix} \cdot \begin{bmatrix} \delta \mathbf{u} \\ \delta \lambda_n \\ \delta \underline{\underline{\boldsymbol{\lambda}}}_t \end{bmatrix} \quad (4.101)$$

The expressions for the corresponding terms of the matrix are the following:

$$\mathbf{K}_{uu}^c = A_i \begin{cases} \epsilon_n \boldsymbol{\nu} \otimes \boldsymbol{\nu} + \epsilon_t (\mathbf{I} - \boldsymbol{\nu} \otimes \boldsymbol{\nu}), & (\text{stick}) \\ \epsilon_n \boldsymbol{\nu} \otimes \boldsymbol{\nu} + \epsilon_n \mu \boldsymbol{\nu} \otimes \mathbf{s} - \frac{\mu \epsilon_t \hat{\lambda}_n}{\|\hat{\lambda}_t\|} (\mathbf{I} - \boldsymbol{\nu} \otimes \boldsymbol{\nu} - \mathbf{s} \otimes \mathbf{s}), & (\text{slip}) \\ \mathbf{0}, & (\text{non-contact}) \end{cases} \quad (4.102a)$$

$$\mathbf{K}_{u\lambda_n}^c = A_i \begin{cases} \boldsymbol{\nu}, & (\text{stick}) \\ \boldsymbol{\nu}, & (\text{slip}) \\ \mathbf{0}, & (\text{non-contact}) \end{cases} \quad (4.102b)$$

$$\mathbf{K}_{\lambda_n u}^c = A_i \begin{cases} \boldsymbol{\nu}^\top, & (\text{stick}) \\ (\boldsymbol{\nu} + \mu \mathbf{s})^\top, & (\text{slip}) \\ \mathbf{0}, & (\text{non-contact}) \end{cases} \quad (4.102c)$$

$$\mathbf{K}_{\lambda_n \lambda_n}^c = A_i \begin{cases} 0, & (\text{stick}) \\ 0, & (\text{slip}) \\ -\frac{1}{\epsilon_n}, & (\text{non-contact}) \end{cases} \quad (4.102d)$$

$$\mathbf{K}_{u\lambda_t}^c = A_i \begin{cases} \underline{\underline{\mathbf{T}}}^\top, & (\text{stick}) \\ -\frac{\mu \hat{\lambda}_n}{\|\hat{\lambda}_t\|} (\mathbf{I} - \mathbf{s} \otimes \mathbf{s}) \cdot \underline{\underline{\mathbf{T}}}^\top + \frac{\mu \epsilon_n}{\epsilon_t} (\boldsymbol{\nu} \otimes \mathbf{s}) \cdot \underline{\underline{\mathbf{T}}}^\top, & (\text{slip}) \\ \mathbf{0}, & (\text{non-contact}) \end{cases} \quad (4.102e)$$

$$\mathbf{K}_{\lambda_t u}^c = A_i \begin{cases} \underline{\underline{\mathbf{T}}}, & (\text{stick}) \\ -\frac{\mu \hat{\lambda}_n}{\|\hat{\lambda}_t\|} \underline{\underline{\mathbf{T}}} \cdot (\mathbf{I} - \mathbf{s} \otimes \mathbf{s}), & (\text{slip}) \\ \mathbf{0}, & (\text{non-contact}) \end{cases} \quad (4.102f)$$

$$\mathbf{K}_{\lambda_n \lambda_t}^c = A_i \begin{cases} \mathbf{0}, & (\text{stick}) \\ -\frac{\mu}{\epsilon_t} \mathbf{s}^\top, & (\text{slip}) \\ \mathbf{0}, & (\text{non-contact}) \end{cases} \quad (4.102g)$$

$$\mathbf{K}_{\lambda_t \lambda_n}^c = \mathbf{0} \quad (4.102h)$$

$$\mathbf{K}_{\lambda_t \lambda_t}^c = A_i \begin{cases} \mathbf{0}, & (\text{stick}) \\ -\frac{1}{\epsilon_t} \underline{\underline{\mathbf{I}}} - \frac{\mu \hat{\lambda}_n}{\epsilon_t \|\hat{\lambda}_t\|} (\underline{\underline{\mathbf{I}}} - \underline{\underline{\mathbf{T}}} \cdot (\mathbf{s} \otimes \mathbf{s}) \cdot \underline{\underline{\mathbf{T}}}^\top), & (\text{slip}) \\ -\frac{1}{\epsilon_t} \underline{\underline{\mathbf{I}}}, & (\text{non-contact}) \end{cases} \quad (4.102i)$$

where $\underline{\underline{\mathbf{I}}} = \underline{\underline{\mathbf{T}}} \cdot \underline{\underline{\mathbf{T}}}^\top$, i.e.

$$\underline{\underline{\mathbf{I}}} = \begin{bmatrix} 1 & 0 \\ 0 & 1 \end{bmatrix}. \quad (4.103)$$

Note that the following equalities were also used:

$$\underline{\underline{\mathbf{T}}} \cdot (\mathbf{I} - \boldsymbol{\nu} \otimes \boldsymbol{\nu}) = \underline{\underline{\mathbf{T}}}, \quad (\mathbf{I} - \boldsymbol{\nu} \otimes \boldsymbol{\nu}) \cdot \underline{\underline{\mathbf{T}}}^\top = \underline{\underline{\mathbf{T}}}^\top. \quad (4.104)$$

4.3 Face-to-rigid-surface discretization approach

Here we introduce contact resolution methods formulated in Sec. 4.1 into the finite-element framework, using the “face-to-rigid-surface” approach, which is an alternative to the discussed above “node-to-rigid-surface” technique, see Sec. 4.2. The “face-to-rigid-surface” approach associates each contact element with an edge (in 2D) or a face (in 3D) of the potential contact zone Γ , rather than with a single node, and, consequently, has considerable benefits for the problem under study involving fluid flow in contact interfaces.

Indeed, as was discussed in Sec. 2.5, the solution of this coupled problem requires partition of the interface into contact, fluid-flow and, possibly multiple, trapped fluid zones. The fluid pressure in the fluid-flow domain is handled by the Reynolds equation, defined on the lubrication surface associated with the rigid flat, see Sec. 2.5.2. In Sec. 6.1, applying a standard finite-element approach to elliptic equations, each fluid-flow element will be based on the projection of a face of the solid’s surface Γ on the rigid flat. Furthermore, the trapped fluid element, which will be introduced in the Chapter 5, is based on an agglomeration of faces of Γ . Therefore, in order to make the identification of the interface status self-consistent, it appears natural to associate contact elements also with faces of the surface Γ , which will be exploited in the resolution procedure in Sec. 6.4. Moreover, as was already mentioned, the computation of the contact area is by itself of great importance for problems of contact between rough surfaces, see for example, [Vakis et al., 2018]. However, the computation of the area corresponding to a contact element in the “node-to-rigid-surface” approach in 3D set-up is not straightforward, see discussion in Sec. 4.2, while using the “face-to-rigid-surface” technique the area of each element is obtained naturally.

In order to use the “face-to-rigid-surface” approach, for every point on the surface Γ we consider the interpolation of the gap and of the normal traction as, respectively:

$$g_n = \sum_{i=1}^m N_i g_{ni}, \quad \sigma_n = \sum_{i=1}^m N_i \sigma_{ni}, \quad (4.105)$$

where g_i is the nodal gap value, σ_{ni} is the nodal value of the contact pressure (treatment of which is method-dependent and will be discussed in detail below), N_i is the shape function associated with the node i , and m is the total number of nodes on surface Γ . Note that the same shape functions are used here for interpolation of geometric gap and surface tractions, however, it is not a necessary condition. Furthermore, we used bilinear shape functions associated with quadrilateral faces of the discretized surface, nonetheless, polynomials of different order could be utilized, see a discussion in [Puso et al., 2008].

It is important to note, that in case of the considered interpolation (4.105) contact constraints (2.68b) cannot be satisfied point-wise on the surface Γ . To overcome this inconsistency, we use the mortar approach [Puso, 2004, Puso and Laursen, 2004a, Puso and Laursen, 2004b] and consider the third condition in (2.68b) in the integral form over the surface Γ :

$$\int_{\Gamma} \sigma_n g_n d\Gamma = 0. \quad (4.106)$$

Substituting (4.105) into (4.106) and considering two first conditions of (2.68b) in

every node of the surface Γ , we obtain the following discrete (nodal) form of the contact conditions:

$$\tilde{g}_i \geq 0, \sigma_{ni} \leq 0, \sigma_{ni} \tilde{g}_i = 0, \quad 1 \leq i \leq m, \quad (4.107)$$

where \tilde{g}_i is termed as the integral (weighted) gap associated with node i and is given by:

$$\tilde{g}_i = \sum_{j=1}^m g_j \int_{\Gamma} N_i N_j d\Gamma. \quad (4.108)$$

The resolution of nodal contact constraints (4.107) also requires the use of the optimization methods. The classic Lagrange multiplier method (Sec. 4.1.1) becomes ineligible for the “face-to-rigid-surface” approach, since the additional degrees of freedom, appended to each node of the surface, will be shared between several contact elements, some of which can be in active contact, while others are not (e.g. in the vicinity of the contact zone’s boundary). Consequently, the active set strategy, see (4.62), and the necessary elimination of the Lagrange multipliers which do not belong to active contact elements become tedious. The penalty method (Sec. 4.1.2) does not introduce additional DOFs, however, using this approach the contact constraints are never satisfied exactly. Thus, the penetration occurs in the contact zone, which could lead to inconsistencies in handling the fluid flow near the boundaries of the contact patches. Therefore, we used the augmented Lagrangian method (Sec. 4.1.3), which possesses the benefits of the classic Lagrange multipliers (exact satisfaction of the constraints) and penalty methods (active set strategy is not needed, nor the elimination of additional DOFs in non-contact zones).

Note that the frictional contact will not be considered in the “face-to-rigid-surface” approach, due to a significant complexity of its implementation in the mortar framework, see [Puso and Laursen, 2004b]. Furthermore, for the problem involving fluid flow in contact interfaces, to simplify our discussion and concentrate it on the two-way coupling aspects, we use the small deformations and small rotations assumptions, which is justified (at least partially) by the requirement of small slopes of the roughness profile for the validity of the Reynolds equation in certain applications, see Section 2.3.3 and discussions in [Brown et al., 1995]. Nevertheless, the necessary modifications to take into account large deformations and/or large rotations could be added into the presented framework. Note also that a separate problem of trapped fluid in contact interface in a plane strain formulation is solved in Chapter 7 considering frictional constraints and large deformations/rotations formulation.

4.3.1 Augmented Lagrangian method

Contact conditions (4.107) lead to a constrained minimization problem for the potential energy of deformed solid Π^s , in order to resolve it we append Lagrange multipliers λ_i , $i = 1 \dots m$ to each node of the surface Γ and introduce the following augmented Lagrangian functional, see also [Alart and Curnier, 1991, Cavalieri and Cardona, 2013]:

$$\mathcal{L}^a(\mathbf{U}, \mathbf{L}) = \Pi^s(\mathbf{U}) + W^c(\mathbf{U}, \mathbf{L}), \quad (4.109)$$

where W^c represents the “potential” energy of the contact and is given by:

$$W^c(\mathbf{U}, \mathbf{L}) = \sum_{i=1}^m \begin{cases} \lambda_i \tilde{g}_i + \frac{\epsilon}{2} \tilde{g}_i^2, & \text{if } \hat{\lambda}_i \leq 0, \\ -\frac{1}{2\epsilon} \lambda_i^2, & \text{if } \hat{\lambda}_i > 0, \end{cases} \quad (4.110)$$

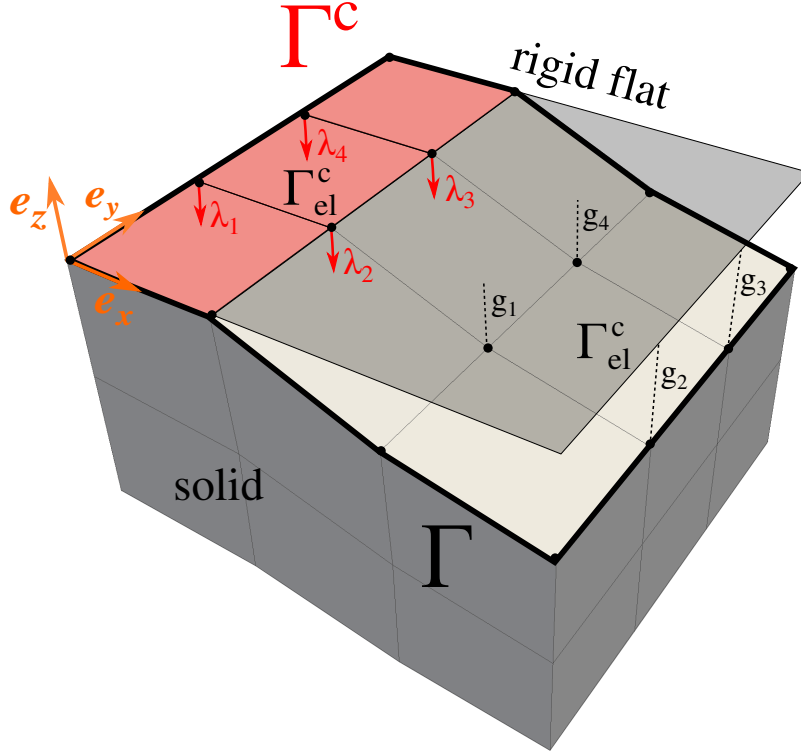


Figure 4.4: Sketch of the interface highlighting contact elements: Γ is the potential contact zone, Γ^c is the active contact zone (*active set*), Γ_{el}^c is a face associated to one contact element, λ is the Lagrange multiplier, which represents contact pressure and is attributed to each node of the surface Γ , g_n is the gap function: $g_n = 0$ on Γ^c and $g_n > 0$ on $\Gamma \setminus \Gamma^c$.

where ϵ is the so-called augmentation parameter and the following notation of the augmented Lagrange multiplier is introduced: $\hat{\lambda}_i = \lambda_i + \epsilon \tilde{g}_i$, the sign of which defines the contact state of the node: if $\hat{\lambda}_i \leq 0$ the node belongs to the active set, while if $\hat{\lambda}_i > 0$ the node is not in contact. Note that in formulas (4.109)-(4.110) we denote by $\mathbf{U} = [\mathbf{u}_1, \mathbf{u}_2, \dots, \mathbf{u}_m]^\top$ and $\mathbf{L} = [\lambda_1, \lambda_2, \dots, \lambda_m]^\top$ vectors of nodal displacements and values of Lagrange multipliers, respectively. Note that once the solution is obtained, values of Lagrange multipliers λ_i are equal to respective nodal values of the contact pressure σ_{ni} .

The solution of the contact problem is equivalent to the stationary saddle point of the Lagrangian (4.109), at which its variation vanishes:

$$\delta \mathcal{L}^a(\mathbf{U}, \mathbf{L}) = \frac{\partial \Pi^s(\mathbf{U})}{\partial \mathbf{U}} \cdot \delta \mathbf{U} + \frac{\partial W^c(\mathbf{U}, \mathbf{L})}{\partial \mathbf{U}} \cdot \delta \mathbf{U} + \frac{\partial W^c(\mathbf{U}, \mathbf{L})}{\partial \mathbf{L}} \delta \mathbf{L} = 0. \quad (4.111)$$

In order to derive the contribution of each contact element to the last two terms in (4.111) and determine the element's status (independently from the neighbouring elements) we define the restrictions of the integral gap (4.108) to the face Γ_{el} associated with the contact element:

$$\tilde{g}_i = \sum_{j=1}^n g_j \int_{\Gamma_{el}} N_i N_j d\Gamma_{el} = \sum_{j=1}^n g_j I_{ij}, \quad (4.112)$$

where n is the total number of nodes of the face Γ_{el} , \tilde{g}_i is the integral gap of the i -th

node computed over the current face only, and the weights I_{ij} are calculated as:

$$I_{ij} = \int_{-1}^1 \int_{-1}^1 N_i N_j J d\xi d\eta, \quad (4.113)$$

where J is the Jacobian of the transformation of the physical coordinates $\mathbf{x} = (x, y, z)$ on the surface Γ_{el} to the face's coordinates in the parent space $\boldsymbol{\xi} = (\xi, \eta)$:

$$J = \left| \frac{\partial \mathbf{x}}{\partial \xi} \times \frac{\partial \mathbf{x}}{\partial \eta} \right|, \quad \mathbf{x} = \sum_{i=1}^n \mathbf{x}_i N_i \quad (4.114)$$

where \mathbf{x}_i is the position of the i -th node of the face. Using the Gauss quadrature rules, the integral in (4.113) is computed as:

$$I_{ij} = \sum_{k=1}^{n_{\text{gp}}} w_k N_i(\boldsymbol{\xi}_k) N_j(\boldsymbol{\xi}_k) J(\boldsymbol{\xi}_k) \quad (4.115)$$

where n_{gp} is the number of Gauss points associated with the face Γ_{el} , w_k is the weight coefficient of the k -th Gauss point, and $\boldsymbol{\xi}_k$ are its coordinates in the parent space.

In order to find the contribution of each contact element to the balance of virtual works, we calculate the variation of (4.110):

$$\delta W_{\text{el}}^{\text{c}} = \sum_{i=1}^n \begin{cases} \hat{\lambda}_i \sum_{j=1}^n I_{ij} \frac{\partial g_j}{\partial \mathbf{u}_j} \delta \mathbf{u}_j + \tilde{g}_i \delta \lambda_i, & \hat{\lambda}_i \leq 0 \\ -\frac{1}{\epsilon} \lambda_i \delta \lambda_i, & \hat{\lambda}_i > 0 \end{cases} \quad (4.116)$$

where \mathbf{u}_j is the displacement vector of the node j . Note that in accordance with the infinitesimal strain formulation the Jacobian is not varied. We shall term hereinafter an element as active if at least at one of its nodes $\hat{\lambda}_i \leq 0$, $i = 1 \dots n$, and inactive otherwise.

In order to perform linearisation of the problem, we calculate the second variation of the virtual work $\delta W_{\text{el}}^{\text{c}}$:

$$\Delta \delta W_{\text{el}}^{\text{c}} = \sum_{i=1}^n \begin{cases} \epsilon \sum_{j=1}^n I_{ij} \frac{\partial g_j}{\partial \mathbf{u}_j} \delta \mathbf{u}_j + \sum_{k=1}^n I_{ik} \frac{\partial g_k}{\partial \mathbf{u}_k} \Delta \mathbf{u}_k \\ + \sum_{j=1}^n I_{ij} \frac{\partial g_j}{\partial \mathbf{u}_j} (\delta \mathbf{u}_j \Delta \lambda_i + \Delta \mathbf{u}_j \delta \lambda_i), & \hat{\lambda}_i \leq 0 \\ -\frac{1}{\epsilon} \delta \lambda_i \Delta \lambda_i, & \hat{\lambda}_i > 0. \end{cases} \quad (4.117)$$

Finally, the virtual work (4.116) and its variation (4.117) could be expressed in a compact form, introducing the residual vector \mathbf{R}^{c} and the tangent matrix \mathbf{K}^{c} of a contact element:

$$\delta W_{\text{el}}^{\text{c}} = \underbrace{\begin{bmatrix} \mathbf{R}_{\mathbf{u}}^{\text{c}} \\ \mathbf{R}_{\lambda}^{\text{c}} \end{bmatrix}}_{\mathbf{R}^{\text{c}}}^{\text{T}} \begin{bmatrix} \delta \mathbf{u} \\ \delta \lambda \end{bmatrix}, \quad \Delta \delta W_{\text{el}}^{\text{c}} = \begin{bmatrix} \Delta \mathbf{u} \\ \Delta \lambda \end{bmatrix}^{\text{T}} \underbrace{\begin{bmatrix} \mathbf{K}_{\mathbf{u}\mathbf{u}}^{\text{c}} & \mathbf{K}_{\mathbf{u}\lambda}^{\text{c}} \\ \mathbf{K}_{\lambda\mathbf{u}}^{\text{c}} & \mathbf{K}_{\lambda\lambda}^{\text{c}} \end{bmatrix}}_{\mathbf{K}^{\text{c}}} \begin{bmatrix} \delta \mathbf{u} \\ \delta \lambda \end{bmatrix}, \quad (4.118)$$

where for brevity we slightly abuse the notation implying $\delta \mathbf{u} = [\delta \mathbf{u}_1, \dots, \delta \mathbf{u}_n]^{\text{T}}$, $\Delta \mathbf{u} = [\Delta \mathbf{u}_1, \dots, \Delta \mathbf{u}_n]^{\text{T}}$ and, accordingly, $\delta \lambda = [\delta \lambda_1, \dots, \delta \lambda_n]^{\text{T}}$, $\Delta \lambda = [\Delta \lambda_1, \dots, \Delta \lambda_n]^{\text{T}}$. We provide also detailed expressions for residual vector and tangent matrix of the contact

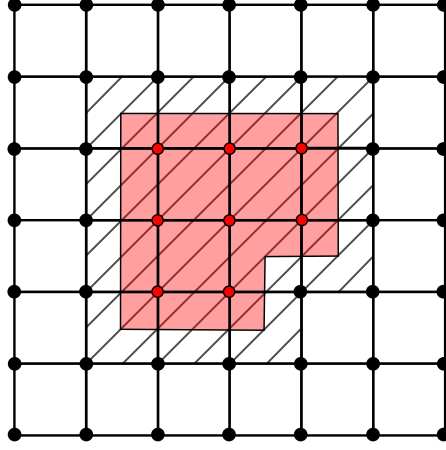


Figure 4.5: Sketch on the computation of the real contact area. Red circles represent nodes with $\hat{\lambda}_i \leq 0$, black ones correspond to $\hat{\lambda}_i > 0$. The dashed area represents the contact area computed by summing up areas of all active elements, see (4.120). The shaded area is obtained by a refined approach of summing up areas corresponding to nodes with $\hat{\lambda}_i \leq 0$, computed using the nearest Gauss point to node i , see (4.121).

element:

$$\mathbf{R}_{\mathbf{u}}^c = [\mathbf{R}_{\mathbf{u}_1}^c, \dots, \mathbf{R}_{\mathbf{u}_n}^c]^\top, \quad \mathbf{R}_{\mathbf{u}_j}^c = \sum_{i=1}^n \begin{cases} \hat{\lambda}_i I_{ij} \frac{\partial g_j}{\partial \mathbf{u}_j}, & \hat{\lambda}_i \leq 0 \\ 0, & \hat{\lambda}_i > 0; \end{cases} \quad (4.119a)$$

$$\mathbf{R}_{\lambda}^c = [\mathbf{R}_{\lambda_1}^c, \dots, \mathbf{R}_{\lambda_n}^c]^\top, \quad \mathbf{R}_{\lambda_i}^c = \begin{cases} \tilde{g}_i, & \hat{\lambda}_i \leq 0 \\ -\frac{1}{\epsilon} \lambda_i, & \hat{\lambda}_i > 0; \end{cases} \quad (4.119b)$$

$$\mathbf{K}_{\mathbf{u}_k \mathbf{u}_j}^c = \sum_{i=1}^n \begin{cases} \epsilon I_{ij} \frac{\partial g_j}{\partial \mathbf{u}_j} I_{ik} \frac{\partial g_k}{\partial \mathbf{u}_k}, & \hat{\lambda}_i \leq 0 \\ 0, & \hat{\lambda}_i > 0; \end{cases} \quad (4.119c)$$

$$\mathbf{K}_{\lambda_i \mathbf{u}_j}^c = \mathbf{K}_{\mathbf{u}_j \lambda_i}^c = \begin{cases} I_{ij} \frac{\partial g_j}{\partial \mathbf{u}_j}, & \hat{\lambda}_i \leq 0 \\ 0, & \hat{\lambda}_i > 0; \end{cases} \quad (4.119d)$$

$$\mathbf{K}_{\lambda_i \lambda_i}^c = \begin{cases} 0, & \hat{\lambda}_i \leq 0 \\ -\frac{1}{\epsilon}, & \hat{\lambda}_i > 0, \end{cases} \quad \mathbf{K}_{\lambda_i \lambda_j}^c = 0 \text{ if } i \neq j. \quad (4.119e)$$

The residual vector \mathbf{R}^c and tangent matrix \mathbf{K}^c are updated on each iteration of the Newton-Raphson method and added to the corresponding entries of the global residual vector and tangent matrix. Note that in the frictionless case considered here the tangent matrix of the contact element is symmetric, i.e. $\mathbf{K}_{\mathbf{u}\lambda}^c = \mathbf{K}_{\lambda\mathbf{u}}^c$.

4.3.2 Post-processing computation of the real contact area

The presented above contact element formulation is sufficient for resolution of the contact constraints (4.107). However, during the post-processing stage, different methods may be applied to compute the real contact area. A possible straightforward approach is to sum up areas A_{el} of faces Γ_{el} associated with active elements, i.e. the ones that have at

least one node with $\hat{\lambda}_i \leq 0$ (dashed areas in Fig. 4.5):

$$A_{\text{el}} = \begin{cases} \sum_{k=1}^{n_{\text{gp}}} w_k J(\boldsymbol{\xi}_k), & \exists i \in [1, \dots, n] : \hat{\lambda}_i \leq 0 \\ 0, & \forall i \in [1, \dots, n] : \hat{\lambda}_i > 0, \end{cases} \quad (4.120)$$

where n is the number of nodes of the contact element, n_{gp} is the number of Gauss points associated with the face Γ_{el} , w_k is the weight coefficient of the k -th Gauss point, and $\boldsymbol{\xi}_k$ are its coordinates in the parent space.

However, our study showed that this method of computation of the contact area leads to a significant overestimation of the latter. We propose here a more precise approach to computing of the contact area: considering separately each contact element, only if $\hat{\lambda}_i \leq 0$ at a node i , we add up to the contact area contribution from the Gauss point closest to this node (shaded area in Fig. 4.5):

$$A_{\text{el}} = \sum_{i=1}^n \begin{cases} w_i J(\boldsymbol{\xi}_i), & \hat{\lambda}_i \leq 0 \\ 0, & \hat{\lambda}_i > 0, \end{cases} \quad (4.121)$$

where w_i and $\boldsymbol{\xi}_i$ are the weight coefficient and the position of a Gauss point closest to the node i . Note that we assumed here that n (the number of element's nodes where Lagrange multipliers λ_i are considered) equals to n_{gp} (the number of Gauss points of the corresponding face). However, it might not be the case if, for example, shape functions of different order are used for interpolation of the geometry and of the contact pressure, cf. (4.105), see also [Puso et al., 2008], and a different refined approach of the real contact area computation will be required. The comparison of two discussed approaches to real contact area computation will be presented below.

Chapter 5

Resolution of the trapped fluid problem

Résumé de Chapitre 5 “Résolution du problème de fluide piégé”

Dans ce chapitre, nous présentons un cadre numérique pour la résolution du problème de fluide piégé dans une interface de contact définie entre un solide déformable et un plan rigide. Nous considérons le cas général et autorisons un remplissage partiel de la cavité. Cette formulation s’ajoute au problème de contact présenté au chapitre 4 par le biais de contraintes supplémentaires associées au fluide piégé. Ensuite, nous proposons deux méthodes pour résoudre ces contraintes, offrant la possibilité de simuler un fluide piégé incompressible ou compressible. Enfin, les deux approches mises en œuvre par éléments finis sont comparées: le nouveau “super-élément” et la formulation standard.

In this chapter we present a numerical framework for the problem of the trapped fluid in a contact interface between a deformable solid and a rigid flat. In Section 2.5 we formulated the statement of the coupled problem involving contact, fluid flow and trapped fluid zones, assuming that the fluid occupies the whole free volume between the contacting surfaces. However, in Chapter 7 we will study separately the effect of the trapped fluid on the contact problem without fluid flow in the interface. In that problem set-up we will consider a more general case and allow a partial filling of the trapped pool by a liquid (while the effect of a gas, which could be present in the remaining part of this volume, is neglected). Therefore, the possibility for partial filling is to be also taken into account in the formulation presented here, while the same framework (without that possibility) will be used for coupled problem involving the fluid flow in Chapters 8 and 9.

Since the trapped fluid problem in the form considered in this dissertation is inseparable from the contact problem, the subsequent developments will be based on the contact resolution framework discussed in Chapter 4. Thus, we will enhance the contact problem by considering additional constraints associated with the trapped fluid, see Sec. 2.5.4. We will discuss two different methods of resolution of these constraints, providing possibility to simulate both incompressible and compressible trapped fluid. Furthermore, two different approaches to the subsequent implementation in a finite-element framework will be given. This model will be formulated for a single trapped fluid pool, implying that the proposed approaches can be used thereupon for an arbitrary number of trapped fluid zones in the interface.

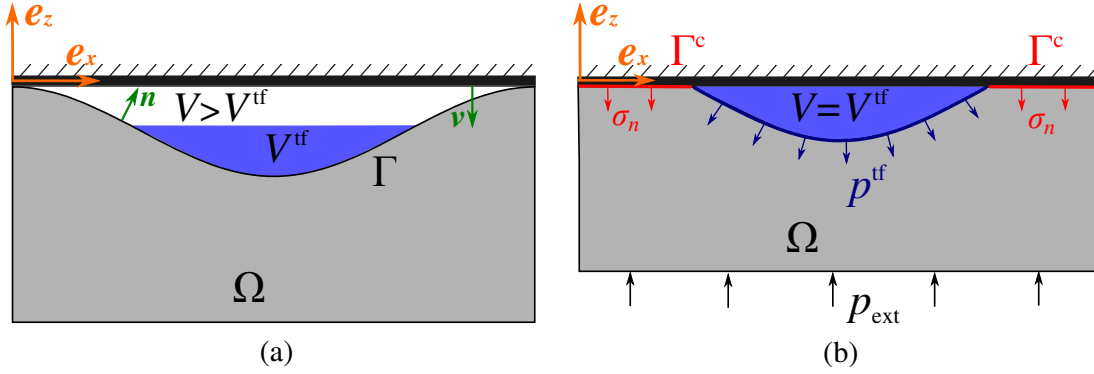


Figure 5.1: (a) Trapped fluid is in inactive state. (b) Trapped fluid is in active state. Note that the presented sketch corresponds to the plane strain problem statement (no dependency on the y -coordinate): fluid is trapped inside of a “valley” contained between two contact zones. In a 3D problem set-up fluid entrapment is possible only inside of a “pool” bounded by a non-simply connected contact patch.

5.1 Trapped fluid constraints

First, we recall that the volume of the gap between the surface of the solid and the rigid flat is given by, see (2.76):

$$V(\mathbf{u}) = \int_{\Gamma \setminus \Gamma^c} g_n(\mathbf{u})(-\mathbf{n} \cdot \boldsymbol{\nu}) d\Gamma, \quad (5.1)$$

where Γ is the potential contact zone (which defines the extent of the contact interface), Γ^c is the active contact zone, g_n is the normal gap function defined in (2.18), \mathbf{n} is the outward normal to the surface of the solid and $\boldsymbol{\nu}$ is the normal to the rigid flat.

Let us consider a volume of fluid trapped inside of a “pool” bounded by a non-simply connected contact patch (in a 3D problem statement), or inside of a “valley” contained between two contact zones (in the plane strain problem set-up, see Fig. 5.1). For simplicity, we assume that the non-contact part of the surface Γ corresponds only to the considered “pool”.

The fluid may fill completely or partially the gap between the contacting surfaces, therefore it can be present in two different states: “inactive”, when $V > V^{\text{tf}}$ and the fluid is not pressurized ($p^{\text{tf}} = 0$), and “active”, when $V = V^{\text{tf}}$, and pressure in the fluid $p^{\text{tf}} > 0$, see Fig. 5.1(a) and 5.1(b), respectively. We may formulate this two states in a way similar to Hertz-Signorini-Moreau constraints for the unilateral contact (2.21):

$$V \geq V^{\text{tf}}, \quad p^{\text{tf}} \geq 0, \quad p^{\text{tf}}(V - V^{\text{tf}}) = 0 \Leftrightarrow \begin{cases} V = V^{\text{tf}}, & p^{\text{tf}} > 0, & \text{(active)} \\ V > V^{\text{tf}}, & p^{\text{tf}} = 0, & \text{(inactive)}. \end{cases} \quad (5.2)$$

Below we will discuss how methods of the optimization theory can be used to handle the constraints (5.2) and also to include the models of incompressible (2.73) and compressible (2.74)-(2.75) trapped fluid into the computational framework.

5.1.1 Incompressible fluid model

Let us consider first the model of the incompressible fluid: while it remains trapped, the fluid volume V^{tf} must be constant and equal to the initial volume V_0^{tf} . If the fluid is in the inactive state, it does not introduce additional constraints, and we obtain a mechanical contact problem between the deformable solid and the rigid flat, which was

already discussed in Chapter 4. If, on the contrary, the fluid is in the active state, we must consider additionally the gap volume constraint: $V = V^{\text{tf}}$, or, since the fluid is incompressible, $V = V_0^{\text{tf}}$. The Lagrange multiplier method (see its application to the contact problem in Sec. 4.1.1) can be used to fulfill this constraint. Thus, the combined Lagrangian for the coupled trapped fluid problem can be defined as:

$$\mathcal{L}(\mathbf{u}, \lambda_n, \lambda^{\text{tf}}) = \Pi^{\text{s}}(\mathbf{u}) + \int_{\Gamma^{\text{c}}} \lambda_n g(\mathbf{u}) d\Gamma^{\text{c}} - \lambda^{\text{tf}} (V(\mathbf{u}) - V_0^{\text{tf}}), \quad (5.3)$$

where $\Pi^{\text{s}}(\mathbf{u})$ the potential energy of the system, $\lambda_n \leq 0$ is the Lagrange multipliers function representing normal contact tractions, and $\lambda^{\text{tf}} \geq 0$ is the Lagrange multiplier for the trapped fluid, which is equivalent to the fluid pressure p^{tf} . The solution of the coupled problem is a stationary point $(\mathbf{u}, \lambda_n, \lambda^{\text{tf}})$, $\mathbf{u} \in \mathbf{V}$, $\lambda_n \leq 0$, $\lambda^{\text{tf}} \geq 0$ of the Lagrangian (5.3) at which its variation vanishes:

$$\delta \mathcal{L}(\mathbf{u}, \lambda_n, \lambda^{\text{tf}}) = D \Pi^{\text{s}}(\mathbf{u}) \cdot \delta \mathbf{u} + \int_{\Gamma^{\text{c}}} \left[\lambda_n \frac{\partial g(\mathbf{u})}{\partial \mathbf{u}} \cdot \delta \mathbf{u} + g(\mathbf{u}) \delta \lambda_n \right] d\Gamma^{\text{c}} \quad (5.4a)$$

$$- \left[\lambda^{\text{tf}} D V(\mathbf{u}) \cdot \delta \mathbf{u} + (V(\mathbf{u}) - V_0^{\text{tf}}) \delta \lambda^{\text{tf}} \right] = 0, \quad (5.4b)$$

$$\forall \delta \mathbf{u} \in \mathbf{V}, \forall \delta \lambda_n \in \mathcal{M}, \forall \delta \lambda^{\text{tf}} \in \mathbb{R}, \quad (5.4c)$$

where the function spaces \mathbf{V} and \mathcal{M} were introduced in (3.3) and (4.4), while the single Lagrange multiplier for the trapped fluid is simply a scalar, and the notation of the directional derivative was used, see (3.34) and (4.11). Note that terms corresponding to the virtual work of contact tractions and to contact constraints, see (5.4a), have the same form as in Sec. 4.1.1, whilst two additional terms appear in the variation of the coupled Lagrangian, see (5.4b). The first term in (5.4b) is the virtual work of the trapped fluid, cf. (3.35), and the second term enforces the gap constraint $V(\mathbf{u}) = V_0^{\text{tf}}$ in the active state, compare with the analogous equation for the contact constraint $g_n(\mathbf{u}) = 0$, see (4.12b).

Note that only the case of frictionless contact is handled by the Lagrangian (5.3), however, the interface friction can be readily taken into account using the penalty method or the augmented Lagrangian method, as discussed in Sec. 4.1.2 and 4.1.3, respectively. Moreover, the study of the problem of the trapped fluid in a frictional contact interface is presented in Chapter 7 of this dissertation. In particular, Sec. 7.8 provides a detailed analysis of frictional tractions in the contact interface during the process of fluid entrapment and the consequent trap opening.

5.1.2 Compressible fluid models

In order to handle the trapped fluid constraints and model the behaviour of the compressible fluid, instead of the Lagrange multiplier method a generalization of the penalty method can be used (see also the application of the linear penalty method to the contact problem in Sec. 4.1.2).

First, we recall the expression for the virtual work of the trapped fluid pool, introduced in (3.35) as:

$$\delta W^{\text{tf}}(\mathbf{u}) = -p^{\text{tf}} D V(\mathbf{u}) \cdot \delta \mathbf{u}, \quad (5.5)$$

which is added to the balance of virtual work of the coupled problem if the fluid is active, and disregarded otherwise. Furthermore, the trapped fluid pressure p^{tf} can be expressed as a function of the gap volume $V(\mathbf{u})$, and, consequently, as a function of the

displacement \mathbf{u} :

$$p^{\text{tf}}(\mathbf{u}) = p_0^{\text{tf}} + K \left(1 - \frac{V(\mathbf{u})}{V_0^{\text{tf}}} \right), \quad (5.6)$$

if the model of compressible fluid with constant bulk modulus is used, see (2.74). Furthermore, if a fluid with pressure-dependent bulk modulus $K = K_0 + K_1 p^{\text{tf}}$ is considered, see (2.75), the fluid pressure reads:

$$p^{\text{tf}}(\mathbf{u}) = \left(p_0^{\text{tf}} + \frac{K_0}{K_1} \right) \left(\frac{V}{V_0^{\text{tf}}} \right)^{-K_1} - \frac{K_0}{K_1}. \quad (5.7)$$

Therefore, substituting Eq. (5.6) or (5.7) into (5.5) and using the expression for the gap volume (5.1), we compute the contribution of the trapped fluid to the balance of virtual work, necessary for the subsequent formulation of the trapped fluid model in the finite-element framework.

Finally, integrating both sides of Eq. (5.5), we may obtain the expression for the penalty functional representing the “potential energy” of the trapped fluid in the active state. For the fluid with constant bulk modulus it takes the following form (omitting the integration constant):

$$W^{\text{tf}}(\mathbf{u}) = \frac{K}{2 V_0^{\text{tf}}} \left[\left(\frac{p_0^{\text{tf}}}{K} + 1 \right) V_0^{\text{tf}} - V(\mathbf{u}) \right]^2, \quad (5.8)$$

while in case of the fluid with pressure-dependent bulk modulus $K = K_0 + K_1 p^{\text{tf}}$ it reads:

$$W^{\text{tf}}(\mathbf{u}) = - \left(p_0^{\text{tf}} + \frac{K_0}{K_1} \right) \frac{V_0^{\text{tf}}}{(1 - K_1)} \left(\frac{V(\mathbf{u})}{V_0^{\text{tf}}} \right)^{1-K_1} + \frac{K_0}{K_1} V(\mathbf{u}), \quad (5.9)$$

which corresponds to a non-linear penalty method.

5.2 “Super-element” formulation

In this section we will show how the discussed above approaches for modelling the trapped fluid can be implemented in a finite-element framework alongside with structural and contact elements. First, we will propose a “super-element” formulation for a single trapped-fluid element containing all faces (in 3D) or segments (in 2D) of the trapped fluid zone Γ^{tf} , which will be used throughout this dissertation. However, for the sake of completeness, in the next section we discuss also the standard finite-element formulation for the trapped fluid, using contributions from each face of the trapped fluid zone.

In the finite-element framework the volume of the gap (5.1) can be calculated by the following formula:

$$V(\mathbf{U}) = \sum_{k=1}^m \int_{-1}^1 \int_{-1}^1 \sum_{i=1}^{n_k} g_n(\mathbf{u}_{k_i}) N_i(\xi, \eta) (-\mathbf{n}_k \cdot \boldsymbol{\nu}) J d\xi d\eta, \quad (5.10)$$

where the summation with respect to index $k = \overline{1, m}$ is performed over all faces (segments in 2D) of the surface Γ^{tf} , and the summation with respect to $i = \overline{1, n_k}$ is over all nodes of the k -th face. Thus, we denote by $\mathbf{U} = [\mathbf{u}_1, \dots, \mathbf{u}_i, \dots, \mathbf{u}_M]^T, i = \overline{1, M}$ vector of displacements of all M nodes on the surface Γ^{tf} . Next, $g_n(\mathbf{u}_{k_i})$ is the normal gap computed for the i -th node of the k -th face, and $N_i(\xi, \eta)$ is the shape function associated with this node; $\boldsymbol{\xi} = (\xi, \eta)$ are convective coordinates in the *parent* space, and J is the

Jacobian defined in (4.114). Finally, \mathbf{n}_k is the normal to the k -th face, which can be computed as:

$$\mathbf{n}_k = \frac{\frac{\partial \mathbf{x}}{\partial \xi} \times \frac{\partial \mathbf{x}}{\partial \eta}}{\left| \frac{\partial \mathbf{x}}{\partial \xi} \times \frac{\partial \mathbf{x}}{\partial \eta} \right|}, \quad \mathbf{x} = \sum_{i=1}^{n_k} \mathbf{x}_i N_i(\xi, \eta), \quad (5.11)$$

where \mathbf{x}_i are the coordinates of the i -th node. The integral in (5.10) can be computed using the standard Gauss quadrature rule, i.e.:

$$V(\mathbf{U}) = \sum_{k=1}^m \sum_{l=1}^{n_k^{\text{gp}}} \sum_{i=1}^{n_k} g_n(\mathbf{u}_{k_i}) N_i(\boldsymbol{\xi}_l) (-\mathbf{n}_k(\boldsymbol{\xi}_l) \cdot \boldsymbol{\nu}) J(\boldsymbol{\xi}_l) w_l, \quad (5.12)$$

where n_k^{gp} is the number of integration (Gauss) points associated with the k -th face of the surface Γ^{tf} , w_l is the weight coefficient of the l -th Gauss point, $\boldsymbol{\xi}_l$ are its coordinates in the parent space, and $J(\boldsymbol{\xi}_l)$ is the associated Jacobian.

5.2.1 Incompressible fluid

The problem of finding a stationary point of the Lagrangian (5.3) is non-linear, and to solve it numerically we use the Newton-Raphson method, which requires calculation of the residual vector of the trapped-fluid element. Note that the vector of degrees of freedom (DOFs) for the considered element includes displacement DOFs of all M nodes of the surface Γ^{tf} and an additional scalar Lagrange multiplier λ^{tf} , which is equivalent to the trapped fluid pressure: $[\mathbf{u}_1, \dots, \mathbf{u}_i, \dots, \mathbf{u}_M, \lambda^{\text{tf}}]^\top = [\mathbf{U}, \lambda^{\text{tf}}]^\top$. Therefore, the contribution of the trapped-fluid element to the global residual vector, based on the terms outlined in (5.4b), reads:

$$\mathbf{R}^{\text{tf}} = \begin{bmatrix} \lambda^{\text{tf}} \left[\frac{\partial V(\mathbf{U})}{\partial \mathbf{U}} \right] \\ V(\mathbf{U}) - V_0^{\text{tf}} \end{bmatrix}, \quad (5.13)$$

where we used the notation

$$\left[\frac{\partial V}{\partial \mathbf{U}} \right] = \left[\frac{\partial V}{\partial \mathbf{u}_1}, \dots, \frac{\partial V}{\partial \mathbf{u}_i}, \dots, \frac{\partial V}{\partial \mathbf{u}_M} \right]^\top. \quad (5.14)$$

Next, the tangent matrix of the trapped-fluid element reads:

$$\mathbf{K}^{\text{tf}} = \begin{bmatrix} \lambda^{\text{tf}} \left[\frac{\partial^2 V(\mathbf{U})}{\partial \mathbf{U}^2} \right] & \left[\frac{\partial V(\mathbf{U})}{\partial \mathbf{U}} \right] \\ \left[\frac{\partial V(\mathbf{U})}{\partial \mathbf{U}} \right]^\top & 0 \end{bmatrix}, \quad (5.15)$$

where each entry of the matrix of second derivatives takes the form:

$$\left[\frac{\partial^2 V}{\partial \mathbf{U}^2} \right]_{ij} = \frac{\partial^2 V}{\partial \mathbf{u}_i \partial \mathbf{u}_j}, \quad i = \overline{1, M}, \quad j = \overline{1, M}. \quad (5.16)$$

We recall here that the method of Lagrange multipliers transforms a constrained minimization problem into a saddle point problem, which is free of constraints on the primal variables (displacements \mathbf{u}_i), however, the dual variables (scalar Lagrange multipliers) are subject to constraints: $\lambda_n \leq 0$ and $\lambda^{\text{tf}} \geq 0$. Thus, the resolution of the saddle point problem (5.4) requires an “active set” strategy for the trapped fluid, termed here by an analogy with the contact problem, where it was used to enforce constraints on Lagrange multipliers and find the active contact zone, see (4.62). For the trapped fluid

element the required strategy also represents a test performed on every iteration of the Newton-Raphson method to find the state:

$$\begin{cases} \text{if } V(\mathbf{U}) > V^{\text{tf}} \text{ or } \lambda^{\text{tf}} < 0 & \Rightarrow \text{trapped fluid element is inactive,} \\ \text{if } V(\mathbf{U}) \leq V^{\text{tf}} \text{ and } \lambda^{\text{tf}} \geq 0 & \Rightarrow \text{trapped fluid element is active.} \end{cases} \quad (5.17)$$

If the contact element is active, then its residual vector \mathbf{R}^{tf} and tangent matrix \mathbf{K}^{tf} are added to the corresponding entries of the global residual vector and tangent matrix. If the element is inactive, then all associated terms are excluded from global structures, since in this case the balance of virtual work does not have a contribution from the trapped fluid. Furthermore, the Lagrange multiplier associated to this element should be eliminated from the global vector of degrees of freedom. However, the possible variation of the global number of unknowns between iterations is often undesirable, especially in a case of an implicit finite-element code. Alternatively, the global residual vector and tangent matrix can be altered to avoid this change, see [Yastrebov, 2013] for more details.

It is important to note, that the actual expressions of components of the residual vector \mathbf{R}^{tf} and the tangent matrix \mathbf{K}^{tf} will depend on the type of the finite-element formulation used. Indeed, let us consider the derivative of the gap volume (5.10) with respect to the displacement vector \mathbf{u}_i . Under assumptions of small deformations and small rotations, the Jacobian J of each element is considered fixed (to its value in the initial configuration), as well as the normal to each face \mathbf{n}_k . Therefore, since the gap function is linear with respect to the displacement, the second derivative $\partial^2 V / \partial \mathbf{u}_i \partial \mathbf{u}_j = 0$, and corresponding components of the tangent matrix vanish. On the contrary, if large deformations and/or large rotations are taken into account, the Jacobian and/or the normal become functions of the current coordinates and, in general, $\partial^2 V / \partial \mathbf{u}_i \partial \mathbf{u}_j \neq 0$.

5.2.2 Compressible fluid

For the numerical simulations of the compressible trapped fluid using the penalty method, we may consider the same “super-element”, as was described previously for the case of the Lagrange multiplier method, with an alteration: no extra degrees of freedom are involved, and therefore the vector of DOFs has the form $\mathbf{U} = [\mathbf{u}_1, \dots, \mathbf{u}_i, \dots, \mathbf{u}_M]^\top$. Thus, using the expression for the virtual work (5.5), the residual vector and the tangent matrix for the fluid with constant bulk modulus read:

$$\mathbf{R}^{\text{tf}} = -\frac{K}{V_0^{\text{tf}}} (V_0^{\text{tf}} - V(\mathbf{U})) \left[\frac{\partial V(\mathbf{U})}{\partial \mathbf{U}} \right], \quad (5.18)$$

$$\mathbf{K}^{\text{tf}} = \frac{K}{V_0^{\text{tf}}} \left(\left[\frac{\partial V(\mathbf{U})}{\partial \mathbf{U}} \right] \otimes \left[\frac{\partial V(\mathbf{U})}{\partial \mathbf{U}} \right]^\top - (V_0^{\text{tf}} - V(\mathbf{U})) \left[\frac{\partial^2 V(\mathbf{U})}{\partial \mathbf{U}^2} \right] \right), \quad (5.19)$$

where \otimes is the tensor product. In the case of fluid with pressure-dependent bulk modulus $K = K_0 + K_1 p^{\text{tf}}$ those structures are expressed as:

$$\mathbf{R}^{\text{tf}} = -\left\{ \left(\frac{K_0}{K_1} + p_0^{\text{tf}} \right) \left(\frac{V(\mathbf{u})}{V_0^{\text{tf}}} \right)^{-K_1} - \frac{K_0}{K_1} \right\} \left[\frac{\partial V(\mathbf{u})}{\partial \mathbf{u}} \right], \quad (5.20)$$

$$\mathbf{K}^{\text{tf}} = \left(\frac{K_0}{K_1} + p_0^{\text{tf}} \right) \frac{K_1}{V_0^{\text{tf}}} \left(\frac{V(\mathbf{U})}{V_0^{\text{tf}}} \right)^{-K_1-1} \left[\frac{\partial V(\mathbf{U})}{\partial \mathbf{U}} \right] \otimes \left[\frac{\partial V(\mathbf{U})}{\partial \mathbf{U}} \right]^\top$$

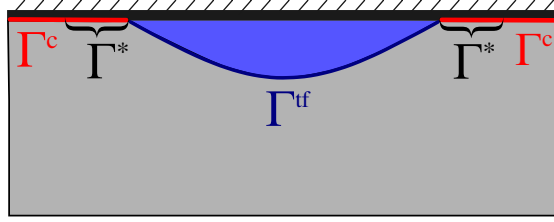


Figure 5.2: Extension of the trapped fluid zone Γ^{tf} on the active contact zone Γ^{c} .

$$- \left\{ \left(\frac{K_0}{K_1} + p_0^{\text{tf}} \right) \left(\frac{V(\mathbf{U})}{V_0^{\text{tf}}} \right)^{-K_1} - \frac{K_0}{K_1} \right\} \left[\frac{\partial^2 V(\mathbf{U})}{\partial \mathbf{U}^2} \right]. \quad (5.21)$$

Since the additional Lagrange multiplier for the trapped fluid is not considered, the “active set” strategy discussed above is not required for the penalty formulation. However, a test to find the state of the trapped fluid element is still needed, e.g. the volume of the gap $V(\mathbf{U})$ is to be compared with the initial volume of the fluid V_0^{tf} . If $V(\mathbf{U}) < V_0^{\text{tf}}$, then the trapped fluid element is active and its residual vector and tangent matrix are to be included into the global structures. If $V(\mathbf{U}) > V_0^{\text{tf}}$, then the element is not active and does not provide any contribution to the balance of the virtual work.

Similarly to the discussed above method of the Lagrange multiplier, the actual expressions of the components of the residual vector and the tangent matrix will depend on the finite-element formulation. In particular, the terms corresponding to the second derivative of the gap volume with respect to the displacement vanish under assumptions of small deformations and small rotations.

5.2.3 Extension of the trapped fluid zone on the active contact zone

Once the trapped fluid becomes pressurized, the active contact zone Γ^{c} and the trapped fluid zone Γ^{tf} are complementary subsets of the potential contact zone Γ : $\Gamma^{\text{tf}} \cap \Gamma^{\text{c}} = \emptyset$ and $\Gamma^{\text{tf}} \cup \Gamma^{\text{c}} = \Gamma$. In accordance with numerical procedures for solving the trapped fluid problem proposed in previous subsections, the trapped fluid zone Γ^{tf} and, consequently, the number of DOFs of the trapped fluid element must be updated on every iteration of the Newton-Raphson method. Thus, the size of the residual vector and the tangent matrix of the trapped fluid element may vary between iterations, which increases the computational complexity.

Below we will show⁴ that the update of the trapped fluid zone between iterations can be avoided, if Γ^{tf} is extended on the active contact zone Γ^{c} , i.e. if the trapped fluid pressure is considered on a surface $\Gamma^{\text{tf}} \cup \Gamma^*$, where $\Gamma^* \subset \Gamma^{\text{c}}$, see Fig. 5.2. Additionally, we need to take into account that on Γ^* the contact pressure will not be equal to the Lagrange multiplier λ_n , but to the difference between λ_n and the value of the trapped fluid pressure: $\sigma_n = \lambda_n - \lambda^{\text{tf}}$ on Γ^* . Note that λ_n , which is equivalent to the normal traction, is negative, while λ^{tf} represent fluid pressure, which is positive by definition.

In order to prove the validity of this extension, we will consider a transformation of the Lagrangian for the coupled system (5.3). We will start by substituting the formula for the gap volume (5.1) into (5.3), assuming that the trapped fluid is in the active state,

⁴We demonstrate it here for the case of Lagrange multipliers method, however, it may be also generalized for the penalty method

so that $\Gamma^{\text{tf}} = \Gamma \setminus \Gamma^c$. Therefore, we obtain:

$$\mathcal{L}(\mathbf{u}, \lambda_n, \lambda^{\text{tf}}) = \Pi(\mathbf{u}) + \int_{\Gamma^c} \lambda_n g_n(\mathbf{u}) d\Gamma - \lambda^{\text{tf}} \left(\int_{\Gamma^{\text{tf}}} g_n(\mathbf{u})(-\mathbf{n} \cdot \boldsymbol{\nu}) d\Gamma - V^{\text{tf}} \right). \quad (5.22)$$

Let us break the integral over the active contact zone Γ^c into two integrals over surfaces $\Gamma^* \subset \Gamma^c$ and $\Gamma^c \setminus \Gamma^*$ and consider the following representation of the Lagrange multiplier λ_n on the surface Γ^* : $\lambda_n = \lambda_n^* - \lambda^{\text{tf}}$, where $\lambda_n^* \leq 0$. Note that this representation is valid only if $|\lambda_n| \geq \lambda^{\text{tf}}$, i.e. the trapped fluid zone can be extended only on the part of the contact zone, where the contact pressure is higher than the trapped fluid pressure. Then we may write:

$$\begin{aligned} \mathcal{L}(\mathbf{u}, \lambda_n, \lambda^{\text{tf}}) &= \Pi(\mathbf{u}) + \int_{\Gamma^c \setminus \Gamma^*} \lambda_n g_n(\mathbf{u}) d\Gamma + \int_{\Gamma^*} (\lambda_n^* - \lambda^{\text{tf}}) g_n(\mathbf{u}) d\Gamma \\ &\quad - \lambda^{\text{tf}} \int_{\Gamma^{\text{tf}}} g_n(\mathbf{u})(-\mathbf{n} \cdot \boldsymbol{\nu}) d\Gamma + \lambda^{\text{tf}} V^{\text{tf}} \\ &= \Pi(\mathbf{u}) + \int_{\Gamma^c \setminus \Gamma^*} \lambda_n g(\mathbf{u}) d\Gamma + \int_{\Gamma^*} \lambda_n^* g_n(\mathbf{u}) d\Gamma - \lambda^{\text{tf}} \int_{\Gamma^*} g_n(\mathbf{u}) d\Gamma \\ &\quad - \lambda^{\text{tf}} \int_{\Gamma^{\text{tf}}} g_n(\mathbf{u})(-\mathbf{n} \cdot \boldsymbol{\nu}) d\Gamma + \lambda^{\text{tf}} V^{\text{tf}}, \end{aligned} \quad (5.23)$$

where we used that λ^{tf} represents a uniform normal traction. Next, we notice that on the surface $\Gamma^* \subset \Gamma^c$ $\mathbf{n} = -\boldsymbol{\nu}$, i.e. $\mathbf{n} \cdot \boldsymbol{\nu} = -1$, which lets us write:

$$\begin{aligned} \mathcal{L}(\mathbf{u}, \lambda_n, \lambda^{\text{tf}}) &= \Pi(\mathbf{u}) + \int_{\Gamma^c \setminus \Gamma^*} \lambda_n g(\mathbf{u}) d\Gamma + \int_{\Gamma^*} \lambda_n^* g_n(\mathbf{u}) d\Gamma \\ &\quad - \lambda^{\text{tf}} \left(\int_{\Gamma^{\text{tf}} \cup \Gamma^*} g_n(\mathbf{u})(-\mathbf{n} \cdot \boldsymbol{\nu}) d\Gamma - V^{\text{tf}} \right). \end{aligned} \quad (5.24)$$

Therefore, the presented transformation of the Lagrangian (5.3) into (5.24) shows that:

- without loss of generality, the trapped fluid zone Γ^{tf} can be extended on the part of the active contact zone Γ^c , where the contact pressure is higher than the trapped fluid pressure: $|\lambda_n| \geq \lambda^{\text{tf}}$ on $\Gamma^* \subseteq \Gamma^c$;
- if the trapped fluid is in the active state, the value of $\lambda_n^* - \lambda^{\text{tf}}$ is equivalent to the normal traction on Γ^* .

5.3 Standard finite-element formulation

Alternatively to the “super”-element formulation, the standard finite-element formulation can be used, according to which the residual vector \mathbf{R}^{tf} and the tangent matrix \mathbf{K}^{tf} are constructed using separate contributions from each face of the trapped fluid zone. Therefore, the matrix \mathbf{K}^{tf} needs not to be stored, and the contributions from each face can be directly included into the global matrix. However, in application to the considered trapped fluid models the standard approach is bound to certain limitations, which will be discussed below.

Indeed, the volume of the gap (5.10) can be computed as sum of volumes V_k corresponding to each single face:

$$V(\mathbf{U}) = \sum_{k=1}^m V_k(\mathbf{U}_k), \quad V_k(\mathbf{U}_k) = \sum_{k=1}^m \int_{-1}^1 \int_{-1}^1 \sum_{i=1}^{n_k} g_n(\mathbf{u}_{k_i}) N_i(\xi, \eta) (-\mathbf{n}_k \cdot \boldsymbol{\nu}) J d\xi d\eta, \quad (5.25)$$

where \mathbf{U}_k is the vector of displacements of the nodes of the k -th face only. Thus, the block $\lambda^{\text{tf}} [\partial^2 V / \partial \mathbf{U}^2]$ of the matrix \mathbf{K}^{tf} , see (5.15), is sparse, and, furthermore, can be constructed by combining separate contributions from each face of the trapped fluid zone, the same is valid for the corresponding entries of the residual vector \mathbf{R}^{tf} (5.13).

However, the stated above is not valid for the model of the compressible fluid. The tangent matrix \mathbf{K}^{tf} for both cases of constant (5.19) and pressure-dependent bulk modulus (5.21) includes the tensor product of the vectors $[\partial V / \partial \mathbf{U}] \otimes [\partial V / \partial \mathbf{U}]^T$ and therefore is not sparse and cannot be constructed using the standard assembly process, combining contribution from each face separately.

Nevertheless, the standard finite-element formulation can be used with the compressible fluid model, if the method of the Lagrange multiplier and the penalty method are used simultaneously. We shall consider the contribution of the fluid to the combined Lagrangian for the coupled problem :

$$W^{\text{tf}} = -\lambda^{\text{tf}} (V(\mathbf{u}) - V^{\text{tf}}), \quad (5.26)$$

where instead of the initial fluid volume V_0^{tf} , we used the current volume of the trapped fluid V^{tf} , which can be expressed as a function of the pressure, both for model of the constant (2.63) and pressure-dependent bulk modulus (2.66). Indeed, in the former case this relation reads:

$$V^{\text{tf}}(p^{\text{tf}}) = V_0^{\text{tf}} \left(1 - \frac{p^{\text{tf}} - p_0^{\text{tf}}}{K} \right), \quad (5.27)$$

and in the latter case:

$$V^{\text{tf}}(p^{\text{tf}}) = V_0^{\text{tf}} \left(\frac{K_0/K_1 + p^{\text{tf}}}{K_0/K_1 + p_0^{\text{tf}}} \right)^{-1/K_1}, \quad (5.28)$$

Finally, substituting p^{tf} by λ^{tf} in Eq. (5.27) or (5.28), we may express the variation of the term W^{tf} as:

$$\delta W^{\text{tf}} = - \left[\lambda^{\text{tf}} \frac{\partial V(\mathbf{u})}{\partial \mathbf{u}} \cdot \delta \mathbf{u} + (V(\mathbf{u}) - V_0^{\text{tf}}) \delta \lambda^{\text{tf}} - \lambda^{\text{tf}} \frac{\partial V^{\text{tf}}(\lambda^{\text{tf}})}{\partial \lambda^{\text{tf}}} \delta \lambda^{\text{tf}} \right]. \quad (5.29)$$

However, it is important to note that if a problem under consideration involves multiple trapped fluid zones, then an additional Lagrange multiplier needs to be considered for each one of them. However, the number and the extent of trapped fluid zones, can vary not only between load steps, but also between iterations of the Newton-Raphson method. The associated inevitable change of the size of the global DOF vector, and consequently, the global matrix, is undesirable, particularly for an implicit finite-element code, and moreover, can make the algorithm for tracking trapped fluid zones (discussed in Chapter 6) more complex. Therefore, in this dissertation we followed the proposed approach of the ‘‘super-element’’ for each trapped fluid zone, which does not require, at least for the model of the compressible fluid, Lagrange multipliers, i.e. additional DOFs. Nevertheless, it is important to bear in mind that in this case the tangent matrix of the trapped fluid element is not sparse, which could increase considerably the storage space

required for the construction of the global matrix. Apart from that, the non-sparse matrix associated with the proposed “super-element” formulation could have an increasing effect on the bandwidth of the global tangent matrix.

Chapter 6

Monolithic resolution of the coupled problem

Résumé de Chapitre 6 “Résolution monolithique du problème couplé”

Nous concluons la Partie II de cette thèse par la résolution numérique du problème couplé, tel que formulé sous la forme forte dans le chapitre 2 et la forme faible dans le chapitre 3. Le traitement des contraintes associées au contact mécanique et au fluide piégé présentées dans les chapitres 4 et 5 est utilisé ici. De plus, nous discutons de la mise en œuvre par éléments finis du sous-problème d'écoulement fluide mince et fournissons la formulation numérique pour l'équilibre des tractions sur l'interface fluide-structure. Enfin, nous proposons une discussion sur l'algorithme utilisé pour distinguer les zones de contact, les canaux d'écoulement de fluide et les zones de fluide piégées, nous présentons aussi la structure du système d'équations linéarisées obtenues par la méthode des éléments finis.

We complete the Part II of this dissertation discussing an approach to the numerical resolution of the coupled problem, formulated in the strong form in Chapter 2 and in the weak form in Chapter 3. This is the problem of a thin fluid flow in a contact interface between a deformable solid and a rigid flat. Furthermore, we take into account fluid tractions acting on the surface of the solid and the effect of trapped fluid pools on the contact problem. Note that the handling of constraints associated with the mechanical contact and the trapped fluid was discussed in Chapters 4 and 5, and will be also used below. In the present Chapter, we address first the thin fluid flow sub-problem and then provide the numerical formulation of the virtual work of the fluid-induced tractions on the surface of the solid. Finally, we discuss in detail the algorithm used to distinguish between fluid-flow channels and trapped fluid zones, which is essential for resolution of this coupled problem, and outline the structure of the linearised system of equations obtained using the finite-element method.

Note that in order to simplify our discussion and concentrate it on the two-way coupling aspects, we use the small deformations formulation. Furthermore, we assume small rotations, which is justified (at least partially) by the requirement of small slopes of the roughness profile for the validity of the Reynolds equation in certain applications, see Section 2.3.3 and discussions in [Brown et al., 1995]. Nevertheless, the necessary modifications to take into account large deformations and/or large rotations could be added into the presented framework.

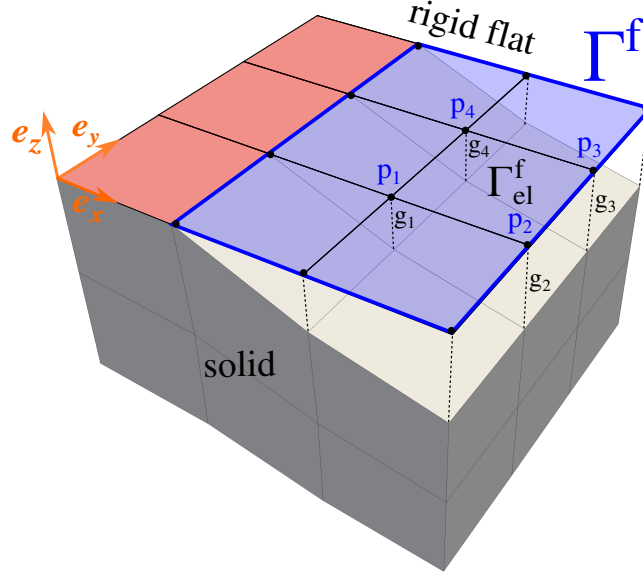


Figure 6.1: Sketch of the interface highlighting fluid flow elements: Γ^f is the lubrication surface (plane $z = 0$), where the Reynolds equation is defined, Γ_{el}^f is a face on this surface associated to one fluid flow element, p is the fluid pressure DOF, added to each node of the surface of the solid (note that the constant fluid pressure across film thickness is assumed).

6.1 Thin fluid flow sub-problem

We start by recalling that the thin isoviscous incompressible Newtonian fluid flow is governed by the Reynolds equation (2.70a) defined on the lubrication surface Γ^f , which is considered here as the projection of the fluid-structure interface Γ^{fsi} (attached to the surface of the solid) on the rigid flat $z = 0$, see Fig. 6.1. Note that $\Gamma^{fsi} \subset \Gamma$, termed as the potential contact zone, which defines the extent of the interface.

For convenience, we reproduce here the weak form of the fluid flow problem (2.70) (see Section 3.2.3 for more details):

$$\int_{\Gamma^f} \frac{g_n(\mathbf{u})^3}{12\eta} \nabla p \cdot \nabla \delta p \, d\Gamma + \int_{\gamma^q} q_0 \delta p \, d\gamma = 0, \quad \forall \delta p \in \mathcal{P}, \quad (6.1)$$

where $p(x, y)$ is the fluid pressure field defined on the lubrication surface Γ^f , q_0 is the prescribed fluid flux on $\gamma^q \subset \partial\Gamma^f$, and the function space \mathcal{P} was introduced in (3.37). In order to concentrate the reader's attention on the aspects of the coupling, we will assume here $q_0 = 0$, however, a non-trivial Neumann boundary condition could be included in the present formulation in the standard manner. Furthermore, for each point $(x, y) \in \Gamma^f$ the thickness of the film is computed as the normal gap $g_n(\mathbf{u})$ of the corresponding point $(x, y, z) \in \Gamma^{fsi}$. For brevity, we will omit below the subscript “ n ” of the normal gap g_n .

To include the weak form (6.1) into the finite-element framework for the solid mechanics problem, we attribute fluid pressure DOF to each node of the surface Γ , which is not contradictory to the fact that the Reynolds equation is formulated on the projection Γ^f of this surface on the rigid flat, since a constant fluid pressure along film thickness is assumed. Then, similarly to the face-to-rigid-surface approach for the contact problem (Section 4.3), we associate a fluid-flow element with each face of the discretised surface Γ^f , formed by faces of Γ^{fsi} projected on the rigid flat, see Fig. 6.1. We use the same interpolation for the normal gap, as in (4.105), while for the fluid pressure p and the

“test” function δp we also have:

$$p = \sum_{i=1}^n N_i p_i, \quad \delta p = \sum_{i=1}^n N_i \delta p_i, \quad (6.2)$$

where n is the number of nodes which belong to the element. Substituting (4.105) and (6.2) into (6.1) we obtain the following contribution of one fluid-flow element to the balance of virtual work:

$$\delta W_{\text{el}}^{\text{f}} = \sum_{i=1}^n \delta p_i \int_{-1}^1 \int_{-1}^1 \left(\sum_{k=1}^n N_k g_k \right)^3 \left(\mathbf{J}^{-1} \sum_{j=1}^n \nabla N_j p_j \right) \left(\mathbf{J}^{-1} \nabla N_i \right) \det(\mathbf{J}) d\xi d\eta, \quad (6.3)$$

where (ξ, η) are coordinates in the parent space, \mathbf{J} is the Jacobian matrix defined as:

$$\mathbf{J} = \begin{bmatrix} \frac{\partial x}{\partial \xi} & \frac{\partial x}{\partial \eta} \\ \frac{\partial y}{\partial \xi} & \frac{\partial y}{\partial \eta} \end{bmatrix} \quad (6.4)$$

and $\det(\mathbf{J})$ is its determinant. The Newton-Raphson method, used for resolution of the essentially nonlinear coupled problem, requires computation of the second variation of the virtual work. For the fluid-flow element it reads:

$$\begin{aligned} \Delta \delta W_{\text{el}}^{\text{f}} = & \sum_{i=1}^n \delta p_i \left\{ \sum_{j=1}^n \Delta p_j \int_{-1}^1 \int_{-1}^1 \left(\sum_{k=1}^n N_k g_k \right)^3 \left(\mathbf{J}^{-1} \nabla N_j \right) \left(\mathbf{J}^{-1} \nabla N_i \right) \det(\mathbf{J}) d\xi d\eta \right. \\ & \left. + \sum_{l=1}^n \frac{\partial g_l}{\partial \mathbf{u}_l} \Delta \mathbf{u}_l \int_{-1}^1 \int_{-1}^1 3 \left(\sum_{k=1}^n N_k g_k \right)^2 N_l \left(\mathbf{J}^{-1} \sum_{j=1}^n \nabla N_j p_j \right) \left(\mathbf{J}^{-1} \nabla N_i \right) \det(\mathbf{J}) d\xi d\eta \right\}. \end{aligned} \quad (6.5)$$

Note that due to the small deformations assumption components of the Jacobian matrix are considered fixed to their values in the initial configuration. Introducing the residual vector \mathbf{R}^{f} and the tangent matrix \mathbf{K}^{f} of a fluid flow element allows us to rewrite (6.3) and (6.5) in a more compact form:

$$\delta W_{\text{el}}^{\text{f}} = \begin{bmatrix} \mathbf{R}_p^{\text{f}} \\ 0 \end{bmatrix}^{\text{T}} \begin{bmatrix} \delta p \\ \delta \mathbf{u} \end{bmatrix}, \quad \Delta \delta W_{\text{el}}^{\text{f}} = \begin{bmatrix} \Delta p \\ \Delta \mathbf{u} \end{bmatrix}^{\text{T}} \begin{bmatrix} \mathbf{K}_{pp}^{\text{f}} & 0 \\ \mathbf{K}_{\mathbf{u}p}^{\text{f}} & 0 \end{bmatrix} \begin{bmatrix} \delta p \\ \delta \mathbf{u} \end{bmatrix}, \quad (6.6)$$

with $\delta p = [\delta p_1, \dots, \delta p_n]^{\text{T}}$ and similarly $\Delta p = [\Delta p_1, \dots, \Delta p_n]^{\text{T}}$. The non-zero components of \mathbf{R}^{f} and \mathbf{K}^{f} are explicitly given as follows:

$$\mathbf{R}_p^{\text{f}} = \left[\mathbf{R}_{p_1}^{\text{f}}, \dots, \mathbf{R}_{p_n}^{\text{f}} \right]^{\text{T}}, \quad (6.7a)$$

$$\mathbf{R}_{p_i}^{\text{f}} = \int_{-1}^1 \int_{-1}^1 \left(\sum_{k=1}^n N_k g_k \right)^3 \left(\mathbf{J}^{-1} \sum_{j=1}^n \nabla N_j p_j \right) \left(\mathbf{J}^{-1} \nabla N_i \right) \det(\mathbf{J}) d\xi d\eta, \quad (6.7b)$$

$$\mathbf{K}_{p_i p_j}^{\text{f}} = \int_{-1}^1 \int_{-1}^1 \left(\sum_{k=1}^n N_k g_k \right)^3 \left(\mathbf{J}^{-1} \nabla N_i \right) \left(\mathbf{J}^{-1} \nabla N_j \right) \det(\mathbf{J}) d\xi d\eta, \quad (6.7c)$$

$$\mathbf{K}_{\mathbf{u}_l p_i}^{\text{f}} = \frac{\partial g_l}{\partial \mathbf{u}_l} \int_{-1}^1 \int_{-1}^1 3 \left(\sum_{k=1}^n N_k g_k \right)^2 N_l \left(\mathbf{J}^{-1} \sum_{j=1}^n \nabla N_j p_j \right) \left(\mathbf{J}^{-1} \nabla N_i \right) \det(\mathbf{J}) d\xi d\eta. \quad (6.7d)$$

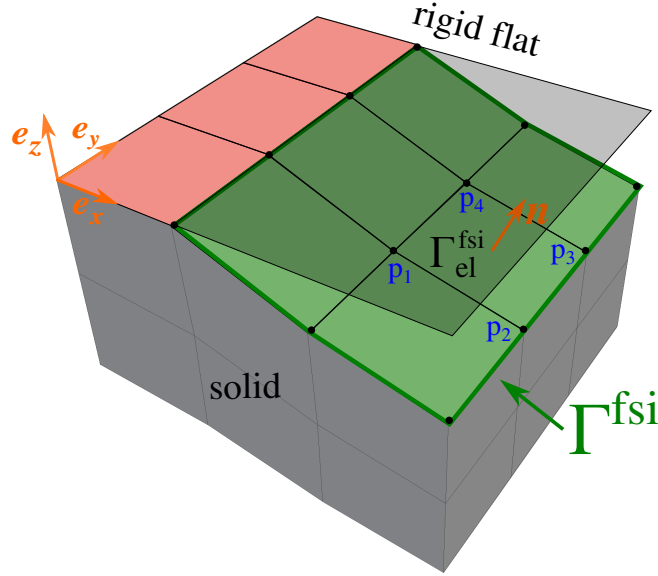


Figure 6.2: Sketch of the interface highlighting FSI elements: Γ^{fsi} is fluid-structure interface on the surface of the solid, $\Gamma_{\text{el}}^{\text{fsi}}$ is a face associated to one FSI element, p is the fluid pressure at each node of this surface and \mathbf{n} is the outer normal.

with $i, j, k, l = \overline{1, n}$. Note the presented formulation of the fluid-flow element was derived for the two-way coupled problem, however, it is also suitable for the one-way coupling. The only required modification to be done to switch to the one way coupling would be to assume rigid walls of the solid, according to which the variation of the virtual work with respect to the displacement in (6.5) vanishes and consequently $\mathbf{K}_{\mathbf{u}p}^{\text{f}} = 0$.

6.2 Balance of tractions on the fluid-structure interface

In order to take into account tractions (2.71) induced by the fluid on the surface Γ^{fsi} of the solid, we consider the virtual work of the surface traction \mathbf{t} acting on the fluid-structure interface (see Section 3.2.1 for more details):

$$\delta W^{\text{fsi}} = \int_{\Gamma^{\text{fsi}}} \left(-p\mathbf{n} - \frac{g_n}{2} \nabla p \right) \cdot \delta \mathbf{u} \, d\Gamma. \quad (6.8)$$

Note that below, for brevity, we will omit the subscript “ n ” of the normal gap g_n .

Subsequently, we associate each fluid-structure interface element with a face of the surface Γ^{fsi} (see Fig. 6.2) and use the same interpolation of the fluid pressure and the gap, as in (6.2) and (4.105), respectively, while for the virtual displacement we also write:

$$\delta \mathbf{u} = \sum_{i=1}^n N_i \delta \mathbf{u}_i. \quad (6.9)$$

Therefore, the contribution of one fluid-structure interface element to the balance of virtual work reads:

$$\delta W_{\text{el}}^{\text{fsi}} = \sum_{i=1}^n \delta \mathbf{u}_i \left\{ \sum_{j=1}^n p_j \int_{-1}^1 \int_{-1}^1 \mathbf{n} N_i N_j J \, d\xi d\eta \right.$$

$$+ \frac{1}{2} \sum_{k=1}^n g_k \int_{-1}^1 \int_{-1}^1 \left(\mathbf{J}^{-1} \sum_{l=1}^n \nabla N_l p_l \right) N_i N_k J d\xi d\eta \Big\}, \quad (6.10)$$

where the gradients of the shape functions ∇N_l are computed on the projection of the face Γ^{fsi} on the rigid flat, i.e. in the same sense as in Section 6.1. The corresponding Jacobian matrix \mathbf{J} was defined in (6.4), and the normal \mathbf{n} is given by:

$$\mathbf{n} = \frac{\frac{\partial \mathbf{x}}{\partial \xi} \times \frac{\partial \mathbf{x}}{\partial \eta}}{\left| \frac{\partial \mathbf{x}}{\partial \xi} \times \frac{\partial \mathbf{x}}{\partial \eta} \right|}, \quad \mathbf{x} = \sum_{i=1}^n \mathbf{x}_i N_i. \quad (6.11)$$

Note that here J is not $\det(\mathbf{J})$, i.e. the determinant of the Jacobian matrix (6.4), but is computed as in (4.114). The second variation then takes the following form:

$$\begin{aligned} \Delta \delta W_{\text{el}}^{\text{fsi}} = & \sum_{i=1}^n \delta \mathbf{u}_i \left\{ \sum_{j=1}^n \Delta p_j \int_{-1}^1 \int_{-1}^1 \mathbf{n} N_i N_j J d\xi d\eta \right. \\ & + \frac{1}{2} \sum_{k=1}^n \frac{\partial g_k}{\partial \mathbf{u}_k} \Delta \mathbf{u}_k \int_{-1}^1 \int_{-1}^1 \left(\mathbf{J}^{-1} \sum_{l=1}^n \nabla N_l p_l \right) N_i N_k J d\xi d\eta \\ & \left. + \frac{1}{2} \sum_{k=1}^n g_k \sum_{l=1}^n \Delta p_l \int_{-1}^1 \int_{-1}^1 \left(\mathbf{J}^{-1} \nabla N_l \right) N_i N_k J d\xi d\eta \right\}, \quad (6.12) \end{aligned}$$

where variations of the Jacobian J and the normal vector \mathbf{n} are not considered due to assumptions of small deformations and small rotations. Finally, the associated virtual work and its variation could be expressed in a compact form using the residual vector \mathbf{R}^{fsi} and the tangent matrix \mathbf{K}^{fsi} of a FSI element:

$$\delta W_{\text{el}}^{\text{fsi}} = \begin{bmatrix} \mathbf{R}_{\mathbf{u}}^{\text{fsi}} \\ 0 \end{bmatrix}^T \begin{bmatrix} \delta \mathbf{u} \\ \delta p \end{bmatrix}, \quad \Delta \delta W_{\text{el}}^{\text{fsi}} = \begin{bmatrix} \Delta \mathbf{u} \\ \Delta p \end{bmatrix}^T \begin{bmatrix} \mathbf{K}_{\mathbf{uu}}^{\text{fsi}} & 0 \\ \mathbf{K}_{p\mathbf{u}}^{\text{fsi}} & 0 \end{bmatrix} \begin{bmatrix} \delta \mathbf{u} \\ \delta p \end{bmatrix}. \quad (6.13)$$

Finally, we outline the non-zero components of the residual vector and the tangent matrix:

$$\mathbf{R}_{\mathbf{u}_i}^{\text{fsi}} = \sum_{j=1}^n p_j \int_{-1}^1 \int_{-1}^1 \mathbf{n} N_i N_j J d\xi d\eta + \sum_{k=1}^n \frac{g_k}{2} \int_{-1}^1 \int_{-1}^1 \left(\mathbf{J}^{-1} \sum_{l=1}^n \nabla N_l p_l \right) N_i N_k J d\xi d\eta, \quad (6.14a)$$

$$\mathbf{K}_{\mathbf{u}_k \mathbf{u}_i}^{\text{fsi}} = \frac{1}{2} \frac{\partial g_k}{\partial \mathbf{u}_k} \int_{-1}^1 \int_{-1}^1 \left(\mathbf{J}^{-1} \sum_{l=1}^n \nabla N_l p_l \right) N_i N_k J d\xi d\eta, \quad (6.14b)$$

$$\mathbf{K}_{p_l \mathbf{u}_i}^{\text{fsi}} = \sum_{k=1}^n \frac{g_k}{2} \int_{-1}^1 \int_{-1}^1 \left(\mathbf{J}^{-1} \nabla N_l \right) N_i N_k J d\xi d\eta. \quad (6.14c)$$

with $i, j, k, l = \overline{1, n}$. Note that in case of one-way coupling the action of the fluid pressure on the surface of the solid is neglected, so that the virtual work (6.8) vanishes completely and no contribution of the FSI element is included into the global matrix, i.e. $\mathbf{R}_{\mathbf{u}}^{\text{fsi}} = 0$, $\mathbf{K}_{\mathbf{uu}}^{\text{fsi}} = \mathbf{K}_{p\mathbf{u}}^{\text{fsi}} = 0$.

6.3 The global residual vector and tangent matrix for the coupled problem

In the spirit of the monolithic approach, in addition to three displacement degrees of freedom an extra DOF for fluid pressure p is attributed to each node of the surface Γ . As will be discussed in the following, p is set to zero if associated to a node that does not belong to the fluid domain, which permits us avoid reinitialization of DOFs after each iteration of the Newton-Raphson method and keep the number of unknowns constant during all solution process. Furthermore, we add to each node of the potential contact zone Γ a Lagrange multiplier λ , which represents the contact pressure, resulting from utilization of the augmented Lagrangian method to satisfy contact constraints in the framework of the face-to-rigid-surface contact discretization approach. Utilization of this method permits us to keep Lagrange multipliers in the non-contact zones, and, similarly to discussed above pressure DOFs, preserve the constant number of unknowns of the problem.

In the previous sections we discussed contribution of all sub-problems to the balance of virtual works and formulation of the residual vectors and tangent matrices. Subsequently, following the monolithic approach, we combine them together, outlining the general structure of the global tangent matrix and residual vector, constructed on each iteration of the Newton-Raphson method. We will denote by $\mathbf{v} = [\mathbf{u}; \lambda, p]^T$ the global vector of the nodal degrees of freedom, consisting of displacement components, Lagrange multipliers for the contact problem and fluid pressure for the fluid flow problem. Note that the trapped fluid elements do not require any additional degrees of freedom, if the non-linear penalty method is used, which corresponds to the model of a compressible fluid with pressure-dependent bulk modulus, see Section 5.2.2. By $\Delta \mathbf{v} = [\Delta \mathbf{u}; \Delta \lambda, \Delta p]^T$ we shall denote here the increment of the DOF vector, corresponding to one iteration. Moreover, according to the quasi-static analysis approach, the solution is obtained in a certain number of load steps, and for each one of them the Newton-Raphson method is invoked. The global linearised system of equations for the coupled problem takes the following form:

$$\begin{bmatrix} \mathbf{K}_{\mathbf{uu}}^* & \mathbf{K}_{\mathbf{u}\lambda}^c & \mathbf{K}_{\mathbf{u}p}^f \\ \mathbf{K}_{\lambda\mathbf{u}}^c & \mathbf{K}_{\lambda\lambda}^c & 0 \\ \mathbf{K}_{p\mathbf{u}}^{\text{fsi}} & 0 & \mathbf{K}_{pp}^f \end{bmatrix} \begin{bmatrix} \Delta \mathbf{u} \\ \Delta \lambda \\ \Delta p \end{bmatrix} = \begin{bmatrix} \mathbf{R}_{\mathbf{u}}^* \\ \mathbf{R}_{\lambda}^c \\ \mathbf{R}_p^f \end{bmatrix}, \quad (6.15)$$

where the matrix $\mathbf{K}_{\mathbf{uu}}^*$ and vector $\mathbf{R}_{\mathbf{u}}^*$ are assembled using corresponding entities of all aforementioned sub-problems, introduced in (4.118), (5.20)-(5.21), (6.6) and (6.13):

$$\mathbf{K}_{\mathbf{uu}}^* = \mathbf{K}_{\mathbf{uu}}^s + \mathbf{K}_{\mathbf{uu}}^c + \mathbf{K}_{\mathbf{uu}}^{\text{fsi}} + \mathbf{K}_{\mathbf{uu}}^{\text{tf}}, \quad \mathbf{R}_{\mathbf{u}}^* = \mathbf{R}_{\mathbf{u}}^s + \mathbf{R}_{\mathbf{u}}^c + \mathbf{R}_{\mathbf{u}}^{\text{fsi}} + \mathbf{R}_{\mathbf{u}}^{\text{tf}}. \quad (6.16)$$

Note that $\mathbf{R}_{\mathbf{u}}^s$ and $\mathbf{K}_{\mathbf{uu}}^s$ are the residual vector and tangent matrix of the solid mechanics problem in absence of contact constraints and fluid flow, computed in a standard way:

$$\mathbf{R}_{\mathbf{u}}^s = \frac{\partial \Pi^s(\mathbf{u})}{\partial \mathbf{u}}, \quad \mathbf{K}_{\mathbf{uu}}^s = \frac{\partial^2 \Pi^s(\mathbf{u})}{\partial \mathbf{u}^2}, \quad (6.17)$$

where we do not introduce any limitations on the constitutive law for the solid.

Note that $\mathbf{R}_{\mathbf{u}}^{\text{tf}}$ and $\mathbf{K}_{\mathbf{uu}}^{\text{tf}}$ represent here the assembly of residual vectors $\mathbf{R}_{\mathbf{u}}^{\text{tf}i}$ and tangent matrices $\mathbf{K}_{\mathbf{uu}}^{\text{tf}i}$, $i = 1, \dots, n_{\text{tf}}$, respectively, where n_{tf} is total number trapped fluid elements considered at the current iteration. Note also that these terms of the global tangent matrix may be omitted, which gives the possibility to perform simulation of the two-way coupling neglecting the presence of trapped fluid and considering only

the effect of fluid pressure in the flow on the deformation of the solid.

It is important to note that in case of two-way coupling the global matrix defined in (6.15) is not symmetric, since non-diagonal block terms $\mathbf{K}_{\mathbf{u}p}^f$ and $\mathbf{K}_{p\mathbf{u}}^{\text{fsi}}$ are obtained upon discretization of different equations (see Sections 6.1 and 6.2, respectively) and therefore are not equal in the general case. However, if the one-way coupling is considered, as was discussed above, these terms vanish, rendering the global tangent matrix symmetric. This permits to decrease significantly the memory required for storage of the matrix, which is essential for the problems involving a significantly fine discretization of the contact interface.

The convergence of the standard Newton-Raphson method is obtained if the value of a norm of the global residual vector falls below a prescribed tolerance. However, for the coupled problem under study in order to ensure the balance between different fields, we consider separately the norms of the subsets of the residual vector corresponding to different types of DOFs: $\mathbf{R}_{\mathbf{u}}^*$, \mathbf{R}_{λ}^c , \mathbf{R}_p^f . The convergence is obtained if all of the following conditions are simultaneously fulfilled:

$$\frac{\|\mathbf{R}_{\mathbf{u}}^*\|_2}{\|\mathbf{R}_{\mathbf{u}}^{\text{ext}}\|_2} < \epsilon_u, \quad \|\mathbf{R}_{\lambda}^c\|_{\infty} < \epsilon_{\lambda}, \quad \|\mathbf{R}_p^f\|_{\infty} < \epsilon_p \quad (6.18)$$

where $\epsilon_u, \epsilon_{\lambda}, \epsilon_p$ are the error tolerance thresholds, chosen separately for each type of the DOF. Note that for the displacements residual $\mathbf{R}_{\mathbf{u}}^*$ we consider the *relative* error, $\mathbf{R}_{\mathbf{u}}^{\text{ext}}$ being the nodal vector related to the external loads, see, for example, [Wriggers, 2008], while for the other two residuals we use the *absolute* error criterion. The following notations are used for two different definitions of a norm of a vector \mathbf{R} :

$$\|\mathbf{R}\|_2 = \sqrt{\sum_{i=1}^N R_i^2}, \quad \|\mathbf{R}\|_{\infty} = \max_{i=1\dots N} |R_i|, \quad (6.19)$$

where N is the length of this vector.

6.4 Resolution algorithm

Finally, the identification of the local status of the interface remains necessary. During the initialisation of the problem we construct a graph of the interface, vertices of which represent faces of the surface Γ . We consider the so-called “4-connected” (von Neumann) neighbourhood, according to which two faces are connected in this graph if they share an edge, see Fig. 6.3.

At every iteration of the Newton-Raphson method we perform following additional steps, summarized in Algorithm 2, which can be easily adjusted to one-way and two-way coupling approaches. We start by identifying active contact elements using the criterion presented in Sec. 4.3, see Fig. 6.3(a). Next, in order to locate the fluid-flow domain governed by the Reynolds equation, we perform the connected-component labelling of non-contact faces using the depth-first search (DFS) [Shapiro, 1996], see Fig. 6.3(b) and Algorithm 3. Note that this recursive procedure is started first from non-contact faces adjacent to the inlet side, and then repeated from those adjacent to the outlet side, in order to find all faces connected to the inlet and/or to the outlet. Once the domain for the flowing fluid is determined, we continue the connected-component labelling of remaining non-contact faces to identify separately each trapped fluid zone, the corresponding procedure is summarized in Algorithm 4, see also Fig. 6.3(c).

Since the behaviour of each trapped fluid pool depends on the volume of this pool at the moment of its formation, and also on the corresponding average pressure of the fluid inside (see Sec. 5.1), a modification of the standard connected-component

Algorithm 2 Resolution procedure for the coupled problem

Require: $v^i, i = 0$

```

1: procedure NEWTONRAPHSONLOOP()
2:   repeat
3:     for all faces of  $\Gamma$  do
4:       if corresponding contact element is active then
5:         face's label  $\leftarrow$  CONTACT
6:       else
7:         face's label  $\leftarrow$  NONE
8:       end if
9:     end for
10:    for all faces with nodes from inlet or outlet do //Dirichlet B.C.
11:      DEPTHFIRSTSEARCH(face, FLOW)
12:    end for
13:    for all faces of  $\Gamma$  do
14:      Construct  $\mathbf{R}^c$  and  $\mathbf{K}^c$  for corresponding contact element
15:      //ALM permits to have contact elements in non-active zone
16:      if face's label = FLOW then
17:        Construct  $\mathbf{R}^f$  and  $\mathbf{K}^f$  for corresponding fluid-flow element
18:        if two-way coupling then
19:          Construct  $\mathbf{R}^{\text{fsi}}$  and  $\mathbf{K}^{\text{fsi}}$  for corresponding FSI element
20:        end if
21:      end if
22:      if two-way coupling then
23:        IDENTIFYTRAPPEDZONES()
24:        for all trapped fluid elements do
25:          Construct  $\mathbf{R}^{\text{tf}}$  and  $\mathbf{K}^{\text{tf}}$  for trapped-fluid element
26:        end for
27:      end if
28:       $\Delta \mathbf{v}^i \leftarrow - [\mathbf{K}^i(\mathbf{v}^i)]^{-1} \cdot [\mathbf{R}^i(\mathbf{v}^i)]$ 
29:       $\mathbf{v}^{i+1} \leftarrow \mathbf{v}^i + \Delta \mathbf{v}^i$ 
30:       $i \leftarrow i + 1$ 
31:    until (6.18) is validated
32: end procedure

```

Algorithm 3 Depth-first search (DFS)

```

1: procedure DEPTHFIRSTSEARCH(face, LABEL)
2:   if face's label = NONE then
3:     face's label  $\leftarrow$  LABEL
4:     for all neighbours of face do
5:       DEPTHFIRSTSEARCH(neighbour, LABEL)
6:     end for
7:   end if
8: end procedure

```

Algorithm 4 Trapped fluid zones identification procedure

```

1: procedure IDENTIFYTRAPPEDZONES()
2:   for all trapped fluid elements do //the same list is used for all load steps
3:     if element did not exist at the previous converged load step then
4:       delete trapped fluid element
5:     else
6:       empty element's list of faces
7:     end if
8:   end for
9:   for all faces do
10:    if face's label = NONE then
11:      if face's label at the previous converged load step = TRAP% then
12:        id ← corresponding trapped fluid element's id
13:        DEPTHFIRSTSEARCH(face, TRAP+id) //TRAP1, TRAP2, ...
14:      else
15:        Create new trapped fluid element
16:        id ← new number of trapped fluid elements
17:        DEPTHFIRSTSEARCH(face, TRAP+id) //TRAP1, TRAP2, ...
18:      end if
19:    end if
20:  end for
21:  for all faces do
22:    if face's label = TRAP% then //“%” meaning any number
23:      append face to corresponding element's list of faces
24:    end if
25:  end for
26:  for all trapped fluid elements do
27:    if element did not exist at the previous converged load step then
28:      Compute mean fluid pressure from the previous converged load step
29:      //the initial pressure is the average fluid pressure over all faces of this element
30:    end if
31:  end for
32: end procedure

```

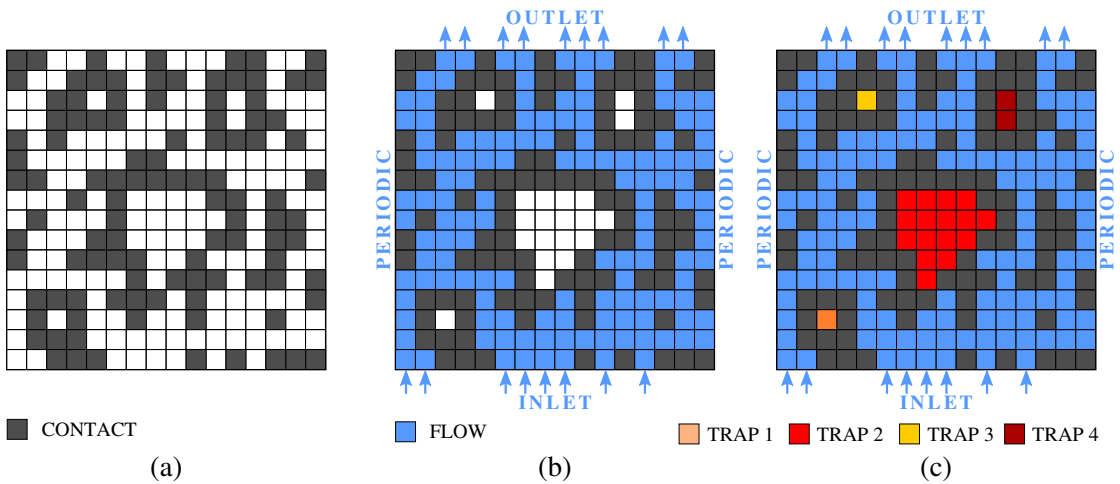


Figure 6.3: Identification of active contact (a), fluid-flow (b) and trapped fluid zones (c) by performing the connected-component labelling of the interface graph based on the 4-connected neighbourhood: two faces are connected if they share an edge.

labelling algorithm is necessary to track creation and evolution of trapped fluid zones. In particular, for each observed trapped fluid pool two cases are possible: some (or all) faces of this zone could have belonged to a trapped fluid zone identified at the end of the previous (converged) loading step, or the considered zone could correspond to a newly trapped fluid pool formed at the current loading step. In the former case, the trapped fluid zone inherits the data (the initial volume and the fluid pressure) from the zone identified at the previous load step. In the latter case, the current volume of a newly created pool is stored and the initial pressure is computed as the mean of the fluid flow pressure values calculated at the end of the previous load step. Note that our study presented in Sec. 8.2 shows that the fluid flow pressure in a zone which would become trapped at the following load step is close to being uniform.

It is important to note, that in a simulation with an increasing external load, the splitting of a trapped fluid pool into multiple zones is possible, which will not be recognised by the presented algorithm, i.e. these multiple pools will still be treated as one volume of trapped fluid. However, the effect of this difference on the transmissivity of rough contact interfaces studied in Chapter 9, based on the observed results, is not expected to be significant. The opposite process, i.e. the merging of multiple trapped fluid zones into one is also not covered by the presented algorithm. However, this process would require elimination of the contact area between separate pools, while the study of the trapped fluid problem presented in Chapter 7 shows that a considerable reduction of the contact area corresponds to a significantly higher external load than the one needed for the complete sealing of the interface (until which we perform our simulations). It should be also noted that the presented algorithm is not suited for tracking trapped fluid zones in the unloading process. Nevertheless, all aforementioned special cases can be included into the presented framework without considerable difficulties.

Finally, at each iteration we compute the number of local status changes with respect to the previous iteration (or previous converged load step in case of the first iteration). At the i -th iteration this value is calculated as:

$$S^i = \sum_{j=1}^m \begin{cases} 1, & s_j^i \neq s_j^{i-1} \\ 0, & s_j^i = s_j^{i-1}, \end{cases} \quad (6.20)$$

where m is the total number of faces of the surface Γ , s_j^i is the label of the j -th face of the surface Γ , corresponding to the i -th iteration, and, accordingly, s_j^{i-1} is the label of the same face at the previous iteration (or previous converged load step, if $i = 1$). The label, according to the Algorithm 2, is from the list {CONTACT, FLOW, TRAP%}. At the post-processing stage this number of local status changes permits to study the convergence of the Newton-Raphson method and verify the proposed resolution procedure.

Part III

Results and discussions

Chapter 7

Trapped fluid in contact interface

Résumé de Chapitre 7 “Fluide piégé dans l’interface de contact”

Dans ce chapitre, nous étudions le contact mécanique entre un corps déformable présentant une surface ondulée et une surface plane rigide, en tenant compte du fluide piégé dans l’interface. À l’aide du modèle éléments finis formulé dans les chapitres 4 et 5, nous étudions l’évolution de la surface de contact réelle, de la traction maximale de frottement et du coefficient de frottement global sous une charge externe croissante. Des modèles de matériaux élastiques et élasto-plastiques, de fluides compressibles et incompressibles et différentes caractéristiques géométriques de la surface ondulée sont considérés. Nous montrons que dans le cas des fluides incompressibles, la surface de contact réelle et le coefficient de frottement global diminuent de manière monotone avec l’augmentation de la pression externe. Une formule analytique de la pression critique d’ouverture du piège s’est révélée indépendante de la pente de la surface lorsque cette dernière est petite. Dans le cas de fluides compressibles présentant un module d’élasticité isostatique dépendant de la pression, nous démontrons un comportement non monotone du coefficient de frottement global dû à une compétition entre l’évolution non linéaire de la surface de contact et de la pression du fluide. Dans le cas de matériaux plastiques parfaitement élastiques, nous observons également une pénétration de fluide dans l’interface de contact. Enfin, nous étudions la distribution des tractions de frottement lors de l’ouverture du piège. Ce processus conduit à des pics de type singularité dans les tractions de frottement bornées par la limite de Coulomb près des bords de contact. Nous soulignons la similitude entre les processus d’ouverture de piège et de propagation de fissure interfaciale et estimons le facteur d’intensité de contrainte complexe à l’aide de la mécanique de la rupture élastique linéaire.

In this Chapter we study the problem of the mechanical contact between a deformable body with a wavy surface and a rigid flat taking into account pressurized fluid trapped in the interface. Using the finite-element model, formulated in Chapters 4 and 5, we investigate the evolution of the real contact area, maximal frictional traction and global coefficient of friction under increasing external load. Elastic and elasto-plastic material models, compressible and incompressible fluid models and different geometrical characteristics of the wavy surface are used. Additionally, we study the distribution of frictional tractions during the process of the fluid entrapment and the subsequent trap opening.

7.1 Problem statement

We consider a mechanical contact problem between a deformable half-plane with a periodic wavy surface and a rigid flat under the action of a far-field external pressure. This case was historically the starting point for the study of contact of rough surfaces [Westergaard, 1939, Johnson et al., 1985]. In addition, we take into account the influence of compressible or incompressible fluid trapped in the free volume between the two bodies, see Fig. 7.1. We assume the plane strain problem and a linear elastic or elastic-perfectly J_2 -plastic (the latter one is presented in Section 7.7) isotropic constitutive laws for the solid. Note that this problem is similar to the one already solved by [Kuznetsov, 1985], with the difference that we assume *small but finite* profile's slope, which, as will be shown below, is of great importance for an accurate treatment of this problem.

The initial gap between the wavy profile and the rigid plane, as well as the volume of this gap for one wavelength of the profile, are given, respectively, by:

$$g_{n0}(X) = \Delta \left(1 - \cos \frac{2\pi X}{\lambda} \right), \quad V_0 = l \int_0^\lambda \Delta \left(1 - \cos \frac{2\pi X}{\lambda} \right) dX = l \lambda \Delta, \quad (7.1)$$

where Δ and λ are the amplitude and wavelength of the wavy surface profile, respectively, X is the horizontal coordinate in the initial (reference) configuration and l is the length in the y -direction, and under the assumption of the plane strain state of deformation l will be assumed hereinafter equal to one length unit. Moreover, due to the symmetry of the problem, we will consider only one wavelength. Finally, we assume here that the fluid is not pressurized at the moment of the trapped zone formation.

7.2 Analytical solutions

7.2.1 Westergaard's solution

The problem of contact between an elastic half-space with a regular wavy surface $y = \Delta \cos(2\pi x/\lambda)$ and a rigid flat without fluid in the interface was solved by [Westergaard, 1939], see also [Johnson et al., 1985], for the case of infinitesimal ratio $\Delta/\lambda \ll 1$, i.e. infinitesimal slope of the roughness profile. According to this solution the pressure distribution inside contact patches ($-a + \lambda n \leq x \leq a + \lambda n$, $n \in \mathbb{Z}$) is given by:

$$p_W(x, a) = \frac{2\pi E}{1-\nu^2} \frac{\Delta}{\lambda} \cos \frac{\pi x}{\lambda} \sqrt{\sin^2 \frac{\pi a}{\lambda} - \sin^2 \frac{\pi x}{\lambda}}, \quad (7.2)$$

where a is the half-length of contact patch within one wavelength of the profile λ , and elsewhere $p_W = 0$. E and ν are Young's modulus and Poisson's ratio, respectively. The

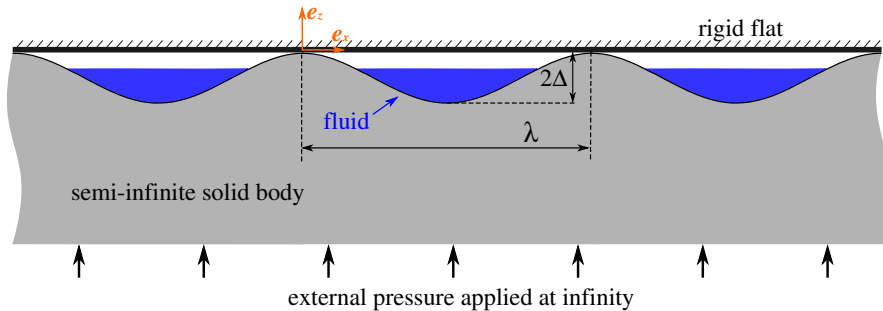


Figure 7.1: A sketch of the problem under study.

mean pressure over the whole contact interface is given by

$$\bar{p}_W(a) = \frac{1}{\lambda} \int_0^\lambda p_W(x, a) dx = p_W^* \sin^2 \frac{\pi a}{\lambda}, \quad (7.3)$$

where $p_W^* = \pi E^* \Delta / \lambda$ is the pressure necessary to bring the entire interface in contact. In the static equilibrium \bar{p}_W is equal to the value of the external pressure that we will denote by p_{ext} . The complete contact is ensured, if $p_{\text{ext}} \geq p_W^*$.

By introducing the notations $A = 2a$ and $A_0 = \lambda$ for the real and apparent contact areas, respectively, the ratio of the real contact area to the apparent one, based on the Westergaard's solution, is given by:

$$\frac{A}{A_0} = \frac{2a}{\lambda} = \frac{2}{\pi} \arcsin \sqrt{\frac{p_{\text{ext}}}{p_W^*}}, \quad 0 \leq p_{\text{ext}} \leq p_W^*. \quad (7.4)$$

7.2.2 Kuznetsov's solution

The Westergaard's solution (7.2) was extended in [Kuznetsov, 1985] by taking into account compressible fluid trapped in the valleys between contacting peaks of the wavy profile. Similarly, under the assumption of infinitesimal slope of the profile⁵, the stress state in the contact interface in the presence of the additional fluid pressure, applied beyond the contact patches, was considered as the superposition of the stress state corresponding to the same contact area, but without influence of the fluid, i.e. the Westergaard's solution (7.2), and a uniform field of the fluid pressure p^{tf} , applied everywhere and assumed not to distort the surface profile:

$$p_K(x, a) = \begin{cases} p^{\text{tf}}(a) + p_W(x, a), & \text{if } -a + \lambda n \leq x \leq a + \lambda n, \quad n \in \mathbb{Z} \\ p^{\text{tf}}(a), & \text{elsewhere.} \end{cases} \quad (7.5)$$

Integration of $p_K(x, a)$ over one period of the waviness gives the following relation between the external pressure p_{ext} and the contact area: $p_{\text{ext}}(a) = p^{\text{tf}}(a) + \bar{p}_W(a)$, where $\bar{p}_W(a)$ was defined in (7.3).

The fluid pressure p^{tf} can be related to the current contact half-width a using models of the compressible fluid discussed in Sec. 2.4. If the fluid's bulk modulus K is assumed constant, the hydrostatic pressure is proportional to the relative change of the volume:

$$p^{\text{tf}} = K \left(1 - \frac{V^{\text{tf}}}{V_0^{\text{tf}}} \right), \quad (7.6)$$

where V_0^{tf} is the volume of the fluid in unpressurised state and a smaller volume V^{tf} corresponds to the fluid pressure p^{tf} . A more precise model of the fluid with pressure-dependent bulk modulus:

$$K = K_0 + K_1 p^{\text{tf}} \quad (7.7)$$

states a non-linear relation between the fluid pressure and the volume change:

$$p^{\text{tf}} = \frac{K_0}{K_1} \left\{ \left(\frac{V^{\text{tf}}}{V_0^{\text{tf}}} \right)^{-K_1} - 1 \right\}. \quad (7.8)$$

⁵ The infinitesimal-slope assumption implies here that (i) the wavy surface behaves as a flat one and that Flamant's solution [Johnson, 1987] holds for every surface point, and (ii) that the horizontal component of the fluid pressure is negligible.

Finally, it can be noted that the volume of the pressurized fluid V^{tf} is equal to the volume of the gap V between the contacting surfaces, which can be found from the displacement field of the Westergaard's solution [Kuznetsov, 1985] and related to the current contact half-width a :

$$V(a) = V_0 \left[1 - \sin^2 \frac{\pi a}{\lambda} \left(1 - \ln \left\{ \sin^2 \frac{\pi a}{\lambda} \right\} \right) \right], \quad (7.9)$$

where $V_0 = \lambda \Delta$ is the initial gap, i.e., corresponding to $a = 0$. We generalize the original results [Kuznetsov, 1985] and allow a partial filling of the initial gap by the fluid, so that $V_0^{\text{tf}} = \theta V_0$, $0 < \theta \leq 1$. Therefore, two cases are possible:

- If the current gap volume is bigger than the initial fluid volume, $V > V_0^{\text{tf}}$, i.e. $V/V_0 > \theta$, then the fluid is not yet pressurized, and the Westergaards solution is valid:

$$p_{\text{ext}}(a) = \frac{\pi E^* \Delta}{\lambda} \sin^2 \frac{\pi a}{\lambda}. \quad (7.10)$$

- If $V < V_0^{\text{tf}}$, or, equivalently, $V/V_0 < \theta$, the equation relating the external load to the contact area has the following form in the case of linear compressible fluid:

$$p_{\text{ext}}(a) = \frac{\pi E^* \Delta}{\lambda} \sin^2 \frac{\pi a}{\lambda} + \frac{K}{\theta} \left[\theta - 1 + \sin^2 \frac{\pi a}{\lambda} \left(1 - \ln \left\{ \sin^2 \frac{\pi a}{\lambda} \right\} \right) \right], \quad (7.11)$$

and in the case of non-linearly compressible fluid:

$$p_{\text{ext}}(a) = \frac{\pi E^* \Delta}{\lambda} \sin^2 \frac{\pi a}{\lambda} + \frac{K_0}{K_1} \left[\theta^{K_1} \left(1 - \sin^2 \frac{\pi a}{\lambda} \left(1 - \ln \left\{ \sin^2 \frac{\pi a}{\lambda} \right\} \right) \right)^{-K_1} - 1 \right]. \quad (7.12)$$

It is important to note that Kuznetsov's solution even in the case of an arbitrary large modulus of compressibility of the fluid shows the growth of the contact patches under the increasing load. Furthermore, in the limit of incompressible fluid $K \rightarrow \infty$ it gives a constant value of the real contact area, which can be found from the equation $V(a) = V_0^{\text{tf}}$. Consequently, Kuznetsov's solution, based on the assumption of infinitesimal slope of the profile, cannot predict depletion of the real contact area and escape of the fluid from the trap, which we demonstrate in following sections dropping out the assumption of infinitesimal slopes.

7.3 Numerical problem set-up

In order to solve the trapped fluid problem numerically, we implemented the monolithic approach to handling the contact and the trapped fluid constraints (see Chapters 4 and 5 of this dissertation) in the finite-element suite *Z-set* [Besson and Foerch, 1997, Z-set, 2019]. Contrary to Kuznetsov's analytical results or BEM analysis based on the Flamant's solution [Johnson, 1987], we did not assume infinitesimal slopes, i.e. the value Δ/λ is arbitrary. We used a finite element mesh with 1024 nodes in the contact interface per wavelength (19364 nodes in total in the structural mesh), see Fig. 7.2. Hereinafter, if not mentioned differently, we considered the roughness profile with $\Delta/\lambda = 0.01$. In the following, we will also discuss how this ratio affects the results. The horizontal dimension of the finite element mesh equals to the wavelength λ and the ratio of the profile amplitude Δ to the vertical mesh dimension H is $\Delta/H = 0.005$.

Apart from considering different models of the fluid, material properties of the solid and different slope of the roughness profile, we study several loading scenarios, corre-

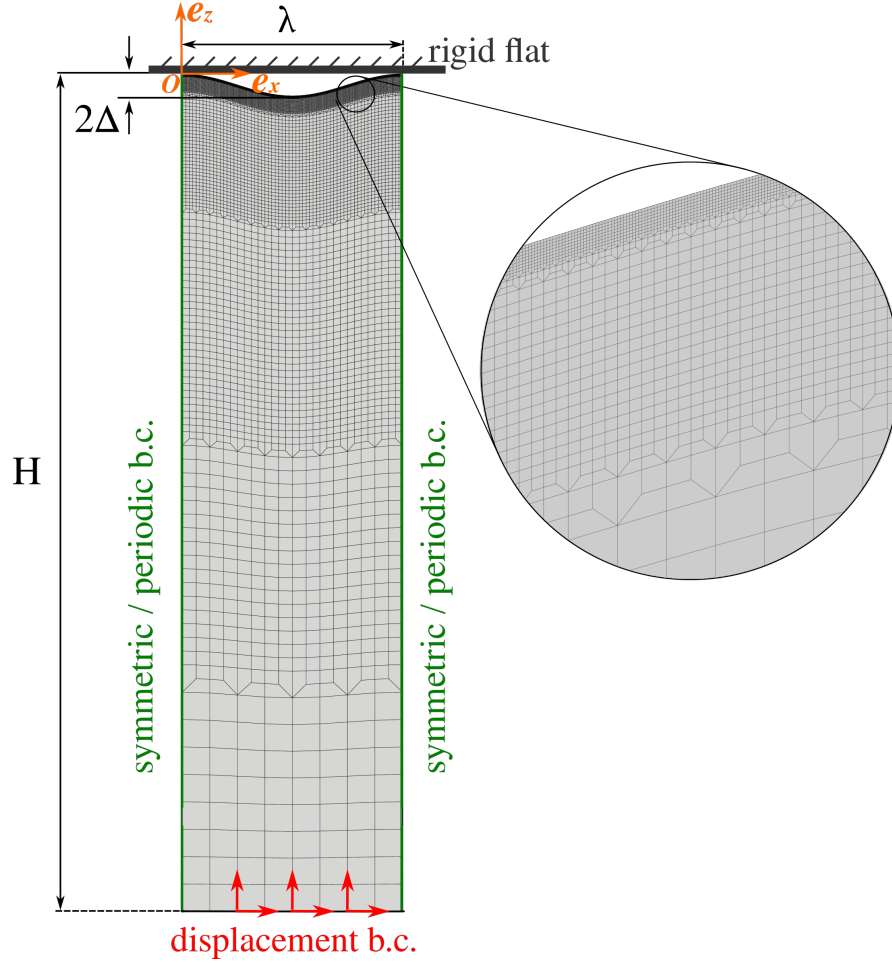


Figure 7.2: Finite-element mesh and boundary conditions for the trapped fluid problem. Several loading scenarios are considered, corresponding to *frictionless* and *frictional* simulations. Accordingly, on the vertical walls $x = 0, x = \lambda$ either symmetric or periodic boundary conditions are enforced, and on the bottom edge of the solid $z = -H$ either only vertical displacement, or a vertical displacement followed by a horizontal one is applied.

sponding to *frictional* and *frictionless* simulations. Accordingly, we apply either symmetric ($u|_{x=0} = 0, u|_{x=\lambda} = 0$) or periodic ($\mathbf{u}|_{x=0} = \mathbf{u}|_{x=\lambda}$) boundary conditions on the vertical walls of the mesh. The bottom edge of the deformable solid is displaced in the z -direction towards the rigid flat within 200 load steps, which is followed by a x -direction displacement in *frictional* simulations. A corotational updated Lagrangian framework was used in our simulations, which is needed to capture properly that the fluid pressure applied to the updated configuration is collinear to element normals. In simulation we measure the vertical reaction, the extension of the contact area, the pressure in the contact zone and the fluid pressure.

Hereinafter, if not mentioned differently, we performed *frictionless* simulations with symmetric boundary conditions on the vertical walls $x = 0, x = \lambda$, vertical motion of the bottom edge $z = -H$ and estimated the value of the global coefficient of friction using the following approach. We distinguish between the global and the local coefficients of friction by observing the problem from macroscopic (calculating the reaction forces on the solid body) and microscopic (studying the traction vector components in the contact interface) levels, respectively, see also [Azushima and Kudo, 1995]. Due to the effect of the pressurized fluid, the macroscopic normal reaction force F_n of the interface is

calculated as a sum of an integral of σ_n over the active contact zone Γ^c and an integral of the fluid pressure p^{tf} over the trapped fluid zone Γ^{tf} :

$$|F_n| = \int_{\Gamma^c} |\sigma_n| d\Gamma + \int_{\Gamma^{\text{tf}}} p^{\text{tf}} d\Gamma \quad (7.13)$$

We also note that in the static equilibrium $|F_n| = p_{\text{ext}}\lambda$. Next, the macroscopic tangential reaction force \mathbf{F}_t of the interface (with shear forces in the fluid being neglected) reads:

$$\mathbf{F}_t = \int_{\Gamma^c} \boldsymbol{\sigma}_t d\Gamma, \quad (7.14)$$

where $\boldsymbol{\sigma}_t$ is the tangential component of the traction vector. The global coefficient of friction μ_{glob} is introduced as the coefficient of proportionality between the maximal macroscopic tangential and normal reaction forces:

$$\|\mathbf{F}_t\| \leq \mu_{\text{glob}} |F_n|. \quad (7.15)$$

Furthermore, observing the problem on the microscopic level, we assume that the local coefficient of friction μ_{loc} is given by the Coulomb's law:

$$\|\boldsymbol{\sigma}_t\| \leq \mu_{\text{loc}} |\sigma_n|, \quad (7.16)$$

i.e. the tangential traction is bounded at every contact point and thus is bounded in the integral sense as follows:

$$\int_{\Gamma^c} \|\boldsymbol{\sigma}_t\| d\Gamma \leq \mu_{\text{loc}} \int_{\Gamma^c} |\sigma_n| d\Gamma. \quad (7.17)$$

Since the local motion at every point of the interface implies the global motion, by equating right parts in (7.15) and (7.17), we obtain the ratio between the global and local coefficients of friction:

$$\frac{\mu_{\text{glob}}}{\mu_{\text{loc}}} = \int_{\Gamma^c} |\sigma_n| d\Gamma / |F_n| = \int_{\Gamma^c} |\sigma_n| d\Gamma / p_{\text{ext}}\lambda, \quad (7.18)$$

which can be rewritten in a more explicit form as:

$$\frac{\mu_{\text{glob}}}{\mu_{\text{loc}}} = 1 - \int_{\Gamma^{\text{tf}}} p^{\text{tf}} d\Gamma / p_{\text{ext}}\lambda = 1 - \frac{p^{\text{tf}}(\lambda - 2a)}{p_{\text{ext}}\lambda}. \quad (7.19)$$

Since the last ratio is always non-negative, it follows that the global coefficient of friction is always smaller than the local one in the case of pressurized fluid, in general: $0 \leq \mu_{\text{glob}} \leq \mu_{\text{loc}}$. By using the above introduced notations for the real $A = 2a$ and apparent $A_0 = \lambda$ contact areas, (7.19) can be rewritten as:

$$\frac{\mu_{\text{glob}}}{\mu_{\text{loc}}} = 1 - \frac{p^{\text{tf}}}{p_{\text{ext}}} \left(1 - \frac{A}{A_0} \right). \quad (7.20)$$

Finally, this expression for estimating the global coefficient of friction was verified using an actual *frictional* simulation with periodic boundary conditions enforced on vertical walls $x = 0$, $x = \lambda$, and a vertical displacement followed by a horizontal one applied at the bottom edge $z = -H$, see Fig. 7.5(d). In this loading scenario, once the global tangential motion of the solid is observed (which means that the whole contact zone is in the *slip*

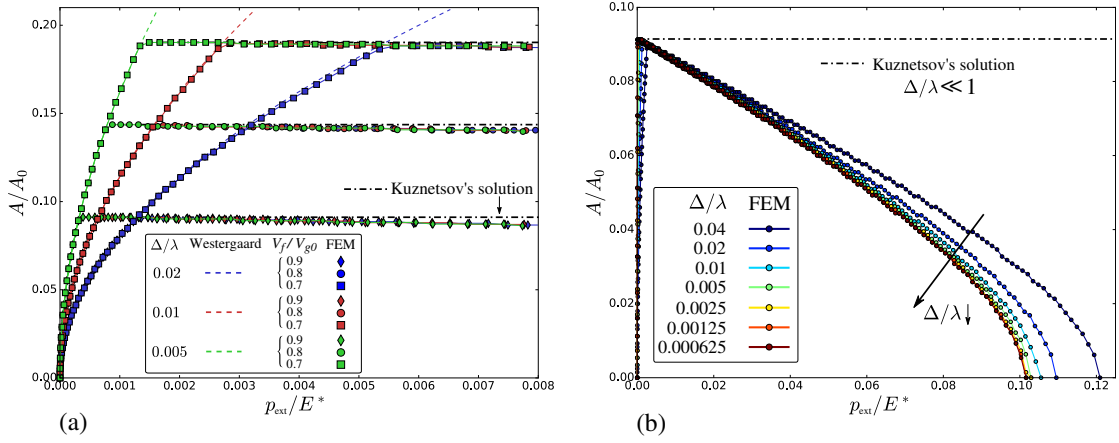


Figure 7.3: (a) The evolution of the real contact area in the vicinity of the “activation” point of the incompressible fluid with respect to the external pressure normalized by E^* for three profiles with different slopes Δ/λ and three cases with different ratios of the fluid volume to the initial gap volume V^{tf}/V_0 . (b) The evolution of the real contact area until the complete opening of the trap for the case $V^{\text{tf}}/V_0 = 0.9$ shown for different slopes Δ/λ .

state) the global coefficient of friction can be computed directly as $\mu_{\text{glob}} = \|\mathbf{F}_t\| / |F_n|$, see its definition in (7.15).

7.4 Incompressible fluid

In this section we study the model of an incompressible fluid trapped in the contact interface. Even if real-life lubricating fluids have significantly lower initial bulk moduli than metals, this idealized model enables us to focus on mechanisms of fluid entrapment and the trap opening by the pressurized fluid. The effect of the fluid compressibility of the contact problem will be considered in the following sections.

7.4.1 Evolution of the real contact area

We study the evolution of the real contact area in the presence of incompressible fluid in the interface under the increasing external pressure using the Lagrange multiplier method. We investigate how the magnitude of the slope of the profile (Δ/λ) and the ratio between the trapped fluid volume and the initial gap volume V^{tf}/V_0 affect the solution of the coupled problem.

The evolution of the contact area close to the moment of the activation of the fluid is presented in Fig. 7.3(a). The regime in which the fluid is not yet pressurized ($V > V^{\text{tf}}$) coincides with Westerdale’s equation (7.2). According to this analytical solution the ratio of the current volume of the gap to the initial one V/V_0 is a monotonically decreasing function of contact area and does not depend on the slope of the profile Δ/λ , see (7.9). Therefore, the contact area A_{act} , reached when the fluid gets pressurized ($V = V^{\text{tf}}$) does not depend on the slope of the profile and is increasing with decreasing V^{tf}/V_0 . For a given Δ/λ the pressure necessary to activate the fluid p_{act} is also increasing with decreasing V^{tf}/V_0 . At the same time, for a given V^{tf}/V_0 , the value of p_{act} is proportional to the slope Δ/λ .

One can note in Fig. 7.3(a) that once the fluid is pressurized, the contact area is slowly decreasing, contrary to the Kuznetsov’s solution, which predicts the contact area to remain constant. In Fig. 7.3(b) we show the evolution of the contact area in a much

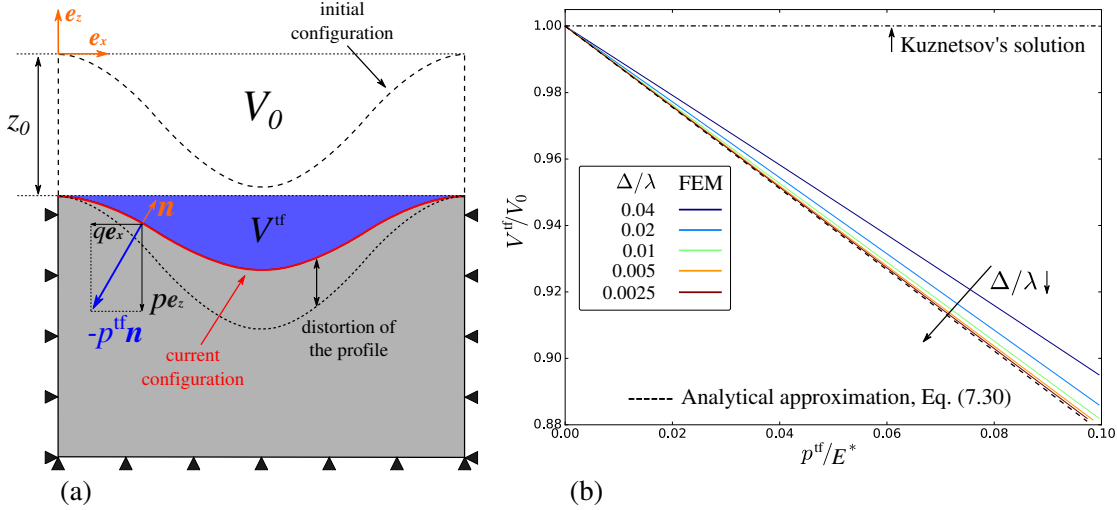


Figure 7.4: (a) Sketch of the auxiliary problem: deformation of the wavy surface under uniform hydrostatic pressure. (b) Evolution of the ratio V^{tf}/V_0 (V^{tf} is the volume between the deformed surface and a horizontal plane $z = z_0$, where z_0 is the current position of the crest, and V_0 is the initial volume of the gap) with the increasing hydrostatic pressure p^{tf} for several profiles with different slope Δ/λ .

wider range of loads, than in Fig. 7.3(a), and observe a monotonic decrease of the contact area, ultimately it reaches zero value, which corresponds to the opening of the trap. Surprisingly, results of simulations with different (decreasing) profile slope Δ/λ do not tend to the Kuznetsov's solution (derived under assumption of infinitesimal Δ/λ and assuming that the wave profile is similar to a flat one), but converge to a different limit! At the same time we observe that the external pressure necessary to open the trap p_{open} also converges to a certain limit with $\Delta/\lambda \rightarrow 0$.

7.4.2 Distortion of the periodic wavy surface under a uniform hydrostatic pressure

In order to explain this intriguing result, first we note that since the solution of linearly elastic problem with and without contact is unique, see, for example, [Truesdell, 1984], the displacement field at the moment of opening of the trap with external pressure $p_{\text{ext}} = p_{\text{open}}$ must be equal (up to a rigid body motion) to the one corresponding to a distributed hydrostatic pressure $p^{\text{tf}} = p_{\text{open}}$ over the whole interface. Let us consider an auxiliary problem of the uniform hydrostatic fluid pressure p^{tf} on the wavy profile, see Fig. 7.4(a). The Kuznetsov's solution is based on an assumption that a uniform distribution of the hydrostatic pressure does not distort the wavy surface [Kuznetsov, 1985]. In our numerical simulations we showed that for small, but finite Δ/λ this assumption does not hold, the wavy surface distorts: the crest's displacement is bigger than the displacement of the trough, which is quite an evident result.

Due to the non-zero slope of the contact interface, the fluid pressure acts not only in the vertical direction but also in the horizontal one, thus leading to the additional in-plane compression of the material near the crest and, on the opposite, to the additional in-plane tensile contribution near the trough, see Fig. 7.4(a). Thus, there exists a linearly elastic solution for a uniformly distributed pressure p^{tf} , which results in such surface deformation, that the integral of the gap equals to the fluid volume V^{tf} , i.e.:

$$\exists p^{\text{tf}} \quad \text{such that} \quad \int_{\Gamma} (z_0 - z) d\Gamma = V^{\text{tf}}, \quad (7.21)$$

where z_0 is the position of the crest after applying the uniform pressure p^{tf} . We will derive an analytical formula relating V^{tf} to p^{tf} , based on the assumption of small, but finite Δ/λ . According to the integrated Flamant's solution, any uniformly distributed pressure on the surface will result in a uniform vertical displacement. However, it is true only if the surface is flat. For a wavy surface, under the action of a uniform pressure, the crest's displacement is bigger than the displacement of the trough. The uniform pressure distribution on the surface is given by $-p^{\text{tf}}\mathbf{n}$, where \mathbf{n} is the outer normal to the surface. We consider the vertical p and horizontal q components of the normal pressure (each one of them contributes to the distortion of the profile):

$$q(x) = -2\pi p^{\text{tf}} \frac{\Delta}{\lambda} \sin \frac{2\pi x}{\lambda} + O\left(\frac{\Delta^3}{\lambda^3}\right) \quad (7.22)$$

and

$$p(x) = -p^{\text{tf}} + O\left(\frac{\Delta^2}{\lambda^2}\right) \quad (7.23)$$

in case of small slope. Therefore, keeping the small values of order Δ/λ , we may calculate the vertical displacement caused by the horizontal component q using the integrated Flamant's solution [Johnson, 1987]:

$$w^q(x) = -\frac{(1-2\nu)(1+\nu)}{2E} \left\{ \int_{-b}^x q(s) ds - \int_x^b q(s) ds \right\} + C, \quad (7.24)$$

where $b \rightarrow \infty$ and C is an arbitrary constant. Substituting $q(s)$ and calculating integrals, we obtain:

$$w^q(x) = -\frac{(1-2\nu)(1+\nu)p^{\text{tf}}}{E} \Delta \cos \frac{2\pi x}{\lambda} + C. \quad (7.25)$$

We are also convinced that the uniformly distributed vertical traction p produces exactly the same vertical displacement:

$$w^p(x) = -\frac{(1-2\nu)(1+\nu)p^{\text{tf}}}{E} \Delta \cos \frac{2\pi x}{\lambda} + D, \quad (7.26)$$

where D is another arbitrary constant. However, this result does not follow from Flamant's solution, which as already mentioned would predict a uniform displacement. This result was guessed and confirmed with a very high accuracy (fractions of percent) by finite-element simulations for different fractions Δ/λ and Poisson's ratios.⁶ At this stage we are content with numerical proof only, which consisted in applying separately horizontal and vertical components of the pressure over a single period with periodic boundary conditions and comparing the numerical results with the equations (7.26) and (7.25). The total vertical displacement reads:

$$w(x) = w^q(x) + w^p(x) = -\frac{2(1-2\nu)(1+\nu)p^{\text{tf}}}{E} \Delta \cos \frac{2\pi x}{\lambda} + \tilde{C}. \quad (7.27)$$

We may define \tilde{C} so that $w(0) = z_0$, where z_0 is the current vertical position of the

⁶The simplest analogy would be the Winkler's foundation [Johnson, 1987] with springs whose lengths follow the distribution $l(x) = L + \Delta \cos(2\pi x/\lambda)$, which would mimic the shape of the wavy surface. However, it is unavailing to obtain the proportionality factor of form $(1-2\nu)(1+\nu)/E$.

crest, thus giving:

$$w(x) = z_0 - \frac{2(1 - 2\nu)(1 + \nu)p^{\text{tf}}}{E} \Delta \left(\cos \frac{2\pi x}{\lambda} - 1 \right). \quad (7.28)$$

We calculate the volume between the distorted wavy surface and the plane $z = z_0$:

$$V^{\text{tf}} = \int_{\Gamma} (z_0 - (Z(x) + w(x))) d\Gamma, \quad (7.29)$$

where $Z(x) = \Delta(\cos \frac{2\pi x}{\lambda} - 1)$ is the initial vertical coordinate. Upon integration, noting that the initial gap volume $V_0 = \Delta\lambda$, we obtain:

$$\frac{V^{\text{tf}}}{V_0} = 1 - \frac{2(1 - 2\nu)(1 + \nu)p^{\text{tf}}}{E}, \quad (7.30)$$

which gives the relative change of the volume between the deformed wavy surface and corresponding plane under action of the uniform hydrostatic pressure p^{tf} . It is important to note, that horizontal $q(x)$ and vertical $p(x)$ tractions produce also a certain horizontal displacement $u(x)$. However, it can be shown, that the contribution of this horizontal displacement to the relative volume change V^{tf}/V_0 is an order of Δ/λ smaller than the contribution of the vertical displacement $w(x)$ computed in (7.30). Therefore, the effect of $u(x)$ can be neglected in this solution valid for $\Delta/\lambda \ll 1$.

Interestingly, the expression for the relative volume change (7.30) does not depend on Δ/λ , however, this result was obtained under assumption of $\Delta/\lambda \ll 1$, therefore it corresponds to the limiting case of small, but finite slope of the profile. Furthermore, the relative change of volume induced by a uniformly applied pressure p^{tf} depends on elastic properties of the solid. In Fig. 7.4(b) the comparison of the derived formula (7.30) with the numerical results for several profiles with different Δ/λ is shown. Numerical results are tending towards the analytical solution with decreasing Δ/λ . Therefore, we have shown that for any given V^{tf}/V_0 there exists uniform pressure p^{tf} , which results in a such distortion of the surface, that the volume between the surface and a rigid flat equals to V^{tf} . Moreover, in the limit of infinitesimal slopes, this critical pressure does not depend on the slope. Note also that the equation (7.30) can be readily used to compute the external load needed to open the trap for a given fluid volume; it is valid for both incompressible and compressible fluid with constant or pressure-dependent bulk modulus. Interestingly, in the latter case, see (2.75), Eq. (7.30) can have several solutions.

The obtained result explains why the curves of evolution of the real contact area with the increasing pressure for surfaces with different slopes tend to a certain limit with decreasing Δ/λ (which remains, however, finite), see Fig. 7.3(b). At the same time; the external pressure necessary to open the trap p_{open} is different for different V^{tf}/V_0 , see Fig. 7.5(a). In the case when the fluid fills completely the initial gap volume (not shown in figures), i.e. $V^{\text{tf}} = V_0$, the real contact area equals zero during the whole process of loading, i.e. the fluid is pressurized, but is never trapped.

7.4.3 Evolution of maximal frictional traction and global coefficient of friction

We present in Fig. 7.5(b) the evolution of the integral of normal tractions over the contact area, normalized by λ and E^* , for different values of Δ/λ and V^{tf}/V_0 . The results show that just after the fluid becomes pressurized, the integral of contact pressure grows

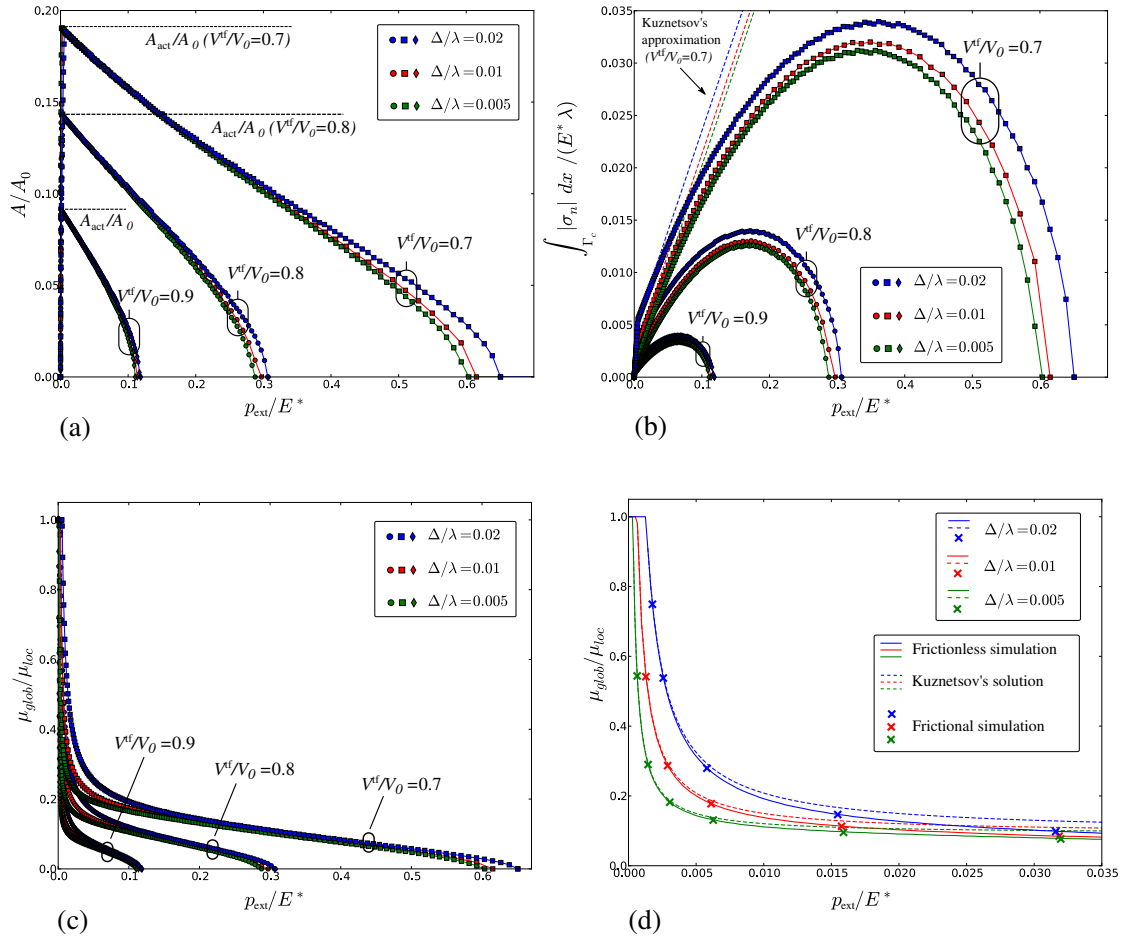


Figure 7.5: (a) Real contact area evolution during opening of the contact, caused by pressurized incompressible trapped fluid (with respect to the external pressure normalized by E^*) (b) Contact normal force evolution during opening of the contact (with respect to the external pressure, normalized by E^*). (c) Evolution of the ratio between global and local coefficients of friction, and (d) a zoom of this evolution for $V^{\text{tf}}/V_0 = 0.9$, where, in addition, the results of *frictional* simulations are plotted (crosses), as well as analytical approximations given by (7.32) (dashed curves).

almost linearly, which is also predicted by the Kuznetsov's solution in the limit $K \rightarrow \infty$:

$$\frac{1}{E^* \lambda} \int_{\Gamma^c} |\sigma_n| d\Gamma^c = \frac{p_{\text{ext}}}{E^*} \frac{A_{\text{act}}}{A_0} + \pi \left(1 - \frac{A_{\text{act}}}{A_0}\right) \frac{\Delta}{\lambda} \sin^2 \frac{\pi}{2} \frac{A_{\text{act}}}{A_0}, \quad (7.31)$$

where, contrary to numerical results, it was assumed that A_{act} remains constant under the increasing external pressure p_{ext} . However, due to the fact that we consider finite slope of the profile in the numerical solution, the linear part in the dependence of contact reaction on external pressure is followed by a non-linear concave part, reaching maximum value and then decreasing to zero. Consequently, the global coefficient of friction also vanishes. The results on the estimation of the ratio between global and local coefficients of friction are presented in Fig. 7.5(c). Before the fluid gets pressurized, the global CoF equals to the local one. After that, the global CoF is monotonically decreasing with the increasing external pressure p_{ext} . This decrease is related to repartition of the external load between the contact and the fluid; the latter is assumed not to resist shear in the quasi-static limit. Note that for high values of p_{ext} , i.e. close to opening of the trap, the evolution of the global CoF is independent from the slope (Δ/λ) and depends only on the ratio V^{tf}/V_0 . On the other hand, for low values of p_{ext} slightly higher than the activation pressure (see Fig. 7.5(d)) the Kuznetsov's solution under the assumption of infinite K shows the global CoF decreasing as $1/p_{\text{ext}}$:

$$\frac{\mu_{\text{glob}}}{\mu_{\text{loc}}} = \frac{A_{\text{act}}}{A_0} + \pi \left(1 - \frac{A_{\text{act}}}{A_0}\right) \frac{\Delta}{\lambda} \frac{E^*}{p_{\text{ext}}} \sin^2 \frac{\pi}{2} \frac{A_{\text{act}}}{A_0}. \quad (7.32)$$

Note, that the term containing $1/p_{\text{ext}}$ is proportional to the ratio Δ/λ .

In addition to estimations of the global coefficient of friction (7.18)-(7.20), based on the *frictionless* simulation of the coupled problem under normal loading, we performed a direct computation of $\mu_{\text{glob}} = \|\mathbf{F}_t\|/|F_n|$ in a *frictional* simulation of the coupled problem during sliding under both normal and tangential loads, supplemented by periodic boundary conditions on vertical walls. Note that in the latter case we used the augmented Lagrangian method for both normal and frictional contact constraints and the classic Lagrange multiplier method for the fluid constraint. The comparison of the results is presented in Fig. 7.5(d) for the case of $V^{\text{tf}}/V_0 = 0.9$ and different ratios of Δ/λ : Kuznetsov's solution (7.32) is presented with dashed curves, estimations based on frictionless simulation are shown as solid curves; results, which were obtained taking explicitly into account friction in the interface, are presented as crosses for a few particular values of external pressure p_{ext} . This comparison shows that the frictionless result, based on the assumption of separate consideration of tangential and normal contributions in the interface [Johnson, 1987], provides a trustworthy estimation of the global coefficient of friction.

Note that these considerations can be applied to multi-cracked materials such as rocks with fluid in contact interfaces. The irreversible deformation in rocks is related to the frictional sliding at crack interfaces, which starts after the mean shear traction $\langle \sigma_t \rangle$ in the interface reaches the frictional limit determined by the coefficient of friction and the contact pressure $\mu_{\text{glob}} \langle \sigma_n \rangle$. Being homogenized over all randomly oriented crack orientations, these considerations give rise to Drucker-Prager-type constitutive behaviour with the initial yield surface given by $f = \sigma_{vM} + \mu_{\text{glob}} p - R_0$, where σ_{vM} is the von Mises stress, $p = -\text{trace}(\boldsymbol{\sigma})/3$ is the hydrostatic pressure and R_0 is the initial yield stress for pure shear. Because of the presence of an incompressible fluid in the interface, the frictional limit does not increase linearly (or equivalently the global coefficient of friction does not remain constant), but reaches its maximum and decreases down to zero as shown in Fig. 7.5(b). This behaviour is very similar to advanced pressure-dependent plasticity models with a so-called cap, which corresponds to the decay of the von Mises

yield stress with increasing pressure [Resende and Martin, 1985]. But contrary to the pore-collapse mechanism [Suarez-Rivera et al., 1990, Perrin and Leblond, 1993, Issen and Rudnicki, 2000], here this decay results from the decrease of the global friction with the hydrostatic pressure in presence of the fluid, this result also holds for non-linearly compressible fluids.

Finally, for the sake of completeness, the distribution of some stress and strain components in the bulk of the deformable solid during the process of trap opening is shown in Fig. 7.6.

7.5 Compressible fluid with constant bulk modulus

Here our analysis is extended to the case of compressible fluids. In Fig. 7.7(a) we present the comparison of the numerical simulation of a linearly compressible trapped fluid under the linear penalty formulation with the analytical solution (7.11). We plot the evolution of the ratio of the real contact area to the apparent one under increasing external pressure for the case when the fluid occupies 70% of the initial gap, i.e. $V_0^{\text{tf}}/V_0 = 0.7$. Different curves correspond to different values of the modulus of compressibility of the fluid K_f , normalized by the bulk modulus of the solid body $K_s = E/3(1 - 2\nu)$, and for each numerical result a corresponding analytical curve is presented for comparison.

Before pressurization of the fluid, the presence of the latter does not affect the solution and all curves follow the Westergaard's solution (7.2). For the pressurized fluid, the results show a good agreement between numerical and analytical solutions for values $K_f/K_s \ll 1$, and for $K_f \approx 0$ the solution coincides completely with the Westergaard's formula. However, with the increase of the K_f , in the region corresponding to the active fluid, the difference between numerical and analytical solutions becomes more pronounced. For the ratio K_f/K_s close to unity, the numerical results shows an almost constant value of the real contact area under the increasing load. Note, that the same result will hold for an incompressible fluid trapped in the interface between two incompressible solids.

For even greater K_f/K_s , the numerical results show a decrease of the real contact area, which means that the pressurized fluid starts to open the contact. Due to inherent assumptions of infinitesimal slopes, these effects cannot be predicted by the analytical solution.

In Fig. 7.7(a) the results were presented for $V_0^{\text{tf}}/V_g = 0.7$, note that the smaller this ratio is, the bigger are the value of pressure necessary to bring the fluid in active state and the corresponding value of the contact area. However, after the fluid becomes pressurized, for sufficiently high values of external pressure, the evolution of the contact area is influenced only by the compressibility modulus of the fluid and the mean slope of the profile. The bigger is the compressibility modulus or the slope, the smaller is the contact area for the same external pressure.

To emphasize the difference between the analytical and numerical solutions for a nearly incompressible fluid, we plot the pressure distribution near a contact patch under the increasing load for both solutions, see Fig. 7.7(b). The representation of the stress state in the contact patches as a superposition of the stress state for the same contact area without the influence of the fluid and a uniform fluid pressure, applied everywhere (7.5) still holds for the numerical solution, but unlike the analytic solution, in our results a significant reduction of the contact area for nearly incompressible fluid is observed. Note that in our numerical solution for sufficiently high external pressure the real contact area vanishes, which means that the fluid separates the contacting surfaces everywhere, and the external pressure is entirely supported by the fluid under the pressure equal to the external one $p^{\text{tf}} = p_{\text{ext}}$.

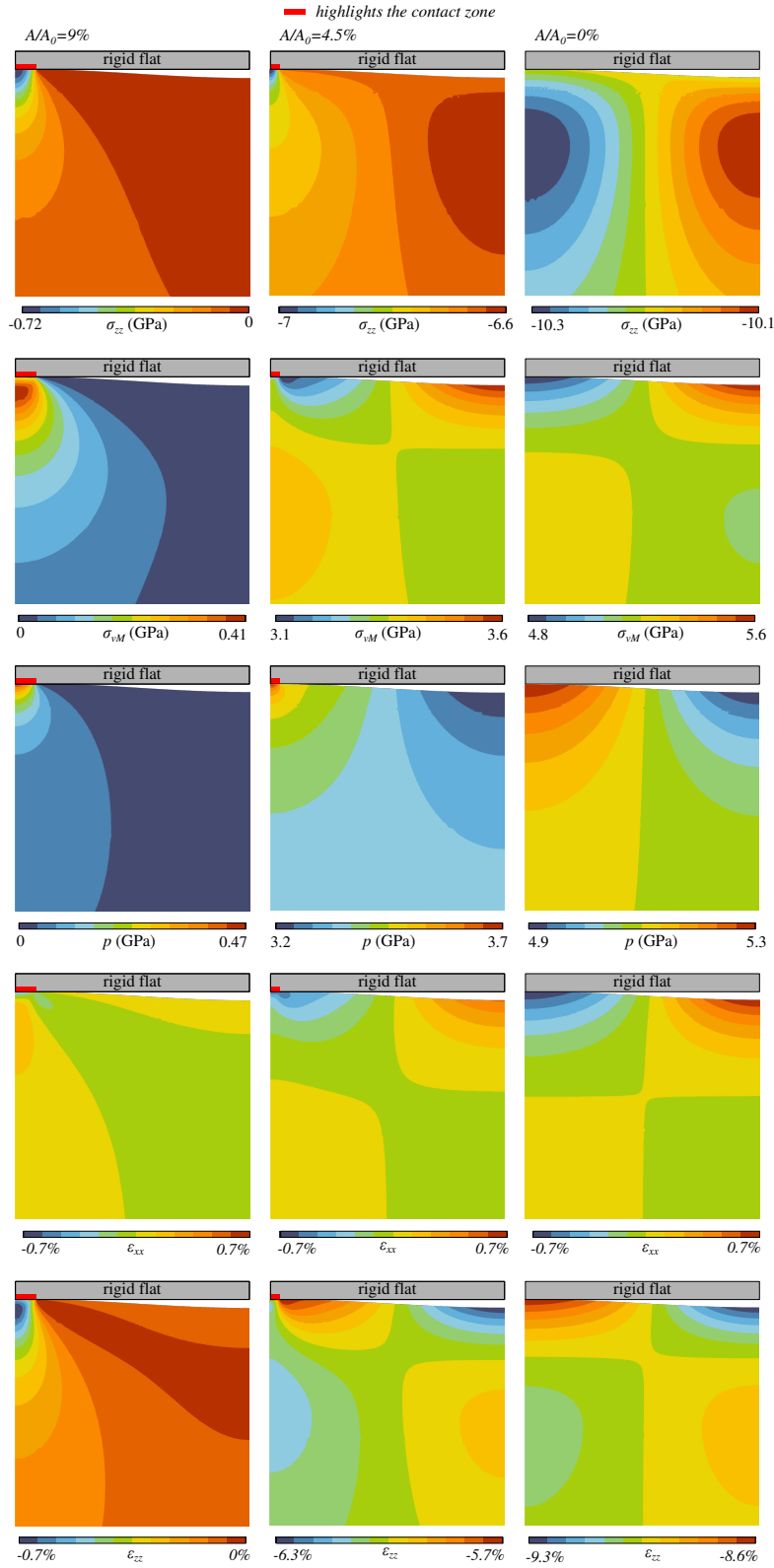


Figure 7.6: Stress and strain components in the bulk of the deformable solid during the process of trap opening due to the increasing pressure in the fluid. Top to bottom: vertical stress component σ_{zz} , von Mises stress σ_{vM} , hydrostatic stress p , horizontal strain component ϵ_{xx} and the vertical one ϵ_{zz} . Three loading steps are considered, corresponding to, left to right: maximal contact area (activation of the fluid), half of the contact opened, contact area is zero (trap is opened). The considered elastic material is typical aluminium ($E = 70$ GPa, $\nu = 0.33$), the fluid is assumed incompressible.

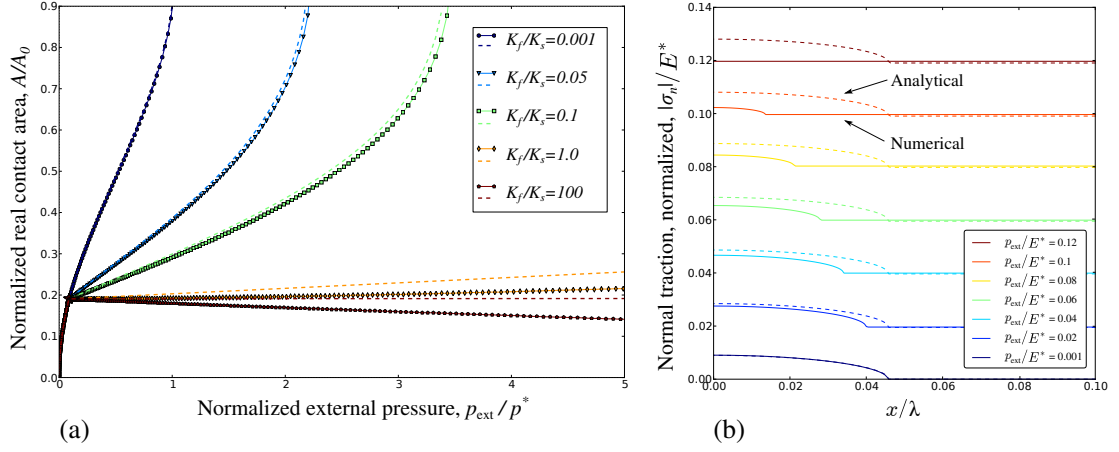


Figure 7.7: (a) Evolution of the ratio of the real contact area to the apparent one under increasing external pressure p_{ext} : comparison of numerical (solid curves with markers) and analytical (dashed curves) results for different values of the fluid modulus of compressibility, normalized by the bulk modulus of the solid K_f/K_s ; $\Delta/\lambda = 0.01$, $V_0^{\text{tf}}/V_0 = 0.7$. (b) Distribution of the normal pressure near the contact patch under the increasing external load p_{ext} . Solid lines are the results of the numerical simulation and dashed lines correspond to the analytical solution under the same external pressure, $\Delta/\lambda = 0.01$, $V_0^{\text{tf}}/V_0 = 0.9$, $K_f/K_s = 6 \cdot 10^4$.

7.6 Compressible fluid with pressure-dependent bulk modulus

As was shown in Fig. 7.7(a) for the case of linearly compressible fluid (with constant bulk modulus), starting from the pressurization of the fluid, the real contact area evolves monotonically with the external pressure: if the fluid bulk modulus is considerably less than the one of the solid ($K_f \ll K_s$), then the real contact area monotonically increases, if $K_f \gg K_s$, then the contact area decreases down to zero, corresponding to the opening of the trap. The latter case is interesting for the study of the process of the fluid permeation into the contact zone and reduction of the global coefficient of friction, however, as it was mentioned in the Sec. 7.4 for the incompressible fluid, the situation when the initial fluid bulk modulus is greater than that of the solid remains non-physical and serves as an idealized model. On the other hand, real fluids behave non-linearly and their bulk modulus increases with increasing pressure, and thus even if the fluid bulk modulus is smaller than that of the solid in the first stage of pressurization, it eventually becomes greater than the one of the solid under the increasing pressure.

We present results of the numerical simulation for coupled problem with non-linear fluids: evolution of the contact area and global coefficient of friction with increasing external pressure, see Figs. 7.8(a),(b), respectively. Physically relevant values for two solid materials are used: a typical steel ($E = 200$ GPa, $\nu = 0.28$, $K_s \approx 151.5$ GPa) and aluminium ($E = 70$ GPa, $\nu = 0.33$, $K_s \approx 83.33$ GPa), and three types of fluid (see Eq. (7.7)): water ($K_0 = 2112.5$ MPa, $K_1 = 6.5$), glycerine ($K_0 = 4151.5$ MPa, $K_1 = 8.74$) and a typical mineral oil ($K_0 = 2000.0$ MPa, $K_1 = 9.25$) [Kuznetsov, 1985, Nellemann et al., 1977]. We limit this study to the contact problem with the fluid completely filling up the gap (but only up to the upper boundary) during the whole process of loading. Such formulation remains rather general since, due to the realistic fluid model, the contact zone will inevitably appear in the beginning of loading.

At low external pressures numerical results coincide with the analytical solutions for non-linear fluids, see (7.12). However, in contrast to the analytical solution, which

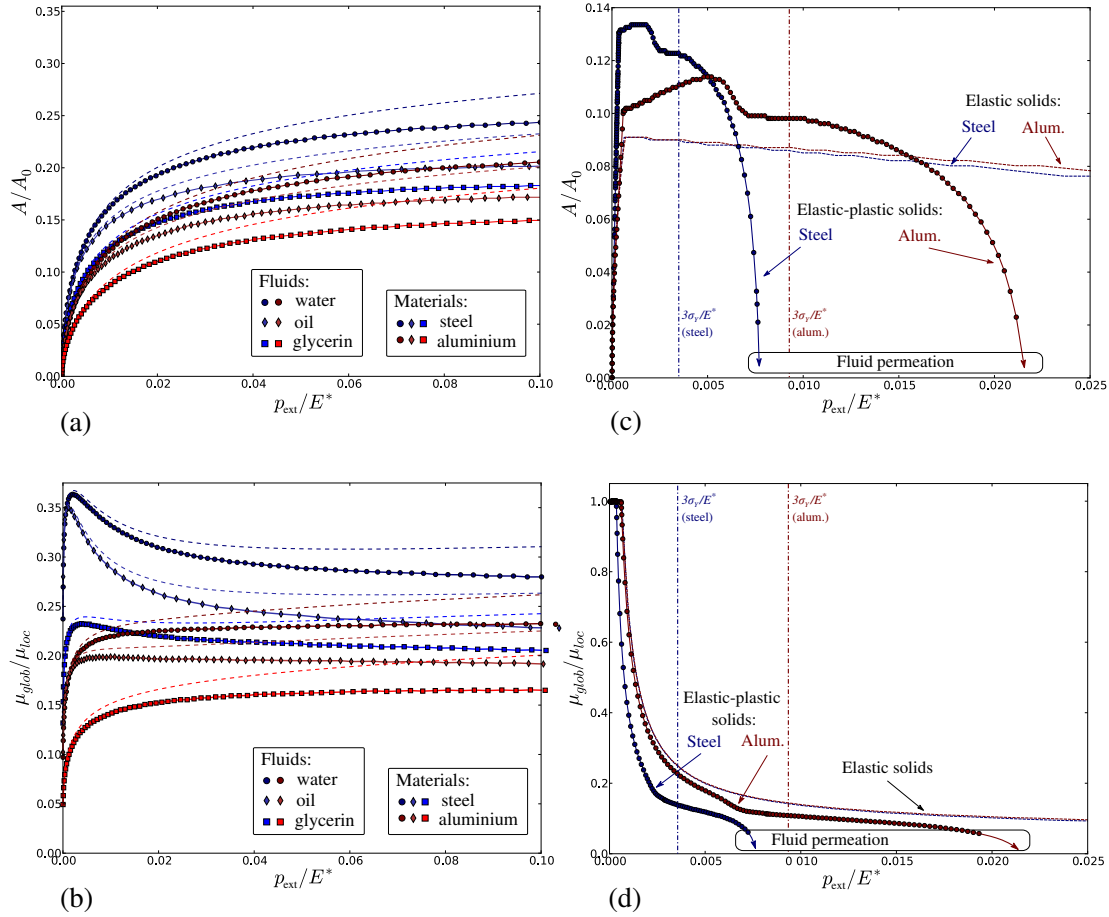


Figure 7.8: Evolution of (a) the ratio of real contact area to the apparent one, (b) the ratio between global and local coefficients of friction under increasing external pressure for two elastic solids representing steel and aluminium, and non-linearly compressible fluids representing water, glycerine and oil. The dashed curves correspond to the analytical solution given by (7.12). Evolution of (c) the ratio of real contact area to the apparent one A/A_0 , and of (d) the global to local coefficients of friction under increasing external pressure in the case of elastic-perfectly plastic solid and incompressible fluid. Note that in the initial configuration the fluid does not occupy the entire gap: $V^{\text{tf}}/V_0 = 0.9$. Dashed curves are presented for comparison with the cases of purely elastic solids, discussed in Sec. 7.4. Vertical dash-dotted line indicates the hardness taken to be $H = 3\sigma_Y$.

cannot account for depletion of the contact zone, the numerically obtained contact area reaches a certain maximal value and then decreases (the latter is observed for external pressures $p_{\text{ext}}/E^* > 0.2$, not shown in figures since the contact area does not reach zero value even for extremely high values of the external pressure $p_{\text{ext}} = E^*$). Note that for each of considered materials, the obtained curves for water and oil coincide in the beginning of loading due to almost equal initial bulk moduli K_0 of these fluids, and deviate for higher external pressures due to difference in K_1 , while for glycerine K_0 is significantly bigger, leading to a smaller contact area in this case.

The global coefficient of friction (CoF) also shows a non-monotonic behaviour, see Figs. 7.8(b), first, it rapidly increases up to a certain maximal value. Within this stage, the numerical and analytical results are very close, while for higher pressures a strong deviation of analytical and numerical results is observed. In analytical solution, even though the global CoF may decrease after the first extremum-maximum (see results obtained for the steel), it eventually increases again after reaching the second extremum-minimum. More accurate numerical results predict a monotonic decrease of the global CoF after reaching the first maximum. Note that in the simplified case considered here, the effect of hydrostatic lubrication lowers significantly the maximal global CoF, which does not exceed $\approx 36\%$ of the local CoF for the steel, and does not exceed $\approx 24\%$ of the local CoF for the aluminium. Such a strongly non-linear behaviour of the global coefficient of friction is explained by a competition between non-linear fluid pressurization and non-linear contact area evolution (see Eq. (7.20)).

The numerical solution shows that the maximal value of the CoF and its slope after passing the extremum both depend on the ratio between the bulk moduli of the fluid $K_f = K_0 + K_1 p^{\text{tf}}$ and the solid K_s . The bigger is the initial modulus K_0 , the higher is the maximal CoF (which explains almost equal peak values of the CoF for water and oil and much lower value for glycerine). At the same time, the bigger is the coefficient K_1 , the faster the CoF decreases.

We performed additional simulations varying the slope of the roughness profile Δ/λ in the interval $[0.005; 0.02]$. The results showed that the evolution of the real contact area is almost independent of the ratio Δ/λ (similarly to the case of the incompressible fluid). On the other hand, variation of this ratio has a considerable effect on the peak value of the global CoF, which increases with increasing Δ/λ . However, for high values of external pressure, the CoF does not depend on the slope of the profile, as it was also observed for the incompressible case.

7.7 Elastic-perfectly plastic solid

As was shown in the previous section, the pressurized fluid can open the contact only at unrealistically high pressures, at which the linearly elastic material model is irrelevant. Thus, here a more realistic case is presented taking into account a non-linearly compressible fluid and an elasto-plastic material behaviour. Moreover, such a study is relevant for the aforementioned experimental observations of entrapment and consequent permeation of the fluid into the contact interface in metal forming processes and during upsetting of an elasto-plastic cylinder [Azushima and Kudo, 1995, Azushima et al., 2011]. Here we consider elastic-perfectly plastic materials (von Mises stress criterion): steel, $E = 200$ GPa, $\nu = 0.28$, yield stress $\sigma_Y = 250$ MPa and aluminium, $E = 70$ GPa, $\nu = 0.33$, $\sigma_Y = 240$ MPa.

It is well known that in elasto-plastic mechanical contact, the contact pressure cannot exceed the material hardness, which can be reliably estimated as $H \approx 3\sigma_Y$ [Bowden and Tabor, 2001, Johnson, 1987, Mesarovic and Fleck, 1999]. Thus it could be expected that after the pressure in the fluid reaches material hardness the contact abruptly opens.

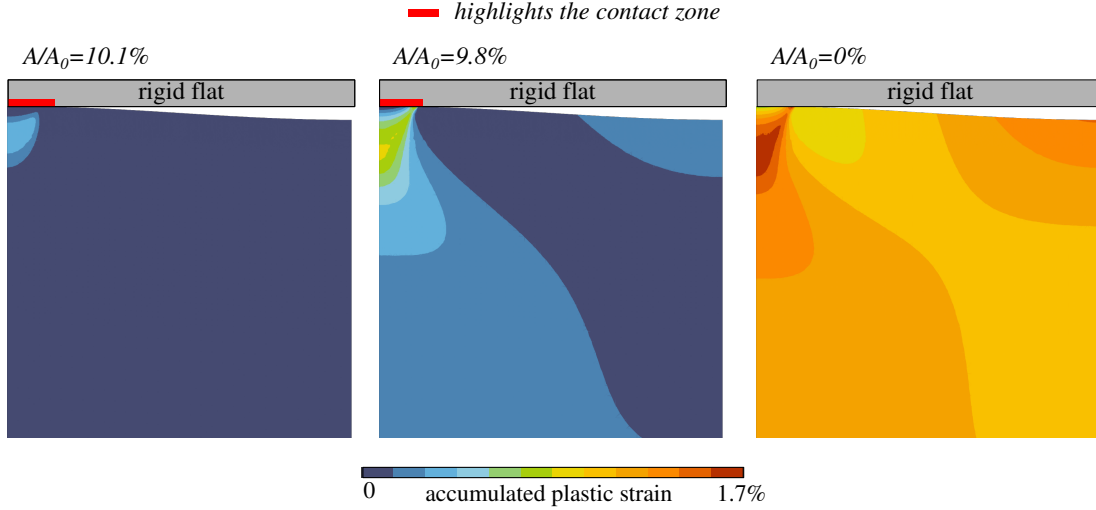


Figure 7.9: Accumulated plastic strain near the contact interface is shown at three different external loads for the incompressible fluid and for $V^{\text{tf}}/V_0 = 0.9$ and $\Delta/\lambda = 0.01$, from left to right: (1) the step corresponding to activation of the fluid; (2) the plastic zone appears in the valley between the asperities; (3) opening of the trap (contact area is zero; as seen from the plastic field, at this moment the entire solid is plastified).

However, as demonstrated by our simulations, due to the high hydrostatic compressive state, the pressure in the contact can significantly overpass the material hardness.

First, we study incompressible fluid, and present in Fig. 7.8(c) the evolution of contact area in the case of $V^{\text{tf}}/V_0 = 0.9$. It shows significantly different behaviour compared to elastic material: after the fluid becomes activated, the contact area is non-monotonic function of external pressure, it has a small increase, and then an abrupt decrease, corresponding to the state when fluid pressure reaches the value of contact pressure, and, consequently, permeation becomes possible. Normal tractions in contact interface increase beyond $6\sigma_Y$ due to hydrostatic pressurization of the solid. In Fig. 7.8(d) the resulting evolution of the global CoF is presented, which shows considerably lower values of the CoF for both considered materials, than the ones observed in the purely elastic case (for the same external pressure). Fields of the accumulated plastic strain in the solid at different loading steps are presented in Fig. 7.9, note that once the fluid gets pressurized, the plastic zone is not limited to the contact vicinity, but spreads over the entire interface and, consequently, the whole bulk of the solid. Notably, a secondary onset of plastic deformation appears in the trough of the wavy profile, it complements the classical plastic core appearing under the contact zone and spreading to the contact interface [Johnson, 1987, Mesarovic and Fleck, 1999, Kogut and Etsion, 2002, Alcalá and Esqué-de los Ojos, 2010].

Varying the slope of the profile as in Sections 7.4 and 7.6, we showed that in contrast to the case of elastic solids, where the evolution of the contact area during the process of trap opening does not depend on the slope of the profile Δ/λ , in case of elasto-plastic solids, for a given ratio V^{tf}/V_0 , once the fluid gets pressurized, the higher is the ratio Δ/λ , the bigger is the contact area.

The behaviour of the system incorporating the elasto-plastic material and non-linearly compressible fluid is shown in Figs. 7.10(a-d): the contact area after reaching its maximum abruptly decreases, resulting in a fast permeation of the fluid in the contact interface and eventual opening of the contact. Note that after a relatively fast saturation of the contact pressure at approximate material hardness $H \approx 3\sigma_Y$, a further increase in pressure without fluid permeation still remains possible up to huge pressure values

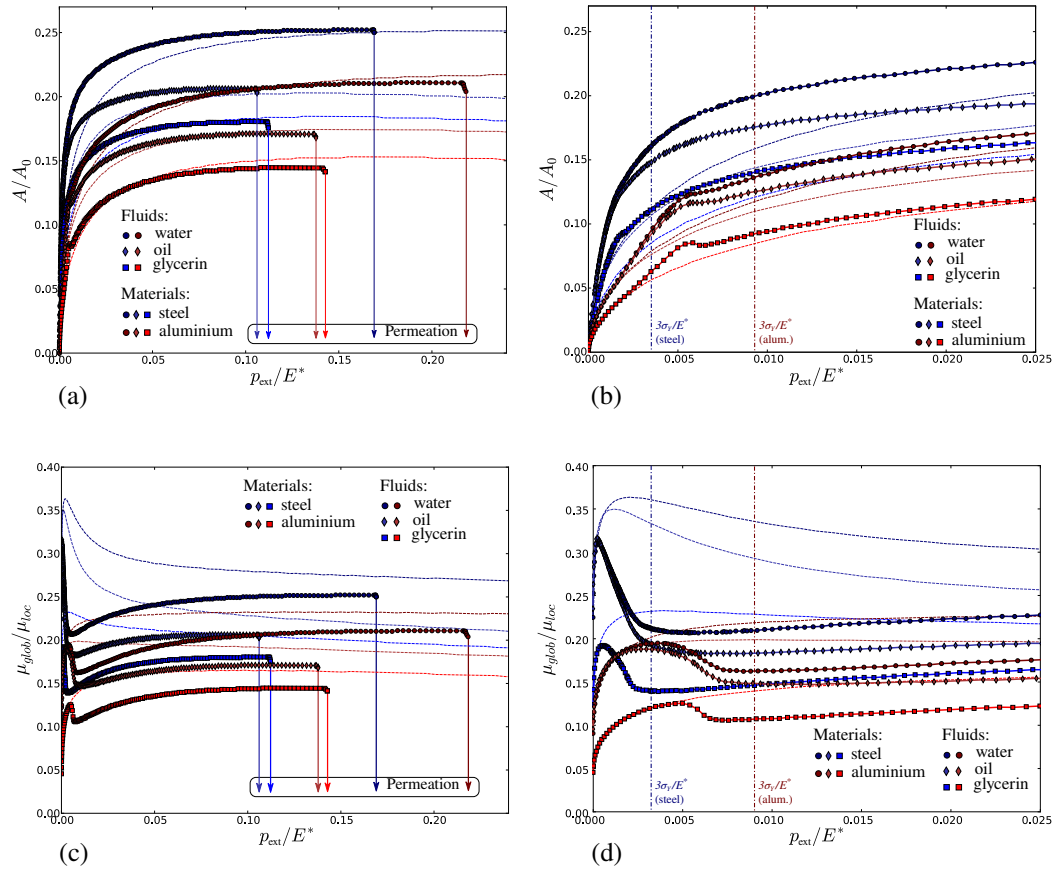


Figure 7.10: The behaviour of the system considering elasto-plastic material and non-linearly compressible fluid: (a) evolution of the ratio of real contact area to the apparent one under increasing external pressure; (b) the same as (a), but the results are shown in range $0 \leq p_{\text{ext}} \leq 0.025E^*$; (c) evolution of the ratio between global and local coefficients of friction; (d) the same as (c), but the results are shown in range $0 \leq p_{\text{ext}} \leq 0.025E^*$. Dashed curves are presented for comparison with the cases of purely elastic solids. Vertical dash-dotted line indicates the hardness $H = 3\sigma_Y$.

$p_{\text{ext}} \gg \sigma_Y$. In reality however, due to the micro-roughness permeation of the fluid in the contact interface may happen on earlier stages of the deformation.

In Fig. 7.10(c,d) the evolution of the global CoF is depicted, which shows a rather similar behaviour to the one observed in the case of the elastic solid, having multiple extrema in the beginning of loading. Note that the amplitude of the first maximum of CoF is increasing with increasing slope of the profile, which was also observed in the simulations with the purely elastic material.

7.8 Friction in the contact interface

In this Section we study the evolution of frictional tractions in the contact interface during the process of the trap opening. Before presenting these results, we start by a brief discussion of an example application of the quasi-static incremental framework for the frictional contact, developed in Chapter 4. Note that here we consider only normal external loading, supplemented by symmetric boundary conditions on vertical walls. Furthermore, in order to obtain more reliable results, we refined the mesh to have 512 nodes within the maximal considered extension of the contact zone $a/\lambda = 0.05$, keeping the total number of contact elements equal to 1024.

7.8.1 Validation of the numerical framework

The main purpose of this discussion is to emphasize the importance of considering a significant number of load steps to obtain physically relevant results using a quasi-static frictional framework (which relates the frictional traction to the increment of the tangential displacement rather than to its rate). We compare two frictional contact simulations with the same final external load and different loading sequences: the full load is applied in either 1 or 100 load steps, see Fig. 7.11. Note that in case of simulation with 100 load steps the displacement of the bottom edge at the i -th step is prescribed as $w^i|_{z=-H} = W (i/N)^2$, where $N = 100$, and W is the full displacement of the bottom edge after 100 steps. This type of loading was chosen instead of an equally-stepped loading in order to improve the representation of the frictional traction at the very beginning of the loading (i.e., in the zone close to $x = 0$). We noted that the obtained result is more smooth if the length of the contact zone $2a$ is growing linearly between increments, while, according to the frictionless solution (7.4), in the very beginning of loading $a \sim \sqrt{p_{\text{ext}}}$, and the external load is proportional to the far-field approach, i.e. $w|_{-H}$, see [Popov, 2010]. Therefore, by increasing the displacement quadratically, we obtain a linear evolution of the contact area.

Clearly, the results of the two presented simulations differ drastically, both in terms of the value of frictional traction and in the partition of the contact into stick and slip zones. Moreover, considering frictional traction as a function of the x -coordinate, we note that in case of 1 load step $\sigma_t(x)$ has a non-smooth transition between stick and slip zones, and, moreover, changes the sign of its second derivative at that point. At the same time, in case of simulation with 100 load steps the transition between stick and slip zones is smooth. Since the considered wavy profile in the region of interest is very close to the parabolic one, the numerical results should be described by the available analytical solution for the frictional contact between parabolic solids [Spence, 1975]. This solution predicts a smooth transition between stick and slip zones, and, therefore, we conclude that the numerical result obtained under a loading sequence of 100 steps is physically relevant, while the other one is not. This conclusion explains a high number of load steps used in simulations with friction presented in this section.

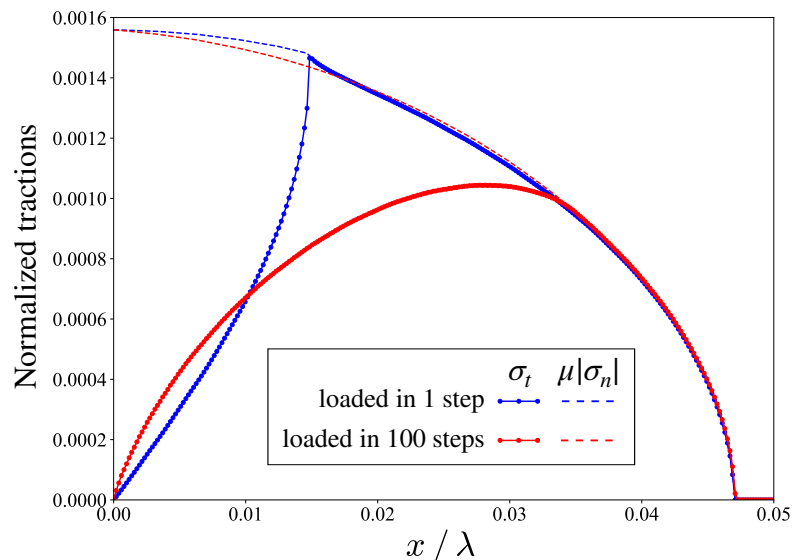


Figure 7.11: Comparison of two frictional (normal loading only) contact simulation with the same final normal load ($p_{\text{ext}}/E^* = 0.00018$), but different loading sequences: the full load is applied in either 1 or 100 load steps. Full curves with markers represent frictional (shear) traction, while dashed ones show normal traction multiplied by the CoF $\mu = 0.3$. Both tractions are normalized by E^* .

7.8.2 Effect of the trapped fluid on frictional tractions

We consider a coupled problem for an incompressible fluid with Coulomb's friction in the contact interface, as in previous analysis the shear forces in the trapped fluid are neglected due to quasi-static analysis. The following geometrical parameters are used: $\Delta/\lambda = 0.01$, $V^{\text{tf}}/V_0 = 0.95$.

We emphasize that the external tangential load is absent in this study, thus we consider here only normal loading, in which two stages can be distinguished. During the first stage the external pressure p_{ext} increases from zero value to p_{act} , the value necessary to bring the fluid into active state, and the contact area reaches the maximum value. Results for the first stage are presented in Fig. 7.12(a), where, in order to visualize stick and slip zones, we plot normal tractions, multiplied by the coefficient of friction (CoF) $\mu = 0.2$. Those results are very close to the classic self-similar (remaining the same for any load under a proper coordinate/pressure scaling [Spence, 1975]) distribution of tractions, because the wavy profile in the region of interest is very close to a parabolic curve. During the second stage of loading ($p_{\text{ext}} > p_{\text{act}}$) the fluid is in the pressurized state and influences the interfacial traction distribution.

Since the slope of the roughness profile is small, the distribution of normal traction should resemble, at least for p_{ext} not much greater than p_{act} , the analytical solution for a fluid bulk modulus tending to infinity ($K \rightarrow \infty$), in which a uniform pressure offset is added everywhere to the field of the normal traction corresponding to the external pressure p_{act} . In accordance to that, tangential traction remains almost unchanged over the majority of the contact interface. Since the contact pressure is increased by the fluid pressure offset, all points pass to the stick state, i.e. adhere to their positions. However, due to the finiteness of the slope being taken into account, the distribution of normal traction slightly differs from the analytical solution in the same way as was discussed in Sec. 7.5, see Fig. 7.7(b), i.e. a slight decrease of the contact area takes place.

For p_{ext} sufficiently greater than p_{act} , see Fig. 7.12(b), the effects of finite slope become more pronounced, the contact area is gradually decreasing and a remarkable

evolution of the tangential traction is observed. A singularity in the tangential traction emerges at the boundary of the contact zone, with the value at the tip of this singularity limited by the Coulomb's law. In order to explain and verify this intriguing result, we consider an analogy between the process of the trap opening with the interfacial friction and the mode-II crack propagation in the framework of linear elastic fracture mechanics (LEFM) theory [Tada et al., 1973].

Note that the analogy is not complete in physical sense: during the process of trap opening due to pressurization of the incompressible fluid, new surface is not created, since no atomic bonds must be broken in order to separate the surfaces. The physical reason for the singularity in tangential stress is the following: when points of the surface loose contact, their normal traction reduces not down to zero, but to the value of fluid pressure, thus the frictional limit near the contact edge remains elevated. Thus, the points of the interface before losing contact have non-zero shear traction, and being liberated from this traction after losing the contact, these points slide freely, in absence of frictional resistance, towards the centre of the contact zone.

The fluid activation corresponds to the maximal extension of the contact zone, we shall denote the maximal contact half-length as a^* , and during the subsequent increase of the external pressure the width of the contact zone is monotonically decreasing. For sufficiently small slope of the roughness profile, the situation corresponding to contact half-length $a < a^*$ can be considered as a configuration of two bonded dissimilar solids with two aligned semi-infinite interfacial cracks in the interface, separated by $2a$, see Fig. 7.12(c). Using the superposition principle, the observed stress state, corresponding to the half-length of the contact patch a , can be represented as a superposition of the initial shear traction $\sigma_t^*(x)$, corresponding to the moment of activation of the fluid, and a stress induced by the same traction with the opposite sign, $\sigma_t^-(x) = -\sigma_t^*(x)$ applied only on the surfaces of the cracks in the intervals $x \in [-a^*, -a]$ and $[a, a^*]$. Such traction induces a singular shear stresses in the region between two cracks $x \in [-a, a]$, thus $\sigma_t^-(x)$ can be written as:

$$\sigma_t^-(x) = \begin{cases} -\sigma_t^*(x), & x \in [-a^*, -a] \cup [a, a^*] \\ \frac{1}{\sqrt{2\pi}} \text{Im} \left\{ K(a, \sigma_t^*) \left(\frac{(x-a)^{i\epsilon}}{\sqrt{|x-a|}} - \frac{(x+a)^{i\epsilon}}{\sqrt{|x+a|}} \right) \right\}, & x \in [-a, a] \\ 0, & |x| > a^*, \end{cases} \quad (7.33)$$

where K is the complex stress intensity factor, see [Rice and Sih, 1965, Rice, 1988], and two terms in brackets in (7.33.2) correspond to two semi-infinite cracks being considered, so that $\sigma_t^-(0) = \sigma_t^*(0) = 0$, Im is the imaginary part. Therefore, the resulting distribution of shear tractions is given by the superposition $\sigma_t(x) = \sigma_t^*(x) + \sigma_t^-(x)$.

The complex stress intensity factor K is calculated using the existing analytical formula for considered configuration and shear traction distribution [Rice and Sih, 1965, Rice, 1988]:

$$K(a, \sigma_t^*) = [k_1(a, \sigma_t^*) + ik_2(a, \sigma_t^*)] \sqrt{\pi} \cosh(\pi\epsilon), \quad (7.34)$$

where

$$\begin{aligned} k_1(a, \sigma_t^*) &= \frac{\sqrt{2}}{\pi} \int_a^{a^*} \frac{\sigma_t^*(x) \sin(\epsilon \ln(x-a))}{\sqrt{x-a}} dx, \\ k_2(a, \sigma_t^*) &= \frac{\sqrt{2}}{\pi} \int_a^{a^*} \frac{\sigma_t^*(x) \cos(\epsilon \ln(x-a))}{\sqrt{x-a}} dx, \end{aligned} \quad (7.35)$$

and the parameter ϵ accounts for the different properties of the two bonded solids, in

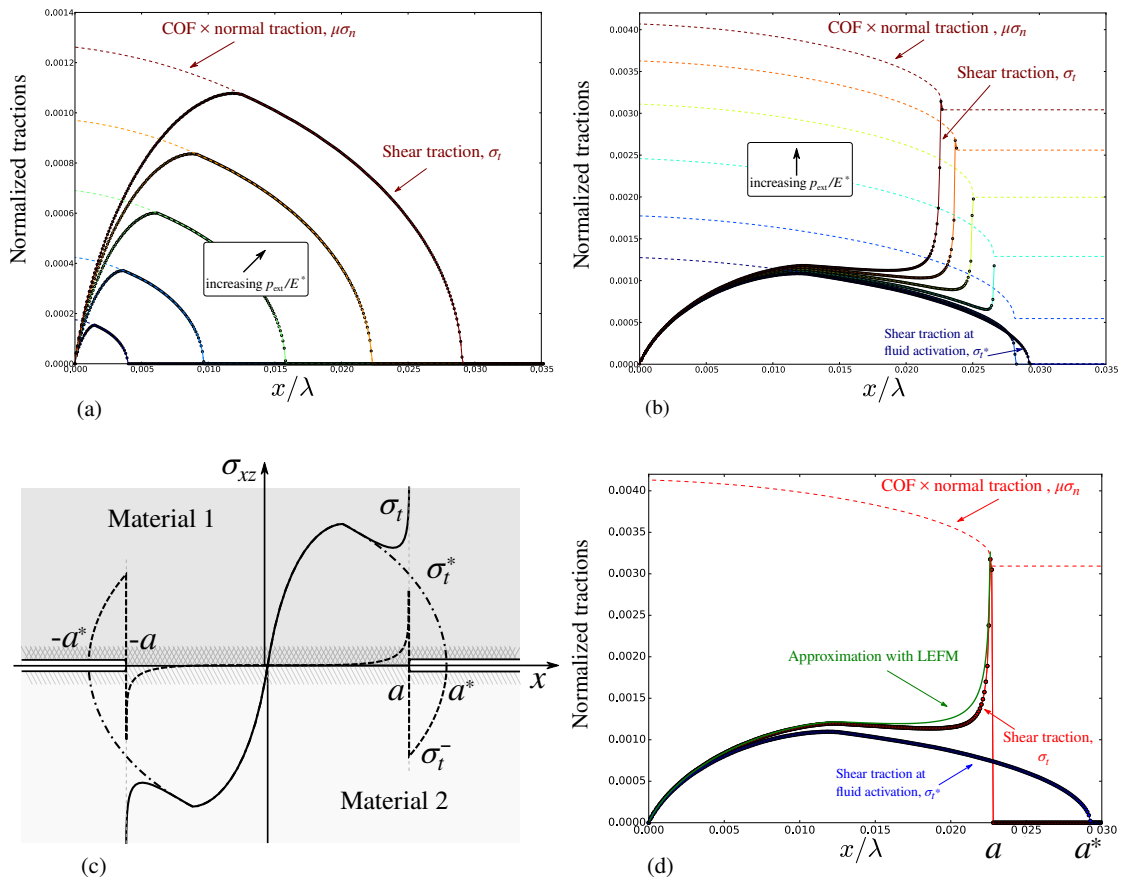


Figure 7.12: Distribution of the tangential tractions in the contact interface: (a) Fluid is not pressurized. (b) Under increasing external load fluid gets pressurized, contact area is decreasing and a singularity in tangential traction appears (limited by the Coulomb's law). (c) Sketch of the analogous problem for two bonded dissimilar solids with two aligned semi-infinite interfacial cracks in the interface. (d) Comparison of the numerical results for the shear tractions and approximation provided by the analogy with the LEFM.

case one of them being rigid, it equals to

$$\epsilon = -\frac{1}{2\pi} \ln(3 - 4\nu). \quad (7.36)$$

In Fig. 7.12(d) we plot the approximation of the shear traction distribution in the interface during trap opening, discussed above. A sound similarity is found between numerical results and analytical formulae provided by the LEFM. Therefore, we have shown that during the process of trap opening due to increasing pressure in the fluid with friction taken into account, the tangential tractions near the contact edges are elevated up to the limit provided by the Coulomb friction law. Consequently, even if the majority of the interface remains in stick state, local slip zones emerge at the boundaries of contact zones. It is important to account for such an elevated shear stress near edges of contact zones surrounding trapped fluid, which appears under normal loading, in the analysis of damage evolution and crack onset under monotonic and cycling loading, including fretting fatigue [Hills, 1994, Proudhon et al., 2005].

7.9 Conclusions

In this chapter we solved the problem of mechanical contact between a deformable body with a wavy surface and a rigid flat, taking into account pressurized fluid trapped in the interface. A mathematical framework for this coupled problem for both incompressible and compressible (with constant or pressure-dependent bulk-modulus) fluid was formulated in Chapters 4 and 5.

The proposed framework accounts for a finite slope of the roughness profile, while in previous investigations using classical boundary element method (which accounts only for vertical displacements) and existing analytical solutions only infinitesimal slopes were considered. We showed that in the considered coupled problem, a reduction of the contact area can occur due to elastic flattening of asperities by fluid pressure. Thus the reduction of the global coefficient of friction is caused not only by the external load repartition between the solid contact and the pressurized fluid, but also by the contact area reduction.

The reduction of the contact area takes place if the fluid bulk-modulus is higher than that of the solid. In case of incompressible fluid this criterion is satisfied and the process of trap opening is observed. However, this case is non-physical, since real lubricating fluids in the unpressurised state have much lower bulk modulus than solids. A more relevant case is a compressible fluid with linear dependence of bulk modulus on pressure, which ensures a non-monotonic variation of the contact area, and thus of the global coefficient of friction, leading to reduction of the both for sufficiently large pressures.

Among other applications, the obtained results are relevant for the mechanical behaviour of multi-cracked materials such as rocks. We showed that due to the presence of pressurized fluid in the interface, the frictional limit does not increase linearly with increasing external load, but reaches its maximum and decreases down to zero. This behaviour is similar to pressure-dependent plasticity models with a cap (e.g. Drucker-Prager cap model), which corresponds to the decay of the von Mises yield stress with the increasing pressure.

In addition to elasticity, we considered physically more relevant elasto-plastic materials in combination with realistic fluids. In this case, the contact pressure is bounded, while the fluid can bear arbitrary pressure, consequently under certain external pressure fluid permeates in the contact zones abruptly.

When interfacial friction is considered in the coupled problem, previously unreported

quasi-singularities appear in shear stresses near edges of contact patches during fluid-trap opening under normal loading. We showed that these singularities can be analytically estimated using the analogy between trap opening and crack propagation in the interface between two bonded dissimilar solids. It is important to account for such an elevated shear stress, caused by the trapped fluid, in the analysis of damage evolution and crack onset under monotonic and cycling loading, including fretting fatigue.

The problem of trapped fluid is relevant for metal forming (drawing and rolling), where a lubricant is present in the interface and involved loads are high. It is also relevant in poromechanics, especially in cracked media filled with fluid and subjected to complex stress states with high hydrostatic component, which can ensure contact between surfaces of internal cracks. Finally, at the microscopic scale, where the surface roughness plays a crucial role, the trapped fluid provides additional load-bearing capacity, and thus reduces the macroscopic static friction. Under increasing load, the trapped fluid is squeezed out of its trap thus resulting in even smaller global coefficient of friction.

Chapter 8

Fluid flow in contact interface with model geometry

Résumé de Chapitre 8 “L’écoulement de fluide à travers l’interface de contact avec une géométrie du modèle”

Dans ce chapitre, nous évaluons les capacités du cadre numérique développé dans la deuxième partie de la thèse. Tout d’abord, l’écoulement induit par la pression dans l’interface de contact entre un solide élastique présentant une surface ondulée et un plan rigide est simulé à l’aide de l’approche de couplage bidirectionnelle. Parallèlement, une solution analytique approchée est obtenue pour ce problème couplé. Une bonne concordance est obtenue entre les deux solutions dans le domaine de validité de la solution analytique. Enfin, nous avons montré que la pression externe nécessaire pour sceller le canal est une fonction affine de la pression d’entrée et ne dépend pas de la pression de sortie. Nous avons également considéré l’écoulement de fluide au travers d’un canal ondulé avec une élévation en forme d’anneau de la surface au centre du canal. Cette structure de type “atoll” forme une zone de fluide piégé. Une fois piégé, le fluide fournit une capacité de charge supplémentaire, nécessitant une charge externe plus importante pour sceller l’interface, c’est-à-dire que le fluide piégé augmente la transmissivité. Enfin, nous avons montré que la convergence quadratique de la méthode de Newton-Raphson est atteinte dès que la partition de l’interface en zone de contact, d’écoulement et de fluide piégé finale est atteinte, ce qui confirme la robustesse de l’algorithme de résolution proposé.

In the previous chapter the developed numerical framework was used to solve the trapped fluid problem without fluid flow in the plane strain formulation. Here, we extend the application range of the proposed monolithic framework and study the fluid flow across an extruded wavy channel brought in contact with the rigid flat. Afterwards, we consider a more complex case, adding a ring-shaped elevation of the surface at the centre of the channel, which serves as a fluid trap. As a result, this geometry allows to test the full coupling of contact, fluid-flow and a trapped fluid zone.

8.1 Fluid flow across a wavy channel brought in contact

We study a pressure driven flow in contact interface between an elastic solid with an extruded wavy surface and a rigid flat, considering the two-way coupling between the contact and the fluid problems. An approximate analytical solution is obtained for this coupled problem, while the finite-element monolithic framework (see Chapter 6) is used

to solve the problem numerically. Furthermore, we calculate the transmissivity of the contact interface and study the dependence of the critical external pressure, needed to seal the channel, on the fluid pressure at inlet and outlet.

8.1.1 Problem set-up

We consider an array of wavy channels of length L along the OY -direction (see Fig. 8.1(a)) with a sine-shape section:

$$z(x') = \Delta[\cos(2x') - 1], \quad (8.1)$$

where $x' = \pi x/\lambda$, brought in contact with a rigid flat⁷, and a pressure driven flow across this interface of an incompressible viscous fluid. The pressure drop is given by $\Delta p = p_i - p_o$, where p_i and p_o are the inlet and outlet pressures, respectively. We assume an isothermal fluid flow at a temperature at which it does not evaporate under the pressure drop on its way from the inlet to the outlet. The system of equations to be solved takes the following form:

$$\begin{cases} \nabla \cdot [g_n^3 \nabla p] = 0 & \text{in } \Gamma^f & (8.2a) \\ p|_{y=0} = p_i, \quad p|_{y=L} = p_o, \quad [\mathbf{q} \cdot \mathbf{e}_x]|_{x=0, \lambda/2} = 0 & (8.2b) \\ \nabla \cdot \boldsymbol{\sigma} = 0 & \text{in } \Omega & (8.2c) \\ u_x|_{x=0, \lambda} = 0, \quad u_y|_{y=0, L} = 0, \quad \sigma_{zz}|_{z=-\infty} = -p_{\text{ext}} & (8.2d) \\ |\sigma_n| - p \geq 0, \quad g_n \geq 0, \quad (|\sigma_n| - p) g_n = 0 & \text{on } \Gamma \subset \partial\Omega, & (8.2e) \end{cases}$$

where Eq. (8.2a) is the Reynolds equation for the pressure-driven stationary incompressible viscous Poiseuille flow (see also Section 2.3.3), g_n is the distance between immobile walls, and p is the fluid pressure. Eq. (8.2b) summarizes boundary conditions for the fluid problem: the fixed inlet p_i and outlet fluid pressure p_o and zero flux \mathbf{q} at crests of the surface resulting from the problem symmetry. Eq. (8.2c) is the momentum balance equation for the quasi-static solid mechanical problem in absence of volumetric forces, while (8.2d) summarizes boundary conditions for the solid problem, where p_{ext} is the squeezing pressure applied at infinity. Due to the symmetry, horizontal displacements are zero at lateral walls orthogonal to the x -axis, which corresponds to an infinite periodic set-up. Vertical walls on the inlet and outlet sides are assumed to remain flat. The adjusted contact conditions (8.2e) will be explained in the following sub-section.

Linear isotropic elasticity is considered for the elastic half-space Ω , so the stress-strain relation is given by the Hooke's law (2.17). Finally, we have one unknown vector field in three dimensions, displacements $\mathbf{u}(x, y, z)$ in Ω , and one unknown scalar field in two dimensions, which is the hydrostatic fluid pressure $p(x, y)$ in Ω_f . We assume that full contact is not reached in any section parallel to OX , so the fluid can always circulate.

In Fig. 8.1(a) we also sketch the expected surface normal traction, note that in the contact zones it is not uniform along the OY axis, but is rather increasing towards the outlet side, which should be caused by the effect of the fluid pressure acting on the surface of the solid. Accordingly, the width of contact patches in sections orthogonal to OY should be also increasing towards the outlet, corresponding to the direction of the fluid pressure drop, see also sketches of the interface under the one-way coupling approach (which neglects the effect of the fluid pressure) in Fig. 8.1(b) and the two-way coupling in Fig. 8.1(c).

⁷Note that all the discussions are valid not only for an elastic solid with a wavy surface in contact with a rigid flat, but for two elastic solids with the effective wavy roughness given by $z = z_1 - z_2 + c$, where z_1, z_2 determine surface geometries of the two contacting solids, and c is an arbitrary constant, see [Barber, 2003].

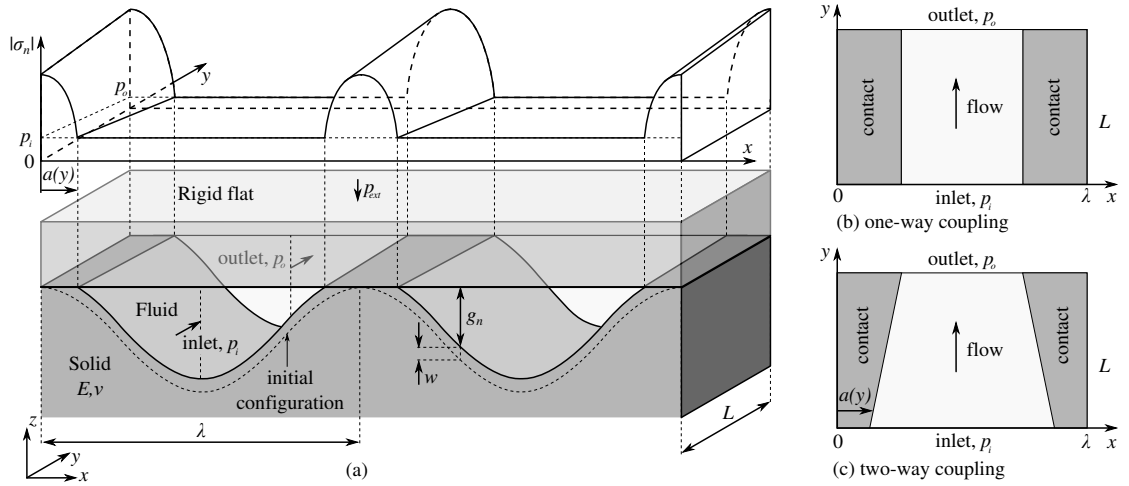


Figure 8.1: Problem set-up: (a) an elastic wavy surface comes in contact with a rigid flat, and an incompressible fluid flows under pressure difference from the inlet to the outlet; the resulting normal traction component σ_n is shown. Sketches of the contact interface are also given, corresponding to (b) one-way and (c) two-way coupling approaches. Note that due to fluid pressure acting on the surface of the solid (two-way coupling), it is expected that the contact patches are wider at the outlet, than at the inlet, corresponding to the direction of the fluid pressure drop.

We study the evolution of the two fields \mathbf{u} and p with the increasing external pressure p_{ext} . In particular, we are interested to know how the contact profile $a(y)$ delimits the contour of the fluid channel and how its depth $g_n(x, y)$ changes. In addition, we will determine under which conditions the flow is possible through the interface, i.e. what are the critical values of p_i, p_o, p_{ext} resulting in channel closure.

8.1.2 Wavy profile with pressurized fluid in the interface

Before making an attempt to solve the three-dimensional problem formulated in the previous section, we focus our attention on a simpler, planar contact problem with a pressurized fluid in the interface. Understanding of this problem will be helpful for the derivation of the approximated solution for the full problem, which is presented in the

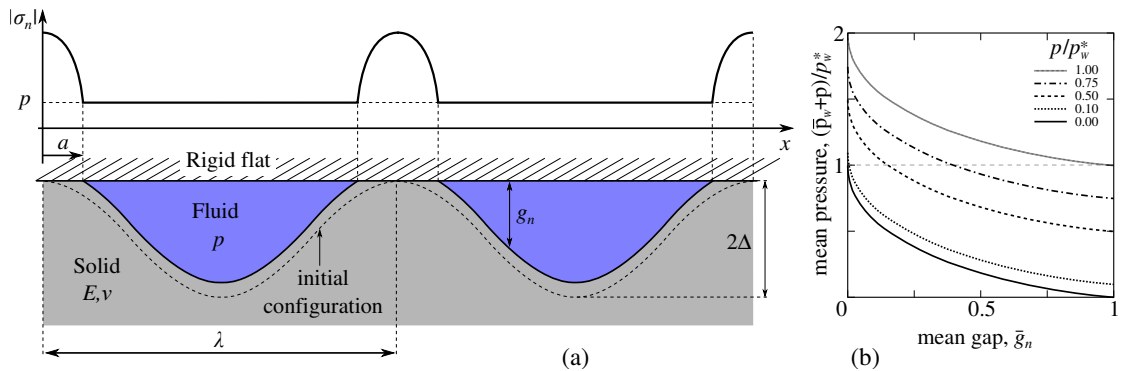


Figure 8.2: (a) - Contact between an elastic wavy profile and a rigid flat with a pressurized fluid in the interface, (b) - variation of the mean pressure on the surface with the mean gap.

following sub-section.

An elastic solid with a wavy surface (Fig. 8.2, Eq. (8.1)) is brought in contact with a rigid flat in a fluid environment, which is retained under a constant pressure p . A plane strain problem is considered. The solid mechanical contact problem was solved for this configuration by Westergaard without fluid pressure ($p = 0$), under the assumption of the infinitesimally small slope of the wavy profile [Westergaard, 1939], see [Johnson et al., 1985] and Section 7.2 of this dissertation. The pressure distribution in contact region was found to be

$$p_W(x', a') = 2\bar{p}_W(a') \frac{\cos(x')}{\sin^2(a')} \sqrt{\sin^2(a') - \sin^2(x')}, \quad (8.3)$$

where $x' = \pi x/\lambda$, $a' = \pi a/\lambda$, and a is the half-width of the contact zone; the mean contact pressure reads as

$$\bar{p}_W(a') = \frac{\pi E^* \Delta}{\lambda} \sin^2(a'), \quad (8.4)$$

i.e. $\bar{p}_W(a') = \int_0^{a'} p_W(x', a') dx'$, and E^* is the effective elastic modulus defined by

$$\frac{1}{E^*} = \frac{1 - \nu_1^2}{E_1} + \frac{1 - \nu_2^2}{E_2},$$

where E_i, ν_i are the Young's moduli and Poisson's ratios of the two contacting solids $i = 1, 2$, respectively. Associated effective displacements (taken with a negative sign) in the contact interface are given by

$$w(x', a') = \begin{cases} -\Delta \cos(2x') + C, & \text{in contact } \cos(x') > \cos(a') \\ -\Delta [\cos(2x') + 2 \sin(x')h(x', a') - 2 \sin^2(a') \times \\ \times \ln\left(\frac{\sin(x') + h(x', a')}{\sin(a')}\right)] + C, & \text{out of contact } \cos(x') \leq \cos(a'), \end{cases} \quad (8.5)$$

where $h(x', a') = \sqrt{\sin^2(x') - \sin^2(a')}$.

The solution of the contact problem for the same configuration in the pressurized environment was given in [Kuznetsov, 1985]. If we assume that the fluid pressure acts only vertically⁸ and that the profile slope is infinitesimal, the stress state in the contact interface in the presence of the additional fluid pressure, applied outside the contact patches, can be considered as a superposition of the stress state corresponding to the same contact area, but without influence of the fluid, i.e. the Westergaard's solution (8.3), and a uniform field of the fluid pressure p :

$$p_K(x', a') = p_W(x', a') + p. \quad (8.6)$$

A detailed rigorous analysis of the trapped fluid in the contact interface without the assumption of infinitesimal slopes and with the fluid pressure acting normally to the surface was carried out in Chapter 7 of this dissertation. However, here the simplified approach (8.6) is sufficient to study analytically the strongly coupled problem (8.2).

In the classical Hertzian contact the pressure decreases to zero towards contact edges [Johnson, 1987], but in a pressurized environment such a situation is impossible as the contact would be opened by the environmental pressure. Therefore, the fluid pressure p represents an offset which can be complemented by the mechanical pressure rising in contact. Since a constant p does not change the shape of the surface in infinitesi-

⁸In Chapter 7 of this dissertation this assumption was shown to be too prohibitive for certain applications even if the surface slope is assumed infinitesimal.

mal slope assumption, displacements obtained for pressures (8.3) and (8.6) differ only by a constant, thus Eq. (8.6) satisfies the unilateral contact conditions (see Section 2.2.1), which can be formulated for the coupled problem in the following way:

$$|\sigma_n| - p \geq 0, \quad g_n \geq 0, \quad (|\sigma_n| - p) g_n = 0, \quad (8.7)$$

where $|\sigma_n|$ is the absolute value of the normal traction, g_n is the gap, and p is the pressure of the environment. That is the form which appears in the main system of equations to be solved (8.2e).

The relation between the mean gap and the contact force almost does not change compared to the unpressurised case [Johnson et al., 1985, Kuznetsov, 1985], only a force offset $p\lambda$ is added for every period. The mean gap can be computed by integrating $g_n(x) = z(x) + w(x)$ in the non-contact region giving

$$\bar{g}_n = \Delta \left(1 - \frac{\bar{p}_W}{p_W^*} \left[1 - \ln \left(\frac{\bar{p}_W}{p_W^*} \right) \right] \right), \quad \text{for } \bar{p}_W \in [0, p_W^*] \quad (8.8)$$

where $p_W^* = \pi E^* \Delta / \lambda$ is the pressure needed to bring the wavy surface in full contact in the absence of fluid pressure; the mean contact pressure in the absence of fluid \bar{p}_W is given by Eq. (8.4). In Fig. 8.2(b) the normalized mean pressure $(\bar{p}_W + p)/p_W^*$ is plotted with respect to the mean gap \bar{g}_n evolution.

Based on this planar solution the following preliminary conclusion can be drawn for the three-dimensional problem. If the hydrostatic pressure changes only weakly along the channel, i.e. $p_i \approx p_o$, then the contact lines would remain almost parallel to the axis OY and the derivative of the gap with respect to y may be neglected. Then the hydrostatic pressure will be an affine function of the coordinate y , i.e. $p = p_i + (p_o - p_i)y/L$. The flux, which would have a non-zero component only along y axis, can be readily found as $q_y(x) = -g^3(x)(p_o - p_i)/(12\mu L)$; note that it depends only on the x -coordinate. Thus, naturally for the situation $p_i \approx p_o$ the channel would be sealed at $p_{\text{ext}} \approx p_W^* + p_o$.

8.1.3 Approximate analytical solution

To provide an approximate analytical solution for the coupled problem formulated in Eqs. (8.2a)-(8.2e) we suggest to make several strong assumptions. We assume (i) that in every section $y = \text{const}$, the pressurized Westergaard-Kuznetsov solution (8.6) is satisfied for $a = a(y)$ and $p = p(y)$. However, it is clear that it should imply that $\partial p / \partial x = 0$, which could seem to exclude the channel narrowing. But since in the following, the problem will be reduced to a one-dimensional flow along OY axis, this assumption (i) is not contradictory: the fluid pressure can be considered as the mean pressure in the section

$$p(y) = \frac{1}{\lambda - 2a} \int_a^{\lambda - a} p(x, y) dx. \quad (8.9)$$

We also assume (ii), which is the strongest and the least realistic assumption, that in every section the applied pressure is balanced, i.e.:

$$p_{\text{ext}} = \bar{p}_W + p = \text{const}, \quad (8.10)$$

for that we require that $p \leq p_{\text{ext}}$ in Ω , which is equivalent to require that $p_i \leq p_{\text{ext}}$. Another simplification would be (iii) to reduce the two dimensional Reynolds equation to a one-dimensional equation for the average gap (8.8), which implies that the hydrostatic pressure is independent of the x -coordinate: $p = p(y)$. Under these three assumptions

Eq. (8.2a)-(8.2b) can be rewritten as

$$\bar{g}_n^3 p' = C_1, \quad p(0) = p_i, \quad p(L) = p_o, \quad (8.11)$$

where the prime sign denotes partial derivative with respect to y , and C_1 is the integration constant. The condition of the zero flow at $x = 0, \lambda$ (see Eq. (8.2a)) is automatically satisfied as p is assumed not to depend on x .

Now we can use the relation between the mean gap and the pressure (8.8) through the relation (8.10), which being substituted in (8.11) yields:

$$\frac{-p_w^* \Delta^3}{C_1} \int_{\rho_i}^{\rho(y)} [1 - \rho \{1 - \ln \rho\}]^3 d\rho = y, \quad (8.12)$$

where $\rho(y) = (p_{\text{ext}} - p(y))/p_w^*$, and $\rho_i = \rho(0) = (p_{\text{ext}} - p_i)/p_w^*$. From (8.12) it follows that $\rho(y)$ should be a monotonically increasing function of y in the range $y \in [0; L]$. The boundary conditions now read as:

$$\rho(0) = \rho_i = (p_{\text{ext}} - p_i)/p_w^*, \quad \rho(L) = \rho_o = (p_{\text{ext}} - p_o)/p_w^*. \quad (8.13)$$

The integral $I(\rho) = \int [1 - \rho \{1 - \ln \rho\}]^3 d\rho$ from (8.12) with zero integration constant is evaluated as:

$$\begin{aligned} I(\rho) = & \rho - \alpha_1 \rho^2 + \alpha_2 \rho^3 - \alpha_3 \rho^4 + \beta_0 \rho^2 (1 - \beta_1 \rho + \beta_2 \rho^2) \ln(\rho) \\ & + \rho^3 (1 - \gamma \rho) \ln^2(\rho) + \frac{\rho^4}{4} \ln^3(\rho), \end{aligned} \quad (8.14)$$

where $\alpha_1 = 9/4$, $\alpha_2 = 17/9$, $\alpha_3 = 71/128$, $\beta_0 = 3/2$, $\beta_1 = 16/9$, $\beta_2 = 13/16$, $\gamma = 15/16$. The solution cannot be provided in the form $p(y)$, but rather $y(p)$, which reads as

$$y = \frac{-p_w^* \Delta^3}{C_1} (I(\rho) + C_2), \quad (8.15)$$

where the integration constants can be found through boundary conditions: $C_1 = -p_w^* \Delta^3 (I(\rho_o) - I(\rho_i)) / L$ and $C_2 = -I(\rho_i)$. The final approximate solution, which determines the average fluid pressure distribution along the channel coordinate y is given below:

$$\frac{y}{L} = \frac{I(\rho) - I(\rho_i)}{I(\rho_o) - I(\rho_i)}. \quad (8.16)$$

Resulting curves for the variation of hydrostatic pressure, mean gap and contact half-width along the channel are depicted in Fig. 8.3, 8.4(a), 8.4(b), respectively. This approximate result is able to capture the non-linear hydrostatic pressure distribution along the channel, to account for the induced deformation of the solid and thus to obtain the narrowing of the channel.

With the derived approximate solution we may calculate the fluid flux in the y -direction as

$$q_y(x, y) = -\frac{g_n^3(x, y)}{12\mu} \frac{dp(y)}{dy}, \quad (8.17)$$

where the gap $g_n(x, y)$ is obtained in each section $y = \text{const}$ using the Westergaard's solution (8.5) corresponding to the mean pressure $\bar{p}_w = p_{\text{ext}} - p(y)$, and the derivative

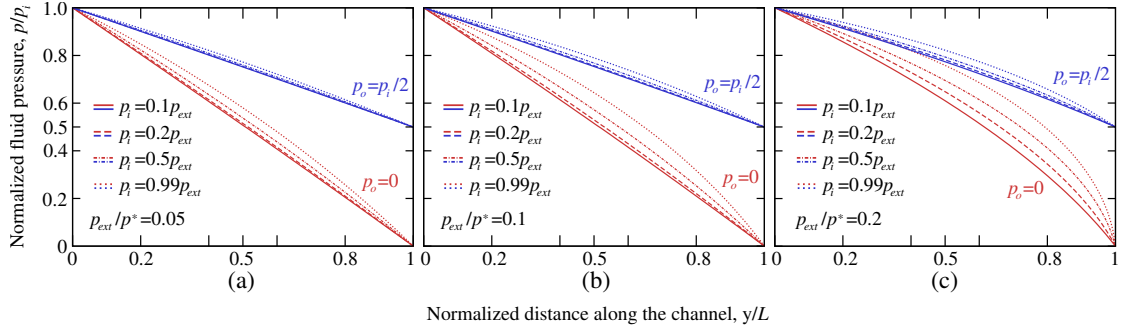


Figure 8.3: Approximate solution (8.16) for the mean hydrostatic fluid pressure distribution along the wavy channel in contact with a rigid flat for $p_o = p_i/2$ and $p_o = 0$ (a) $p_{\text{ext}}/p_W^* = 0.05$, (b) $p_{\text{ext}}/p_W^* = 0.1$, (c) $p_{\text{ext}}/p_W^* = 0.2$; the fluid pressure is normalized by the inlet pressure p/p_i and the coordinate is normalized by the channel length y/L .

dp/dy is calculated using (8.16) as

$$\frac{dp}{dy} = \left(-\frac{1}{p_W^*} \frac{L}{I(\rho_o) - I(\rho_i)} \frac{dI(\rho)}{d\rho} \right)^{-1} = \left(-\frac{1}{p_W^*} \frac{L}{I(\rho_o) - I(\rho_i)} [1 - \rho \{1 - \ln \rho\}]^3 \right)^{-1}. \quad (8.18)$$

This result will be used in the following for computation of the mean flux and the effective transmissivity of the interface and comparison with the numerical solution.

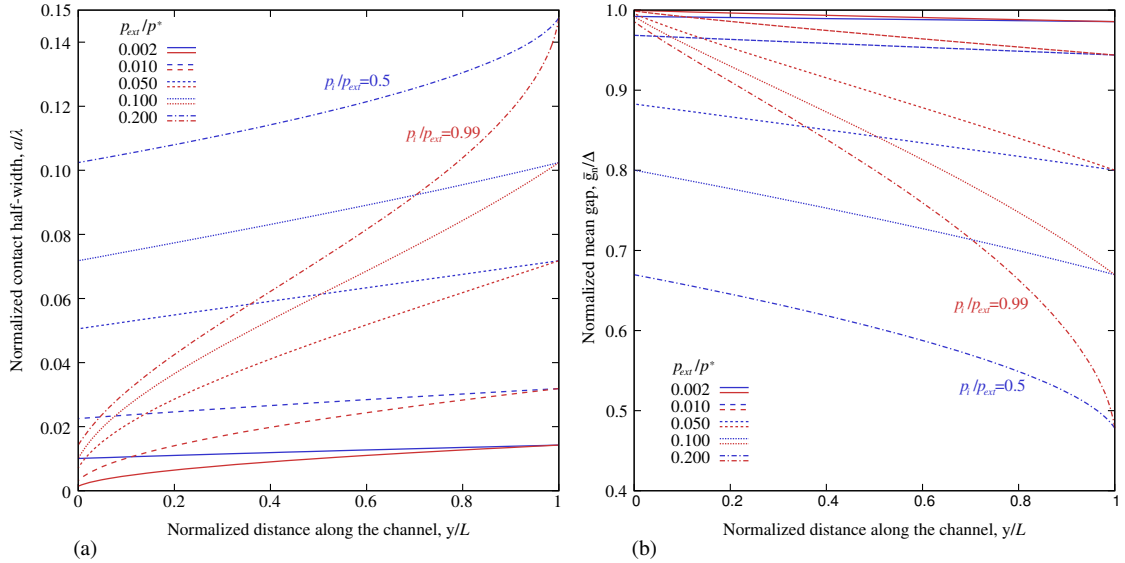


Figure 8.4: Approximate solutions for (a) normalized contact region half-width a/λ and (b) normalized mean gap \bar{g}_n/Δ evolution along the channel.

8.1.4 Numerical results and discussions

Using the constructed monolithic coupling scheme, we carried out several simulations for three different fixed inlet fluid pressures $p_i = 2, 10, 50$ MPa, respectively, and for outlet pressures $p_o/p_i = \{0; 0.25; 0.5; 0.75\}$. The solid is gradually brought in contact by applying vertical displacement on its bottom side. Due to the reflection symmetry of the geometry and loads, only the half wavelength is simulated using structured finite element mesh of hexahedral linear elements, with 128×128 square-shaped faces on the surface, the mesh gradually coarsens with the depth. The mesh is depicted in Fig. 8.5,

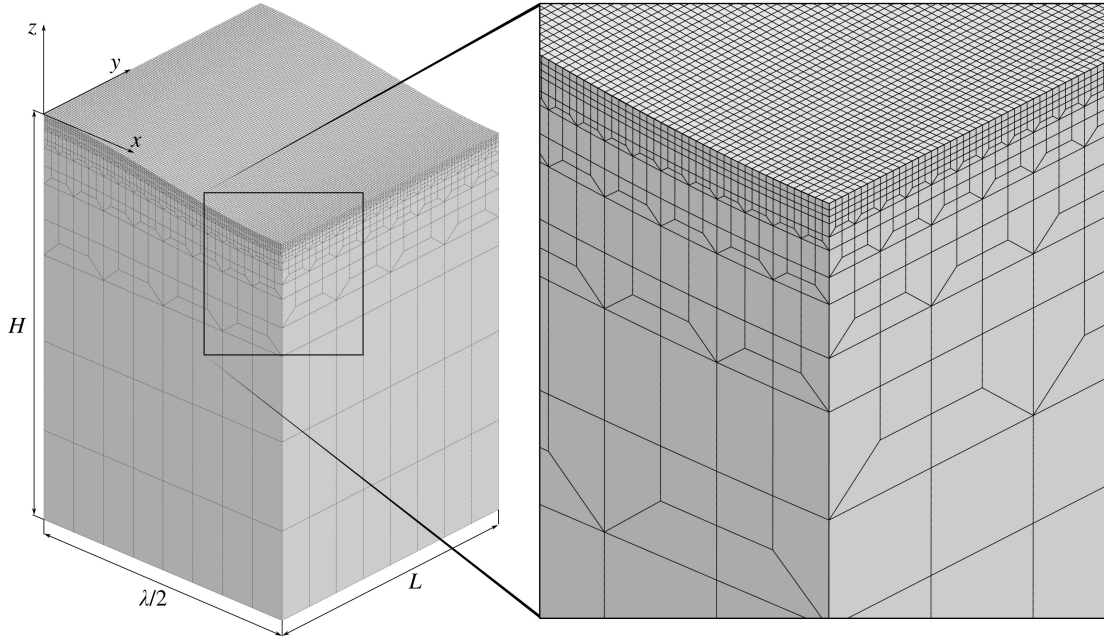


Figure 8.5: Finite element mesh with 128×128 elements on the contact surface, which was used to solve the coupled solid-fluid problem.

it contains approximately 109 000 nodes and approximately 98 000 elements with 8 integration points per element. At the bottom surface $z = -H$, the displacement vector is prescribed as $u_x = u_y = 0, u_z = kt$, where k is a load factor, t is the time. Geometrical parameters of the problem are the following: $L = 1$ cm, $\lambda = 2$ cm, $\Delta = 0.2$ mm, $H = 1.4$ cm, Young's modulus $E = 2$ GPa and Poisson ratio $\nu = 0.3$, thus $E^* \approx 2.2$ GPa.

We present the detailed results of numerical simulations in Fig. 8.6 and Fig. 8.7: the distribution of the fluid pressure and the contact pressure, as well as the gap and the fluid flux for the case $p_i = 50$ MPa, $p_o = 0$ and for two particular load steps: $p_{\text{ext}}/p_W^* = 0.48, 0.8$, respectively. On the initial stage of loading no contact occurs and the load is supported by the fluid solely, which flows along the entire channel (this classical situation is not presented in the figures). For higher loads, the solid comes in contact with a rigid flat, the contact starts from the outlet zone (see Fig. 8.6). With the increasing load the contact zone spreads out and at a certain load reaches the inlet zone (see Fig. 8.7); starting from this moment the approximate solution (8.16) becomes applicable. The gap, being bigger at the inlet due to higher inlet pressure, narrows towards the outlet region. The flow is localized within the trough of the wavy profile, and the flux intensifies towards the outlet. Due to the narrowing of the channel along the flow direction, the current lines converge towards the outlet, it results in a small but still distinguishable fluid pressure gradient in the OX direction, which was not explicitly taken into account in the derivation of the approximate solution.

In Fig. 8.8 numerical results for the variation along the channel of mean fluid pressure, mean gap and the contact width, as well as the contact and fluid pressure profiles in the section $y = L/2$ are compared with approximate solution from Section 8.1.3. A rather good agreement is obtained in the range of validity of the approximate result: the inlet pressure and external pressure satisfy the following conditions $p_i \leq p_{\text{ext}}, p_{\text{ext}} < p_W^*$, and they are chosen such that the contact zone reaches the inlet, see (8.10) and the discussion in Section 8.1.3. These limitations are quite strong and in reality ensure only a limited range of validity of the approximate solution.

In Fig. 8.9(a) the numerically computed evolution of the width of the contact zone on

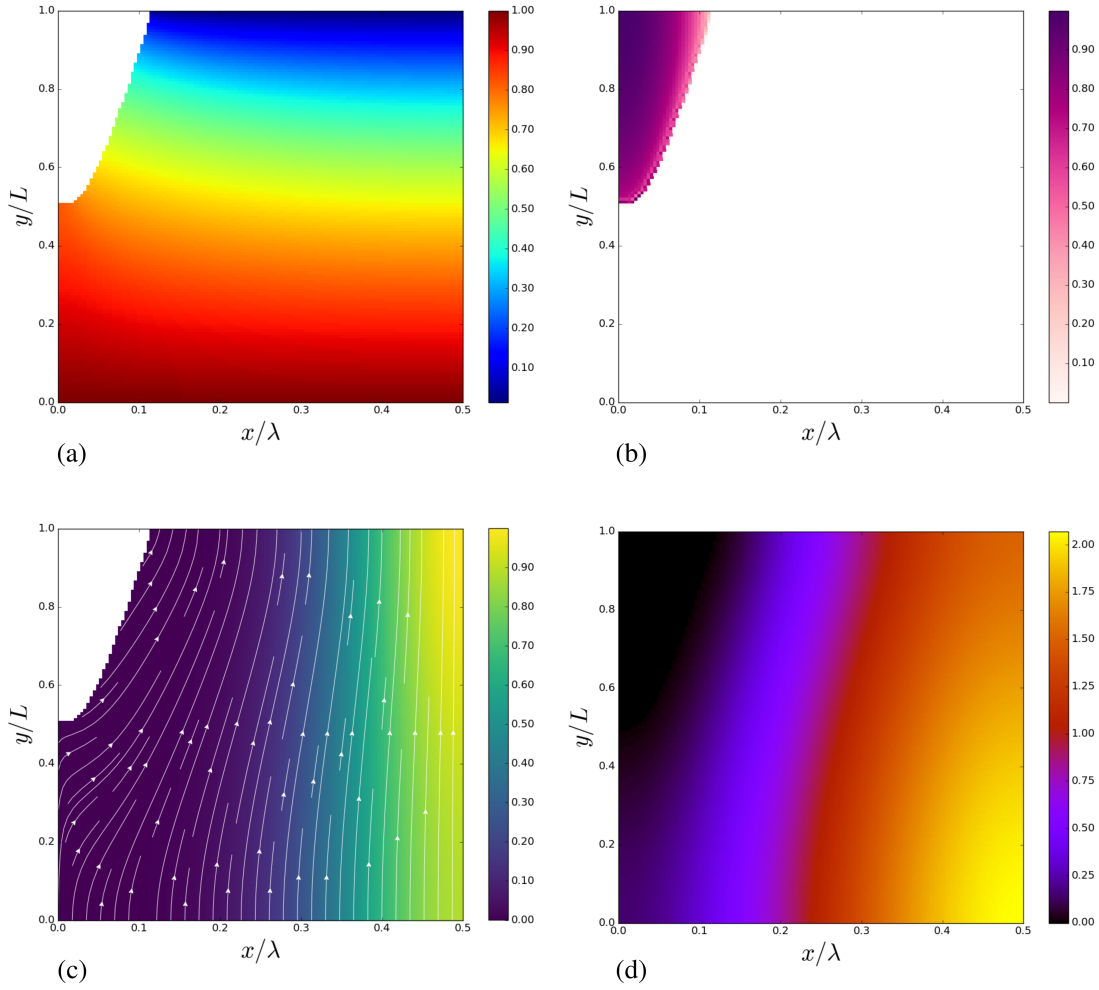


Figure 8.6: Results of the numerical simulation: (a) normalized fluid pressure p/p_i , (b) normalized contact pressure $|\sigma_n|/|\sigma_n|^{max}$, (c) normalized fluid flux intensity $|q|/|q_{max}|$, (d) normalized gap g/Δ ; $p_{ext}/p_w^* = 0.48$, $p_i/p_w^* = 0.72$, which corresponds to $p_i/p_{ext} = 1.5$.

the inlet and the outlet sides with the increasing pressure is depicted for three different inlet pressures $p_i/p_w^* = 0.03, 0.14, 0.72$ and $p_o = 0$. These results are compared with the analytical solution, which is valid if the external pressure is in the interval $p_i < p_{ext} < p_w^*$. In agreement with the assumptions of the approximate solution, the evolution of the width of the contact zone on the outlet side is independent of the inlet fluid pressure. However, in the numerical results curves both for inlet and outlet sides shift into the region of higher external pressures with the increasing inlet pressure. Note also that in the numerical results the outlet contact width grows faster than the inlet one. Finally, the strongly coupled numerical model shows that the higher is the inlet pressure p_i , the higher external load is needed to completely seal the channel.

In Fig. 8.9(b) the effective transmissivity K_{eff} of the wavy channel brought in contact is plotted: it is defined as

$$K_{eff} = -\frac{12\mu QL}{\Delta^3(p_o - p_i)}, \quad (8.19)$$

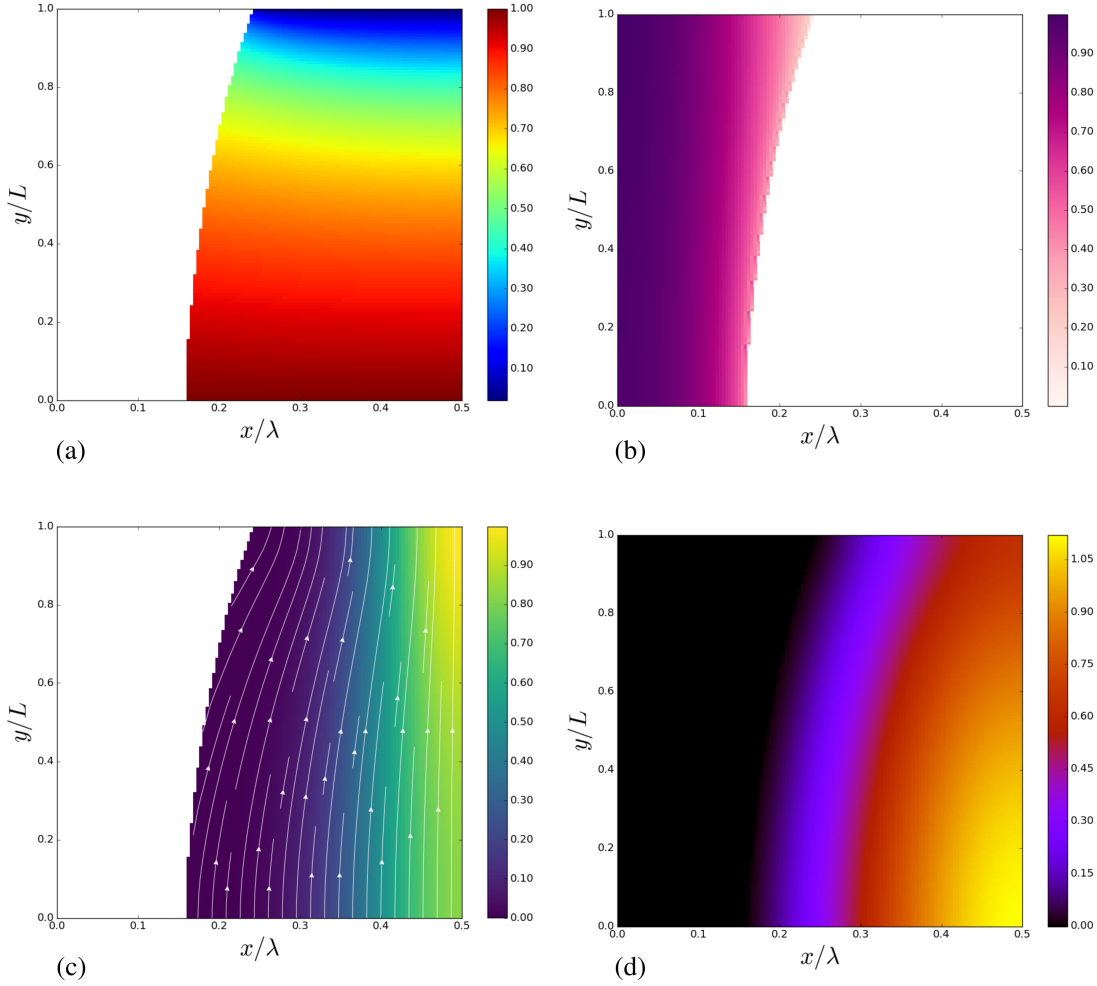


Figure 8.7: Results of the numerical simulation: (a) normalized fluid pressure p/p_i , (b) normalized contact pressure $|\sigma_n|/|\sigma_n|^{max}$, (c) normalized fluid flux intensity $|q|/|q_{max}|$, (d) normalized gap g/Δ ; $p_{ext}/p_w^* = 0.8$, $p_i/p_w^* = 0.72$, which corresponds to $p_i/p_{ext} = 0.9$.

where Q is the mean flux over the area $\lambda \times L$, i.e.

$$Q = \frac{1}{\lambda L} \int_0^\lambda \int_0^L q_y dx dy. \quad (8.20)$$

For computation of the local flux $q_y(x, y)$ we used the results of numerical simulations as well as the approximate solution (8.16)-(8.18). We considered the same three cases as before with different inlet pressures. For each case we highlight the corresponding external pressure necessary for the contact to appear at the inlet and outlet sides. As soon as the contact appears on both sides, the evolution of the transmissivity becomes exponential with respect to the external pressure normalized by p_w^* with the exponent ≈ -8 in all three cases. We note that this coefficient is lower than the one observed in simulations of the interface transmissivity for the surfaces with representative random roughness, where it was reported to be of order ≈ -12 [Dapp and Muser, 2016]. Closer to the complete sealing (the percolation limit) the transmissivity decays faster and can be very accurately described by a power law with respect to the difference between the critical external pressure p_{crit} , necessary to seal the channel, and p_{ext} , i.e. $K_{eff} \sim$

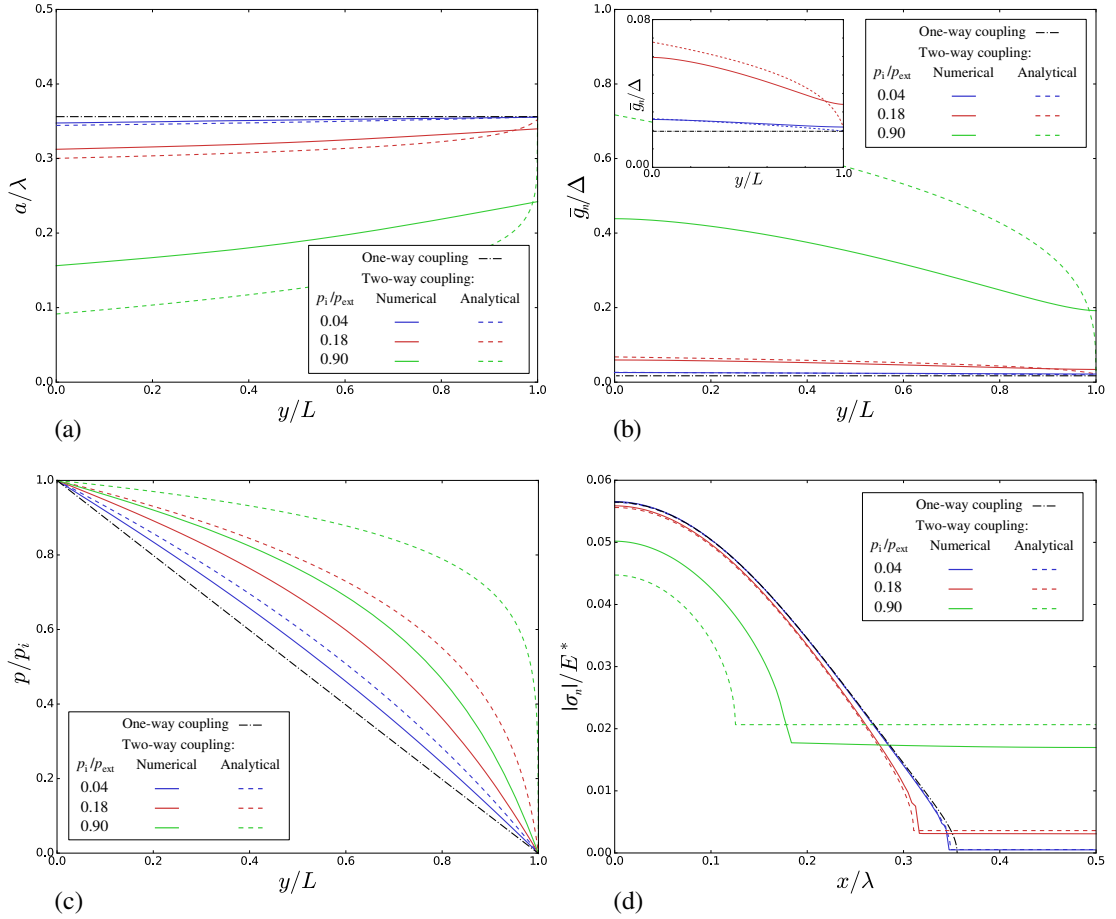


Figure 8.8: Comparison of results of numerical simulations with the approximate analytical solutions for (a) normalized contact region half-width a/λ , (b) normalized mean gap \bar{g}_n/Δ and (c) normalized fluid pressure p/p_i evolution along the channel, (d) normal traction component $|\sigma_n|/E^*$ in the section $y = L/2$.

$(p_{\text{crit}} - p_{\text{ext}})^\gamma$. Note that for our results γ was estimated as 6 ± 0.5 , while in accurate but one-way coupled studies of the percolation limit of bi-sinusoidal surfaces it was found to be equal to 3.45 [Dapp and Müser, 2015, Dapp and Müser, 2016].

The transmissivity for the lowest inlet pressure $p_i/p_W^* = 0.03$ almost coincides with that of the one-way coupling analysis and is well described by Kuznetsov's analytical solution. For higher inlet pressures we obtain significantly higher transmissivity. In the region of the exponential decay in case of two-way coupling we have ≈ 1.6 times higher transmissivity than in the case of the one-way coupling for $p_i/p_W^* = 0.14$ and ≈ 32 times higher for $p_i/p_W^* = 0.72$. Note that the transmissivity curves based on the analytical approximation (8.17)-(8.18) are in a very good agreement with the numerical ones in the range of the validity of the former. However, the analytical result cannot be used to study the flow near the percolation, since the pressure needed to seal the channel given by the approximate solution (i.e. $p_{\text{ext}} = p_W^* + p_o$) strongly underestimates the real one, which can be accurately studied using the numerical approach.

In the inset of Fig. 8.9(b) we plot the effective transmissivity with respect to the real contact area fraction, curves coincide for three different cases in the beginning of loading, while the complete sealing occurs at different values of the real area fraction $A/A_0 = 80\% - 90\%$. Note that in one-way coupled studies of the percolation limit of the *randomly rough* surfaces in contact, the complete sealing was found to correspond to $\approx 42\%$ of the real contact area [Dapp et al., 2012].

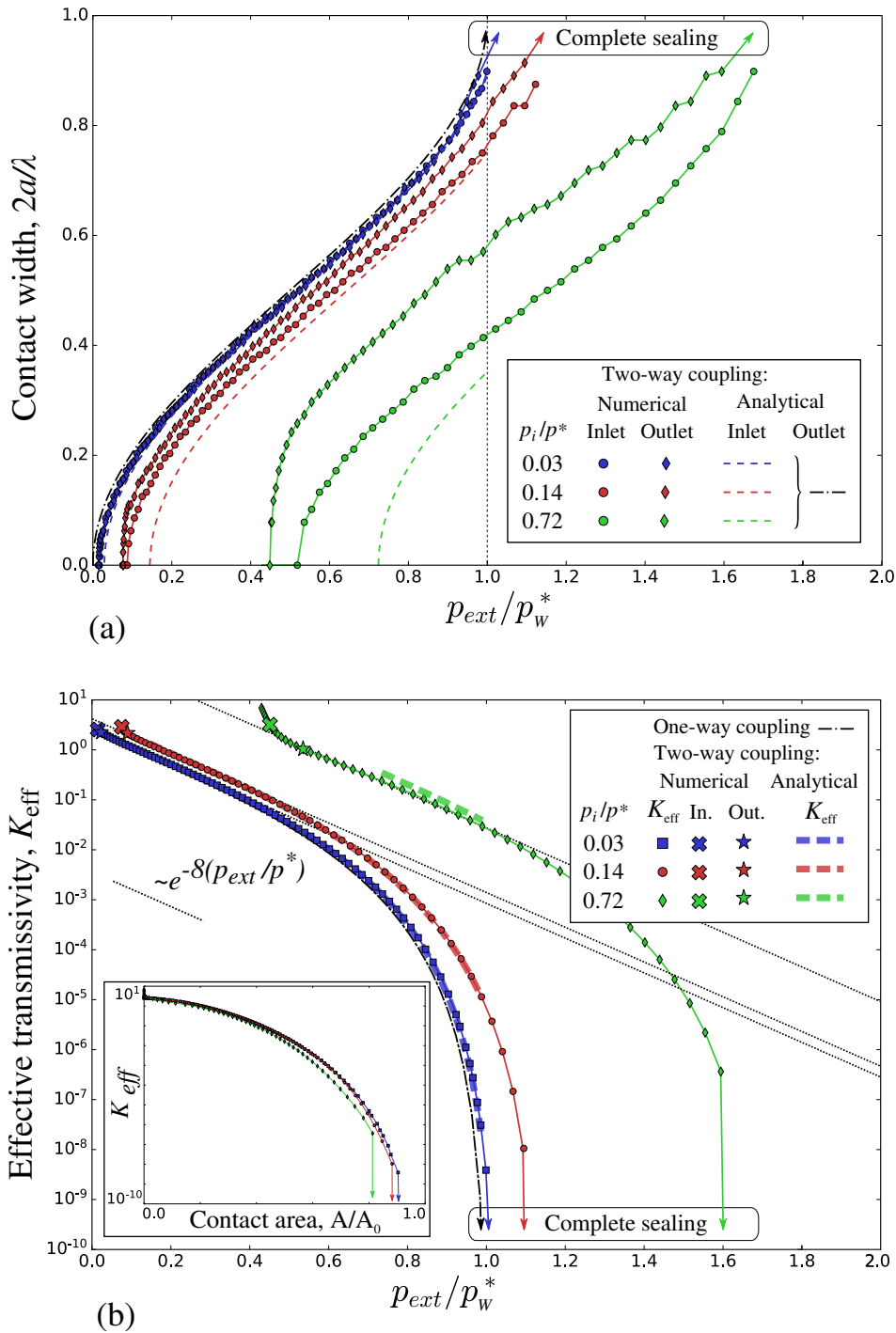


Figure 8.9: The evolution with the increasing external pressure of: (a) the width of the contact zone on the inlet and the outlet sides; (b) the effective transmissivity K_{eff} of the interface; results are plotted for three different values of the inlet fluid pressure p_i/p_w^* and zero outlet pressure $p_o = 0$. Analytical results (8.17)-(8.18) are shown as thick dashed curves, numerical results are presented using markers, while full curves are fittings of power law $K_{eff} \sim (p_{crit} - p_{ext})^\gamma$, where $\gamma = 6 \pm 0.5$. “Cross” and “star” markers are used to highlight the external pressure necessary for the contact to appear at the outlet and inlet sides, respectively. Inset in (b) shows the evolution of the effective transmissivity with respect to the ratio of the real contact area to the apparent one.

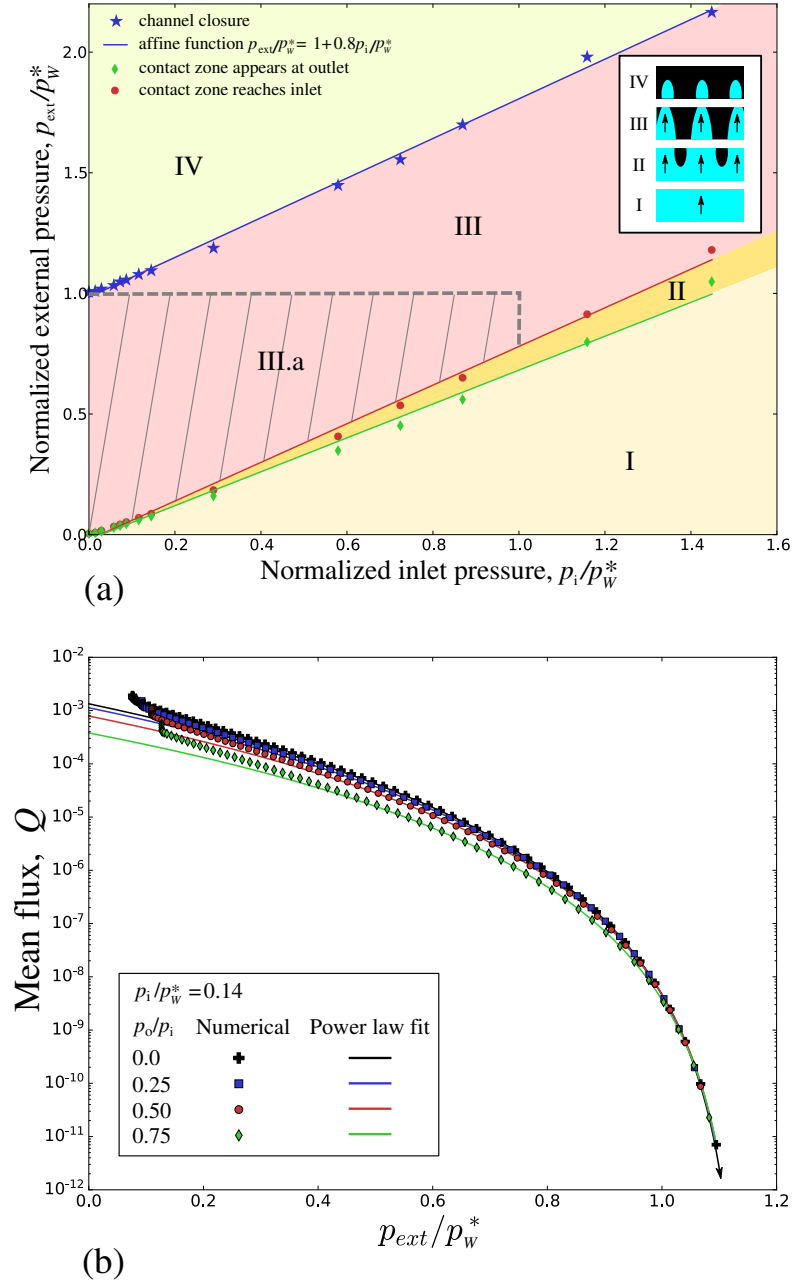


Figure 8.10: (a) The phase diagram found for $p_o = 0$ demonstrating different flow regimes: I - no contact occurs in the interface, the solids are separated by the fluid flow, the external pressure is balanced by the fluid pressure; II - the contact occurs near the outlet but does not extend until the inlet, thus the initially continuous flow fingers toward the outlet; III - the contact zones connect the inlet and the outlet forming separate channels for the fluid flow; zone III.a corresponds to the combination of loads for which the approximate analytical solution remains valid; IV - the contact interface is completely sealed, no flow passes through it, the fluid is under the inlet hydrostatic pressure and ensures some load-bearing capacity in the non-contact region. (b) Evolution of the mean flux across the interface with the increasing external pressure for $p_i/p_w^* = 0.14$ and four cases of the outlet pressure $p_o/p_i = 0, 0.25, 0.5, 0.75$, showing that the critical pressure, necessary to seal the channel, is independent of the outlet pressure. Markers represent numerical results, while full curves are fittings to the power law discussed above.

Finally, we evaluated the critical external pressure necessary to seal the channel, i.e. to prevent the fluid flow across the interface. The results are presented in Fig. 8.10(a). The relationship between the inlet pressure and the critical external pressure is found to be close to linear, the results of the least squares fitting are presented in Fig. 8.10(a). So the critical external pressure p_{crit} needed to seal the channel can be approximately found as:

$$p_{\text{crit}} \approx p_W^* + 0.8p_i, \quad (8.21)$$

where 0.8 is a fit parameter. In order to verify the effect of the outlet pressure, we performed additional simulations with different outlet pressures for a given inlet one. The results are presented in Fig. 8.10(b), where we plot evolution of the mean flux Q (8.20) with the increasing external pressure. In the beginning of loading the mean flux is lower in case of a smaller pressure drop, however, under the increasing external load curves converge, and complete sealing of the channel occurs at the same value of the critical external pressure, which therefore is determined only by the inlet pressure. The explanation comes from the fact that close to the complete sealing of the channel, the fluid pressure drop occurs in the vicinity of the outlet, while in the remaining channel the pressure is close to the inlet one. Therefore, remarkably, the load-carrying capacity of the fluid in the interface close to percolation is defined only by the inlet pressure.

In addition, in Fig. 8.10(a) we highlight the external pressure at which the contact appears on the inlet side, this corresponds to the onset of validity of the approximate solution. The end of its validity corresponds to $p_{\text{ext}}/p_W^* = 1$. The narrow validity range of our approximate solution can be improved by dropping the assumption (ii) in Section 8.1.3 and by including strong elastic interaction between y -sections, which would lead to a much more complicated analysis and is not addressed here.

8.2 Fluid flow across a wavy channel with an ‘‘atoll’’ island and a trapped ‘‘lagoon’’

In this section we present examples which show full capabilities of the proposed computational framework, considering the flow in the contact interface with the possibility of fluid entrapment. We highlight the difference between solutions obtained under one-way and two-way coupling approaches, and, moreover, discuss the status-wise and the DOF-wise convergence of the Newton-Raphson method.

We consider the fluid flow across an extruded wavy channel with an added ring-shaped elevation of the surface at the centre of the channel. Once the solid is gradually brought in contact with a rigid flat, this elevation forms a contact patch in a shape of an ‘‘atoll’’, which encircles a ‘‘lagoon’’ where the fluid gets trapped, see Fig. 8.11. The surface of the solid is given by the formula:

$$z(x, y) = \Delta \left(A(x, y) \cos \frac{2\pi x}{\lambda} - 1 \right), \quad (8.22)$$

$$A(x, y) = 1 - 2\alpha \left[(x - \lambda/2)^2 + (y - L/2)^2 \right] e^{1-\alpha[(x-\lambda/2)^2+(y-L/2)^2]},$$

where Δ and λ are the amplitude and the wavelength of the channel profile, L is the length of the channel, and coefficient α controls the radius of the ‘‘atoll’’ $R_a = 1/\sqrt{\alpha}$. Note that the centre of the ‘‘lagoon’’ is at $(\lambda/2, L/2)$, and the atoll’s elevation is equal to the elevation of the crest on the periphery of the simulated geometry. Therefore, the contact zone will appear simultaneously at the crest of the wavy profile and at the atoll’s ridge line.

We apply the following boundary conditions. On the vertical faces of the solid we

apply zero normal displacement: $\mathbf{u}_y|_{y=0} = \mathbf{u}_y|_{y=L} = 0$ and $\mathbf{u}_x|_{x=0} = \mathbf{u}_x|_{x=\lambda/2} = 0$. The bottom face of the solid is displaced vertically towards the rigid flat within 100 load steps until the fluid channel is completely sealed. We consider throughout the whole loading process a constant fluid pressures prescribed at the inlet: $p|_{y=0} = p_{\text{in}}$ and the outlet $p|_{y=L} = p_{\text{out}}$, accompanied by conditions of zero flux at the remaining part of the boundary of the fluid domain Γ^f : $q_0|_{x=0} = q_0|_{x=\lambda/2} = 0$. Note that these boundary conditions account for the reflection symmetry with respect to planes $x = 0$ and $x = \lambda/2$.

The geometrical parameters are given in the caption of Fig. 8.11. For the solid we consider material parameters typical for a soft matter: Young's modulus $E = 1$ GPa and Poisson ratio $\nu = 0.4$ (effective elastic modulus is $E^* = E/(1 - \nu^2) \approx 1.19$ GPa), while fluid parameters are of a typical mineral oil with initial bulk modulus $K_0 = 2$ GPa and $K_1 = 9.25$. The inlet fluid pressure is chosen to be $p_{\text{in}} = 10$ MPa and the outlet one $p_{\text{out}} = 0$.

The results of the simulation are presented in Fig. 8.12. Note that only three of hundred loading steps are shown. At the beginning of the loading sequence, see Fig. 8.12(a), the atoll's contact zone grows from two opposite (inlet and outlet) sides, therefore the fluid is not yet trapped and is flowing inside the "lagoon". Simultaneously a contact zone on the crest at $x = 0$ also starts to grow starting from the outlet end. Note that the contact zones are not symmetric with respect to a line $y = L/2$ (which would be the case for the considered geometry if the one-way coupling was used), since the fluid pressure applied to the surface of the solid is maximal at the inlet and is monotonically decreasing towards the outlet. Interestingly, the fluid pressure inside the lagoon before its closure is almost uniform and is significantly higher than the mean value between the inlet and

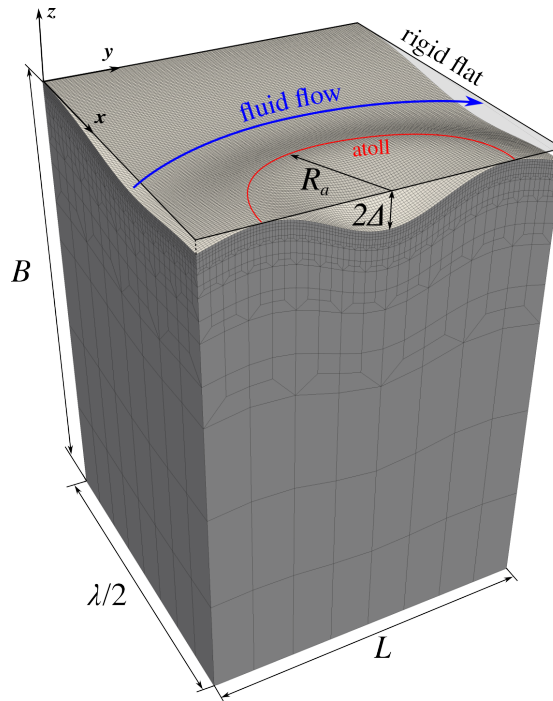


Figure 8.11: Finite-element mesh with 128×128 faces in the contact interface which was used to solve the problem of the fluid flow across a channel with an "atoll" island. Note that the amplitude of the surface profile is exaggerated to highlight its features, while in the actual simulation the following geometrical parameters were used: $\Delta = 0.02$ mm, $\lambda = 2$ mm, $L = 1$ mm, $B = 1.4$ mm, $R_a = 0.333$ mm, $\alpha = 9$ mm⁻².

outlet fluid pressures $(p_{\text{in}} + p_{\text{out}})/2$, even if the centre of the lagoon is at $(\lambda/2, L/2)$. This is also an effect of considering the two-way coupling, since the fluid pressure decrease from the inlet to the outlet is not linear (which is the case under one-way coupling), but is rather concave, cf. Fig. 8.6, 8.7 and 8.8(c). At the second loading stage, see Fig. 8.12(b), corresponding to a higher external load, two atoll's zones of contact merge and form a non-simply connected patch, which encircles an out-of-contact lagoon with the trapped fluid inside. Under increasing external pressure, see Fig. 8.12(c), the contact area continues to grow, reducing the area corresponding to the fluid flow. At the same time, the area of the trapped fluid zone is also decreasing, however, much slower compared to the contact area increase at the crest of the profile, which is caused by a higher pressure in the lagoon than in the channel, the former being governed by the compressibility model (2.75). Note that the effect of considerably higher pressure in the trapped fluid than in the fluid flow may be observed by comparing the value of stress component σ_{zz} at Γ^{fsi} (bottom of the channel) and at Γ^{tf} (bottom of the lagoon).

8.2.1 Comparison of the interface transmissivity between one-way and two-way coupling approaches

In Fig. 8.13 we present the comparison of the transmissivity of the interface in case of one-way and two-way coupling approaches, the second is also presented with and without taking into account the trapped fluid. We compute the effective transmissivity as (see also [Pérez-Ràfols et al., 2016]):

$$K_{\text{eff}} = -\frac{12\mu QL}{\Delta^3(p_{\text{out}} - p_{\text{in}})}, \quad (8.23)$$

where Q is the mean flux over the area $\lambda/2 \times L$, i.e.

$$Q = \frac{2}{\lambda L} \int_0^{\lambda/2} \int_0^L q_y dx dy, \quad (8.24)$$

and $q_y = -g^3/(12\mu) \partial p/\partial y$ is the fluid flux in the y -direction.

Clearly, one-way coupling neglects the additional fluid-induced normal traction on the surface of the solid, which in its turn impacts the fluid flow. As a result, the transmissivity of the interface is underestimated, and, consequently, the critical pressure needed to seal the channel is higher if the two-way coupling is considered. We recall that in Section 8.1 we studied the fluid flow across a wavy channel brought in contact with a rigid flat using the same framework. We showed that the critical sealing pressure is an affine function of the inlet pressure and does not depend on the outlet pressure. In case of the channel with an atoll island studied here, once a trapped fluid pool is formed, it provides additional load-bearing capacity, while its pressure is increasing with the increasing external load. Therefore, the critical sealing pressure is further elevated if the effect of the trapped fluid is taken into account, see Fig. 8.13.

Note also that in the same figure we plotted the curve of evolution of transmissivity, obtained under one-way coupling and shifted by an external pressure offset $p_{\text{in}}/2$. This offset represents a simple estimation of the additional fluid-induced load-bearing capacity, which is accounted for in the two-way coupling approach (we recall that $p_{\text{out}} = 0$). Remarkably, the shifted curve almost exactly coincides with the transmissivity of the two-way coupling in the region of intermediate loads, and underestimates the transmissivity closer to the complete sealing. Moreover, the simple estimation of the load-bearing capacity used here obviously cannot take into account the effect of the trapped fluid, which was shown to further increase the transmissivity in the numerical simulation.

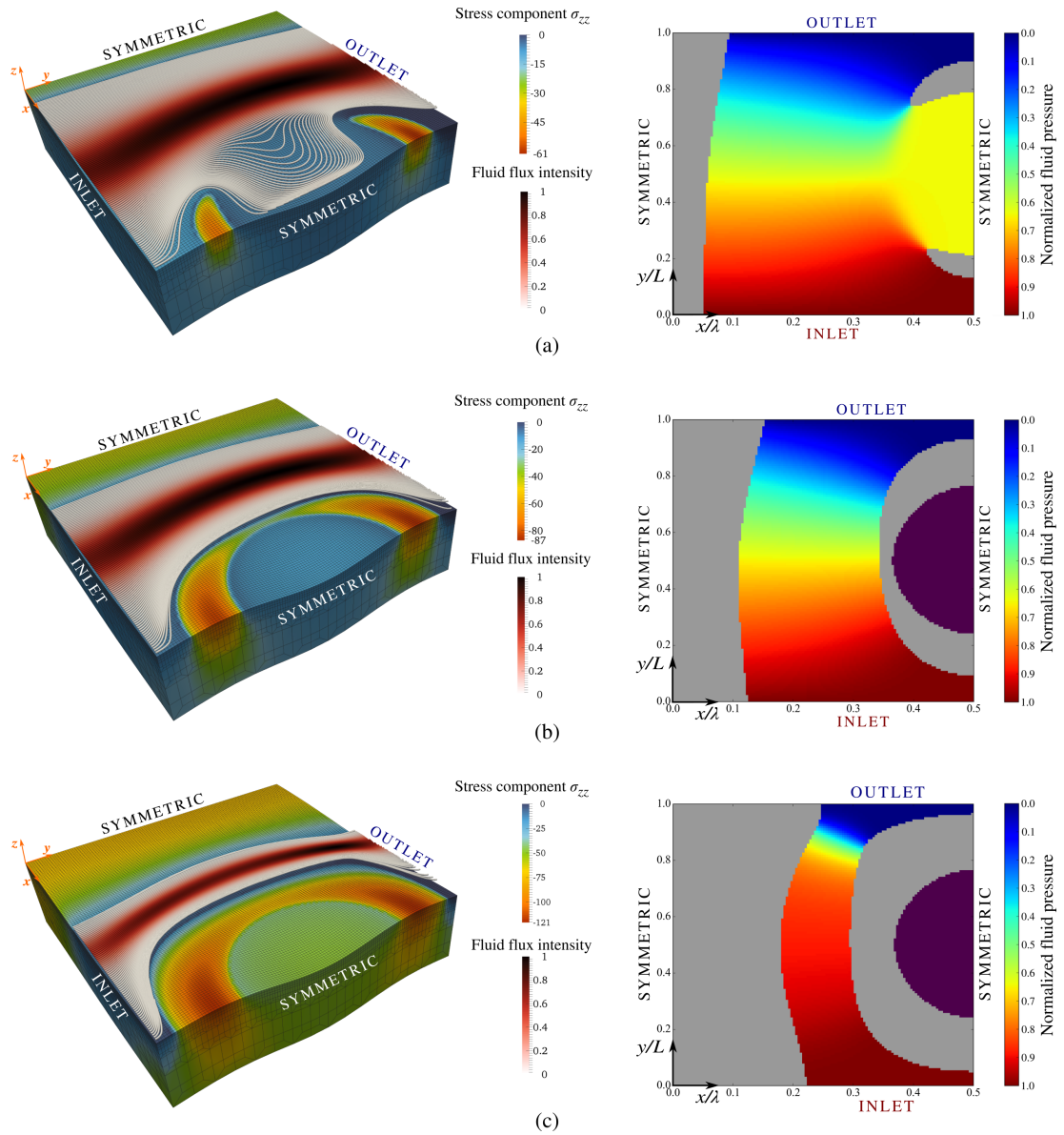


Figure 8.12: Fluid flow across a wavy channel with an “atoll” island. Three different load steps are presented: (a) beginning of loading, contact occurs only at the crest of channel profile and at two opposite sides of the atoll, therefore fluid is not trapped yet (at $p_{\text{ext}}/E^* \cong 0.007$); (b) two atoll's contact zones merge and fluid is trapped (at $p_{\text{ext}}/E^* \cong 0.015$); (c) under increasing load trapped fluid is further pressurized (at $p_{\text{ext}}/E^* \cong 0.037$). For each loading step in the left column the bulk view of the solid is shown, with colour representing the σ_{zz} component of the stress tensor, moreover, fluid flow lines with the colour representing the normalized fluid flux intensity q/q_{max} are added. In the right column the interface view is given, with colour representing the normalized fluid pressure in the flow p/p_{in} , the contact patches are shown in grey colour and the trapped fluid zone is purple. Note that the trapped fluid pressure corresponding to loading step (b) is $p^{\text{tf}}/p_{\text{in}} \cong 1.2$, step (c): $p^{\text{tf}}/p_{\text{in}} \cong 4.5$.

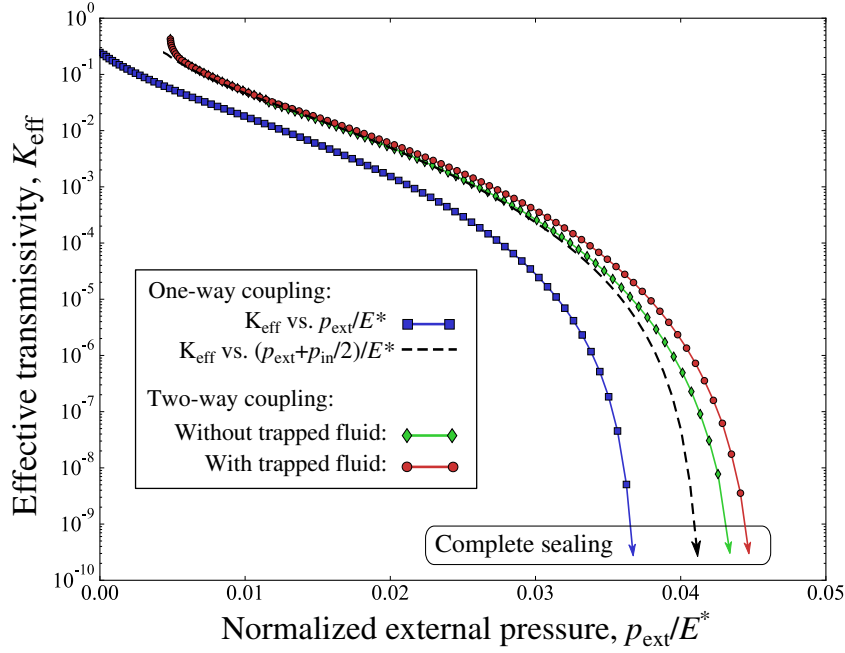


Figure 8.13: The evolution of the effective interface transmissivity K_{eff} under increasing external load with comparison between 3 simulations: one-way coupling approximation, two-way coupling neglecting effect of the trapped fluid and two-way coupling with the trapped fluid. Additionally, the results of the one-way coupling simulation are shown shifted by an offset of the external load equal to $p_{\text{in}}/2$ (see explanations in the text).

8.2.2 Convergence of the Newton-Raphson method

We demonstrate in Fig. 8.14 the DOF-wise and the status-wise convergence of the Newton-Raphson method corresponding to one particular load step, during which two atoll's contact patches merge and encircle the trapped fluid zone. Note that this step is the most challenging of the whole sequence, since the highest number of local status changes is observed after this step, see (6.20). We present for comparison results obtained in 2 simulations with different values of the fluid inlet pressure: $p_{\text{in}} = 2$ MPa, see Fig. 8.14(a), and $p_{\text{in}} = 10$ MPa, see Fig. 8.14(b), while for both cases $p_{\text{out}} = 0$. We also used in both simulations the same tolerance thresholds for different types of DOF: $\epsilon_u = 10^{-6}$, $\epsilon_\lambda = \epsilon_p = 10^{-12}$.

According to the presented results for both cases, while the local status of faces keeps changing between the iterations, see (6.20), the DOF-wise convergence is not quadratic. Note that a high peak of the number of status changes, corresponding to the 2nd iteration in both cases, is caused by the first detection of the trapped fluid zone. However, the number of status changes monotonically decreases starting from the 3rd iteration. Eventually, the quadratic DOF-wise convergence of the Newton-Raphson method is recovered once the number of status changes reaches zero value, meaning that the tangent matrix (6.15) was implemented correctly. In case of a lower fluid pressure, see Fig. 8.14(a), the convergence under the specified error tolerance is obtained after 6 iterations. However, in case of higher fluid pressure, see Fig. 8.14(b), more iterations are needed to find the correct status for each face. Note also that the quadratic DOF-wise convergence is recovered only for displacement DOFs and the Lagrange multipliers (equivalent to the contact pressure). The possible reason for the lack of quadratic convergence for the fluid pressure DOFs is that when the correct tangent matrix is obtained, the norm $\|\mathbf{R}_p^f\|$ is already below the convergence threshold ϵ_p (and even close to the double machine precision $\approx 10^{-16}$).

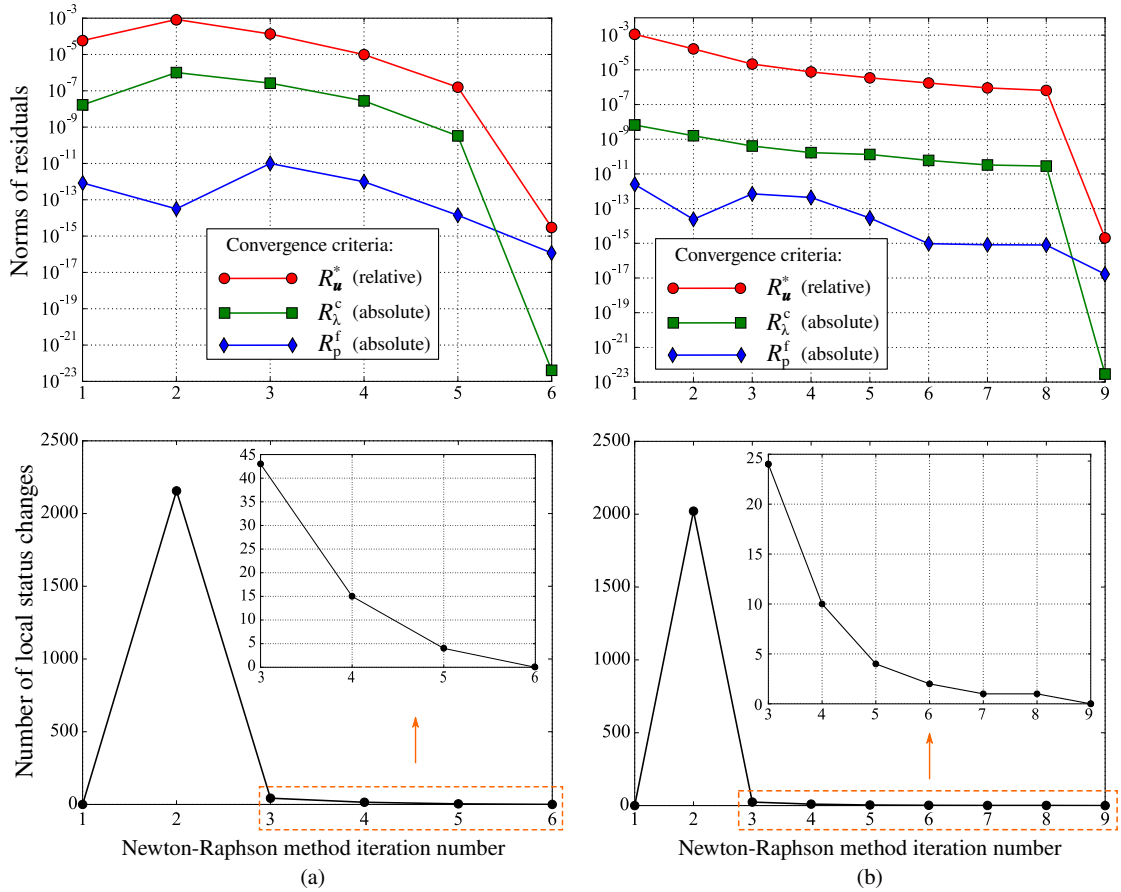


Figure 8.14: DOF-wise (top) and status-wise (bottom) convergence of the Newton-Raphson method corresponding to a load step during which the trapped fluid zone is formed. Results presented for 2 simulations with different values of the fluid inlet pressure: (a) $p_{\text{in}} = 2$ MPa and (b) $p_{\text{in}} = 10$ MPa. DOF-wise convergence is shown in terms of the relative criterion for the residual corresponding to the displacement DOFs and the absolute criterion for the other two residuals, see Section 6.3. The status-wise convergence is shown for the number of status changes defined in (6.20). Note that the evolution of the number of status changes from the 3rd iteration until the last one is shown in insets for each considered case.

We would like to remark that the parameter ϵ of the augmented Lagrangian method, see (4.110), was chosen to be $\epsilon = 10^8$ in presented examples. Interestingly, our studies showed an unusual dependence on this parameter, which was, however, rather weak. A small oscillation of the surface traction field appeared in the solution at the border between the contact and the fluid flow and/or trapped fluid zones: see surface tractions in the trapped fluid zone in Fig. 8.12(c) and also contact tractions in Fig. 8.6(b) and Fig. 8.7(b). The reasoning of this oscillation may come from utilization of the integral (weighted) gap in the contact constraints (4.107), while for the thin fluid flow the actual nodal gap is used, see, for example, (6.1). Our studies showed that this oscillation is dumped if the value of the augmentation parameter is increased. Unfortunately, it cannot be arbitrary high, since it may lead to bad conditioning of the global tangent matrix. However, the discussed artefact does not affect the solution in the whole domain, and therefore does not undermine the consistency of the proposed method. Nevertheless, it presents an interesting topic of the future investigation.

8.3 Conclusions

In this Chapter we presented a theoretical study of the pressure driven creeping flow in contact interface formed between a deformable solid with regular wavy surfaces and a rigid flat. This problem is relevant for certain applications of thin fluid flow in contact interfaces, including sealing, hydrogeology and biological systems. A two-way coupling between fluid flow and deformation of the solid was assumed, which is crucial for applications in which the fluid pressure is comparable with the mean contact pressure, for example, for the soft matter or biological tissue.

We derived an approximate analytical solution based on the Westergaard-Kuznetsov solution and a one-dimensional formulation of the Reynolds equation. This solution describes both the solid deformation and the fluid pressure distribution in the strongly coupled case. A finite-element monolithically coupled framework developed in the Part II of this dissertation was also used to solve this non-linear multi-field problem and to prove the validity of the approximate solution. Despite a rather limited interval of loads within which the latter is applicable, it can provide a useful first-order approximation for the analysis of transmissivity of contact interfaces. At the same time, numerical results showed that in a wide range of the external loads up to the complete sealing of the channel, the transmissivity of the interface can be described by a power law, which has already been reported in the studies of contact interfaces having representative and model roughness.

Both numerical and analytical results, which take into account two-way coupling, showed that the interface transmissivity is significantly higher than this predicted by the one-way coupling if the fluid pressure is high enough. An additional result of this study is the affine dependence of the external critical pressure which seals the channel on the inlet fluid pressure: this relation may be shown useful in sealing applications as well as in soft porous or cracked media, in zones where the flow can be described by the Reynolds equation. Remarkably, this critical pressure was found to be independent of the outlet pressure.

We considered also the fluid flow across an extruded wavy channel with a ring-shaped elevation of the surface at the centre of the channel, which forms a non-simply connected contact patch, when the solid is brought into contact with a rigid flat. A study of this problem showed again, that the transmissivity of the interface is higher if the two-way coupling is considered. Furthermore, once the fluid gets trapped and pressurized, it provides an additional load-bearing capacity, requiring a larger external load to seal the interface, i.e. the trapped fluid further increases transmissivity. Finally, the study of DOF-wise and status-wise convergence of the Newton-Raphson method showed that the quadratic convergence is recovered once the correct partition of the interface into contact, fluid-flow and trapped fluid zone is found, which confirms the robustness of the proposed resolution algorithm and the validity of the global tangent matrix implementation.

Chapter 9

Fluid flow through rough contact interface

Résumé de Chapitre 9 “L’écoulement du fluide à travers l’interface de contact rugueux représentative”

Le neuvième chapitre présente des simulations d’écoulement de fluide mince à travers une interface de contact entre un solide avec une surface rugueuse représentative et une surface plane rigide. Nos résultats confirment que le couplage unidirectionnel sous-estime la perméabilité de l’interface et la charge externe critique nécessaire pour sceller complètement l’interface. Nous avons effectué une étude de la transmissivité des surfaces rugueuses gaussiennes, isotropes et auto-affines en contact avec un plan rigide pour une large gamme de pressions d’entrée et de sortie. Nous avons élaboré une équation phénoménologique régissant la transmissivité des interfaces de contact rugueuses. Enfin, le cadre développé a été utilisé pour calculer la fuite de fluide dans une interface de contact entre une surface métallique et un saphir, en utilisant les mesures de surface réelles. Une loi de comportement élasto-plastique a été introduite dans le modèle numérique, ce qui a permis d’étudier la performance de véritables joints d’étanchéité utilisés dans les centrales nucléaires. Les résultats numériques proposés dans cette thèse sont en meilleur accord avec l’expérience que les estimations provenant des études précédentes.

In this chapter we solve two problems involving fluid flow through representative rough contact interfaces. The roughness of many natural and engineering surfaces can be considered as random, self-affine down to atomistic scale [Nayak, 1971]. The roughness of contacting surfaces has strong implications in mechanics and physics of contact: the evolution of the ratio of the real contact area to the apparent one under increasing external load determines essential contact properties such as friction, wear and adhesion. Furthermore, the distribution of the free volume between contacting surfaces governs the fluid transport along the interface and thus is responsible for leakage/percolation phenomena [Dapp et al., 2012, Paggi and He, 2015], which is one of the main topics of this dissertation.

9.1 Fluid flow through rough contact interface with multiple trapped fluid pools

The first problem under study is the contact between a deformable solid with a *rough* surface and a rigid flat in presence of a thin fluid flow in the free volume between the two surfaces, see Fig. 9.1 for the sketch of the problem set-up. A physically relevant

simulation of a rough surface requires a very fine discretization, which becomes a bottleneck in FEM studies. One possible approach is to model a part of the surface, which is small enough to make the computation possible, and at the same time big enough to act as a representative surface element (RSE), see [Yastrebov et al., 2011, Durand, 2012].

It is important to note, that the resolution of problems involving thin fluid flow in contact interfaces is often performed using the boundary element method [Pérez-Ràfols et al., 2016] or Green's function molecular dynamics [Dapp et al., 2012] for the mechanical contact problem and the finite-differences method for the Reynolds equation. On the one hand, this approach permits to use a much finer discretization of the surface than is possible with FEM, however, on the other hand, the consideration of the two-way coupling is problematic with the aforementioned approach. The one-way coupling is often used under the assumption that the deformation of the solids results mainly from the contact interaction and the fluid pressure effect on the solid is negligible. However, a justification for this choice (see, for example, [Dapp and Müser, 2016]), lacks a quantitative study of the range of applicability of the one-way coupling depending on the material properties of the solid and the fluid, and also on the fluid pressure, which will be addressed in the present chapter using the finite-element method.

It should be also noted that the spectrum of the roughness has to be rich enough to be physically representative at least to a certain extend, i.e. the frequency cut-offs in the model spectrum have to be chosen with some physical motivation and kept at values for which the continuum mechanics remains valid see, for example, discussion in [Luan and Robbins, 2005]. Using the approach discussed in [Yastrebov et al., 2015], we generated Gaussian, isotropic and self-affine surface with the following parameters: smallest wavenumber $k_l = 8\pi/L$ (which corresponds to the longest wavelength $\lambda_l = L/4$), highest wavenumber $k_s = 64\pi/L$ (corresponding to the shortest wavelength $\lambda_s = L/32$), number of points on each side of the surface $N = 256$, Hurst exponent $H = 0.8$. The standard deviation (the root mean squared, or the rms) of height of the generated surface, defined as:

$$S_q = \langle (z - \bar{z})^2 \rangle^{\frac{1}{2}} = \sqrt{\frac{1}{L^2} \int_0^L \int_0^L (z(x, y) - \bar{z})^2 dx dy}, \quad (9.1)$$

equals to $S_q = 1 \mu\text{m}$, while the standard deviation of the height gradient (the rms of slope)

$$S_{dq} = \langle |\nabla z|^2 \rangle^{\frac{1}{2}} = \sqrt{\frac{1}{L^2} \int_0^L \int_0^L |\nabla z(x, y)|^2 dx dy} \quad (9.2)$$

equals to $S_{dq} \cong 0.055$. Note also that the generated surface geometry is periodic, i.e.

$$z(x, y) = z(x + iL, y + jL), \quad i, j \in \mathbb{Z}. \quad (9.3)$$

The boundary conditions for the problem under study are as follows. We consider throughout the whole loading process a constant fluid pressures prescribed at the inlet: $p|_{y=0} = p_{\text{in}}$ and the outlet $p|_{y=L} = p_{\text{out}}$. However, following the approach of a representative surface element (RSE), here we consider periodic boundary conditions at two other sides of the fluid domain: $p|_{x=0} = p|_{x=L}$. On vertical faces adjacent to the inlet and the outlet zones we apply the boundary conditions of zero normal displacement $\mathbf{u}_y|_{y=0} = \mathbf{u}_y|_{y=L} = 0$, while on two other faces we prescribe the periodic boundary condition: $\mathbf{u}|_{x=0} = \mathbf{u}|_{x=L}$. The bottom face of the solid is displaced vertically towards the

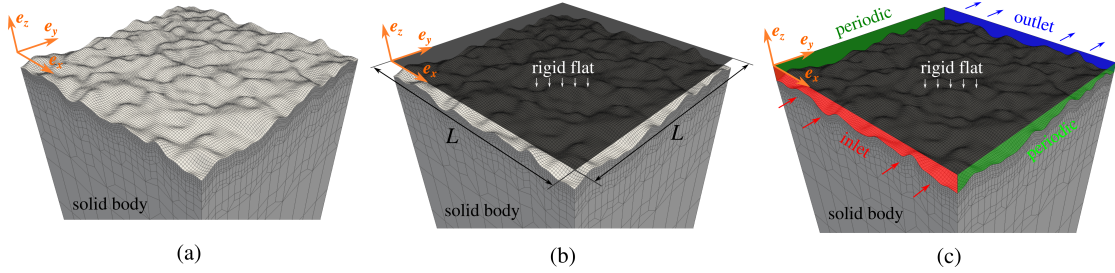


Figure 9.1: Sketch of the second problem under study: contact between a deformable solid with a representative rough surface (a), brought in contact with a rigid flat (b), in presence of the thin fluid flow in the free volume between the two surfaces (c). Note that the amplitude of the surface roughness is exaggerated, while in the actual simulation we used a surface with root mean square of heights $S_q = 1 \mu\text{m}$ (see definition in the text), and the lateral size of the studied square surface is $L = 1 \text{ mm}$. The vertical size of the FEM mesh is $B = 1.4 \text{ mm}$.

rigid flat within 100 load steps until all channels connecting the inlet and the outlet is closed, i.e. the fluid flow is no more possible. We use here the same material properties as in the “atoll” example considered in Sec. 8.2, i.e. parameters typical for a soft matter: Young’s modulus $E = 1 \text{ GPa}$ and Poisson ratio $\nu = 0.4$, therefore the effective elastic modulus is $E^* = E/(1 - \nu^2) \approx 1.19 \text{ GPa}$.

The results of the simulation with the fluid inlet pressure $p_{\text{in}} = 4 \text{ MPa}$ and zero outlet pressure are presented in Fig. 9.12, note that only 3 load steps out of 100 are shown. At the first considered step (a) trapped fluid zones are not yet observed, however, they appear during further loading. Interestingly, atoll-type zones, which were studied previously in a model geometry, appear naturally in case of a representative rough interface, see Fig. 9.2(b) and (c), at the last presented step the number of these zones is $n_{\text{tf}} = 54$. Similarly to the previous example, we may observe elevated surface traction at the bottoms of the trapped fluid zones, caused by a pressure in the trapped fluid, which is higher than the fluid pressure in the flow.

It is also important to note, that the spatial distribution of the fluid pressure on its way from the inlet to the outlet changes drastically with the increasing external load. In Fig. 9.2(a) the pressure decreases rather gradually over the whole interface, with a more rapid change closer to the outlet, which is an effect of considering the two-way coupling, see discussion in Sec. 8.2, Fig. 8.12 and also Fig. 8.8. However, under a higher external load, see Fig. 9.2(b), we observe a certain “clusterisation” of the fluid pressure field, which becomes divided into zones partially surrounded by contact patches. Within these “clusters” the fluid pressure varies little and the intensity of the fluid flow is low, however, the fluid pressure gradient in narrow channels connecting these “clusters” is high. Under the external pressure close to the complete sealing of the interface, see Fig. 9.2(c), the major part of the area is under the inlet pressure, while almost all remaining part is under the outlet pressure, and virtually all pressure drop is happening over a narrow constriction connecting these two zones, which is in agreement with theoretical predictions [Persson and Yang, 2008, Persson, 2010] and previous numerical simulations [Dapp and Müser, 2016].

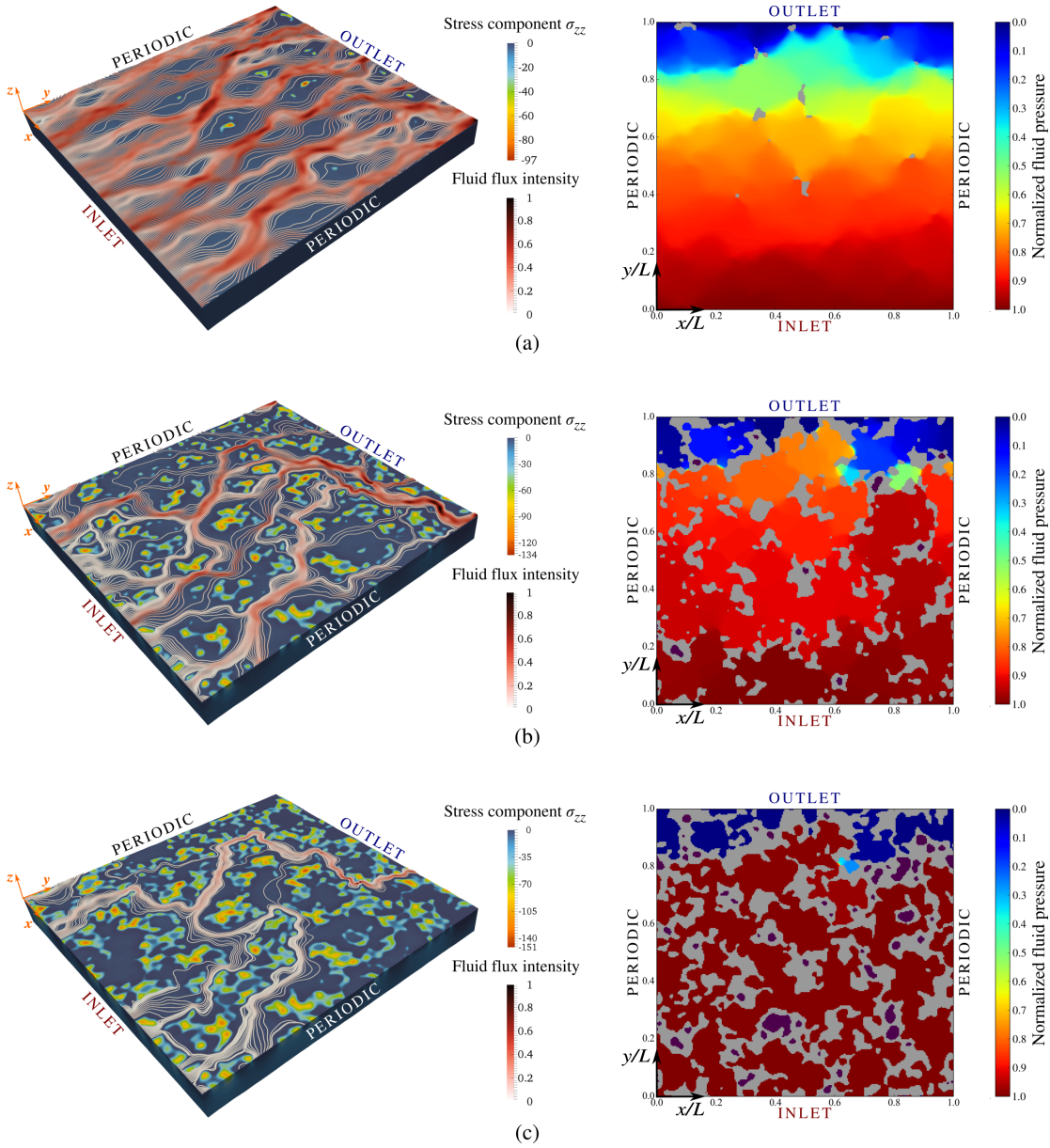


Figure 9.2: Fluid flow through the contact interface between a deformable solid with representative rough surface and a rigid flat. Three different load steps with increasing external pressure are presented: (a) $p_{\text{ext}}/E^* \cong 0.002$, (b) $p_{\text{ext}}/E^* \cong 0.007$, (c) $p_{\text{ext}}/E^* \cong 0.013$. For each loading step in the left column the bulk view of the solid is shown, with colour on the surface representing σ_{zz} component of the stress tensor, moreover, fluid flow lines with the colour representing the normalized fluid flux intensity q/q_{\max} are added. In the right column the interface view is given, with colour representing the normalized fluid pressure in the flow p/p_{in} , the contact patches are shown in grey colour and all trapped fluid zone are purple (note that the fluid pressure in each trapped zone is different and is increasing with the increasing external loading). At the step (b) 7 trapped fluid zones are present ($n_{\text{tf}} = 7$), the highest trapped fluid pressure is $p^{\text{tf}}/p_{\text{in}} \cong 3.6$, at the step (c) $n_{\text{tf}} = 54$, highest pressure $p^{\text{tf}}/p_{\text{in}} \cong 6.4$.

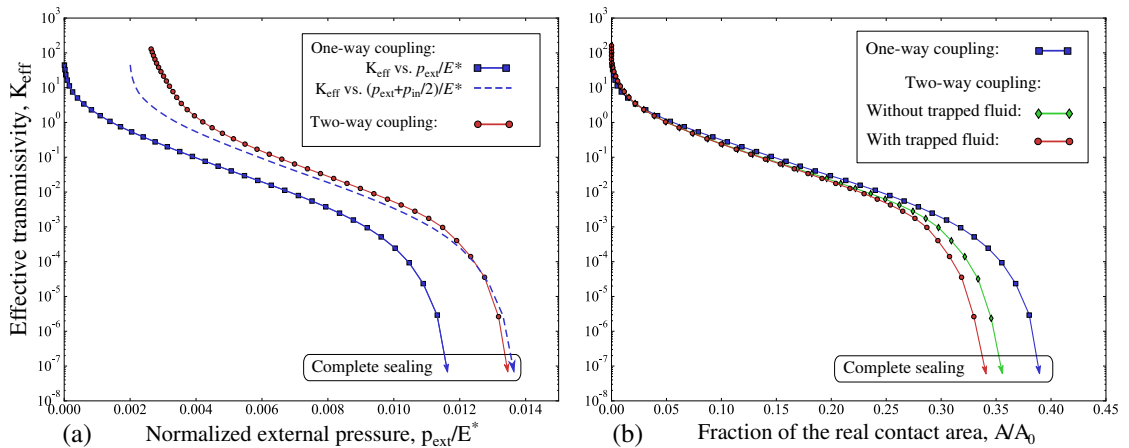


Figure 9.3: Fluid flow through representative rough contact interface: comparison of the effective transmissivity for different coupling approaches.

9.2 Comparison of the interface transmissivity in one- and two-way coupling approaches

We compare the effective transmissivity of the contact interface between the representative surface element and a rigid flat in case of one-way and two-way coupling approaches. Considering the representative surface roughness we compute the effective transmissivity as

$$K_{\text{eff}} = -\frac{12\mu QL}{S_q^3(p_{\text{out}} - p_{\text{in}})}, \quad (9.4)$$

where Q is the mean flux over the apparent contact area $A_0 = L \times L$:

$$Q = \frac{1}{L^2} \int_0^L \int_0^L q_y dx dy, \quad (9.5)$$

and S_q is the standard deviation (the root mean squared) of height in the undeformed state. Note that in this study we consider $p_{\text{in}} = 5$ MPa, while $p_{\text{out}} = 0$ MPa.

In Fig. 9.3(a) we present the evolution of the transmissivity under increasing external load. Again we observe a higher transmissivity of the interface (for the same given external pressure) in case of the two-way coupling than under the one-way approach. Consequently, the critical external pressure necessary to completely close the interface for the fluid flow is also higher if the effect of the fluid pressure is taken into account. Note also that in Fig. 9.3(a) we plotted the curve corresponding to the one-way coupling shifted by an offset of the external load $(p_{\text{in}} + p_{\text{out}})/2$ (however, in the considered simulation $p_{\text{out}} = 0$). As was already discussed in Sec. 8.2 devoted to the ‘‘atoll’’ example, this shift represents a simple estimation of the fluid load-bearing capacity, i.e. an approximation of the transmissivity evolution with increasing external load corresponding to the two-way coupling approach. However this estimation does not work for the evolution of transmissivity with the contact area, see 9.3(b).

Alongside with the critical external pressure, another parameter important for sealing applications is the ratio of the real contact area A to the apparent one $A_0 = L \times L$, computed at the moment when the fluid flow through the interface stops. The corresponding value of A/A_0 is often termed as the *percolation threshold*, see [Dapp et al., 2012, Dapp and Müser, 2016]. These studies show that for randomly rough self-affine surfaces $A/A_0 \approx 0.42$ at the percolation, being valid for a wide range of the roughness

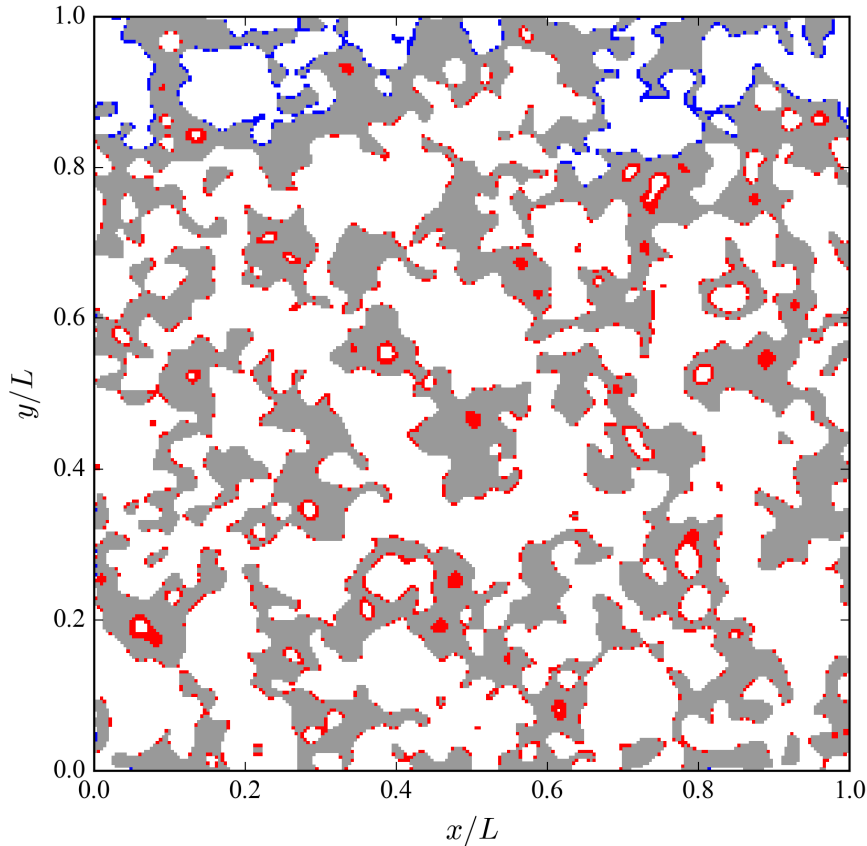


Figure 9.4: Comparison of the real contact area morphology for one-way and two-way coupling simulations, shown results correspond to approximately equal effective transmissivity $K_{\text{eff}} \approx 10^{-6}$ (close proximity of the percolation threshold). The real contact area in the one-way coupling simulation: $A/A_0 = 0.36$, in the two-way: $A/A_0 = 0.33$. Grey colour: contact zones observed in both simulations; red colour: contact zones observed only in the one-way simulation; blue colour: contact zones observed only in the two-way simulation.

parameters. However, these studies neglected the effect of the fluid pressure, i.e. were limited to the one-way coupling approach.

In Fig. 9.3(b) we plot the effective transmissivity with respect to the fraction of the real contact area, comparing one-way and two-way coupling (the latter is considered with and without trapped fluid). For the considered surface the percolation threshold is $A/A_0 \approx 0.4$ under the one-way coupling approach, which is in agreement with the aforementioned studies. However, if the two-way coupling is considered (even without trapped fluid), our results show that the same effective transmissivity corresponds to a smaller contact area, than observed in the one-way coupling case. Accordingly, the percolation threshold is also lower: $A/A_0 \approx 0.36$. Moreover, if the effect of numerous trapped fluid pools is taken into account, the percolation threshold is further decreased down to $A/A_0 \approx 0.34$, which is in agreement with the results of the “atoll” example, see Sec. 8.2, with only one trapped fluid zone. The contact patches expand into the zones previously occupied by the fluid flow much faster, than into the trapped fluid zone, due to a considerably elevated trapped fluid pressure. Note that here we used the refined approach to the contact area computation, proposed in Section 4.3.2. The comparison of the two methods of the area computations is presented in Sec. 9.4.

In order to investigate further the difference between one- and two-way coupling

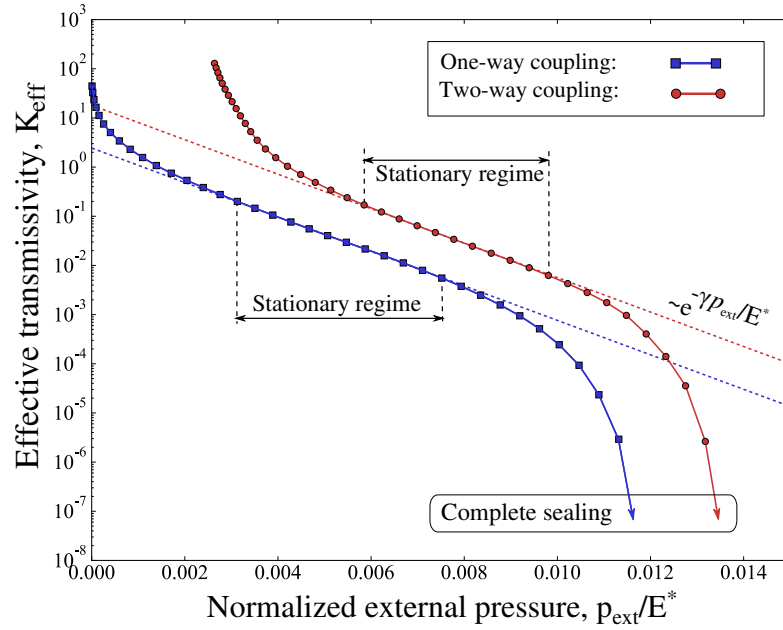
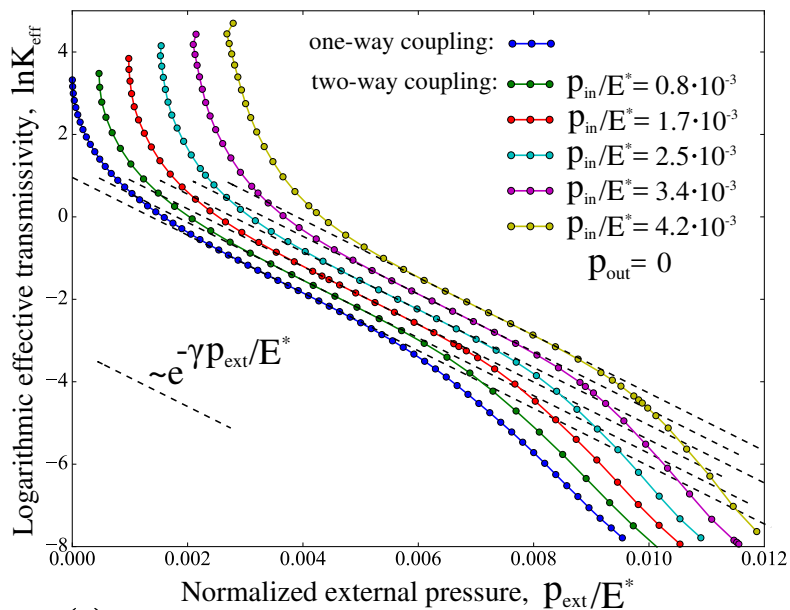


Figure 9.5: The decrease of the transmissivity with the increasing external load, shown for one- and two-way coupling simulations. The stationary regime corresponding to the exponential decay is highlighted.

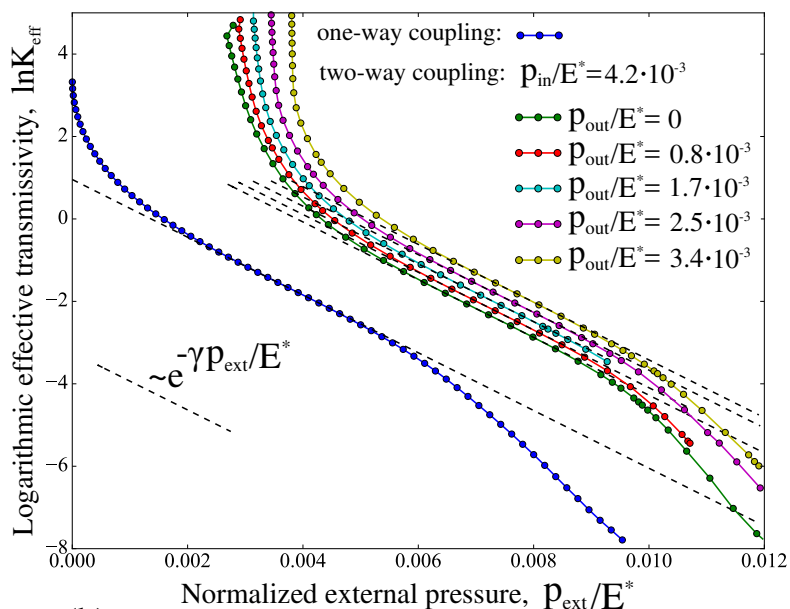
simulations, namely, the difference in the real contact area close to percolation, see Fig. 9.3(b), we show in Fig. 9.4 the comparison of the contact area morphology for these two approaches. Note that the presented results correspond to an approximately equal effective transmissivity: in both cases $K_{\text{eff}} \approx 10^{-6}$. We use different colours to highlight contact zones which are observed in both simulations, zones present only in the one-way simulation, and only in the two-way simulation. As expected, due to the additional fluid pressure applied to the surface of the solid, in the major part of the interface the extent of contact zones is smaller in two-way coupling than in one-way simulation. However, in the part of the interface located close to the outlet, where the fluid pressure is almost equal to the outlet pressure $p_{\text{out}} = 0$, see Fig. 9.2(c), contact patches observed in two-way coupling simulation are larger than in the one-way study. In other words, a certain redistribution of the real contact area, corresponding to approximately the same transmissivity, takes place in the two-way coupling. At the same time, Fig. 9.4 shows that in case of the one-way coupling the contact area grows freely inside of the zones considered as trapped in the two-way coupling, which confirms the results presented in Fig. 9.3(b).

9.3 Effective interface transmissivity as a function of the mean fluid pressure and its gradient

The comparison of one- and two-way coupling approaches for the problem of the thin fluid flow in contact interfaces with model (Chapter 8) and rough (the current chapter) surface geometry showed that the transmissivity of the interface is higher if the two-way coupling is considered. The fluid provides additional load-bearing capacity, so that for the same external load the real contact area is smaller, and, accordingly, the volume of the gap between the contacting surfaces is bigger, than if the effect of the fluid pressure is neglected. Therefore, for a given external load and the fluid pressure drop between the inlet and outlet, the mean fluid flux is higher in the two-way coupling approach, than



(a)



(b)

Figure 9.6: Fluid flow through representative rough contact interface: comparison of the effective transmissivity: for (a) fixed outlet pressure and several inlet pressures, (b) fixed inlet pressure and several outlet pressures.

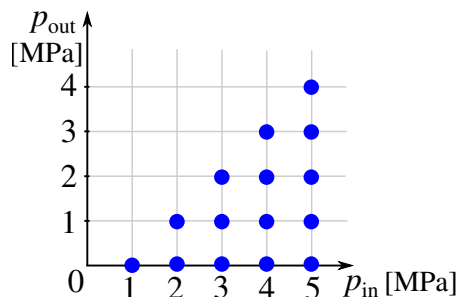


Figure 9.7: Sketch showing the considered pairs of inlet and outlet pressures.

if the one-way coupling is considered. Furthermore, as was demonstrated above, by accounting for the mean fluid pressure shift of the curve corresponding to the evolution of transmissivity for the one-way coupling, a satisfactory estimation of the two-way coupling transmissivity can be obtained, see Fig. 8.12 and Fig. 9.3.

Nevertheless, a question remains: how does the interface transmissivity depend quantitatively on the fluid pressure if the two-way coupling is considered? We will address this question here, and, moreover, motivated by the results presented in Sec. 8.1, we will extend this study by considering the dependence not only on the mean fluid pressure: $(p_{\text{in}} + p_{\text{out}})/2$, but also on the mean gradient of the fluid pressure: $(p_{\text{out}} - p_{\text{in}})/L$, where L is the distance between the inlet and outlet boundaries.

Observing the results presented in Fig. 9.3(a) for the one-way coupling, we may conclude that there are three regimes of the evolution of the effective transmissivity under the increasing external load. Two of them are transitional; the first one in the beginning of loading, when the first contact patches form. The second transitional regime is in the end of the curve, before the complete sealing (percolation) of the interface, when the fluid flux is rapidly decreasing due to the last possible channels closing. Between these two transitional regimes we observe a stationary phase, where transmissivity is decreasing exponentially with the increasing external load, see Fig. 9.5:

$$K_{\text{eff}} \propto e^{-\gamma p_{\text{ext}}/E^*}. \quad (9.6)$$

We performed a set of simulations varying the inlet pressure with constant outlet pressure, and varying outlet pressure with constant inlet pressure, see sketch in Fig. 9.7. The results presented in Fig. 9.6 show that the coefficient γ in the exponential law is almost the same for all considered cases, meaning that the change of the inlet and outlet pressures provides an offset to the exponential law. Therefore, we proposed the following formula for fitting the results:

$$\ln K_{\text{eff}} = a_o - \gamma \frac{p_{\text{ext}}}{E^*} + \alpha \frac{p_{\text{in}} + p_{\text{out}}}{2E^*} - \beta \frac{p_{\text{out}} - p_{\text{in}}}{LE^*}, \quad (9.7)$$

taking into account the dependence of the transmissivity on the external load and the effect of both the mean fluid pressure and the mean gradient of the pressure. Thereupon, performing the fitting of the results obtained in simulations with 10 different realizations of the random surface roughness (however, with the same spectrum cut-offs $\lambda_l = L/4$, $\lambda_s = L/32$, Hurst exponent $H = 0.8$, the rms of heights $S_q = 1 \mu\text{m}$ and the rms of slopes $S_{dq} \cong 0.055$) for each pair of inlet and outlet fluid pressures (see again Fig. 9.7), we obtained the following averaged results for fitting parameters:

$$a_o \approx 1.1, \quad \gamma \approx 727.7, \quad \alpha \approx 708.8, \quad \beta \approx 75.7 \text{ [mm]}. \quad (9.8)$$

It is important to note, that the coefficient α in the term corresponding to the mean fluid pressure is very close to coefficient γ (for all studied cases, the relative difference between these two coefficients did not exceed 3%), which is in accordance with mentioned above estimations of the two-way coupling using the mean pressure offset.

Moreover, the proposed formula can also serve for a quantitative estimation of the range of applicability of the one-way coupling. Let us rewrite it in the following way:

$$\ln K_{\text{eff}} = a_o + \frac{1}{E^*} \left(-\gamma p_{\text{ext}} + \alpha \frac{p_{\text{in}} + p_{\text{out}}}{2} - \beta \frac{p_{\text{out}} - p_{\text{in}}}{L} \right). \quad (9.9)$$

If the solid is considered linearly elastic, then the sealing external pressure is about $p_{\text{ext}} \approx 0.01E^*$, see [Yastrebov et al., 2012], meaning that for a soft matter with $E^* \approx 1 \text{ GPa}$, as in the results of simulations presented above, the sealing pressure is $p_{\text{ext}} \approx 10 \text{ MPa}$.

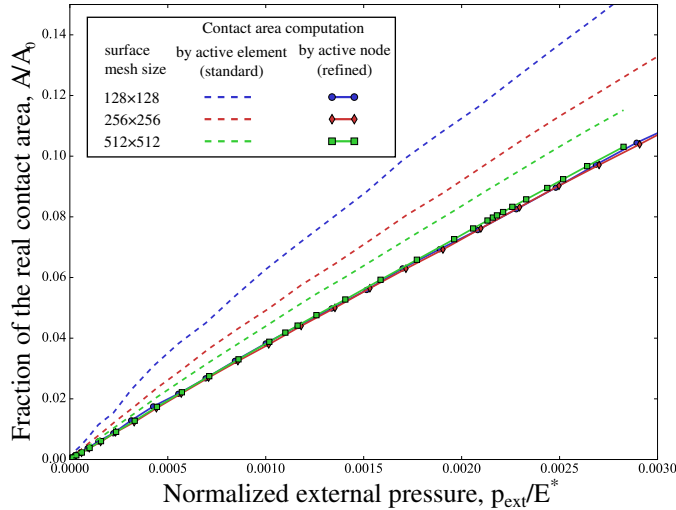


Figure 9.8: Comparison of two different methods of the real contact area computation: (4.120) and (4.121). Results of simulations using three different meshes are presented (with 128×128 , 256×256 and 512×512 face elements on the surface).

Therefore, the term corresponding to the mean fluid pressure is of the same order of magnitude as the first term in brackets in (9.9), and the effect of the fluid pressure, observed if the two-way coupling is considered, is significant. However, if the solid is hard, e.g. with $E^* \approx 100$ GPa, then, accordingly, a high external pressure is necessary to seal the interface, such as $p_{ext} \approx 1$ GPa. However, this high pressure is unphysical for fluids used in sealing and lubrication applications. Therefore, the terms in the bracket corresponding to the mean fluid pressure and its gradient are negligible compared to the first term during almost all process of loading, except for the very beginning of it.

9.4 Comparison of two methods of the real contact area computation

The real contact area and its morphology are important not only for the study of the percolation in the sealing applications, but represent the key quantity determining the interfacial behaviour in many other physical problems, see e.g. [Vakis et al., 2018, Bowden and Tabor, 2001, Pei et al., 2005]. Therefore, it is important to ensure the accurate estimation of the contact area in numerical simulations, see also [Yastrebov et al., 2017a]. We present in Fig. 9.8 the comparison of the two methods of the real contact area computation, discussed in Section 4.3.2.

We perform a mesh convergence study, comparing the values of the real contact area obtained in simulations with three different meshes: with 128×128 , 256×256 and 512×512 face elements on the surface Γ , respectively. It is important to note that the spectrum of the surface roughness is preserved exactly the same for all considered meshes. Using the approach discussed in [Yastrebov et al., 2015], we generated the surface with following parameters: smallest wavenumber $k_l = 8\pi/L$, highest wavenumber $k_s = 64\pi/L$, Hurst exponent $H = 0.8$. The generated roughness with 513×513 points is mapped on the corresponding mesh. In order to obtain the surface geometry with coarser discretisations (257×257 and 129×129 points), a point-wise sampling was used, which is easy to perform, since the generated finite-element mesh has a regular quadrilateral grid on the surface.

The results show a significant difference between different meshes in case of the con-

tact area computation based on simple summing up of areas of active contact elements, see (4.120). The convergence seems to take place, but it is very slow. On the contrary, a refined approach to contact area computation (4.121), that we proposed, leads to a rather mesh-independent calculation of the real contact area.

9.5 Effect of elasto-plastic material behaviour on sealing properties

One of the most common industrial applications of the problem under discussion is the sealing engineering. The sealing engineering is particularly important in the nuclear industry, where commonly used fluid pressures are significantly high, and, at the same time, even micro-leakage is a critical issue. Due to operational conditions, the polymers are of limited use in such applications, and metal-to-metal contact seals are often utilized. In this case the problem is further complicated by the non-linear behaviour of the material, such as plastic flow, which results in irreversible changes of the surface geometry.

Recently, an experimental tool for measurement of the fluid micro-leakage in a contact interface between a rough metallic surface and a flat sapphire was developed [Marie and Lasseux, 2007]. This apparatus was used in the Ph.D. dissertation of C. Vallet [Vallet, 2008] to study the fluid leakage through an annular seal and to measure the interface transmissivity with respect to the applied external load in a loading-unloading cycle. Furthermore, measurements of the actual topography of the rough seal's surface were performed and approximate numerical estimations of the interface transmissivity were compared against the aforementioned experimental results. These estimations were further elaborated in the subsequent Ph.D. thesis of J. Durand [Durand, 2012], where a simplified model of contact and fluid flow was proposed. However, the agreement between numerical and experimental results in both studies was only qualitative: a difference of the transmissivity of an order of magnitude was observed.

Therefore, the purpose of this study is to perform a more rigorous numerical simulation of the fluid leakage in the same problem set-up, as in aforementioned works. The novel monolithic coupling component of Z-set framework, developed in this dissertation, was used to study the fluid leakage through a metallic seal brought in contact with a flat sapphire.

9.5.1 Problem set-up

A physically relevant contact simulation involving rough surfaces requires a very fine discretization, which becomes a bottleneck in finite-element studies. Therefore, a commonly used approach is to model a part of the surface, which is small enough to make the computation possible, and at the same time big enough to act as a representative surface element, see [Yastrebov et al., 2011, Durand, 2012] for details. We study here the thin fluid flow in the contact interface formed between a deformable solid Ω , which initially occupies a domain $[0; L_x] \times [0; L_y] \times [-H; 0]$ in the Cartesian coordinate system $\{\mathbf{e}_x, \mathbf{e}_y, \mathbf{e}_z\}$, and a rigid flat $z = 0$, see Fig. 9.9. We outline briefly boundary conditions for the solid problem:

$$\begin{cases} u_x|_{x=0} = u_x|_{x=L_x} = 0, & u_y|_{y=0} = u_y|_{y=L_y} = 0, & (9.10a) \\ u_z|_{z=-H} = u_z^0(t), & & (9.10b) \end{cases}$$

where (9.10a) are the symmetry (zero normal displacement) conditions on the vertical walls of the solid and (9.10b) is the Dirichlet B.C. on the bottom face of the solid,

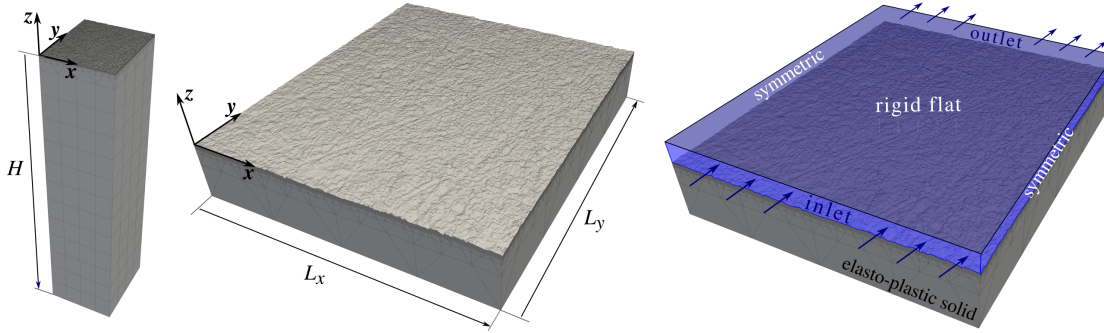


Figure 9.9: A sketch of the problem set-up: contact between a deformable solid with a rough surface and a rigid flat in presence of the thin fluid flow in the free volume between two surfaces.

which enforces the displacement control of the contact problem. Note that the normal approach is performed in 50 load steps, followed by the unloading (also in 50 steps). The boundary conditions for the fluid problem read:

$$\begin{cases} p_f|_{y=0} = p_i, & p_f|_{y=L} = p_o & (9.11a) \\ \mathbf{e}_y \cdot \mathbf{q}|_{x=0} = \mathbf{e}_y \cdot \mathbf{q}|_{x=L_x} = 0, & & (9.11b) \end{cases}$$

where (9.11a) are the Dirichlet B.C. with prescribed inlet p_i and outlet p_o fluid pressure, and (9.11b) are the no-flow Neumann B.C. on the remaining of the boundary of the fluid domain.

9.5.2 Material properties

In experiments performed in [Vallet, 2008] the seal's rough surface was made of Stellite, a cobalt-based alloy designed for high wear and erosion resistance [Kennametal Inc., 2012, Beaurin, 2012]. This material is frequently used in the sealing industry, however, its application in nuclear power plants was associated with certain problems: even tiny amounts of this material released into the process fluid caused significant radiation upon entering the reactor. A number of materials for replacing Stellite in nuclear applications were developed, including an alloy called Norem, which was used for numerical simulation in [Durand, 2012]. Mechanical properties of these two alloys are summarized in Table 9.1:

Table 9.1: Mechanical properties of two alloys used in the current study:

Alloy	Young's modulus E , [GPa]	Poisson's ratio, ν	Yield strength $\sigma_{0.2}$, [MPa]	Ultimate tensile strength, σ_u , [MPa]
Norem 02	175	0.3	678	949
Stellite 6	237	0.3	750	1265

Here we use the same J_2 plastic constitutive law with a non-linear isotropic hardening model, as in the numerical study [Yastrebov et al., 2011, Durand, 2012]. According to this model, the yield stress is represented by the following function:

$$\sigma_Y = R_0 + Q \left(1 - e^{-bp} \right), \quad (9.12)$$

where p is the accumulated plastic strain, R_0 is the initial yield stress, while for large strains the yield stress tends to $R_0 + Q$, and the parameter b controls how fast this

saturation limit is reached. The model parameters for Norem were identified in [Durand, 2012] using the experimental data, and for Stellite we used the parameters obtained by fitting the mechanical properties, given in Table 9.1, to the model (9.12). For both materials the parameters are provided in Table 9.2, and the corresponding stress-strain curves are presented in Fig. 9.10.

Table 9.2: Parameters of the non-linear hardening model (9.12) for two studied alloys:

Alloy	R_0 , [MPa]	Q , [MPa]	b
Norem 02	442.7	493.5	242.2
Stellite 6	493.1	771.9	202.4

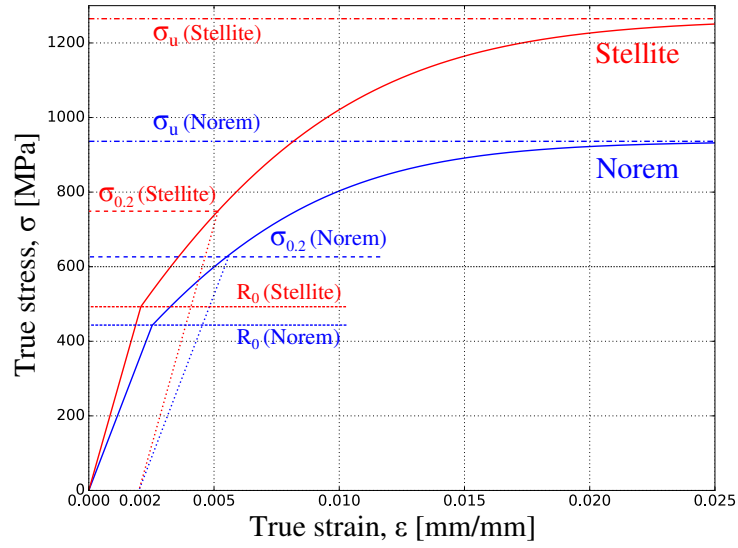


Figure 9.10: Stress-strain curves of two studied alloys, corresponding to the non-linear hardening model (9.12).

9.5.3 Surface topography

Surface measurements of four different zones of Stellite annular seal were performed in [Vallet, 2008] and are used here, see Fig. 9.11 for these surface topographies. The lateral extent of all zones is the same and equals approximately to $L_x = 606.3 \mu\text{m}$, $L_y = 461.1 \mu\text{m}$, which corresponds to a measurements grid of 736×480 points. Assuming that $z(x, y)$ is the height of the surface, A is the surface area, \bar{z} is the mean value of surface height, the following properties of roughness were identified and listed in Table 9.3.

- Average of absolute values of height S_a , [μm]:

$$S_a = \frac{1}{A} \int_A |z(x, y) - \bar{z}| dA$$

- Standard deviation (root mean squared) of height S_q , [μm]:

$$S_q = \sqrt{\frac{1}{A} \int_A (z(x, y) - \bar{z})^2 dA}$$

- Maximal valley depth S_v , [μm]: $S_v = \min_A z(x, y)$
- Maximal peak height S_p , [μm]: $S_p = \max_A z(x, y)$
- Skewness S_{sk} , [adim]:

$$S_{sk} = \frac{1}{AS_q^3} \int_A (z(x, y) - \bar{z})^3 dA$$

- Kurtosis S_{ku} , [adim]:

$$S_{ku} = \frac{1}{AS_q^4} \int_A (z(x, y) - \bar{z})^4 dA$$

- Average of absolute value of gradient (slope) S_{da} , [adim]:

$$S_{da} = \frac{1}{A} \int_A |\nabla z(x, y)| dA$$

- Standard deviation (root mean squared) of height gradient (slope) S_{dq} , [adim]:

$$S_{dq} = \sqrt{\frac{1}{A} \int_A |\nabla z(x, y)|^2 dA}.$$

Table 9.3: Surface roughness properties of four zones of Stellite annular seal:

Name	S_a [μm]	S_q [μm]	S_v [μm]	S_p [μm]	S_{sk} [adim]	S_{ku} [adim]	S_{da} [adim]	S_{dq} [adim]
Surface N	0.351	0.450	-3.767	2.926	0.002	3.756	0.273	0.322
Surface S	0.374	0.482	-3.105	2.811	-0.057	3.783	0.288	0.341
Surface E	0.364	0.470	-3.898	2.571	-0.111	3.836	0.289	0.342
Surface O	0.342	0.443	-3.142	3.502	-0.112	4.095	0.275	0.326

9.5.4 Computational framework

In the problem under study, we neglect the effect of the fluid pressure on the contact problem and therefore follow the one-way coupling approach. The justification comes from the fact that the physically relevant fluid pressure is considerably lower (≈ 1 MPa) than the local pressure arising in metal-to-metal contact (≈ 1 GPa), see also discussions in [Pérez-Ràfols et al., 2016]. Furthermore, we do not consider here the possibility of fluid entrapment inside pools completely bounded by contact zones (i.e., inside non-simply connected contact patches), since the real contact area does not exceed 12% during the whole loading process, and therefore the “trapped” part of the interface is negligible compared to the fluid-flow zones. Moreover, the pressure developed inside trapped fluid zones (if any of them appear) does not considerably differ from the mean fluid pressure.

The utilization of elasto-plastic material requires application of a special stabilization technique due to combination of nonlinearities due to contact constraints and to the

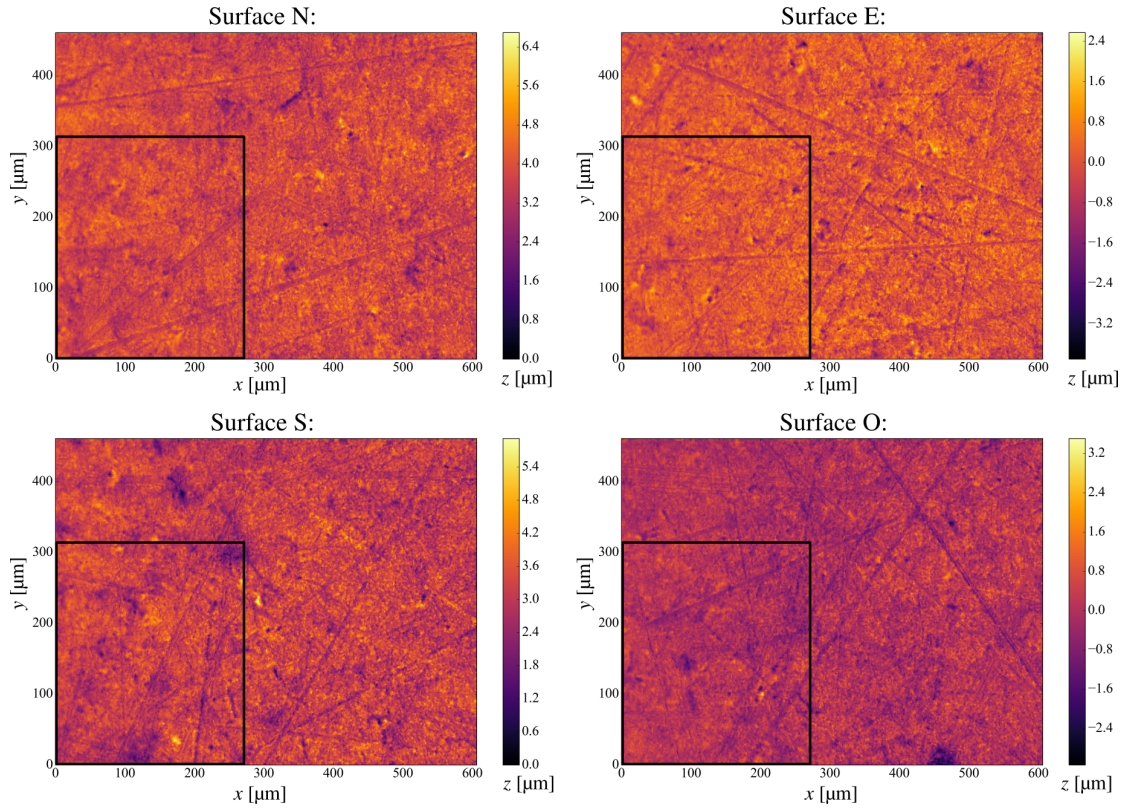


Figure 9.11: Surface topography measurements of 4 zones of the Stellite seal (736×480 measurement points). Black frame shows the part of the surface used in simulations (325×325 points).

material behaviour. It consists in splitting each increment (load step) into 2 successive phases:

- severe non-linear iterations: during this initial phase, material non-linearities are deactivated (i.e. the material behaviour is linearised around the state obtained at the end of the last converged increment), and only contact non-linearities are active;
- standard equilibrium iterations: once a preliminary stabilized contact state has been obtained at the end of the previous phase, material non-linearities are reactivated, and conventional equilibrium iterations proceed until convergence. Note that the contact non-linearities are included, such that the contact state may indeed change during this phase. However, smaller contact-state variations are expected compared to the case where the first phase is not done.

9.5.5 Results

In our numerical simulations we studied, following [Vallet, 2008, Durand, 2012], a part of each of four surfaces, corresponding to a frame of 325×325 points, see Fig. 9.11 and also Fig. 2.11. The whole computational mesh consists of ≈ 542000 nodes, and the coupled problem includes ≈ 1.8 million DOFs.

The results of one of the simulations with the surface “S” and material properties of alloy Stellite are presented in Fig. 9.12, note that 4 load steps out of 100 are shown. The first step corresponds to the beginning of loading, when almost all interface is occupied by the fluid flow. During the next two steps, due to increasing external load, the real

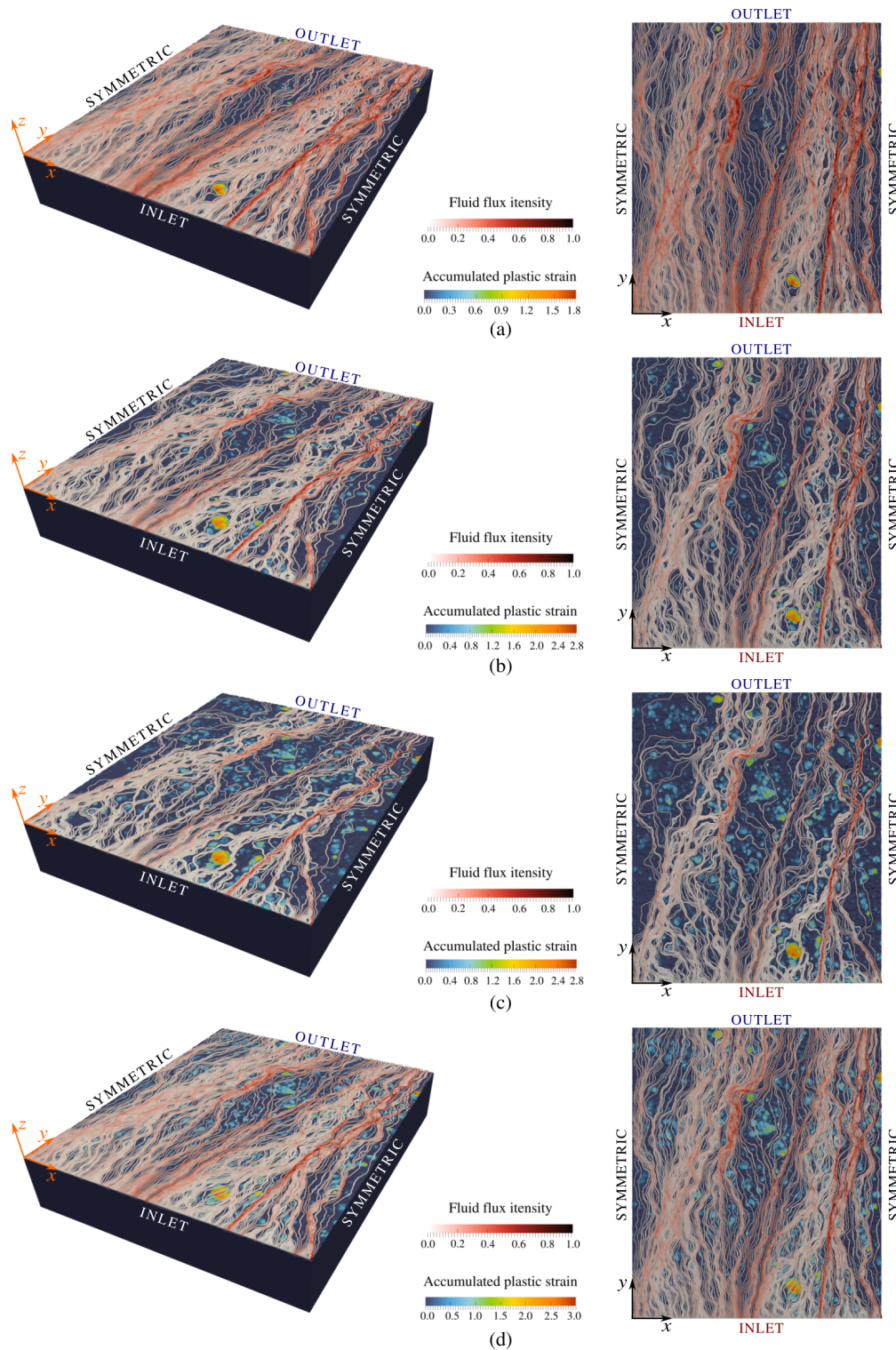


Figure 9.12: Fluid flow through a contact interface between deformable solid with a rough surface a rigid flat. Four different load steps are shown, corresponding to (top to bottom): (a) $p_{\text{ext}} = 5$ MPa, (b) $p_{\text{ext}} = 50$ MPa, (c) $p_{\text{ext}} = 290$ MPa, (d) $p_{\text{ext}} = 0$ MPa, where the last step corresponds to the fully unloaded state. For each loading step in the left column the bulk view of the solid is given, with colour on the surface representing accumulated plastic strain, and the stream lines are shown with colour representing the normalized fluid flux intensity q/q_{max} . In the right column the interface view, corresponding to the same loading steps, is given.

contact area is growing and, accordingly, the free volume is decreasing and the intensity of the fluid flow is diminishing. The 3rd step corresponds to the maximal external load (minimal fluid flow). Finally, the last step shows the interface in the completely unloaded state (when the external load reaches zero value). Note that, however, the displacement in the z -direction of the bottom of the solid is not zero at this stage due to irreversible changes of the surface topography caused by the plastic deformation. Interestingly, the fluid flow pattern at this stage is not similar to the one corresponding to beginning of loading ($p_{\text{ext}} = 5 \text{ MPa}$), but is rather close to the one of the intermediate load ($p_{\text{ext}} = 50 \text{ MPa}$).

Next, we computed the effective transmissivity K [μm^3] of the fluid flow in the numerical simulation as [Vallet, 2008, Durand, 2012]:

$$K = -\frac{QL_y\mu}{p_o - p_i}, \quad (9.13)$$

where Q_y is the mean flux in y -direction over the area $L_x \times L_y$, i.e.

$$Q_y = \frac{1}{L_x L_y} \int_0^{L_x} \int_0^{L_y} q_y dx dy, \quad (9.14)$$

and $q_y = -g^3/(12\mu) \partial p/\partial y$ is the fluid flux in the y -direction. The evolution of the effective transmissivity of the interface during the whole loading-unloading process for all four zones is shown in Fig. 9.13: (a) corresponds to the simulation with material properties of Norem alloy, and (b) with those of Stellite.

In Fig. 9.13(a) our results are compared with the approximate numerical estimations of [Durand, 2012]: the current plots show an approximately 2 times smaller transmissivity in the whole loading range from 0 to 300 MPa than the previous ones. The transmissivity obtained in simulations using properties of Stellite, Fig. 9.13(b), is compared with both experimental and numerical results from [Vallet, 2008]. Since this alloy has a higher Young's modulus (and the yield stress), than Norem, the transmissivity of a Stellite seal is higher than the one made of Norem, for the same external load. Again, we observe that our numerical results show ≈ 2 times smaller transmissivity than previous estimations. However, our computations differ from the experimental data, nevertheless, this difference is smaller than the one observed between the experiment and previous estimations.

9.6 Conclusions

In this Chapter we performed simulations of the thin fluid flow through a contact interface between a solid with a representative rough surface and a rigid flat. Obtained results confirmed that the one-way coupling underestimates the interface permeability and the critical external load needed to completely seal the interface. Additionally, we performed a study of transmissivity for a wide range of inlet and outlet pressures and formulated a non-local phenomenological equation for the transmissivity of rough contact interfaces. We showed that the logarithm of the effective transmissivity is an affine function of the applied pressure, the mean fluid pressure and the mean fluid pressure gradient.

Finally, the developed framework was used to calculate the fluid leakage in a contact interface between a metallic surface and a sapphire plate, using the real surface measurements. An elasto-plastic material behaviour with nonlinear hardening was introduced into the computational model, which permitted to study the performance of real seals

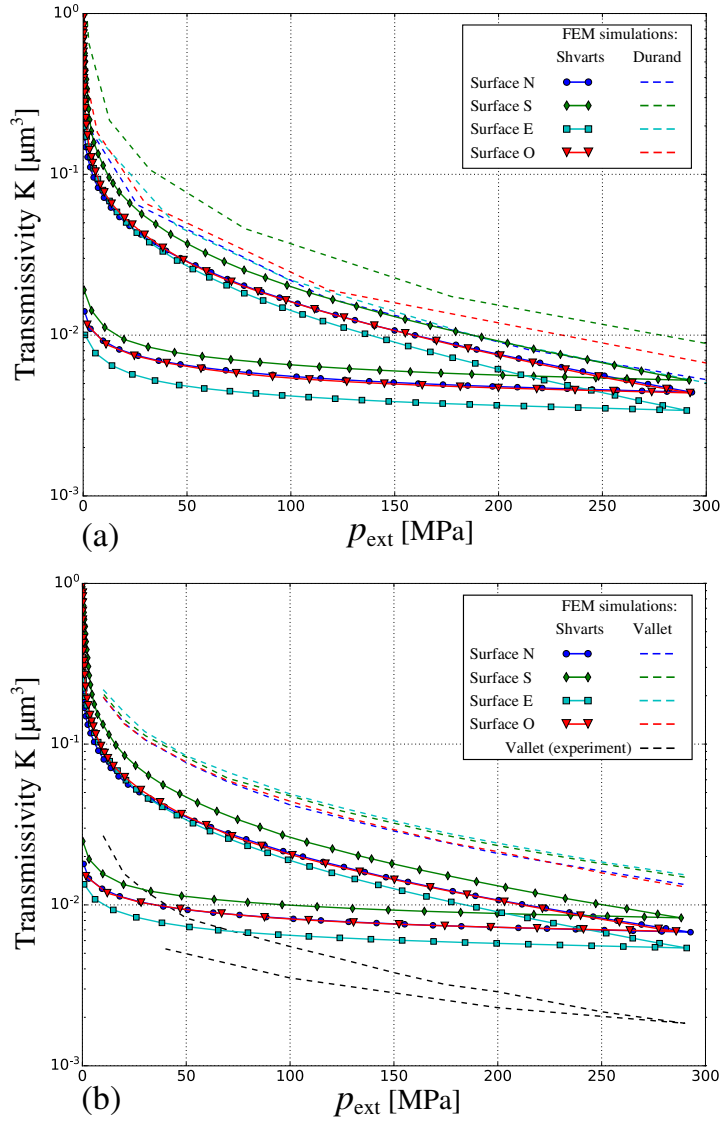


Figure 9.13: Evolution of the interface transmissivity during loading-unloading process. Simulations performed using material properties of two alloys: (a) Norem and (b) Stellite.

used in nuclear power plants.

In order to obtain a robust convergence in case of combination of contact and material nonlinearities a stabilization technique was successfully utilized. We showed that the direct monolithic simulation provides a possibility to resolve the coupled problem without introducing any additional assumptions and simplifications. Furthermore, it provides output data for easy combined visualization of the solid’s deformation and the fluid flow’s patterns.

The results of our simulations are quantitatively different from numerical approximations of C. Vallet and J. Durand: in all studied cases the transmissivity is approximately 2 times smaller in current computations, than in the previous ones. However, our results still differ from the experiment data, nevertheless this difference is smaller than using the previous estimations.

To find the explanation of the difference between the experiment and simulations, further studies under these both approaches may be needed. From the numerical side, additional simulations with other parts and/or larger zones of the seal’s surface should be

performed, which could require bigger meshes and, possibility, additional measurements of the surface topography. From the experimental side, the verification of previous results and the method of computation of the effective transmissivity could be useful.

Chapter 10

Conclusions and perspectives

Résumé de Chapitre 10 “Conclusions et perspectives”

Dans le dernier chapitre de la thèse, nous énonçons les remarques finales. Premièrement, nous mettons en évidence les contributions originales en lien avec la mécanique numérique :

- (i) développement d’un cadre monolithique en éléments finis pour l’écoulement d’une couche mince de fluide dans une interface de contact entre un solide déformable et un plan rigide ;*
- (ii) formulation d’un élément de fluide piégé ;*
- (iii) la mise en œuvre d’une procédure de partitionnement de l’interface en zones de contact, d’écoulement de fluide et de fluide piégé.*

Ensuite, nous rappelons les résultats obtenus. Pour le problème du fluide piégé dans l’interface entre un solide déformable avec une surface ondulée et un plan rigide :

- (iv) la surface de contact diminue en raison de l’augmentation de la pression du fluide piégé ;*
- (v) une formule analytique pour la déviation du profil ondulé provoquée par une pression hydrostatique uniforme ;*
- (vi) la limite de frottement n’augmente pas linéairement avec l’augmentation de la charge externe, mais atteint un maximum et diminue jusqu’à zéro ;*
- (vii) des quasi-singularités apparaissent dans les contraintes de frottement près des bords des zones de contact lors de l’ouverture du piège à fluide.*

Pour le problème d’écoulement de fluide à travers des interfaces de contact avec une géométrie du modèle ou une surface rugueuse :

- (viii) une solution analytique approximative dans le cas d’une surface ondulée ;*
- (ix) une dépendance affine de la pression externe dite d’étanchéité, qui scelle le canal d’entrée du fluide ;*
- (x) une équation phénoménologique pour la transmissivité des interfaces de contact rugueuses.*

Enfin, nous décrivons les perspectives d’évolution possible du cadre actuel et d’autres problèmes mécaniques importants.

In the final chapter of this dissertation we make concluding remarks highlighting original contributions to the computational mechanics and to the study of problems involving thin fluid flow in contact interfaces. Furthermore, we outline perspectives for possible improvements of the current framework, and for further problems that are worth investigating.

10.1 Original contributions

First, we will outline contributions to the computational framework from Part II, and after that summarize the results of the studies presented in Part III.

10.1.1 Computational framework

In this dissertation *(i) a monolithic finite-element framework was developed aimed at solving a problem of thin fluid flow in a contact interface between a deformable solid and a rigid flat subject to a normal load.* Both one-way and two-way coupling approaches were considered. This framework combines the state-of-the-art contact resolution algorithms, fluid-flow elements for solving the Reynolds equation for incompressible viscous flow and fluid-structure interface elements to transfer fluid tractions onto the solid. Additionally, the possibility of fluid entrapment in the contact interface and its consequent pressurization was considered using both incompressible and compressible fluid models. In the latter case, constitutive laws with constant or pressure-dependent bulk modulus were used. *(ii) We introduced all aforementioned models of the trapped fluid into the finite-element framework formulating a “super-element” for each trapped fluid zone.*

One of the main complexities of the problem of fluid flow in contact interfaces is caused by the dependency of the extent of fluid-flow domain and the trapped fluid zones on the solution of the contact problem, which can be enhanced by a sophisticated morphology of the contact area resulting from deterministic or random features of the surface geometry. In the developed framework this complexity is handled by a procedure of *(iii) partitioning the interface into contact, fluid-flow and trapped fluid zones, performed at every iteration of Newton-Raphson method using connected-component labelling of the interface graph; the standard algorithm based on the depth-first search was further elaborated to take into account formation and evolution of trapped fluid zones.*

The proposed framework was implemented in the non-linear finite-element code *Z-set*, in particular: contact elements based on two discretization approaches: “node-to-rigid-surface” (2D, with and without friction) and “face-to-rigid-surface” (3D, in the spirit of the mortar approach, frictionless); fluid-flow, trapped-fluid, and fluid-structure interface elements, and, finally, modifications of the Newton-Raphson iterative procedure to perform connected-component labelling of the interface graph and tracking of trapped fluid zones at every iteration.

The description of the discussed above computational framework is presented in a paper entitled “*Computational framework for monolithic coupling for thin fluid flow in contact interfaces*” submitted for consideration of publication [Shvarts et al., 2019].

10.1.2 Trapped fluid in contact interface

We considered separately the problem of mechanical contact between a deformable body with a wavy surface and a rigid flat, taking into account pressurized fluid trapped in the interface, accounting for a finite variation of the slope of the surface profile. We showed that *(iv) a reduction of the contact area can occur due to the fluid pressure applied to the solid’s surface beyond the contact patches, and therefore, the reduction of the global*

coefficient of friction is caused not only by the external load repartition between the solid contact and the pressurized fluid, but also by the contact area reduction.

(v) We derived an analytic formula for the deflection of the wavy profile (in case of small, but finite ratio of the amplitude to the wavelength) caused by a uniform hydrostatic pressure. This result is used to derive an expression for the external pressure required to open a trap of a given volume. We showed how the evolution of the real contact area and of the global coefficient of friction under increasing external load depends on properties of the fluid and the solid, and on geometry characteristics of the surface profile.

(vi) We showed that in case of of an incompressible trapped fluid and an elastic solid due to the presence of pressurized fluid in the interface, the frictional limit does not increase linearly with increasing external load, but reaches a maximum and decreases down to zero. Such a behaviour is similar to pressure-dependent plasticity models with a cap (e.g. Drucker-Prager cap model), which corresponds to the decay of the von Mises yield stress with the increasing pressure. A compressible fluid with pressure-dependent bulk modulus is responsible for a non-monotonous behaviour of the global coefficient of friction, due to a competition between a non-linear evolution of the contact area and of the fluid pressure. At the same time, in case of elastic-perfectly plastic materials we observed an abrupt fluid permeation into the contact interface.

(vii) When interfacial friction is considered in the coupled problem, previously unreported quasi-singularities appear in shear stresses near edges of contact patches during fluid-trap opening under normal loading. We showed that these singularities can be analytically estimated using an analogy between the trap opening and a crack propagation in the interface between two bonded dissimilar solids.

The results of this study have been already published [Shvarts and Yastrebov, 2018b].

10.1.3 Fluid flow in contact interface with model geometries

To validate the robustness and optimal convergence rate of the proposed monolithic formulation and the efficiency of the resolution algorithm we studied a fluid flow through an extruded wavy interface and a channel with an “atoll”-shaped elevation of the profile, which forms a trapped fluid zone (“lagoon”). According to obtained results, once the local interface status is preserved between two Newton-Raphson iterations, the quadratic convergence is recovered.

Furthermore, for the problem of the thin fluid flow across a wavy channel *(viii) we derived an approximate analytical solution based on the Westergaard-Kuznetsov solution and a one-dimensional formulation of the Reynolds equation.* A good agreement between this result and a numerical solution was found in the range of the validity of the approximate one.

Both numerical and analytical results, which take into account two-way coupling, showed that the interface transmissivity is higher than this predicted by the one-way coupling. An additional result of this study is *(ix) the affine dependence of the external sealing pressure on the inlet fluid pressure only, i.e the outlet pressure does not affect the pressure needed to seal the channel.* If the effect of the trapped fluid is taken into account, the critical pressure further increases, while the contact area corresponding to the complete sealing of the interface is found to be smaller.

The results of this study have been already published [Shvarts and Yastrebov, 2018a].

10.1.4 Fluid flow through representative rough contact interface

Simulations of the thin fluid flow through a contact interface between a solid with a rough surface and a rigid flat showed that the one-way coupling approach underestimates the interface permeability and critical external load needed to completely seal the interface.

At the same time, for an elastic solid with the value of Young's modulus typical for soft matter the real contact area observed close to the percolation is approximately 15% smaller if the two-way coupling is considered.

We performed a study of transmissivity of representative Gaussian, isotropic and self-affine rough surface in contact with a rigid flat for a wide range of inlet and outlet pressures, and *(x) formulated a non-local phenomenological equation for the transmissivity of rough contact interfaces. We showed that the logarithm of the effective transmissivity is an affine function of the applied pressure, the mean fluid pressure and the mean fluid pressure gradient. Using this equation it is now possible to quantitatively estimate the range of applicability of the one-way coupling approach.*

Finally, the developed framework was used to calculate the fluid leakage in a contact interface between a metallic surface and a sapphire plate, using the real surface measurements. An elasto-plastic material behaviour with nonlinear hardening was introduced into the computational model, which permitted to study the performance of real static seals used in water cycles of nuclear power plants. The novel numerical results are in a better agreement with the experiment than the previous estimations.

10.2 Perspectives

We outline here perspective developments for the computational framework, as well as propositions of additional studies.

10.2.1 Computational framework

- Consider large deformations and large rotations formulations, which would require taking into account variations of Jacobian and normals, i.e derivation of a more elaborated structure of consistent tangent matrices. This modification would permit to study the effect of more complex, e.g. hyper-elastic material models, and also consider the variation of the surface geometry in a wider range of parameters.
- Including Coulomb's friction into the face-to-rigid-surface approach, using the penalty or augmented Lagrangian methods, would permit to expand the study of the trapped fluid problem to 3D set-up and investigate further the observed phenomenon of quasi-singularities in tangential tractions.
- A higher order interpolation for the formulated elements would enhance the representation of the contact interface, in particular, description of the gap and of the surface tractions, as well as of the fluid flux.
- Include tangential motion of the solid walls into the problem, consider the corresponding terms of the Reynolds equation. This would permit to expand the developed framework to mixed lubrication problems.
- Consider compressible fluid and/or pressure-dependent viscosity within the Reynolds equation, which is relevant, e.g. for gas seals and elasto-hydrodynamic lubrication problems.
- Introduce parallel implementation for contact, fluid-flow, fluid-structure interface and trapped fluid elements, which would permit to consider a finer discretization of the contact interface.
- Consider the standard approach to finite element formulation instead of the "super"-element formulation, permitting to avoid the storage of a matrix of the "super-element", which can be vast if a fine discretization of the surface is used and

the trapped fluid zone is large. However, the standard formulation would require adding and removing additional degrees of freedom (changing the size of the global DOF vector) after each iteration, making the resolution procedure more complex. The comparison of effectiveness of the “super-element” and standard formulations is therefore of interest.

10.2.2 Studies

- Using the parallel implementation, perform simulation with a finer mesh, which would allow to use a richer spectrum of roughness, and study effects of the two-way coupling close to percolation.
- Elaborate the study of the elasto-plastic seal’s performance in order to find out the reason for the remaining difference between the numerical simulations and experimental results, investigate other parts and/or larger zones of the seal’s surface.
- Perform a more detailed study of the novel phenomenological law for the rough interface transmissivity, consider realistic problems of cracked medium, e.g. in hydrogeology, for which this law would be of importance.
- Study the mixed lubrication problem, considering relative tangential motion of the contacting solids, the developed framework could allow to compute the global coefficient of friction in the two-way coupling.

Bibliography

- [Adams and Fournier, 2003] Adams, R. A. and Fournier, J. J. (2003). *Sobolev spaces*. Elsevier.
- [Alart and Curnier, 1991] Alart, P. and Curnier, A. (1991). A mixed formulation for frictional contact problems prone to newton like solution methods. *Computer methods in applied mechanics and engineering*, 92(3):353–375.
- [Alcalá and Esqué-de los Ojos, 2010] Alcalá, J. and Esqué-de los Ojos, D. (2010). Re-assessing spherical indentation: Contact regimes and mechanical property extractions. *International Journal of Solids and Structures*, 47(20):2714–2732.
- [Archard, 1953] Archard, J. (1953). Contact and rubbing of flat surfaces. *Journal of applied physics*, 24(8):981–988.
- [Archard, 1957] Archard, J. (1957). Elastic deformation and the laws of friction. In *Proceedings of the Royal Society of London A: Mathematical, Physical and Engineering Sciences*, volume 243, pages 190–205. The Royal Society.
- [Azushima, 2000] Azushima, A. (2000). Fem analysis of hydrostatic pressure generated within lubricant entrapped into pocket on workpiece surface in upsetting process. *Journal of Tribology*, 122(4):822–827.
- [Azushima, 2016] Azushima, A. (2016). *Tribology in Sheet Rolling Technology*. Springer.
- [Azushima and Kudo, 1995] Azushima, A. and Kudo, H. (1995). Direct observation of contact behaviour to interpret the pressure dependence of the coefficient of friction in sheet metal forming. *CIRP Annals - Manufacturing Technology*, 44(1):209–212.
- [Azushima et al., 2011] Azushima, A., Yanagida, A., and Tani, S. (2011). Permeation of lubricant trapped within pocket into real contact area on the end surface of cylinder. *Journal of Tribology*, 133(1):011501.
- [Baaijens, 2001] Baaijens, F. P. (2001). A fictitious domain/mortar element method for fluid–structure interaction. *International Journal for Numerical Methods in Fluids*, 35(7):743–761.
- [Bao-Tong and Laird, 1989] Bao-Tong, M. and Laird, C. (1989). Overview of fatigue behavior in copper single crystals – I. Surface morphology and stage I crack initiation sites for tests at constant strain amplitude. *Acta Metallurgica*, 37(2):325–336.
- [Barber, 2003] Barber, J. (2003). Bounds on the electrical resistance between contacting elastic rough bodies. In *Proceedings of the Royal Society of London A: Mathematical, Physical and Engineering Sciences*, volume 459, pages 53–66. The Royal Society.
- [Bažant et al., 2014] Bažant, Z. P., Salviato, M., Chau, V. T., Viswanathan, H., and Zubelewicz, A. (2014). Why fracking works. *Journal of Applied Mechanics*, 81(10):101010.

- [Bazilevs et al., 2006] Bazilevs, Y., Calo, V. M., Zhang, Y., and Hughes, T. J. (2006). Isogeometric fluid–structure interaction analysis with applications to arterial blood flow. *Computational Mechanics*, 38(4-5):310–322.
- [Bazilevs et al., 2011] Bazilevs, Y., Hsu, M.-C., Kiendl, J., Wüchner, R., and Bletzinger, K.-U. (2011). 3d simulation of wind turbine rotors at full scale. part ii: Fluid–structure interaction modeling with composite blades. *International Journal for Numerical Methods in Fluids*, 65(1-3):236–253.
- [Beaurin, 2012] Beaurin, G. (2012). *Modelisation and experimental study of residual stresses in Norem hardfacing coatings used in valve parts*. PhD thesis, INSA de Lyon. (in French).
- [Bech et al., 1999] Bech, J., Bay, N., and Eriksen, M. (1999). Entrapment and escape of liquid lubricant in metal forming. *Wear*, 232(2):134–139.
- [Besson et al., 2009] Besson, J., Cailletaud, G., Chaboche, J.-L., and Forest, S. (2009). *Non-linear mechanics of materials*. Springer Science & Business Media.
- [Besson and Foerch, 1997] Besson, J. and Foerch, R. (1997). Large scale object-oriented finite element code design. *Computer methods in applied mechanics and engineering*, 142(1-2):165–187.
- [Bowden and Tabor, 2001] Bowden, F. P. and Tabor, D. (2001). *The friction and lubrication of solids*. Oxford University Press.
- [Bower, 1988] Bower, A. (1988). The influence of crack face friction and trapped fluid on surface initiated rolling contact fatigue cracks. *Journal of Tribology*, 110(4):704–711.
- [Brown et al., 1995] Brown, S. R., Stockman, H. W., and Reeves, S. J. (1995). Applicability of the reynolds equation for modeling fluid flow between rough surfaces. *Geophysical Research Letters*, 22(18):2537–2540.
- [Budiansky and O’connell, 1976] Budiansky, B. and O’connell, R. J. (1976). Elastic moduli of a cracked solid. *International Journal of Solids and Structures*, 12(2):81–97.
- [Bush et al., 1975] Bush, A., Gibson, R., and Thomas, T. (1975). The elastic contact of a rough surface. *Wear*, 35(1):87–111.
- [Caligaris and Ateshian, 2008] Caligaris, M. and Ateshian, G. A. (2008). Effects of sustained interstitial fluid pressurization under migrating contact area, and boundary lubrication by synovial fluid, on cartilage friction. *Osteoarthritis and Cartilage*, 16(10):1220–1227.
- [Carbone and Bottiglione, 2008] Carbone, G. and Bottiglione, F. (2008). Asperity contact theories: Do they predict linearity between contact area and load? *Journal of the Mechanics and Physics of Solids*, 56:2555–2572.
- [Cavaleri and Cardona, 2013] Cavaleri, F. J. and Cardona, A. (2013). An augmented lagrangian technique combined with a mortar algorithm for modelling mechanical contact problems. *International Journal for Numerical Methods in Engineering*, 93(4):420–442.
- [Chan et al., 2011] Chan, S., Neu, C., Komvopoulos, K., and Reddi, A. (2011). The role of lubricant entrapment at biological interfaces: Reduction of friction and adhesion in articular cartilage. *Journal of Biomechanics*, 44(11):2015–2020.

- [Ciavarella et al., 2008] Ciavarella, M., Greenwood, J., and Paggi, M. (2008). Inclusion of “interaction” in the greenwood and williamson contact theory. *Wear*, 265(5):729–734.
- [Coussy, 2004] Coussy, O. (2004). *Poromechanics*. Wiley Online Library.
- [Cuffey and Paterson, 2010] Cuffey, K. M. and Paterson, W. S. B. (2010). *The Physics of Glaciers*. Academic Press.
- [Dapp et al., 2012] Dapp, W. B., Lücke, A., Persson, B. N., and Müser, M. H. (2012). Self-affine elastic contacts: percolation and leakage. *Physical Review Letters*, 108(24):244301.
- [Dapp and Müser, 2015] Dapp, W. B. and Müser, M. H. (2015). Contact mechanics of and reynolds flow through saddle points: On the coalescence of contact patches and the leakage rate through near-critical constrictions. *EPL (Europhysics Letters)*, 109(4):44001.
- [Dapp and Müser, 2016] Dapp, W. B. and Müser, M. H. (2016). Fluid leakage near the percolation threshold. *Scientific Reports*, 6:19513.
- [Dapp et al., 2014] Dapp, W. B., Prodanov, N., and Müser, M. H. (2014). Systematic analysis of persson’s contact mechanics theory of randomly rough elastic surfaces. *Journal of Physics: Condensed Matter*, 26(35):355002.
- [De Hart et al., 2003] De Hart, J., Peters, G., Schreurs, P., and Baaijens, F. (2003). A three-dimensional computational analysis of fluid–structure interaction in the aortic valve. *Journal of Biomechanics*, 36(1):103–112.
- [Demkowicz and Oden, 1982] Demkowicz, L. and Oden, J. (1982). On some existence and uniqueness results in contact problems with nonlocal friction. *Nonlinear Analysis: Theory, Methods & Applications*, 6(10):1075–1093.
- [Donea et al., 1982] Donea, J., Giuliani, S., and Halleux, J.-P. (1982). An arbitrary lagrangian-eulerian finite element method for transient dynamic fluid-structure interactions. *Computer Methods in Applied Mechanics and Engineering*, 33(1-3):689–723.
- [Dormieux et al., 2002] Dormieux, L., Molinari, A., and Kondo, D. (2002). Micromechanical approach to the behavior of poroelastic materials. *Journal of the Mechanics and Physics of Solids*, 50(10):2203–2231.
- [Durand, 2012] Durand, J. (2012). *Multiscale Modelling of Contact of Rough Surfaces*. PhD thesis, MINES ParisTech.
- [Evans, 2010] Evans, L. C. (2010). *Partial differential equations*. American Mathematical Society.
- [Farhat et al., 2003] Farhat, C., Geuzaine, P., and Brown, G. (2003). Application of a three-field nonlinear fluid–structure formulation to the prediction of the aeroelastic parameters of an F-16 fighter. *Computers & Fluids*, 32(1):3–29.
- [Farhat et al., 1998] Farhat, C., Lesoinne, M., and Le Tallec, P. (1998). Load and motion transfer algorithms for fluid/structure interaction problems with non-matching discrete interfaces: Momentum and energy conservation, optimal discretization and application to aeroelasticity. *Computer Methods in Applied Mechanics and Engineering*, 157(1-2):95–114.

- [Fischer and Clarke, 1997] Fischer, U. H. and Clarke, G. K. (1997). Stick slip sliding behaviour at the base of a glacier. *Annals of Glaciology*, 24:390–396.
- [Garagash and Germanovich, 2012] Garagash, D. I. and Germanovich, L. N. (2012). Nucleation and arrest of dynamic slip on a pressurized fault. *Journal of Geophysical Research: Solid Earth*, 117(B10).
- [Gerbeau and Vidrascu, 2003] Gerbeau, J.-F. and Vidrascu, M. (2003). A quasi-newton algorithm based on a reduced model for fluid-structure interaction problems in blood flows. *ESAIM: Mathematical Modelling and Numerical Analysis*, 37(4):631–647.
- [Gerstenberger and Wall, 2008] Gerstenberger, A. and Wall, W. A. (2008). An extended finite element method/Lagrange multiplier based approach for fluid-structure interaction. *Computer Methods in Applied Mechanics and Engineering*, 197(19-20):1699–1714.
- [Gitterle, 2012] Gitterle, M. (2012). *A dual mortar formulation for finite deformation frictional contact problems including wear and thermal coupling*. PhD thesis, Technische Universität München.
- [Goryacheva and Shpenev, 2012] Goryacheva, I. and Shpenev, A. (2012). Modelling of a punch with a regular base relief sliding along a viscoelastic foundation with a liquid lubricant. *Journal of Applied Mathematics and Mechanics*, 76(5):582–589.
- [Greenwood, 2006] Greenwood, J. (2006). A simplified elliptic model of rough surface contact. *Wear*, 261(2):191–200.
- [Greenwood and Williamson, 1966] Greenwood, J. and Williamson, J. (1966). Contact of nominally flat surfaces. In *Proceedings of the Royal Society of London A: Mathematical, Physical and Engineering Sciences*, volume 295, pages 300–319. The Royal Society.
- [Hamrock et al., 2004] Hamrock, B. J., Schmid, S. R., and Jacobson, B. O. (2004). *Fundamentals of fluid film lubrication*. CRC press.
- [Heegaard and Curnier, 1993] Heegaard, J.-H. and Curnier, A. (1993). An augmented lagrangian method for discrete large-slip contact problems. *International Journal for Numerical Methods in Engineering*, 36(4):569–593.
- [Heil, 1998] Heil, M. (1998). Stokes flow in an elastic tube – a large-displacement fluid-structure interaction problem. *International Journal for Numerical Methods in Fluids*, 28(2):243–265.
- [Heil, 2004] Heil, M. (2004). An efficient solver for the fully coupled solution of large-displacement fluid-structure interaction problems. *Computer Methods in Applied Mechanics and Engineering*, 193(1-2):1–23.
- [Hestenes, 1969] Hestenes, M. R. (1969). Multiplier and gradient methods. *Journal of Optimization Theory and Applications*, 4(5):303–320.
- [Hills, 1994] Hills, D. A. (1994). Mechanics of fretting fatigue. *Wear*, 175(1-2):107–113.
- [Hübner et al., 2004] Hübner, B., Walhorn, E., and Dinkler, D. (2004). A monolithic approach to fluid-structure interaction using space-time finite elements. *Computer Methods in Applied Mechanics and Engineering*, 193(23-26):2087–2104.

- [Hüeber, 2008] Hüeber, S. (2008). *Discretization techniques and efficient algorithms for contact problems*. PhD thesis, University of Stuttgart.
- [Hyun et al., 2004] Hyun, S., Pei, L., Molinari, J. F., and Robbins, M. O. (2004). Finite-element analysis of contact between elastic self-affine surfaces. *Phys Rev E*, 70(2):026117.
- [Ibrahimbegovic, 2009] Ibrahimbegovic, A. (2009). *Nonlinear solid mechanics: theoretical formulations and finite element solution methods*, volume 160. Springer Science & Business Media.
- [Issen and Rudnicki, 2000] Issen, K. and Rudnicki, J. (2000). Conditions for compaction bands in porous rock. *Journal of Geophysical Research: Solid Earth*, 105(B9):21529–21536.
- [Johnson et al., 1985] Johnson, K., Greenwood, J., and Higginson, J. (1985). The contact of elastic regular wavy surfaces. *Int J Mech Sci*, 27(6):383 – 396.
- [Johnson, 1987] Johnson, K. L. (1987). *Contact mechanics*. Cambridge University Press.
- [Kennametal Inc., 2012] Kennametal Inc. (2012). Stellite 6 alloy.
- [Kikuchi and Oden, 1988] Kikuchi, N. and Oden, J. T. (1988). *Contact problems in elasticity: a study of variational inequalities and finite element methods*, volume 8. siam.
- [Kogut and Etsion, 2002] Kogut, L. and Etsion, I. (2002). Elastic-plastic contact analysis of a sphere and a rigid flat. *Journal of Applied Mechanics*, 69(5):657–662.
- [Konyukhov and Schweizerhof, 2012] Konyukhov, A. and Schweizerhof, K. (2012). *Computational Contact Mechanics: geometrically exact theory for arbitrary shaped bodies*, volume 67. Springer Science & Business Media.
- [Krim and Palasantzas, 1995] Krim, J. and Palasantzas, G. (1995). Experimental observations of self-affine scaling and kinetic roughening at sub-micron length scales. *International Journal of Modern Physics B*, 9:599–632.
- [Kudo, 1965] Kudo, H. (1965). A note on the role of microscopically trapped lubricant at the tool-work interface. *International Journal of Mechanical Sciences*, 7(5):383–388.
- [Küttler and Wall, 2008] Küttler, U. and Wall, W. A. (2008). Fixed-point fluid–structure interaction solvers with dynamic relaxation. *Computational Mechanics*, 43(1):61–72.
- [Kuznetsov, 1985] Kuznetsov, Y. (1985). Effect of fluid lubricant on the contact characteristics of rough elastic bodies in compression. *Wear*, 102(3):177–194.
- [Luan and Robbins, 2005] Luan, B. and Robbins, M. O. (2005). The breakdown of continuum models for mechanical contacts. *Nature*, 435(7044):929.
- [Lurie and Belyaev, 2005] Lurie, A. and Belyaev, A. (2005). Theory of elasticity. foundations of engineering mechanics. *Springer, Berlin*, 10(1007):978–3.
- [Lurie, 2012] Lurie, A. I. (2012). *Non-linear theory of elasticity*, volume 36. Elsevier.
- [Majumdar and Bhushan, 1991] Majumdar, A. and Bhushan, B. (1991). Fractal model of elastic-plastic contact between rough surfaces. *Journal of Tribology*, 113(1):1–11.

- [Manners and Greenwood, 2006] Manners, W. and Greenwood, J. A. (2006). Some observations on Persson’s diffusion theory of elastic contact. *Wear*, 261:600–610.
- [Marie and Lasseux, 2007] Marie, C. and Lasseux, D. (2007). Experimental leak-rate measurement through a static metal seal. *Journal of fluids engineering*, 129(6):799–805.
- [Matsuda et al., 2016] Matsuda, K., Hashimoto, D., and Nakamura, K. (2016). Real contact area and friction property of rubber with two-dimensional regular wavy surface. *Tribology International*, 93:523–529.
- [Matthies and Steindorf, 2003] Matthies, H. G. and Steindorf, J. (2003). Partitioned strong coupling algorithms for fluid–structure interaction. *Computers & structures*, 81(8-11):805–812.
- [Mayer et al., 2010] Mayer, U. M., Popp, A., Gerstenberger, A., and Wall, W. A. (2010). 3d fluid–structure-contact interaction based on a combined XFEM FSI and dual mortar contact approach. *Computational Mechanics*, 46(1):53–67.
- [Mesarovic and Fleck, 1999] Mesarovic, S. D. and Fleck, N. A. (1999). Spherical indentation of elastic–plastic solids. In *Proceedings of the Royal Society of London A: Mathematical, Physical and Engineering Sciences*, volume 455, pages 2707–2728. The Royal Society.
- [Michler et al., 2004] Michler, C., Hulshoff, S., Van Brummelen, E., and De Borst, R. (2004). A monolithic approach to fluid–structure interaction. *Computers & fluids*, 33(5-6):839–848.
- [Mittal and Iaccarino, 2005] Mittal, R. and Iaccarino, G. (2005). Immersed boundary methods. *Annu. Rev. Fluid Mech.*, 37:239–261.
- [Mróz and Stupkiewicz, 1994] Mróz, Z. and Stupkiewicz, S. (1994). An anisotropic friction and wear model. *International Journal of Solids and Structures*, 31(8):1113–1131.
- [Müller and Nau, 1998] Müller, H. K. and Nau, B. S. (1998). *Fluid Sealing Technology: Principles and Applications*. M. Dekker.
- [Muskhelishvili, 2013] Muskhelishvili, N. I. (2013). *Some basic problems of the mathematical theory of elasticity*. Springer Science & Business Media.
- [Nayak, 1971] Nayak, P. R. (1971). Random process model of rough surfaces. *J Lubr Technol (ASME)*, 93:398–407.
- [Nellemann et al., 1977] Nellemann, T., Bay, N., and Wanheim, T. (1977). Real area of contact and friction stress—the role of trapped lubricant. *Wear*, 43(1):45–53.
- [Paggi and He, 2015] Paggi, M. and He, Q.-C. (2015). Evolution of the free volume between rough surfaces in contact. *Wear*, 336:86–95.
- [Païdoussis et al., 2010] Païdoussis, M. P., Price, S. J., and De Langre, E. (2010). *Fluid-structure interactions: cross-flow-induced instabilities*. Cambridge University Press.
- [Pei et al., 2005] Pei, L., Hyun, S., Molinari, J. F., and Robbins, M. O. (2005). Finite element modeling of elasto-plastic contact between rough surfaces. *Journal of the Mechanics and Physics of Solids*, 53:2385–2409.
- [Pérez-Ràfols et al., 2016] Pérez-Ràfols, F., Larsson, R., and Almqvist, A. (2016). Modelling of leakage on metal-to-metal seals. *Tribology International*, 94:421 – 427.

- [Perrin and Leblond, 1993] Perrin, G. and Leblond, J. (1993). Rudnicki and rice’s analysis of strain localization revisited. *Journal of Applied Mechanics*, 60(4):842–846.
- [Persson, 2010] Persson, B. (2010). Fluid dynamics at the interface between contacting elastic solids with randomly rough surfaces. *Journal of Physics: Condensed Matter*, 22(26):265004.
- [Persson et al., 2012] Persson, B., Prodanov, N., Krick, B., Rodriguez, N., Mulakaluri, N., Sawyer, W., and Mangiagalli, P. (2012). Elastic contact mechanics: Percolation of the contact area and fluid squeeze-out. *The European Physical Journal E*, 35(1):5.
- [Persson and Yang, 2008] Persson, B. and Yang, C. (2008). Theory of the leak-rate of seals. *Journal of Physics: Condensed Matter*, 20(31):315011.
- [Persson, 2001] Persson, B. N. (2001). Theory of rubber friction and contact mechanics. *The Journal of Chemical Physics*, 115(8):3840–3861.
- [Peskin, 2002] Peskin, C. S. (2002). The immersed boundary method. *Acta Numerica*, 11:479–517.
- [Pietrzak and Curnier, 1999] Pietrzak, G. and Curnier, A. (1999). Large deformation frictional contact mechanics: continuum formulation and augmented lagrangian treatment. *Computer Methods in Applied Mechanics and Engineering*, 177(3-4):351–381.
- [Ponson et al., 2006] Ponson, L., Bonamy, D., Auradou, H., Mourot, G., Morel, S., Bouchaud, E., Guillot, C., and Hulin, J. P. (2006). Anisotropic self-affine properties of experimental fracture surfaces. *Int J Fracture*, 140(1):27–37.
- [Popov, 2010] Popov, V. L. (2010). *Contact Mechanics and Friction: Physical Principles and Applications*. Springer-Verlag, Berlin.
- [Popp, 2012] Popp, A. (2012). *Mortar methods for computational contact mechanics and general interface problems*. PhD thesis, Technische Universität München.
- [Powell, 1969] Powell, M. J. (1969). A method for nonlinear constraints in minimization problems. In Fletcher, R., editor, *Proceedings of a Symposium of the Institute of Mathematics and its Applications, held at University of Keele, England, 1968*, pages 283–298. Academic Press, London.
- [Power and Tullis, 1991] Power, W. L. and Tullis, T. E. (1991). Euclidean and fractal models for the description of rock surface roughness. *Journal of Geophysical Research: Solid Earth*, 96(B1):415–424.
- [Prodanov et al., 2014] Prodanov, N., Dapp, W. B., and Müser, M. H. (2014). On the contact area and mean gap of rough, elastic contacts: Dimensional analysis, numerical corrections, and reference data. *Tribol Lett.*, 53:433–448.
- [Prodanov et al., 2013] Prodanov, N., Gachot, C., Rosenkranz, A., Mücklich, F., and Müser, M. H. (2013). Contact mechanics of laser-textured surfaces. *Tribology Letters*, 50(1):41–48.
- [Proudhon et al., 2005] Proudhon, H., Fouvry, S., and Buffière, J.-Y. (2005). A fretting crack initiation prediction taking into account the surface roughness and the crack nucleation process volume. *International Journal of fatigue*, 27(5):569–579.
- [Puso, 2004] Puso, M. A. (2004). A 3D mortar method for solid mechanics. *International Journal for Numerical Methods in Engineering*, 59(3):315–336.

- [Puso et al., 2008] Puso, M. A., Laursen, T., and Solberg, J. (2008). A segment-to-segment mortar contact method for quadratic elements and large deformations. *Computer Methods in Applied Mechanics and Engineering*, 197(6-8):555–566.
- [Puso and Laursen, 2004a] Puso, M. A. and Laursen, T. A. (2004a). A mortar segment-to-segment contact method for large deformation solid mechanics. *Computer Methods in Applied Mechanics and Engineering*, 193(6):601–629.
- [Puso and Laursen, 2004b] Puso, M. A. and Laursen, T. A. (2004b). A mortar segment-to-segment frictional contact method for large deformations. *Computer methods in applied mechanics and engineering*, 193(45-47):4891–4913.
- [Putignano et al., 2012] Putignano, C., Afferrante, L., Carbone, G., and Demelio, G. (2012). The influence of the statistical properties of self-affine surfaces in elastic contacts: A numerical investigation. *Journal of the Mechanics and Physics of Solids*, 60:973–982.
- [Resende and Martin, 1985] Resende, L. and Martin, J. B. (1985). Formulation of drucker-prager cap model. *Journal of Engineering Mechanics*, 111(7):855–881.
- [Rice, 1988] Rice, J. (1988). Elastic fracture mechanics concepts for interfacial cracks. *Journal of Applied Mechanics*, 55(1):98–103.
- [Rice and Sih, 1965] Rice, J. and Sih, G. C. (1965). Plane problems of cracks in dissimilar media. *Journal of Applied Mechanics*, 32(2):418–423.
- [Rockafellar, 1973] Rockafellar, R. T. (1973). The multiplier method of hestenes and powell applied to convex programming. *Journal of Optimization Theory and applications*, 12(6):555–562.
- [Sahlin et al., 2010] Sahlin, F., Larsson, R., Marklund, P., Almqvist, A., and Lugt, P. (2010). A mixed lubrication model incorporating measured surface topography. part 2: roughness treatment, model validation, and simulation. *Proceedings of the Institution of Mechanical Engineers, Part J: Journal of Engineering Tribology*, 224(4):353–365.
- [Scaraggi and Persson, 2012] Scaraggi, M. and Persson, B. (2012). Time-dependent fluid squeeze-out between soft elastic solids with randomly rough surfaces. *Tribology letters*, 47(3):409–416.
- [Sergeant et al., 2018] Sergeant, A., Yastrebov, V. A., Mangeney, A., Castelnaud, O., Montagner, J.-P., and Stutzmann, E. (2018). Numerical modeling of iceberg capsizing responsible for glacial earthquakes. *Journal of Geophysical Research: Earth Surface*.
- [Shapiro, 1996] Shapiro, L. G. (1996). Connected component labeling and adjacency graph construction. In *Machine Intelligence and Pattern Recognition*, volume 19, pages 1–30. Elsevier.
- [Shvarts et al., 2019] Shvarts, A. G., Julien, V., and Yastrebov, V. A. (2019). Computational framework for monolithic coupling for thin fluid flow in contact interfaces. *Submitted to a journal*.
- [Shvarts and Yastrebov, 2018a] Shvarts, A. G. and Yastrebov, V. A. (2018a). Fluid flow across a wavy channel brought in contact. *Tribology International*, 126:116–126.
- [Shvarts and Yastrebov, 2018b] Shvarts, A. G. and Yastrebov, V. A. (2018b). Trapped fluid in contact interface. *Journal of the Mechanics and Physics of Solids*, 119:140–162.

- [Simo and Laursen, 1992] Simo, J. C. and Laursen, T. (1992). An augmented lagrangian treatment of contact problems involving friction. *Computers & Structures*, 42(1):97–116.
- [Šiška et al., 2006] Šiška, F., Forest, S., Gumbsch, P., and Weygand, D. (2006). Finite element simulations of the cyclic elastoplastic behaviour of copper thin films. *Modelling and Simulation in Materials Science and Engineering*, 15(1):S217.
- [Soltz et al., 2003] Soltz, M. A., Basalo, I. M., and Ateshian, G. A. (2003). Hydrostatic pressurization and depletion of trapped lubricant pool during creep contact of a rippled indenter against a biphasic articular cartilage layer. *Journal of biomechanical engineering*, 125(5):585–593.
- [Spence, 1975] Spence, D. (1975). The hertz contact problem with finite friction. *Journal of elasticity*, 5(3-4):297–319.
- [Stupkiewicz, 2001] Stupkiewicz, S. (2001). Extension of the node-to-segment contact element for surface-expansion-dependent contact laws. *International Journal for Numerical Methods in Engineering*, 50(3):739–759.
- [Stupkiewicz, 2009] Stupkiewicz, S. (2009). Finite element treatment of soft elastohydrodynamic lubrication problems in the finite deformation regime. *Computational Mechanics*, 44(5):605–619.
- [Stupkiewicz, 2018] Stupkiewicz, S. (2018). Finite wear and soft elasto-hydrodynamic lubrication: Beyond the classical frictional contact of soft solids. In Popp, A. and Wriggers, P., editors, *Contact Modeling for Solids and Particles*, volume 585, chapter 3, pages 125–176. Springer.
- [Stupkiewicz et al., 2016] Stupkiewicz, S., Lengiewicz, J., Sadowski, P., and Kucharski, S. (2016). Finite deformation effects in soft elastohydrodynamic lubrication problems. *Tribology International*, 93:511–522.
- [Stupkiewicz and Marciniszyn, 2009] Stupkiewicz, S. and Marciniszyn, A. (2009). Elastohydrodynamic lubrication and finite configuration changes in reciprocating elastomeric seals. *Tribology International*, 42(5):615–627.
- [Stupkiewicz and Mróz, 1999] Stupkiewicz, S. and Mróz, Z. (1999). A model of third body abrasive friction and wear in hot metal forming. *Wear*, 231(1):124–138.
- [Suarez-Rivera et al., 1990] Suarez-Rivera, F., Cook, N., Cooper, G., Zheng, Z., et al. (1990). Indentation by pore collapse in porous rocks. In *The 31th US Symposium on Rock Mechanics (USRMS)*. American Rock Mechanics Association.
- [Tada et al., 1973] Tada, H., Paris, P. C., and Irwin, G. R. (1973). The stress analysis of cracks. *Handbook, Del Research Corporation*.
- [Takashi and Hughes, 1992] Takashi, N. and Hughes, T. J. (1992). An arbitrary lagrangian-eulerian finite element method for interaction of fluid and a rigid body. *Computer Methods in Applied Mechanics and Engineering*, 95(1):115–138.
- [Thomas, 1999] Thomas, T. R. (1999). *Rough Surfaces*. Imperial College Press, second edition.
- [Truesdell, 1984] Truesdell, C. (1984). *Mechanics of Solids, Volume II, Linear Theories of Elasticity and Thermoelasticity*. Springer-Verlag Berlin Heidelberg.

- [Tur et al., 2009] Tur, M., Fuenmayor, F., and Wriggers, P. (2009). A mortar-based frictional contact formulation for large deformations using lagrange multipliers. *Computer Methods in Applied Mechanics and Engineering*, 198(37-40):2860–2873.
- [Utku and Carey, 1982] Utku, M. and Carey, G. F. (1982). Boundary penalty techniques. *Computer Methods in Applied Mechanics and Engineering*, 30(1):103–118.
- [Vakis et al., 2018] Vakis, A., Yastrebov, V., Scheibert, J., Minfray, C., Nicola, L., Dini, D., Almqvist, A., Paggi, M., Lee, S., Limbert, G., et al. (2018). Modeling and simulation in tribology across scales: An overview. *Tribology International*.
- [Vallet, 2008] Vallet, C. (2008). *Liquid leakage through a rough contact: application to the internal sealing of valves*. PhD thesis, Arts et Métiers ParisTech. (in French).
- [van Loon et al., 2006] van Loon, R., Anderson, P. D., and van de Vosse, F. N. (2006). A fluid–structure interaction method with solid-rigid contact for heart valve dynamics. *Journal of Computational Physics*, 217(2):806–823.
- [Viesca and Rice, 2012] Viesca, R. C. and Rice, J. R. (2012). Nucleation of slip-weakening rupture instability in landslides by localized increase of pore pressure. *Journal of Geophysical Research: Solid Earth*, 117(B3).
- [Wackers et al., 2011] Wackers, J., Koren, B., Raven, H. C., Van der Ploeg, A., Starke, A., Deng, G., Queutey, P., Visonneau, M., Hino, T., and Ohashi, K. (2011). Free-surface viscous flow solution methods for ship hydrodynamics. *Archives of Computational Methods in Engineering*, 18(1):1–41.
- [Westergaard, 1939] Westergaard, H. M. (1939). Bearing pressures and cracks. *Journal of Applied Mechanics*, 6(2):A49–A53.
- [Whitehouse, 2010] Whitehouse, D. J. (2010). *Handbook of surface and nanometrology*. CRC press.
- [Wohlmuth, 2000] Wohlmuth, B. I. (2000). A mortar finite element method using dual spaces for the lagrange multiplier. *SIAM Journal on Numerical Analysis*, 38(3):989–1012.
- [Wriggers, 2006] Wriggers, P. (2006). *Computational Contact Mechanics*. Springer-Verlag Berlin Heidelberg.
- [Wriggers, 2008] Wriggers, P. (2008). *Nonlinear finite element methods*. Springer Science & Business Media.
- [Yang and Laursen, 2009] Yang, B. and Laursen, T. A. (2009). A mortar-finite element approach to lubricated contact problems. *Computer Methods in Applied Mechanics and Engineering*, 198(47):3656–3669.
- [Yastrebov, 2013] Yastrebov, V. A. (2013). *Numerical methods in contact mechanics*. John Wiley & Sons.
- [Yastrebov, 2018] Yastrebov, V. A. (2018). The elastic contact of rough spheres investigated using a deterministic multi-asperity model. *Journal of Multiscale Modelling*, page 1841002.
- [Yastrebov et al., 2012] Yastrebov, V. A., Anciaux, G., and Molinari, J. F. (2012). Contact between representative rough surfaces. *Phys Rev E*, 86(3):035601(R).

- [Yastrebov et al., 2015] Yastrebov, V. A., Anciaux, G., and Molinari, J.-F. (2015). From infinitesimal to full contact between rough surfaces: evolution of the contact area. *International Journal of Solids and Structures*, 52:83–102.
- [Yastrebov et al., 2017a] Yastrebov, V. A., Anciaux, G., and Molinari, J.-F. (2017a). On the accurate computation of the true contact-area in mechanical contact of random rough surfaces. *Tribology International*, 114:161–171.
- [Yastrebov et al., 2017b] Yastrebov, V. A., Anciaux, G., and Molinari, J.-F. (2017b). The role of the roughness spectral breadth in elastic contact of rough surfaces. *Journal of the Mechanics and Physics of Solids*, 107:469–493.
- [Yastrebov et al., 2011] Yastrebov, V. A., Durand, J., Proudhon, H., and Cailletaud, G. (2011). Rough surface contact analysis by means of the finite element method and of a new reduced model. *CR Mecanique*, 339:473–490.
- [Yu and Cheng, 2002] Yu, B. and Cheng, P. (2002). A fractal permeability model for bi-dispersed porous media. *International Journal of Heat and Mass Transfer*, 45(14):2983–2993.
- [Z-set, 2019] Z-set (2019). Non-linear material and structure analysis suite, version 9.0. MINES ParisTech and Onera, the French Aerospace Lab. <http://www.zset-software.com>.
- [Zienkiewicz and Taylor, 1977] Zienkiewicz, O. C. and Taylor, R. L. (1977). *The finite element method*. McGraw-hill London.

RÉSUMÉ

Cette thèse traite du problème de l'écoulement d'un fluide dans des interfaces étroites entre des solides en contact sous un chargement normal, ce qui est important pour de nombreuses applications en tribologie, ingénierie et géophysique. Le traitement de ce problème nécessite de prévoir un couplage entre la mécanique des fluides et celle des solides. Les contraintes liées à la présence du contact, ainsi que les caractéristiques complexes de la géométrie de surface rajoutent un niveau de complexité significatif. Dans cette thèse, un solveur monolithique par éléments finis permettant la gestion du contact frottant, des écoulements visqueux incompressibles et du transfert des efforts induits par le fluide sur le solide est développé. De plus, la possibilité que le fluide se retrouve piégé dans des cavités délimitées par des zones de contact est prise en compte par l'élaboration d'un nouvel élément dit "de fluide piégé", qui utilise une loi de comportement compressible non linéaire. Le code résultant de cette méthode comprend des algorithmes d'analyse d'image permettant de distinguer les zones de contact, d'écoulement de fluide et de fluide piégé. En outre, le code convient aux approches de couplage uni- et bidirectionnel. Le cadre développé a été appliqué dans un premier temps à l'étude d'un fluide piégé entre un solide déformable présentant une surface de contact ondulée et un plan rigide. Pour un système soumis à une charge externe croissante, nous avons examiné l'évolution de la surface de contact et du coefficient de frottement global en fonction des propriétés du fluide et du solide, ainsi que de la pente du profil de surface. Nous avons ensuite étudié l'écoulement d'un fluide entre un plan rigide et un solide déformable avec une géométrie modèle ou une surface rugueuse. Nous avons obtenu une solution analytique approchée qui gouverne le flux de fluide à travers une interface de contact ondulée, et cette dernière a été comparée à nos résultats numériques. Enfin, nous avons montré pour un intervalle de paramètres physiquement pertinents, que le couplage unidirectionnel sous-estime, par rapport à une approche bidirectionnelle, la perméabilité de l'interface ainsi que la charge externe critique nécessaire à la fermeture de l'interface. Une loi phénoménologique raffinée de perméabilité macroscopique des interfaces de contact rugueuses a été proposée. Enfin, le cadre développé a été utilisé pour calculer l'évolution de la fuite de fluide à travers une interface de contact métal sur saphir en utilisant un comportement matériau élasto-plastique et des mesures réelles de la rugosité de surface.

MOTS CLÉS

Méthode des éléments finis, contact frottant, rugosité de surface, écoulement de fluide mince, couplage multi-physique, fluide piégé

ABSTRACT

This thesis deals with the problem of a thin fluid flow in narrow interfaces between contacting solids subject to a normal loading, which is relevant for a range of tribological and engineering applications, as well as for geophysical sciences. The treatment of this problem requires coupling between fluid and solid mechanics, further complicated by contact constraints and potentially complex geometrical features of contacting surfaces. In this thesis a monolithic finite-element framework for handling frictional contact, thin incompressible viscous flow and transfer of fluid-induced tractions to the solid is developed. Additionally, we considered fluid entrapment in "pools" delimited by contact patches and formulated a novel trapped-fluid element using a non-linear compressible constitutive law. This computational framework makes use of image analysis algorithms to distinguish between contact, fluid flow and trapped fluid zones. The constructed framework is suitable for both one- and two-way coupling approaches. First, the developed framework was applied to a study of a fluid trapped between a deformable solid with a wavy surface and a rigid flat. We showed how the contact area and the global coefficient of friction evolve under increasing external load, depending on fluid and solid properties and on the slope of the surface profile. Next, we studied a thin fluid flow between a rigid flat and a deformable solid with a model geometry or random surface roughness. An approximate analytical solution for the fluid flow across a wavy contact interface was derived and compared with numerical results. We showed that for a range of physically relevant parameters, one-way coupling underestimates the interface permeability and the critical external load needed to seal the interface, compared to the two-way approach. A refined non-local phenomenological law for macroscopic permeability of rough contact interfaces was proposed. Finally, the developed framework was used to calculate the evolution of the fluid leakage through a metal-to-sapphire contact interface using an elasto-plastic material behaviour and real measurements of surface roughness.

KEYWORDS

Finite-element method, frictional contact, surface roughness, thin fluid flow, multi-physical coupling, trapped fluid